IN-SITU CONDUCTIVITY, TEMPERATURE, AND DISSOLVED OXYGEN (CT-DO) SENSOR SYSTEM FOR MARINE MEASUREMENT

By

Xi Huang

A thesis submitted for the degree of Doctor of Philosophy

School of Electronics and Computer Science,
University of Southampton,
United Kingdom.

November, 2011

UNIVERSITY OF SOUTHAMPTON

ABSTRACT

FACULTY OF PHYSICAL AND APPLIED SCIENCES

SCHOOL OF ELECTRONICS AND COMPUTER SCIENCE

Doctor of Philosophy

IN-SITU CONDUCTIVITY, TEMPERATURE, AND DISSOLVED OXYGEN (CT-DO) SENSOR SYSTEM FOR MARINE MEASUREMENT

by Xi Huang

This works describes the development of a miniature high accuracy, low power CT-DO sensor system for in-situ oceanographic measurements. The sensors were fabricated on glass wafers, using micro-fabrication techniques. Three chip designs were made. The sensors in designs 1 and 2 include a seven-electrode conductivity sensor set in a flow channel, a four-ring-electrode open conductivity sensor, a Platinum Resistance Thermometer (PRT) bridge temperature sensor, and a DO sensor based on a platinum electrode inset into five 25 μm deep wells.

A 16-bit impedance measurement circuit was made to support the CT sensor. This has a typical battery life of one month with 10 s sampling interval. The initial CT accuracies are ±0.01 mS/cm and ±0.003 ^{o}C respectively. The seven-electrode conductivity sensor with channel suffered from a durability problem, which was discovered on a mid-Atlantic deployment. This problem was solved with the four-ring-electrode open conductivity and PRT bridge temperature sensor. Dock deployments and 8-week test in a calibration lab showed that the monthly drift was 0.02 mS/cm for the conductivity sensor, and less than 0.01 ^{o}C for the temperature sensor.

The DO sensor was calibrated to have an initial accuracy of ±5 μm. A simple analytical model is proposed to estimate the effect of fluid flow. Tests show that the measured flow effect leads to an error of 1% DO, compared with an estimate of 10%.

The complete CT-DO sensor was tested during a 75 day Indian Ocean cruise. A novel method of bio-fouling mitigation was tested utilizing electro-chemical reactions on the electrodes of the conductivity and DO sensors, and first results are promising. The CT system was also modified to measure low-conductivity solutions. This system was deployed in Greenland and results showed that the CT sensor can also work in fresh water and harsh environments. Future plans are to integrate the electronics into an ASIC, and to include a miniature sensor chip (design 3), to make a package the size of a pen for fish tag applications.

Contents

Chapter 1 Introduction ... 1

1.1 Importance of the work ... 1

1.2 Contributions ... 2

1.3 Document structure ... 3

1.4 Declaration ... 4

Chapter 2 Research Background ... 6

2.1 Salinity measurement ... 6

2.2 Conductivity ... 10

2.2.1 Electrode sensor ... 10

2.2.2 Inductive sensor ... 16

2.2.3 Comparison of both techniques ... 19

2.3 Temperature ... 19

2.4 Depth sensor ... 21

2.5 Impedance measurement circuit ... 22

2.5.1 Voltage-current based circuit ... 22

2.5.2 Frequency based circuit ... 24

2.5.3 Comparison ... 26

2.6 Literature on CTD system ... 27

2.6.1 CT system developed by Gong ... 27

2.6.2 Neil's four-electrode conductivity sensor with zero external field ... 28

2.6.3 Hyldgard's multi-sensor system ... 29

2.6.4 Broadbent's PCB MEMS-based CTD ... 30

2.6.5 Sea-bird serial CTD systems ... 31

2.6.6 Alec CTW ... 32

2.6.7 Cefas G5 DST ... 33

2.6.8 Star-Oddi DST CTD ... 33

2.6.9 Summary of the mentioned CTD systems ... 34

2.7 Dissolved oxygen ... 36

2.7.1 Electrode sensor ... 36

2.7.2 Optode sensor ... 38

2.8 Summary and conclusion ... 39

Chapter 3 The Electrode-Electrolyte Interface 41
3.1 The structure of the electrode-electrolyte interface 41
3.2 Double layer capacitance 44
3.3 Faradaic impedance 46
3.3.1 Charge transfer resistance 49
3.3.2 Warburg impedance 50
3.4 Randles model for AC excitation 51
3.5 Model for DC excitation 52
3.6 Electrochemical reactions in sea water 54
3.6.1 Ag/AgCl electrode 56
3.6.2 Platinum Electrode 56
3.7 Discussions 58
3.7.1 Conductivity sensor 58
3.7.2 Dissolved oxygen sensor 59
3.7.3 Electrochemical cleaning 61
Chapter 4 Sensor Chip Design 62
4.1 Overview of sensor design 62
4.2 Conductivity sensor 70
4.2.1 Channel conductivity sensor 70
4.2.2 Open conductivity cell 75
4.3 Temperature sensor 80
4.3.1 PRT-bridge 80
4.3.2 Response time and sensor package 82
4.4 Dissolved oxygen sensor 85
4.4.1 Diffusion modelling 86
4.4.2 Measurement method and other factors 93
4.4.3 Sensor design 99
Chapter 5 Electronics Design 104
5.1 Impedance measurement circuit for CT sensor 104
5.1.1 Analogue circuit 104
5.1.2 Digital circuit design 109
5.2 Electronics for DO sensor 113
5.2.1 Analogue circuit for two/three electrode system 115
5.2.2 Waveform and measurement 116

Chapter 6 Experimental results 119
6.1 Test of impedance measurement circuit 119
6.1.1 Measurement time 119
6.1.2 Power consumption 120
6.1.3 Measurement accuracy 121
6.2 Calibration and deployment of the CT sensors in design 1 124
6.2.1 PRT-bridge temperature sensor calibration 124
6.2.2 Thermistor calibration 126
6.2.3 Temperature response time test 127
6.2.4 Conductivity sensor calibrations 128
6.2.5 Repeatability testing of the conductivity sensor 130
6.2.6 Deployment of version 1 CT system 131
6.3 Calibration and deployment of the CT sensors in design 2 134
6.3.1 CT sensor calibration 135
6.3.2 Proximity effects of conductivity sensor 137
6.3.3 Dock deployment of version 2 CT sensor system 138
6.4 Improvements in the CT sensors in design 2 141
6.4.1 Summary of existing problems 141
6.4.2 PRT-bridge temperature sensor probe coated with ECG-2702 143
6.4.3 Calibration of conductivity sensor probe in water buckets 147
6.5 Dissolved oxygen sensor 150
6.5.1 Experimental setup 150
6.5.2 Cyclic voltammetry of the DO sensor 152
6.5.3 Calibration of DO sensor 153
6.5.4 Flow effects 155
6.6 Deployment of a complete CT-DO system 156
6.7 Bio-fouling cleaning experiment 162
6.8 Calibration in fresh water 164

Chapter 7 Conclusions and Further Work 166
7.1 Conclusions 166
7.2 Future work 169

References 173

Appendix A – Matlab Script for Salinity Calculation 181

Appendix B – Chip Fabrication Flow 182

List of Figures

Figure 2-1 Plot of salinity versus conductivity, at different temperature (T) and depth (D). Depth of 0 m means surface water with 1 standard atmosphere. 8

Figure 2-2 Plot of salinity versus temperature, at different conductivity (C) and depth (D). 8

Figure 2-3 Plot of salinity versus depth, at different conductivity (C) and temperature (T). 9

Figure 2-4 A simplified equivalent circuit for a two-electrode conductivity sensor. 11

Figure 2-5 Plot of the frequency response of the impedance magnitude for a 10x1x1 mm two-electrode conductivity cell with 1 mm^2 electrode area 12

Figure 2-6 Diagram and equivalent circuit of a four-electrode conductivity cell 13

Figure 2-7 FEM simulation of the electrical potential (greyscale shading) and current distribution (red streamlines) in the conductivity cell. This simulation demonstrates the proximity effect: the current outside the cell is increased by the presence of a conducting object. The conductivity of the surrounding seawater is 60 mS/cm, and the conducting object (7 mm x 2 mm) is set to be platinum, with a conductivity of 9.5×10^7 mS/cm. 14

Figure 2-8 Diagram of the three-electrode Sea-bird conductivity sensor [21]. 15

Figure 2-9 Diagram of the seven-electrode CTW conductivity sensor [25] 16

Figure 2-10 (a) Diagram of single transformer inductivity sensor, M is the water loop which makes the second coil, G is the toroidal case, and K is the coil of the transformer [27]. (b) Circuit of the single transformer sensor. (c) Equivalent circuit of (b). 17

Figure 2-11 (a) Diagram of double transformer inductivity sensor [27]. (b) A trans-impedance amplifier for detecting the current of the second transformer. (c) Equivalent circuit of the double transformer sensor. 18

Figure 2-12 Cross-sectional and top view of a single diaphragm piezo-resistive pressure sensor [53] 22

Figure 2-13 A schematic of an impedance measurement system using square wave for current excitation, and synchronous rectifier for converting the AC voltage response into DC signal. 23

Figure 2-14 A diagram of a Wien bridge oscillator. 25

Figure 2-15 Diagrams of Gong's CT system including: (a) a two-electrode cell; (b) a two-electrode cell with a thin plastic tube to enhance cell constant; (c) schematic of a temperature measurement circuit; (d) schematic of a conductivity measurement circuit [22]. 27

Figure 2-16 Diagrams of a four-electrode conductivity sensor with zero external field [65]. 28

Figure 2-17 Diagrams of Hyldgard's multi-sensor chip [36]: (a) a schematic of the 4 mm wide chip layout including a pressure sensor (p), temperature sensor (t), pn-junction light sensor (l), and four-electrode open conductivity cell (c); (b) a photograph of the multi-sensor chip. 29

Figure 2-18 A schematic of H. A. Broadbent's Φ10x10 cm PCB MEMS-based CTD showing the independent expendable sensor plugs and environmentally protected circuit boards [38]. 30

Figure 2-19 Photographs of Sea-bird's 911plus CTD including: (a) SBE 9plus Underwater Unit; (b) SBE 11plus V2 Deck Unit[17]... 31

Figure 2-20 A photograph of Alec CTW conductivity and temperature sensor system [62]. 32

Figure 2-21 A photograph of Cefas G5 DST [69]. 33

Figure 2-22 A photograph of the Ø17x46 mm Star-Oddi DST CTD [16]. 34

Figure 2-23 A diagram of Clark-type electrode DO sensor... 36

Figure 2-24 A schematic representation of the Sosna's DO calibration system. A: humidifier, B: saturated solution reservoir, C: measurement cell, D: inlet capillary, E: outlet connector, F: argon feed neck, G: valve, H: oxygen feed, WE: working electrode, and RE: reference electrode [55].. 38

Figure 3-1 A diagram demonstrating the structure of the electrode-electrolyte interface, where x_1 is the distance between electrode surface and inner Helmholtz plane (IHP), x_2 is the distance for outer Helmholtz plane (OHP), Φ_M is the potential of the metal electrode, Φ_1 and Φ_2 are the potentials on the IHP and the OHP respectively, σ^i is the charge density in the IHP, σ^d is the charge density in the OHP and diffusion layer. 42

Figure 3-2 A diagram demonstrating the potential profile at the electrode-electrolyte interface. Φ_M is the potential of the metal electrode, Φ^2 is the potential on the OHP, and Φ_S is the potential of the solution bulk, which is set to 0 here....................... 43

Figure 3-3 Plot of the expected behaviour of C_{DL} according to GCS theory as the electrolyte concentration changes, where V_z is the voltage on the electrode at the point of zero charge. 46

Figure 3-4 Randles equivalent circuit for electrode-electrolyte interface. 51

Figure 3-5 Plot of the V-I relation. V is the applied DC voltage on the electrode-electrolyte interface, while I is the stabilized current. 53

Figure 3-6 V-I profile of the platinum electrode-sea water interface. V is the DC voltage applied on the electrode-electrolyte interface, while I is the stabilized current..... 57

Figure 3-7 Diagram of a reference electrode – auxiliary electrode system. 60

Figure 4-1 A diagram of sensor chip structure with a 500 µm thick glass substrate, a platinum layer, and an insulating material layer. 63

Figure 4-2 A diagram showing the masks of the CT sensor chips in design 1, including chip 1-A – a seven-electrode conductivity sensor with a PRT electric-bridge temperature sensor and chip 1-B – a four-electrode conductivity sensor with a PRT electric-bridge temperature sensor. 64

Figure 4-3 A Photograph of the CT sensor chips in design 1, including chip 1-A (left) and chip 1-B (right). 64

Figure 4-4 A diagram of the 4-inch mask of design 1. Two types of chips are implemented in this mask including chip 1-A and chip 1-B. 65

Figure 4-5 A diagram showing the masks of the CT sensor chips in design 2, including chip 2-A – four-ring-electrode open conductivity and DO sensor, chip 2-B – a PRT-bridge temperature sensor, chip 2-C – a seven-electrode conductivity sensor chip to couple with a 2x2 mm water channel, and chip 2-D – a seven-electrode open conductivity sensor. 66

Figure 4-6 A Photograph of the sensor chips in design 2, including chip 2-A (left) and chip 2-B (right). 66

Figure 4-7 A diagram of the 6-inch mask of design 2. Four types of chips are implemented in this mask, including chip 2-A, chip 2-B, chip 2-C, and chip 2-D. 67

Figure 4-8 A diagram showing the mask of the double-side CT sensor chip in design 3: (left) conductivity side; (right) DO side. 68

Figure 4-9 A diagram of the 6-inch mask of design 3. Two types of chips are implemented in this mask, with conductivity chips on the left half, and DO chips on the right half. 69

Figure 4-10 A diagram showing the dimension and signal exciting method of a five-electrode cell. 70

Figure 4-11 An equivalent circuit built in ORCAD of the five-electrode conductivity cell with 50 mS/cm seawater. The sum of resistances R_6, R_7 and R_8 is less than R_{19} because of the conductivity and non zero dimension of electrodes 2 and 3. 71

Figure 4-12 ORCAD simulation result of the inner current and leakage current of the five-electrode conductivity cell 71

Figure 4-13 (a) A diagram showing the signal excitation scheme for the seven-electrode cell, and 2D drawing in COMSOL. Electrode 4 is set to 1 V, and electrodes 1 and 7 are set to 0 V; (b) FEM simulation result for the seven-electrode conductivity cell, where the gray scale is the electrical potential and the streamlines are current density. 73

Figure 4-14 A diagram of the seven-electrode cells with 2x2mm water channel: (left) the conductivity cell using chip 1-A; (right) the conductivity cell using chip 2-C. 75

Figure 4-15 Diagrams of four kinds of geometries of open conductivity cells, including: (Cell A) two electrodes on the same side of the substrate; (Cell B) two electrodes on the opposite sides of the substrate; (Cell C) three electrodes on the same side of the substrate; (Cell D) a round electrode and a ring electrode on the same side of the substrate. 76

Figure 4-16 Diagrams of the electric potential distributions of the four open conductivity cells by FEM simulation. 77

Figure 4-17 A diagram of the four-electrode open conductivity cell on chip 1-B. 79

Figure 4-18 A diagram showing the configuration of chip 2-A: the conductivity and DO multi-sensor chip. 79

Figure 4-19 A diagram of the PRT-bridge temperature sensor chips in both wafer designs 1 and 2. 81

Figure 4-20 A schematic of the PRT-bridge temperature sensor. 81

Figure 4-21 A diagram demonstrating the 3D drawing of a Ø10x15cm sensor package. 82

Figure 4-22 FEM simulation result of the average temperature change of the PRT in static water, when water temperature is 1 K higher and sensor head is 6 mm high. 83

Figure 4-23 FEM simulation result of the average temperature change of the PRT in static water, when water temperature is 1 K higher and sensor head is 11 mm high. 84

Figure 4-24 FEM simulation result of the average temperature change of the PRT in flowing water, when water temperature is 1 K higher and sensor head is 6 mm high 85

Figure 4-25 A diagram demonstrating the one dimensional diffusion for planar electrode. 87

Figure 4-26 Concentration profiles of one dimension diffusion with several times after oxygen diffusion starting. Diffusion constant *D* is set to 2x10^{-5} cm^2/s here. 88

Figure 4-27 A diagram demonstrating semi-infinite spherical diffusion (left), and the semi-infinite hemispherical diffusion (right), in spherical coordinates, with the stream lines showing the oxygen flux 89

Figure 4-28 Concentration profiles of a semi-infinite spherical/hemispherical diffusion with 5 μm radius electrode. Diffusion constant *D* is set to 2x10^{-5} cm^2/s here. 90

Figure 4-29 A diagram demonstrating a micro-disc electrode oxygen cell in a cylindrical coordinates. 92

Figure 4-30 Velocity profile of water flow in a rectangular channel, where the maximum flow rate is v_0, and the width of the channel is *2h*. 96

Figure 4-31 Plot of the transient current and the additional current induced by flow versus time for a disc electrode with 10 μm radius. The plotted additional current induced by the flow is magnified by 100 to estimate when the flow changes the current by 1% (point identified on plot). The diffusion coefficient is set to 2x10^{-5} cm^2/s, with a maximum flow velocity of 100 cm/s in a 2 cm wide rectangular channel. 97

Figure 4-32 A diagram of oxygen sensor cell with a disc platinum electrode in a well, using micro fabrication technique 100

Figure 4-33 FEM simulation in COMSOL for flow velocity field of a rectangular water channel with 3 wells, where the colour shows the velocity field. The mesh dimension is about 0.1 mm in the wells 101

Figure 4-34 Plot of FEM simulated flow velocity in the wells along the *y*-direction. 102

Figure 5-1 A block diagram of CT sensor system, including CT sensors and supporting circuit for impedance measurement. 104

Figure 5-2 A photograph of the analogue circuit PCB for the impedance measurement system. 105

Figure 5-3 Schematic of a common design for the trans-impedance amplifier. 106

Figure 5-4 Schematic of the improved trans-impedance amplifier design for the conductivity cell. 107

Figure 5-5 Schematic of the simplified equivalent circuits for the trans-impedance amplifier: (a) for DC signal; (b) for AC signal. 107

Figure 5-6 A schematic of the trans-impedance amplifier with multiplexers. 108

Figure 5-7 Photographs of the digital circuit PCBs for the impedance measurement system: (a) FPGA board; (b) optional USB communication board. 110

Figure 5-8 Diagrams showing the software development kits: (a) CCS C compiler; (b) program downloading software. 111

Figure 5-9 Block diagram of two/three electrode electrochemical sensor system, supporting DO measurement. 113

Figure 5-10 A photograph of the PCB for the DO analogue circuit and USB communication. Two amplifiers (U6 and U7) for the feedback module are unsoldered here as this PCB is configured as for two-electrode electrochemical system. 114

Figure 5-11 A photograph of the complete CT-DO electronics with three layers of PCBs, where the CT analogue circuit PCB is on the bottom, the digital circuit PCB is in the middle, and the PCB of DO analogue circuit and USB connection is on the top. 115

Figure 5-12 A schematic of the circuit design for the trans-impedance and amplifying module, where the voltage of working electrode is set to 0V, and the current passing through the working electrode is converted into a voltage output for ADC. 116

Figure 5-13 Plot of the voltage waveform applied on working electrode against solution bulk for DO measurement. 117

Figure 5-14 Plot of the voltage waveform in the waveform module for DO measurement. 118

Figure 6-1 Plot of the transient voltage response sampled by the ADC of the impedance measurement circuit, when measuring a 500 Ω resistor using a 1 kΩ gain resistor. 120

Figure 6-2 Plot of the battery life of the CT sensor system versus measurement time interval. 121

Figure 6-3 Plot of the measurement error of the impedance measurement circuit for four resistors, X-axis is the resistor value read from a multimeter, curve shows the average error (i.e. the difference between the value measured with a multimeter (accuracy 0.1 Ω) and the mean of 100 measurements made with the impedance circuit), and error bar shows the distribution (range) of this difference. 122

Figure 6-4 Plot of voltage responses from two calibration resistors, when the temperature of the analogue circuit was changed by touching the PCB............ 123

Figure 6-5 A photograph of the unpackaged CT sensor system using chip 1-A as the CT sensor. 124

Figure 6-6 Plot of the measurement error of PRT-bridge temperature sensor, with error bar showing the standard deviation of the 100 repeated measurements on each temperature point. 125

Figure 6-7 Plot of the thermistor calibration results, where the curve shows the average bias errors, and the error bar shows the standard deviation errors...................... 126

Figure 6-8 A photograph of the version 1 CT system with a Ø10x15 cm cylinder package. 127

Figure 6-9 Plot of the temperature data from the thermistors with heights of 0 mm and 3 mm, response time is estimated by comparing the temperature data from the thermistors and the reference temperature probe.. 128

Figure 6-10 Plot of the conductivity sensor calibration results, where the curves show the average bias errors, and the error bars show the standard deviation errors: (a) four-electrode open cell; (b) seven-electrode cell with channel. 129

Figure 6-11 Plot of the calibration results of the seven-electrode cell with channel (chip 1-A) in three seawater samples. 130

Figure 6-12 Plot of the four-electrode open cell (chip 1-B) calibration results in two seawater samples... 131

Figure 6-13 Photographs of the deployment of the version 1 CT system in the Atlantic. 132

Figure 6-14 Plot of temperature and salinity data collected at 24.5N, -62.55W, at a depth of 0.4 m, with sampling interval of 10 s. Data shown is from a 40 minute deployment... 132

Figure 6-15 Plot of the conductivity calibration results of a version 1 CT system, before and after the Atlantic cruise. 133

Figure 6-16 Plots of the conductivity sensor voltage of a version 1 CT system during the calibrations: (a) before the Atlantic cruise; (b) after the Atlantic cruise. 134

Figure 6-17 Photograph of a version 2 CT system in the Ø10X15cm package, where the chip 2-A and chip 2-B are placed horizontally on the top of the package.......... 135

Figure 6-18 Plot of calibration results for the four-ring-electrode open conductivity sensor on chip 2-A. The sensor was placed in 30 psu seawater, with temperature changed from 4 to 34 ^{o}C in 5 ^{o}C increments for each calibration. The calibration was performed for three times. 136

Figure 6-19 Plot of calibration results for the PRT-bridge temperature sensor on chip 2-B. The surrounding water temperature was changed from 4 to 34 ^{o}C in 5 ^{o}C increments for each calibration. The calibration was performed for three times. 136

Figure 6-20 A photograph of the experiment setup for the proximity effect test of chip 2-A, where plastic pen is place 5 mm away from the centre of the ring-electrode. 138

Figure 6-21 Plot of temperature and salinity data from the version 2 CT system during the first two weeks dock deployment.. 139

Figure 6-22 Plot of salinity data from the version 2 CT system and recorded water depth during the first two weeks dock deployment. 139

Figure 6-23 A photograph of the version 2 CT system after first two weeks dock deployment.. 140

Figure 6-24 Plot of the temperature data sampled from the version 2 CT system (blue curve) and the Idronaut CTD probe (red curve) in a dock deployment.............. 140

Figure 6-25 Plot of the salinity data sampled from the version 2 CT sensor system (blue curve) and the Idronaut CTD probe (red curve) in a dock deployment.............. 141

Figure 6-26 Photograph of the CT sensor probe, where the temperature sensor probe (chip 2-B) is on the left, and conductivity sensor probe (chip 2-A) is on the right. 142

Figure 6-27 Photograph of a version 2 CT sensor system, where the conductivity sensor chip is placed vertically on the left, and temperature sensor chip is coated inside a aluminium sleeve on the right.. 143

Figure 6-28 Calibration results for the temperature sensor probe of chip 2-B coated with ECG-2702. The surrounding water temperature was changed from 5 to 35 ^{o}C in 5 ^{o}C increments for each calibration. The calibration was performed for three times.. 144

Figure 6-29 Plot of calibration result for the temperature sensor probe of chip 2-B coated with ECG-2702. The surrounding water temperature was changed from 5 to 35 ^{o}C in 5 ^{o}C increments for each calibration.. 145

Figure 6-30 Plot of the measurement error of the ECG-2702 coated temperature sensor probe in a 5-week test. The surrounding water temperature was changed periodically from 5 to 35 °C in 5 °C increments. 146

Figure 6-31 Plot of the data for the dip in test of the temperature sensor probe. The probe was firstly kept in the air of about 20.5 °C, and then immersed into water with temperature of 14.89 °C at 63 s.. 147

Figure 6-32 Plot of the calibration result for the conductivity probe of chip 2-A in four seawater samples. *R* in the equation is cell resistance, and *C* is water conductivity. 148

Figure 6-33 Plot of the drift error for the conductivity sensor probe of chip 2-A after 8 weeks in water, with temperature changing from 5 to 30 °C periodically........... 149

Figure 6-34 A photograph of the DO sensor probe, which consists of a DO sensor chip and an external Ag/AgCl electrode in front of the sensor chip........................... 150

Figure 6-35 (a) Photograph of the experimental apparatus used to test the DO sensor. (b) Schematic of the experimental apparatus used to test the DO sensor................. 151

Figure 6-36 Plot of current-voltage relationship of the DO sensor during the CV test. The CV was performed in two water samples. One was purged with N_2 resulting in a near zero oxygen concentration, and the other was bubbled with air and had an oxygen concentration of about 270 μM. The transient current was measured at 10ms, 15ms, 25ms, and 35ms after the ramp of the measurement voltage. 152

Figure 6-37 Plot of the calibration result of the DO sensor. Transient current was measured at 10 ms, 15 ms, 25 ms, and 35 ms after the ramp of the measurement voltage, and is plotted versus the oxygen concentration.................................... 154

Figure 6-38 Plot of the flow test data of the DO sensor probe. Transient current was measured at 15 ms and 35 ms after the ramp of the measurement voltage. Water flow was applied between 600 and 1200 s... 155

Figure 6-39 A photograph of the CT-DO sensor head. 157

Figure 6-40 A photograph of the complete CT-DO system, including the main electronics box with USB connection cable, and two CT-DO sensor heads. 157

Figure 6-41 A diagram demonstrating the routing of the Indian Ocean rowing boats. The CT-DO system was installed in the boat which followed the route shown by a dark purple trace. 158

Figure 6-42 Plot of the recorded salinity data for the Indian Ocean of May, 2005. 159

Figure 6-43 Plot of the recorded temperature data for the Indian Ocean of April, 2011. 159

Figure 6-44 Plot of the salinity, temperature, and oxygen data from the CT-DO system of the Indian Ocean rowing boat. The data is from 21st April, 2011 to 1st May, 2011. 160

Figure 6-45 Plot of the salinity, temperature, and oxygen data from the CT-DO system on the Indian Ocean rowing boat. The data is from 7th May, 2011 to 17th May, 2011. 160

Figure 6-46 Plot of the salinity, temperature, and oxygen data from the CT-DO system of the Indian Ocean rowing boat. The data is from 6th June, 2011 to 18th June, 2011. 161

Figure 6-47 Plot of the 2 s periodical waveform for chlorine generation........ 162

Figure 6-48 Photograph of the two 2-A sensor chips before a 2 weeks dock deployment for bio-fouling test. The chip on the left is applied with the cleaning wave form, while the chip on the right is not........ 163

Figure 6-49 Photograph of the two sensor chips after a 2-week deployment in Empress Dock Southampton for bio-fouling test. The chip on the left had the cleaning wave form applied to it, while the chip on the right did not. Note that the electrodes are only present on one side of the chip and the chip is transparent. The bio-fouling seen on the chip with the waveform applied is predominantly on the side without electrodes. 164

Figure 6-50 Plot of the conductivity calibration result for the version 2 CT system, in the conductivity range of 8~94 µS/cm for fresh water application. 165

Figure 7-1 Diagram of an unfinished PCB design for CT-DO system with bio-fouling cleaning function........ 171

Figure 7-2 3D diagram of the version 3 CT-DO system with a Ø5x14 cm stainless steel packaging and a sensor chip of design 3........ 172

List of Tables

Table 1-1 Specifications of the CT-DO sensor system.. 2
Table 2-1 Estimated components values for an 10x1x1 mm two-electrode conductivity cell with 1 mm^2 electrode area.. 12
Table 2-2 Resistance values for various popular PRTs and thermistors with a temperature range of 0~30 °C... 21
Table 2-3 Comparison of the existing CTD systems... 35
Table 3-1 Thickness of the diffuse layer for KCl solution of different concentrations at 25 °C [32]... 45
Table 3-2 Concentrations of major species present in seawater @ Salinity = 35 psu [101]... 54
Table 3-3 List of electrochemical reactions for sea water, ordered by their standard electrode potential from low to high. The legends behind the reagents' names indicate the reagents' form: *(s)* – solid, *(l)* – liquid, *(g)* – gas, *(aq)* – aqueous. Reagents in red text are rare in sea water, in blue text are provide by the electrode, in black are in sea with certain concentrations. 55
Table 4-1 FEM simulation results for the resistances of the open cells with different diameters of surrounding water. 78
Table 7-1 Comparison of our sensor system and other salinity sensor systems.......... 168

Acknowledgements

First of all, I'd like to thank Prof. Hywel Morgan and Dr. Matt Mowlem for their wonderful supervision. Their guidance, ideals and resources are essential to this project. I also greatly appreciate the independence they allowed me to have in this PhD project, and the help they gave in my personal life. I thank Katie Chamberlain, who manufactured the sensor chips for me, and Robin Pascal, who helped me to set up the calibration environment. I'd like to thank the people who helped me for the sensor deployments, including Chris Banks, Alex Beaton, Alexandra Meier, and the Indian Ocean Team. My thanks also go to Edward Waugh for his help in both my work and life.

I would also like to thank Nurul, Robert, Diego, Dan, Mark, Marcel, Veronica, Nefeli, Mahadji, Dave, Iain, and all the past and present members of Morgan's and Mowlem's groups for making this PhD experience so enjoyable. Particularly my thanks go to these Chinese guys– Tao, Xiaojun, Yan, Chunxiao, and Shilong.

Finally and most importantly, I'd like to thank all my family, and in particular to my wife – Shimin, who accompanied me here for three years, and gave me great present – my daughter Yue.

Definitions and Abbreviations Used

CT	Conductivity and Temperature
CTD	Conductivity, Temperature and Depth
DO	Dissolved Oxygen
C-DO	Conductivity and Dissolved Oxygen
CT-DO	Conductivity, Temperature and Dissolved Oxygen
DST	Data Storage Tag
MEMS	Micro-Electro-Mechanical Systems
RTD	Resistance Temperature Device
PRT	Platinum Resistance Thermometer
PTC	Positive Temperature Coefficient
NTC	Negative Temperature Coefficient
IHP	Inner Helmholtz Plane
OHP	Outer Helmholtz Plane
IPE	Ideal Polarized Electrode
SCE	Saturated Calomel Electrode
SHE	Standard Hydrogen Electrode
NHE	Normal Hydrogen Electrode
AC	Alternating Current
DC	Direct Current
ADC	Analogue-to-Digital Converter
DAC	Digital-to-Analogue Converter
DSP	Digital Signal Processing
PCB	Printed Circuit Board
LPF	Low-pass Filter
OPA	Operational Amplifier
IA	Instrument amplifier
MUX	Multiplexer
FEM	Finite Element Methods
MCU	Micro Controllor Unit
ASIC	Application Specific Integrated Circuit
FPGA	Field Programmable Gata Array
SOC	System-on-a-Chip

SNR	Signal-to-Noise Ratio

Chapter 1 Introduction

1.1 Importance of the work

The oceans cover over approximately 71% of the planet (Data Announcement 88-MGG-02, Digital relief of the Surface of the Earth. NOAA, National Geophysical Data Center, Boulder, Colorado, 1988.), and play an important role in maintaining global climate and ecosystems. With increasing environmental change, the importance of studying the oceans has increased dramatically. The determination of ocean temperature and salinity is essential for the study of the marine environments. These measurements can be used to trace water masses, and to describe ocean circulation, mixing and climate processes. Measurements of temperature and salinity also provide a physical context for measurements of biogeochemical cycles and marine ecosystems.

A Conductivity, Temperature, and Depth (CTD) sensor is the primary tool for determining the properties of sea water. Depth sensors are occasionally omitted because the calculation of salinity is only weakly affected by pressure (depth). Dissolved Oxygen (DO) is another vital parameter for ocean and environment science. It gives important information on biological processes, water masses mixing and movements.

In addition to ocean and environment applications, in-situ CT-DO sensor systems are required by many industries, including water industry, aquaculture, boreholes and catchments, etc. A NERC funded pathfinder project report (“Ultra Miniature CT-DO: Commercial Opportunities Assessment”, Jan Peter Katalytic Ltd) indicates a global annual market of £200M for these sensors, and this market is expected to grow substantially as the cost of the sensors is reduced.

Existing best commercial CTD systems measure salinity to 0.001 psu accuracy, but they are large, power hungry and very expensive (typically £12,000). Smaller data storage tags (DSTs) have been developed to measure temperature and salinity. However they are inaccurate (typically 1 psu accuracy). Commercial DO sensors are also large. Therefore, there is not a miniature system combining CT and DO sensor together.

1.2 Contributions

This PhD project has developed a miniature, low power, high accuracy CT-DO system. The system is designed primarily for oceanographic applications, but considerations are also given to fresh water applications. The system is portable, with up to one year battery life and the currently achieved accuracies are shown in Table 1-1.

Sensors	Conductivity	Temperature	Dissolved oxygen
Range	10~70 mS/cm	-2~30 °C	0~1000 µM
Accuracy	±0.01 mS/cm	±0.003 °C	±5 µM

Table 1-1 Specifications of the CT-DO sensor system.

The key contributions of this project are as follows:

1. Three designs of CTDO sensors were made in this work. Chip designs 1 and 2 were tested, and design 3 is still being manufactured. Two versions of the complete system were developed. Version 1 used the CT sensors of chip design 1, and version 2 used the CT-DO sensors of chip design 2.
2. A novel seven-electrode channelled conductivity sensor with no external field was made and tested using design 1.
3. A novel sensor chip was made and tested using chip design 2. This can be used as either a four-electrode open conductivity sensor, or a DO sensor with five 25 µm deep wells.
4. Platinum Resistance Thermometer (PRT) bridge temperature sensor was made and tested using both chip designs 1 and 2. Different insulation materials were evaluated to solve drift problem, and finally a monthly drift of less than 0.01 °C was achieved.
5. A 16-bit impedance measurement circuit with three-parameter sine fitting algorithm was developed to support the CT sensor, with a typical battery life of 1 month at 10 s sampling interval.

6. The electrochemical reactions were summarised for the platinum–seawater interface. The relationship between the applied voltage and measured current of this interface was analysed, defining suitable voltages for DO measurement.
7. A conservative analytical model was purposed to estimate the effect of DO from fluid flow. Test result showed that the actual flow effect is 1%, 10% of that predicted by the model.
8. A novel method for bio-fouling prevention was tested utilizing electro-chemical reactions on the electrodes of the conductivity and DO sensors. This has provided promising result.
9. Several deployments of the sensor system were carried out. CT system version 1 was tested in a 7 weeks mid-Atlantic cruise. CT system version 2 was tested during a 6 week dock deployment. The complete CT-DO sensor was tested over a 75 day Indian Ocean cruise. Furthermore, a Greenland deployment of CT system version 2 was carried out to evaluate the performance in fresh water applications.
10. Considerations were given to future work, including system versions 3 and 4. The electronics in version 3 will be redesigned from version 2 to have smaller dimension and 1 year+ battery life. In version 4, the electronics will be integrated into an ASIC to produce a system size of a pen.

1.3 Document structure

The structure of the thesis is listed as below:

- Chapter 2 introduces the background and related literature for the CT-DO systems, giving project targets.
- Chapter 3 describes the theory of the electrode-electrolyte interface for conductivity and DO sensors, and discusses an electrochemical method for bio-fouling remediation.
- Chapter 4 presents the three different designs of CT-DO sensor, and proposes a method to estimate flow effects on the DO sensor.
- Chapter 5 describes the electronic circuit design for CT and DO system.

- Chapter 6 presents experimental results for the CT-DO sensor, and test result of bio-fouling cleaning.
- Chapter 7 presents conclusions and makes recommendations for future work.

1.4 Declaration

This thesis describes the research undertaken by the author while working within a collaborative research environment. This report documents the original work of the author except in the following sections:

- The sensor chips were manufactured by Katie Chamberlain in the Nano Group, School of Electronics and Computer Science, University of Southampton, UK.
- The waveform of DO sensor was suggested by Robin Pascal (Sensor Group of the National Oceanography Centre, UK) and Dr Guy Denuault (School of Chemistry, University of Southampton, UK).
- The deployment in a mid-Atlantic cruise was carried out by Dr. Chris Banks in the Satellite Group of the National Oceanography Centre, UK.
- The deployment in the Indian Ocean cruise was carried out by Team Indian Ocean 3100 [1].
- The deployment in Greenland was carried out by Alex Beaton in the Sensor Group of the National Oceanography Centre, UK.
- The bio-fouling cleaning experiment was carried out cooperation with Alexandra Meier in the Sensor Group of the National Oceanography Centre, UK.

Parts of this work have been published as:

- X. Huang, M. Mowlem, R. Pascal, K. Chamberlain, C. Banks, and H. Morgan, "A Miniature High Precision Conductivity and Temperature Sensor System for Ocean Monitoring," the 14th International Conference on Miniaturized Systems for Chemistry and Life Sciences, Groningen, The Netherlands, 2010.
- X. Huang, R. Pascal, K. Chamberlain, C. Banks, M. Mowlem, and H. Morgan, "A Miniature, High Precision Conductivity and Temperature

Sensor System for Ocean Monitoring," Sensors Journal, IEEE, vol. PP, pp. 1-1, 2011.

Chapter 2 Research Background

Salinity, temperature and dissolved oxygen are three important parameters for study of the marine environment. This chapter presents background knowledge for the measurement of these properties, including measurement principles, supporting electronics, and related work.

2.1 Salinity measurement

The classical method of salinity determination is to analyze seawater by chlorinity titration. Another way is to use a refractometer, as the refractive index of seawater is a function of salinity [2-6]. However devices using these methods are either too large [3-5] or not accurate enough [2, 4, 6] to be used for an in-situ miniature high precision sensor system.

In 1893, the Norwegian chemist Hercules Tornóe proposed that salinity of seawater could be determined by measuring the electrical conductivity of the water. and showed that the conductivity is also influenced by temperature [7]. Based on this principle, Martin Knudsen designed an instrument which made it possible to determine the salinity and temperature of the seawater without collecting water samples or pulling the thermometer out of the water [7]. In 1978, salinity was formally redefined in Practical Salinity Scale (PSS) based on the electrical conductivity of seawater by the Joint Panel of the United nations Educational, Scientific and cultural Organization (UNESCO) [8]. PSS is defined in terms of the ratio (K_{15} see equation 2-1) of the electrical conductivity of the seawater sample at a temperature of 15 °C and a pressure of one standard atmosphere, to that of a potassium chloride (KCl) solution with a mass fraction of 32.4356 g/kg, at the same temperature and pressure [9-11]. As PSS is a function of a ratio, it has no units, but normally is written in the unit “psu” (Practical Salinity Unit). 1 psu is similar but not exactly equal to 1 gram of salt per litre. The relation between the ratio K_{15} and PPS (S) is not linear but defined as a 5th-order polynomial in the range of 2 to 42 psu shown by equation 2-1, and a ratio of 1 is equivalent to 35 psu.

$$S = a_0 + a_1 K_{15}^{1/2} + a_2 K_{15} + a_3 K_{15}^{3/2} + a_4 K_{15}^{2} + a_5 K_{15}^{5/2} \qquad [2\text{-}1]$$

As the conductivity of seawater is directly related to temperature and pressure, the PSS is a function of conductivity, temperature, and pressure, and defined in [8].
The relation between CTD and salinity can be described by a simple Matlab [12] script, and presented in appendix A [8, 13, 14]. Measuring these three parameters together, and then calculating the salinity has become the most popular and precise method for salinity measurement.

According to the World Ocean Atlas (WOA 2009, NOAA, National Geophysical Data Center, 2010), the ocean salinity varies from 33 to 37 psu, with an average of 35 psu. Similarly, the ocean temperature varies from -2 to 30 ^{o}C. The deepest part of the ocean is the Challenger Deep in the Marianas Trench (10911 m) [15], yet approximately 98.8% of the surface area of the oceans is less than 6000 m deep (Data Announcement 88-MGG-02, Digital relief of the Surface of the Earth. NOAA, National Geophysical Data Center, Boulder, Colorado, 1988.). As salinity, temperature and depth change in these ranges, the conductivity of the seawater varies from 26~62 mS/cm [8]. Coastal water may have a higher or lower salinity than ocean water, taking the conductivity out of the 26~62 mS/cm range. Therefore commercial conductivity sensors extend the measurement range from 10mS/cm [16] or lower [17] to 70mS/cm [17]. As an aid to understanding the relationship between the measured parameters C (conductivity), T (temperature), and D (depth) and the calculated salinity, figures 2-1 to figure 2-3 show plots of salinity versus each of these parameters, whilst keeping the other two parameters fixed.

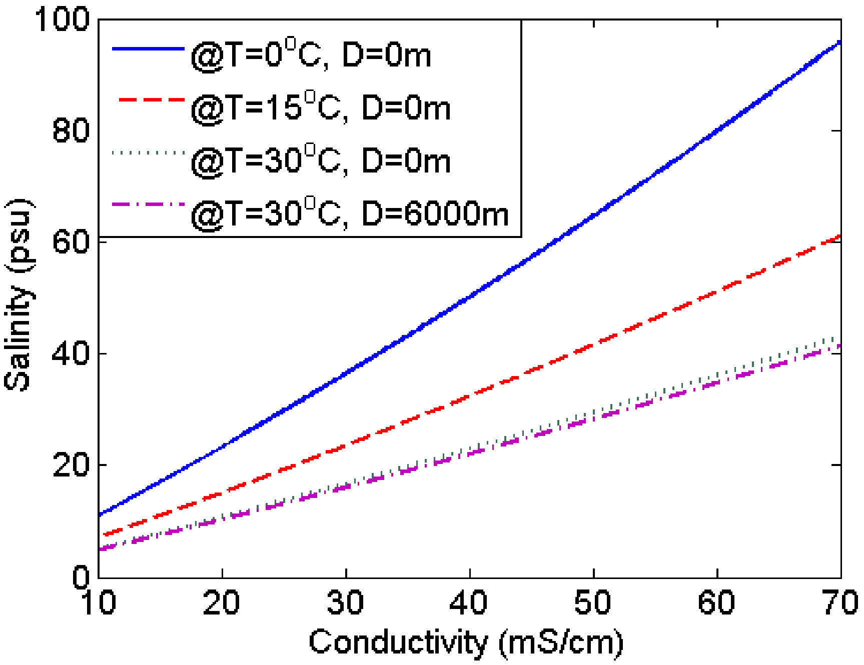

Figure 2-1 Plot of salinity versus conductivity, at different temperature (T) and depth (D). Depth of 0 m means surface water with 1 standard atmosphere.

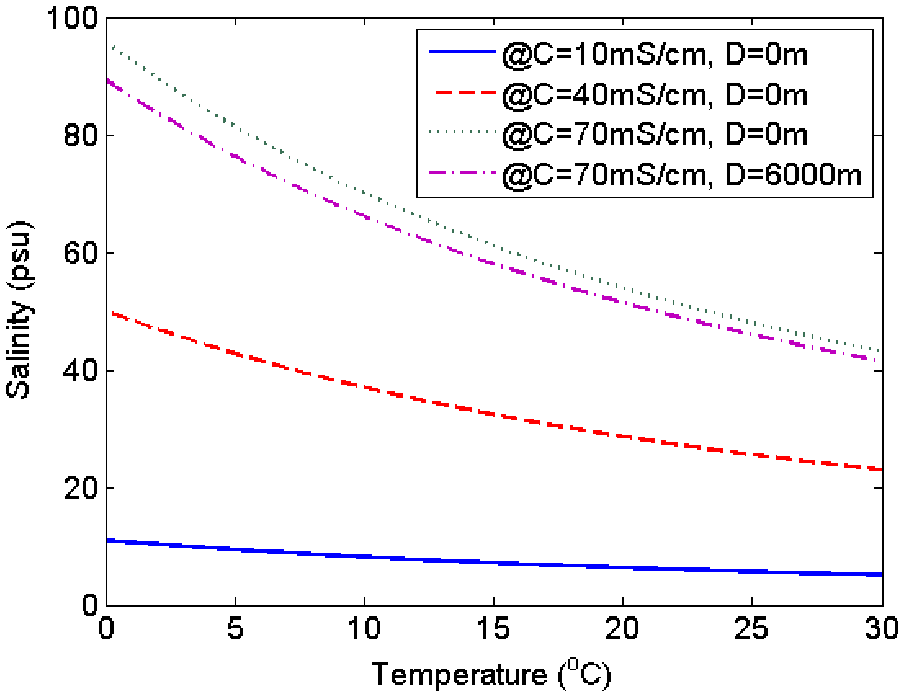

Figure 2-2 Plot of salinity versus temperature, at different conductivity (C) and depth (D).

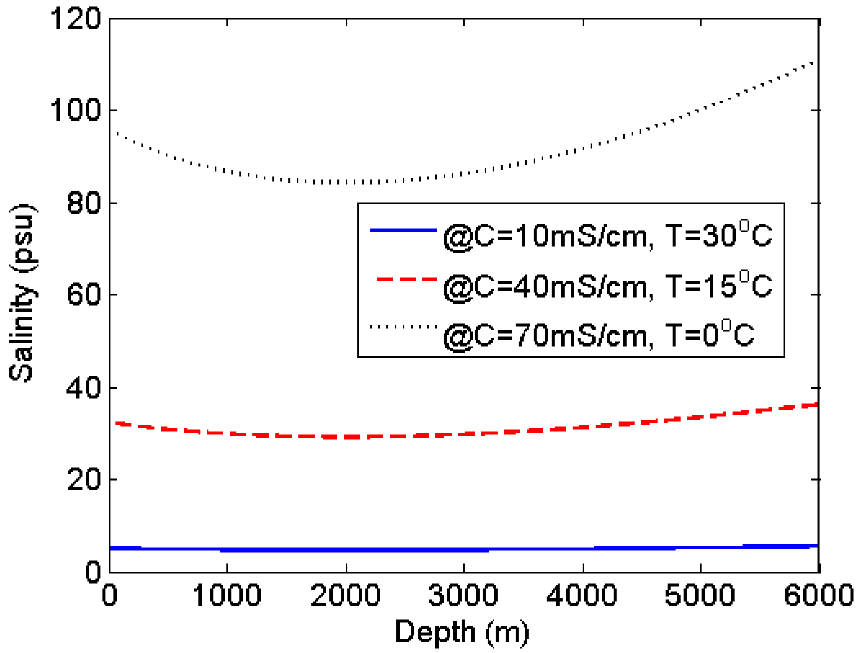

Figure 2-3 Plot of salinity versus depth, at different conductivity (C) and temperature (T).

As shown in the figures, calculated salinity has an almost linear relationship with conductivity, with an average coefficient of 0.9 psu per mS/cm at 15 °C. Temperature also has a significant effect on calculated salinity (because conductivity for a fixed salinity is a strong function of temperature), but the effect is not linear, with an average slope of 0.9 psu/°C at a conductivity of 40 mS/cm. However, depth has very little effect on salinity measurement. It only causes about 10% change in calculated salinity over the depth range from 0 to 6000 m.

As many applications only focus on salinity measurements within a depth of 0~200 m, it is reasonable to omit depth measurement, and assume a depth of 100 m. The salinity error caused by this assumption is only about ±0.4 psu. Furthermore, the deployment depths in many applications are roughly known, so this information can be used to reduce the error. Even in applications where this is not true (i.e. the depth is not know and the accuracy required demands its measurement), there are commercially available sensors with a range of competitive performance and prices [18-20]. Therefore, depth sensing was not considered rate limiting and further development of this technology was not included within the project.

2.2 Conductivity

There are two main types of conductivity sensors: electrode [21-26] and toroidal or inductive [27-29] sensors. Electrode sensors contain two [22], three [21], four [23, 24] or seven [25, 26] electrodes. In both two and four electrode based systems all of these electrodes are used to measure the resistance (R) of the liquid. Additional electrodes are included in other designs to constrain the electric field. Conductivity (C, or σ) is directly proportional to the conductance ($1/R_s$). The proportionality coefficient (Cell constant, κ) depends on the geometry of the electrodes and the geometry and size of the water volume in the vicinity of the electrodes. Toroidal or inductive sensors usually contain two coils, sealed within a nonconductive housing. The first coil induces an electrical current in the water, while the second coil detects the magnitude of the induced current, which is proportional to the conductivity of the water.

2.2.1 Electrode sensor

Electrode sensors use electrodes directly in contact with a liquid to measure the liquid resistance (R_s), and determine the conductivity (σ) by:

$$\sigma = \frac{\kappa}{R_S} \qquad [2\text{-}2]$$

The cell constant κ depends on the geometry of the surrounding liquid and the electrodes. Normally a channel is used to define the geometry of the liquid.

The interface between the electrode and the liquid is describe by a Randles model [30, 31], and is normally simplified to a double-layer capacitance when AC excitation is used. A further introduction to this electrode-electrolyte interface is present in chapter 3.

Two-electrode conductivity sensor

The two-electrode conductivity sensor is the simplest electrode sensor. A simplified equivalent circuit for a two-electrode conductivity sensor is presented in figure 2-4:

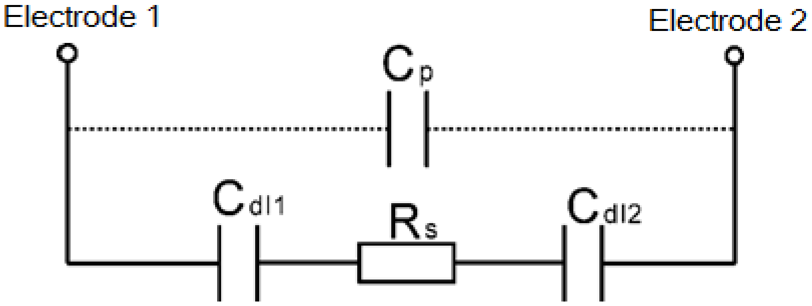

Figure 2-4 A simplified equivalent circuit for a two-electrode conductivity sensor.

where R_s is the liquid resistance, C_{dl1} and C_{dl2} are the double-layer capacitance on the two electrodes, and C_p is the stray capacitance between the two electrodes.

The magnitude of the impedance measured by the two electrodes is assumed to be the resistance of the liquid (R_s). Obviously, measurement accuracy is affected by the voltage drop across the double-layer capacitance of the electrode. This effect is called electrode polarization. Since the impedance of a capacitor changes with frequency, the measurement accuracy will also depend on the frequency of the excitation signal.

To illustrate this, consider the geometry of a two-electrode cell, defined as follows: the cross section of a water channel has the same dimension as each electrode and is 1 mm^2 (1 mm by 1 mm); the distance between the two electrodes is 10 mm. This geometry gives a cell constant κ = 100 cm^{-1} (distance divided by cross section). Therefore R_s can be calculated from this cell constant and equation 2-2 accordingly. The double-layer capacitance is estimated to be 40 µF/cm^2 [32], therefore a 1 mm^2 electrode has a double-layer capacitance of 400 nF. The stray capacitance between the two electrodes can be estimated using the plate capacitance model:

$$C_p = \frac{\varepsilon_0 \varepsilon_r A}{d} \qquad [2\text{-}3]$$

where ε_0 is the permittivity of free space with a value of 8.854187817620× 10^{-12} F·m^{-1} [33], ε_r is the relative permittivity of the water, which is about 80 at 20^{o}C [34], A is the 1 mm^2 electrode area, and d is the 10 mm distance between the two electrode. The calculated C_p is about 0.7 pF and insignificant. However, larger stray capacitance may be induced by the connection wires for the electrode. Therefore C_p is estimated to be 10 pF.

For seawater with conductivities ranging from 5~70 mS/cm, estimates of the components are shown in table 2-1. The frequency response of the impedance magnitude for the two-electrode cell is presented in figure 2-5:

C_p	C_{dl1}	C_{dl2}	R_s (Conductivity)				
10 pF	400 nF	400 nF	20000 Ω (5 mS/cm)	10000 Ω (10 mS/cm)	3333 Ω (30 mS/cm)	2000 Ω (50 mS/cm)	1429 Ω (70 mS/cm)

Table 2-1 Estimated components values for an 10x1x1 mm two-electrode conductivity cell with 1 mm^2 electrode area.

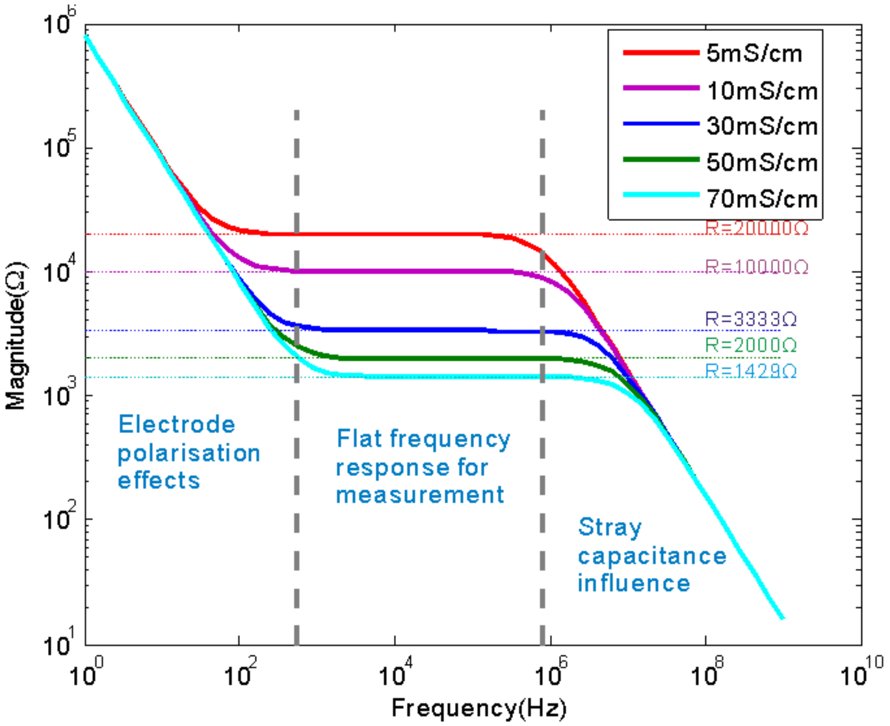

Figure 2-5 Plot of the frequency response of the impedance magnitude for a 10x1x1 mm two-electrode conductivity cell with 1 mm^2 electrode area.

As shown in figure 2-5, when the frequency is low, the impedance of C_p ($^{1}/_{j\omega C_p}$, where ω is the angular frequency of the excitation signal) is very big, and most of the current goes through R_s. But because of the voltage drop across the double-layer capacitances (C_{dl1} and C_{dl2}), the measured impedance magnitude will be higher than R_s. This electrode polarisation effect diminishes at increasing frequencies. However, at higher frequencies, the impedance of C_p will decrease, so that a part of the injected current will go through C_p. Therefore the impedance magnitude will be lower than R_s because of stray capacitance.

For a certain R_s, we find a frequency range where the measurement gives only the resistance R_s. However, because R_s changes with conductivity, it is still hard to use a single frequency that allows measurement of an unknown conductivity with accuracy better than 99.9%. For example, for the 10x1x1 mm two-electrode cell, using a frequency window of 50 kHz results in a maximum measurement error of about 0.1% (in a conductivity range 5~70 mS/cm). This leads to a 0.07 mS/cm error when the conductivity is 70 mS/cm. As we are aiming to achieve 0.01 mS/cm accuracy, the two-electrode sensor is not suitable.

Four-electrode conductivity sensor

The four-electrode conductivity sensor is designed to remove electrode polarisation effects. Figure 2-6 presents the design and the equivalent circuit for the four-electrode sensor with a water channel.

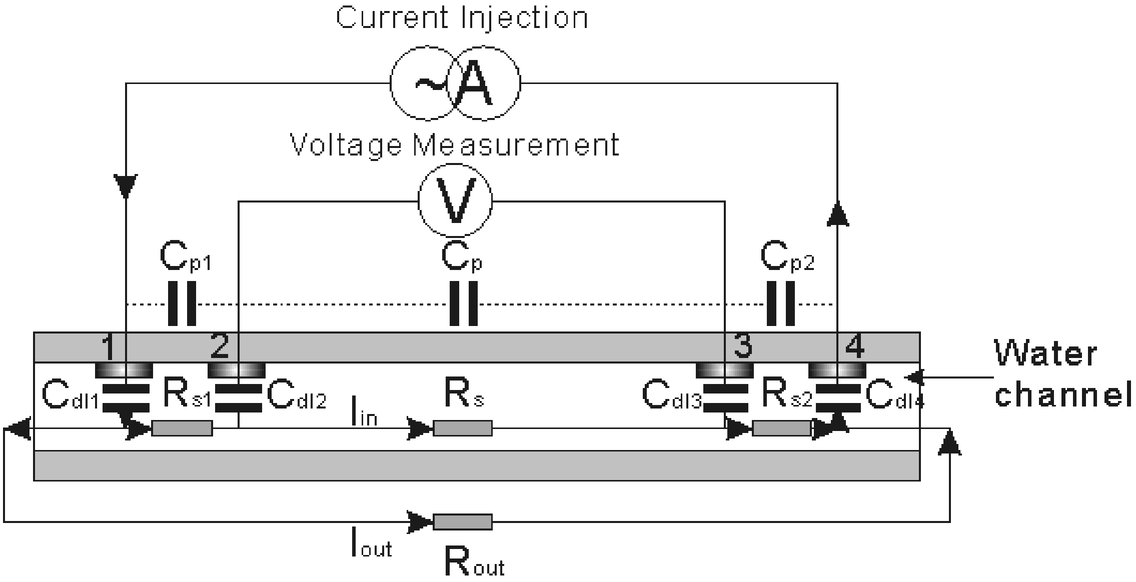

Figure 2-6 Diagram and equivalent circuit of a four-electrode conductivity cell.

It uses four-terminal measurement technique. The excitation current is injected from electrode 1 and 4. A differential amplifier is used to detect the voltage from electrode 2 and 3. When exciting with a relatively low frequency signal (to prevent stray capacitance influence), the current through the stray capacitances (C_{p1}, C_{p2}, C_p) can be ignored. Therefore, because the differential amplifier has very high input impedance, no current flows through the double layer capacitances on electrodes 2 and 3 (C_{dl2}, C_{dl3}). This means that there is no voltage drop across C_{dl2} and C_{dl3}, and we measure the voltage drop of the water resistance (R_s) directly. Hence the polarisation effect is removed.

Proximity effects

The electric field generated by the electrodes is distributed over a relatively large volume. Therefore the cell constant κ will be modified if any insulating or conducting object moves into the electric field; this is called the proximity effect.

Proximity effects are commonly reduced by constraining the electric field inside a channel. However, for the conductivity sensor with a water-filled channel, part of the electric field is still external and susceptible to proximity effects. Figure 2-7 shows a 2D numerical simulation (using COMSOL [35]) of the electric potential and current distribution for a four-electrode sensor, showing that the external current is affected by a conducting object causing proximity effects.

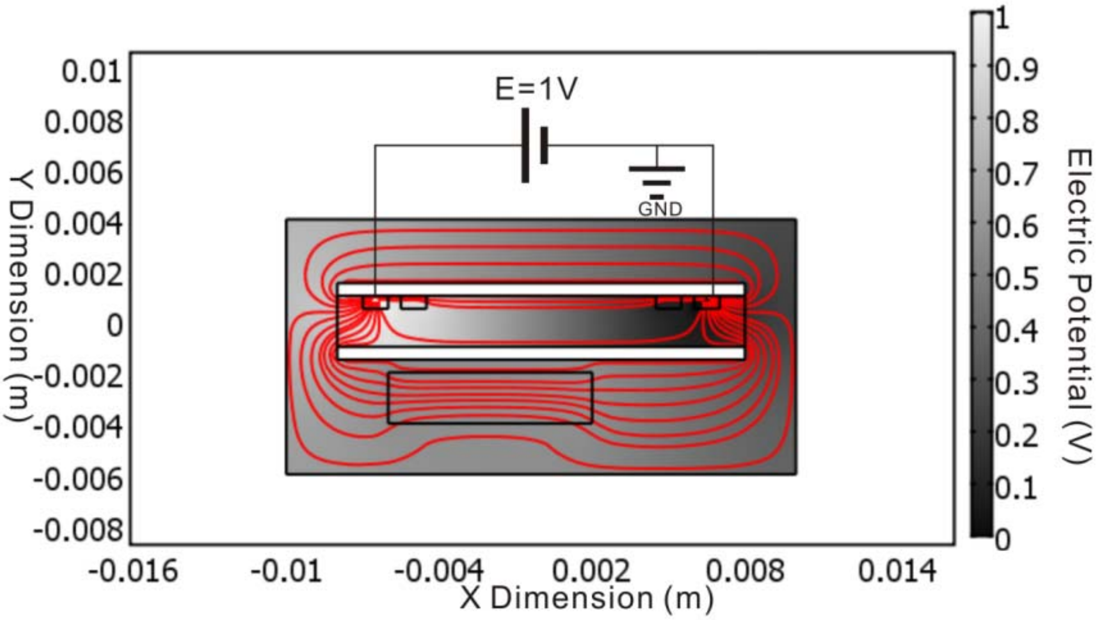

Figure 2-7 FEM simulation of the electrical potential (greyscale shading) and current distribution (red streamlines) in the conductivity cell. This simulation demonstrates the proximity effect: the current outside the cell is increased by the presence of a conducting object. The conductivity of the surrounding seawater is 60 mS/cm, and the conducting object (7 mm x 2 mm) is set to be platinum, with a conductivity of 9.5×10^7 mS/cm.

As shown by simulation, when the cell is immersed in seawater, part of the current leaks into the surrounding water. If a conducting object (rectangular metal object 7x2 mm) moves near (within 1 mm of) the channel, the external current increases from 1.036 to 1.182 A/m, while the internal current reduces from 1.019 to 1.015 A/m. This simulation uses a constant voltage for cell excitation. Normally the cell is excited by a constant current I_{total}, and the internal current $I_{internal}$ keeps a certain ratio k to I_{total} if no proximity effect occurs. The response voltage V is measured from the two inner electrodes, which is directly proportional to $I_{internal}$:

$$V = I_{internal} R_{inner} \tag{2-4}$$

where R_{inner} is the water resistance between the two inner electrodes. The cell constant κ is:

$$\kappa = \sigma \frac{V}{I_{total}} = \sigma R_{inner} k \tag{2-5}$$

Because κ is directly proportional to the ratio k of the internal current to the total current, any changes in this ratio will affect the cell constant, causing measurement error. In the simulation, the proximity effect causes a 7% measurement error by changing this ratio by 7%. Another simulation also shows that, when an insulating object is placed 1 mm from the channel, the proximity effect causes a 5% error. This error is bigger than the 0.01 mS/cm accuracy we are aiming to achieve. Therefore methods need to be found to reduce the proximity effect.

There are two main methods to reduce this proximity effect. One is to reduce the external electric field. The other is to constrain the electric field only to the cell volume.

The external electric field can be reduced by extending the length of the water channel [24], but this method will increase the dimension of the sensor. Some designs add counter electrodes to the opposite end of the channel, and keep the geometry and voltage of the sensor symmetrical. Therefore a symmetrical version of a two-electrode sensor becomes a three-electrode sensor, and that of a four-electrode sensor becomes a seven-electrode sensor. As an example, the Sea-bird conductivity sensor [21] uses a three-electrode sensor as shown in figure 2-8. By setting electrode 1 and 3 to the same potential, the external electric field is much reduced. Another example is the CWT conductivity sensor [25], which uses a seven-electrode sensor as shown in figure 2-9.

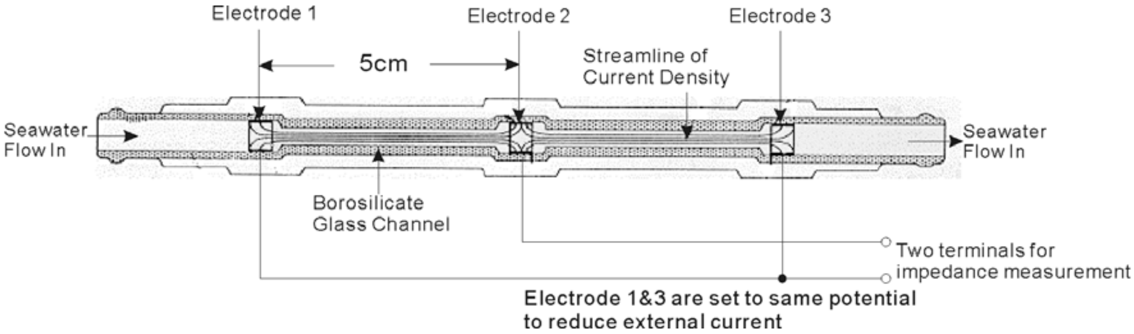

Figure 2-8 Diagram of the three-electrode Sea-bird conductivity sensor [21].

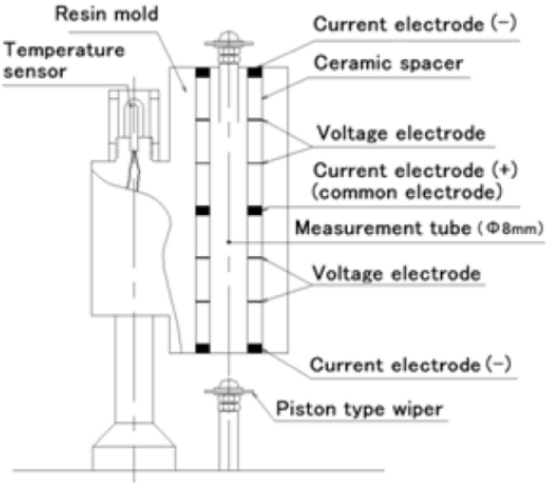

Figure 2-9 Diagram of the seven-electrode CTW conductivity sensor [25].

A longer channel reduces the ratio of external current to internal current. However, it also makes the external current distributed over a larger volume. To confine all the electric field close to the sensor area, some designs eliminate the channel [36-38]. These open conductivity cells may be manufactured on micro chips, and electrodes with specialized patterns are designed to constrain most of the electric field very close to the cell area. These designs don't require a large volume of surrounding water. In addition, if an insulating or conducting object moves close to the cell, the electric field isn't significantly affected. Hence proximity effects can be reduced. However, if objects move very close to the electrodes, the electric field is severely affected, and an error in the measurement occurs.

2.2.2 *Inductive sensor*

Inductive sensors contain one or two transformers. A toroidal case is used to protect the coils of the transformers, and allow water to flow through the centre of the coils.

Single transformer sensor

The single transformer sensor is the simplest inductive sensor. Figure 2-10 shows an inductive sensor with one transformer, and its equivalent circuit. The second coil is formed by the surrounding liquid.

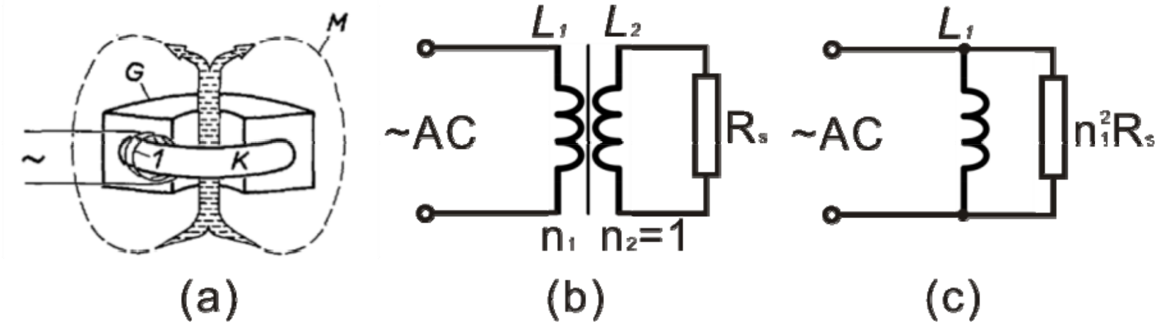

Figure 2-10 (a) Diagram of single transformer inductivity sensor, M is the water loop which makes the second coil, G is the toroidal case, and K is the coil of the transformer [27]. (b) Circuit of the single transformer sensor. (c) Equivalent circuit of (b).

As shown in the figure, R_s is the liquid resistance. As described in the electrode sensor section, the liquid conductivity σ is determined by equation 2-2, where the cell constant κ depends on the geometry of the surrounding liquid. According to figure 2-10 (c), the relation between the excitation AC voltage U and current I is given by equation 2-6:

$$I = \left(\frac{1}{j\omega L_1} + \frac{1}{{n_1}^2 R_S}\right) U \qquad [2\text{-}6]$$

Because the inductance of the primary coil L_1, coil number n_1, and excitation frequency are known, by measuring U and I, R_s and σ can be calculated.

Double transformer sensor

Double transformer sensors contain two transformers. Figure 2-11 shows a diagram of a double transformer sensor, and the equivalent circuit:

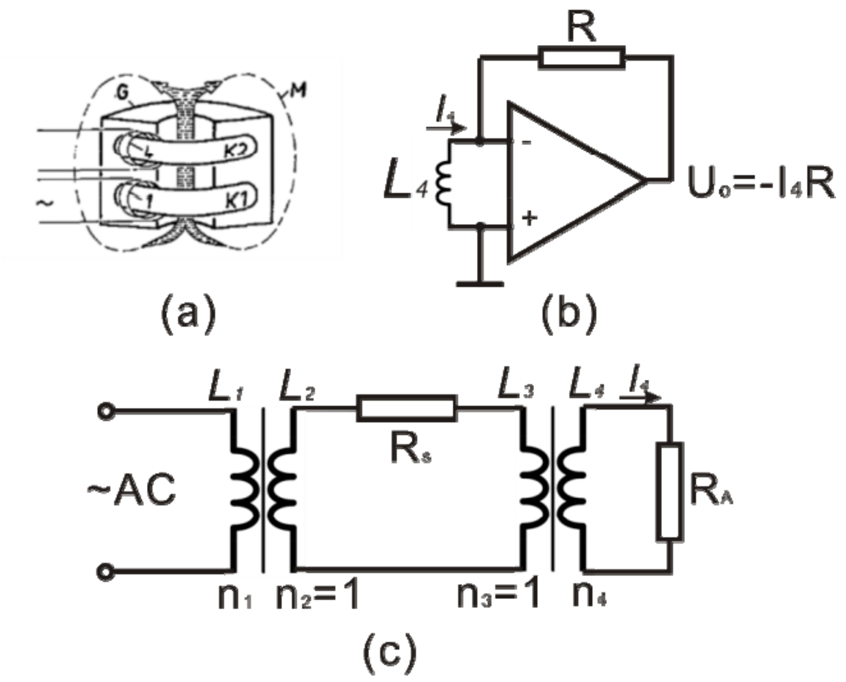

Figure 2-11 (a) Diagram of double transformer inductivity sensor [27]. (b) A trans-impedance amplifier for detecting the current of the second transformer. (c) Equivalent circuit of the double transformer sensor.

The first transformer is used for signal excitation, and the second transformer for signal detection. The relation between the excitation voltage U_1 on the first transformer and response voltage U_4 on the second transformer is:

$$U_4 = \frac{n_4}{n_1}\frac{1}{1+{n_4}^2R_S(\frac{1}{R_A}+\frac{1}{j\omega L_4})}U_1 \qquad [2\text{-}7]$$

As shown in figure 2-11(b), a trans-impedance amplifier is used to measure the current in the second transformer (I_4):

$$I_4 = -{}^{U_o}\!/_{R} \qquad [2\text{-}8]$$

where U_o is the output voltage of the amplifier, and R is the trans-impedance resistor. The input impedance of this amplifier (R_A) is 0. Therefore, I_4 becomes:

$$I_4 = \lim_{R_A\to 0}\left({}^{U_4}\!/_{R_A}\right) = \frac{U_1}{n_1 n_4 R_S} \qquad [2\text{-}9]$$

Compared with the single transformer sensor, the advantage of the double transformer sensor is that it doesn't need to measure the phase of the excitation signal. Furthermore, as the inductance of the transformers does not appear in equation 2-8 and 2-9, the double transformer is independent of inductance.

2.2.3 Comparison of both techniques

Both electrode and inductive sensors are based on impedance measurement. Therefore they have similar requirements for the supporting electronics, and similar accuracy.

The cell constant of the conductivity sensor is defined by the geometry of the surrounding water. Therefore, both electrode and inductive sensors will be influenced by proximity effects. The AC magnetic field of the water loop makes the electric field of inductive sensors distributed over a relatively large area, without any good method of constraining it. However electrode sensors can use a symmetric design to constrain all the electric field within a water channel, or a specific electrode pattern to constraint the electric field very close to the sensor cell, minimizing the proximity effect. Furthermore, as the proximity effect is often caused by bio-fouling, the electrode sensor can be used to generate chlorine, potentially removing any bio-fouling (this will be discussed in chapter 3). Therefore, the electrode sensor can be designed to have less proximity effect than the inductivity sensor.

The inductive sensor is protected by a toroidal case, while the electrode sensor is in direct contact with water. Therefore inductive sensors should have better durability. However, if the electrode sensor is made from inert materials like glass and platinum, it will also have a very good durability. Electrode sensors, especially without a channel, can be made on a micro chip with tiny dimension. However the dimension of the inductive sensor is relatively large due to the toroidal case, and is more costly to produce than a chip based on planar electrodes.

In summary, the electrode sensor has similar accuracy to the inductive sensor, but has advantages in minimizing proximity effect and smaller dimensions, but the possible disadvantage of durability. With further development this could be mitigated by using inert materials and developing methods of bio-fouling reduction. Therefore it was decided to use an electrode sensor for the conductivity sensor.

2.3 Temperature

The oceans have a relative small temperature range, generally between -2 and 30 ^{o}C. The surface temperature of the ocean can be easily monitored by satellite using a microwave sensor with a typical accuracy of 0.5 ^{o}C [39]. However, as there is significant subsurface structure to the deep sea, temperature profiles and more accurate surface measurements are of scientific value. Therefore a temperature sensor is required in an in-situ sensor system.

Some common temperature sensors are not suitable for in-situ ocean measurement, such as mercury glass tube thermometer, thermocouple, and quartz thermometer. For mercury glass tube thermometer, it is hard to convert the reading into a digital signal and record it. Thermocouples have a very large temperature measurement range of -180 to 2320 °C, however they do not have sufficient resolution and precision over the ocean temperature range [40-42]. Quartz thermometers can measure temperature in atmospheric pressure with very high resolution of 0.0001 °C [43-45], based on the frequency of a quartz crystal oscillator. However, they are very sensitive to water pressure and not suitable for under water measurement.

The most popular sensors for measuring the temperature of seawater are RTDs (Resistance Temperature Devices) [36-38, 46, 47] and thermistors [22, 48-50].

RTDs use a sensing element whose resistance varies with temperature, usually with a positive temperature coefficient. RTDs are usually made of coils or films of metals such as platinum, gold, copper and nickel. For MEMS (Micro-Electro-Mechanical Systems) sometimes some silicides are also used as RTDs, for example, Ti_2Si [36, 37]. The relation between temperature and resistance of RTD can be described by a polynomial:

$$R_T = R_0(1 + a_1T + a_2T^2 + \cdots + a_nT^n) \qquad [2\text{-}10]$$

Here, R_T is the resistance at temperature T; R_0 is the resistance at 0 °C; $a_1 \sim a_n$ are the polynomial coefficients. The coefficients values and polynomial order n depend on the material of the RTD and the required accuracy.

Platinum RTDs, usually called PRTs (Platinum Resistance Thermometers), have a near perfect linear resistance-temperature relationship and are very chemically inert. PRT elements are commercially available and widely used in industry. They have nominal resistance of 100 Ω or 1000 Ω at 0 °C, and are called Pt-100 or Pt-1000 sensors respectively.

Thermistors can be classified into two types depending on the temperature coefficient of resistance (k_T). If k_T is positive, the resistance increases with increasing temperature, and the device is called a Positive Temperature Coefficient (PTC) thermistor. If k_T is negative, the resistance decreases with increasing temperature, and the device is called a Negative Temperature Coefficient (NTC) thermistor.

For comparison, table 2-2 lists the resistance values for various popular PRTs and thermistors with a temperature range of 0~30 °C:

Temperature (°C)	Pt100 (Ω)	Pt1000 (Ω)	PTC Type: 201 (Ω)	NTC Type: 101 (Ω)
0	100,00	1000,0	1628	23868
5	101,95	1019,5	1700	18299
10	103,90	1039,0	1771	14130
15	105,85	1058,5	1847	10998
20	107,79	1077,9	1922	8618
25	109,73	1097,3	2000	6800
30	111,67	1116,7	2080	5401

Table 2-2 Resistance values for various popular PRTs and thermistors with a temperature range of 0~30 °C.

Compared to PRTs, NTC thermistors are more sensitive to small temperature changes. They are suitable for low cost and simplified applications. However, as PRTs have higher stability [51] and repeatability [52], they are suitable for high stability demanded applications.

2.4 Depth sensor

The piezo-resistor is a popular material for a depth sensor [36, 37, 53-55]. As shown in figure 2-11, a depth sensor usually consists of several piezo-resistors distributed at different positions in a hollow die. By applying pressure to the die, different stresses will be applied to the piezo-resistors at different positions and the resistance change of these piezo-resistors will be different. Normally a Wheatstone bridge [56, 57] is used to convert the differences of these resistance into a voltage signal. The pressure and depth can be calculated from this voltage signal.

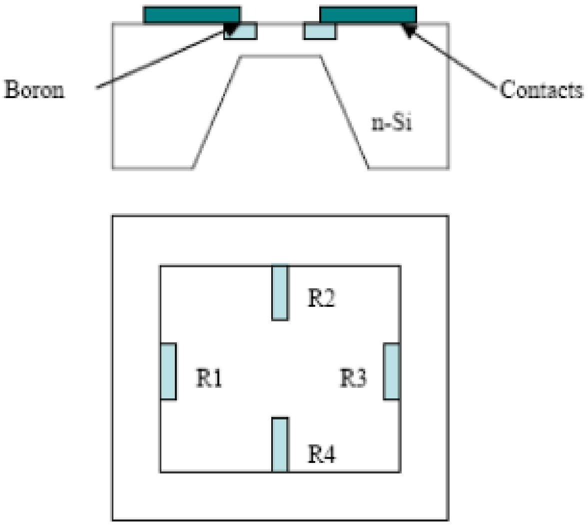

Figure 2-12 Cross-sectional and top view of a single diaphragm piezo-resistive pressure sensor [53].

Depth is a minor parameter for salinity measurement as discussed before. Furthermore, many miniature depth sensors are commercially available, including [18-20]. Therefore this PhD project did not focus on developing a depth sensor, and commercial sensors can be easily embedded into our system if needed.

2.5 Impedance measurement circuit

All CTD sensors are impedance-based sensors. An impedance measurement circuit is extremely important for supporting the sensors, and issues include accuracy, response time, sampling rate, power consumption, dimension, and storage capability of the sensor system. There are two main types of impedance measurement circuit. One uses the ratio of voltage to current to calculate the impedance, while the other converts impedance into frequency signal to calculate impedance.

2.5.1 Voltage-current based circuit

This kind of circuit usually uses an AC current source to excite the sensors, and an analogue-to-digital converter (ADC) to collect the voltage response from the sensors. The impedance value(s) of the sensor(s) can be calculated from the ratio of the response voltage to the excitation current.

Most existing systems use square waves for excitation [22, 23, 58]. A schematic of a square wave excitation system is presented in figure 2-13:

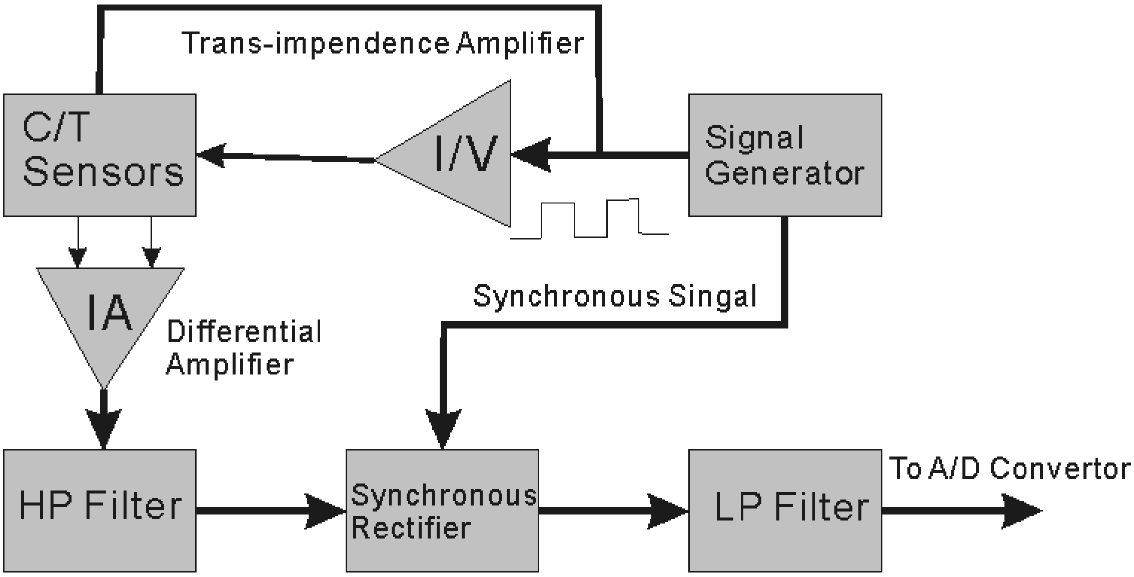

Figure 2-13 A schematic of an impedance measurement system using square wave for current excitation, and synchronous rectifier for converting the AC voltage response into DC signal.

A signal generator is used to generate a square wave voltage signal. A trans-impedance amplifier is used to translate the voltage signal to current signal, and excite the sensor as a current source. Then a differential amplifier is used to amplify the voltage signal response from the sensor, while a high-pass filter is used to remove the DC component of the square wave. Subsequently, a synchronous rectifier is used to rectify the negative part of the square wave into a positive part. Therefore the square wave will be converted into a DC signal, whose amplitude is proportional to the voltage response from the CT sensor. Finally, a low-pass filter is used to remove the remaining ripple components present in the DC signal which is then digitised by the ADC.

In the square wave excitation system, most of the signal processing work is done in the analogue domain, but this has several disadvantages. First, errors are induced by the imperfect synchronous rectifying system and the non-linear response of the rectifier. Second, the low-pass filter needs a relative long time for signal setup, which decreases the maximum measurement frequency and increases the power consumption. Furthermore, it cannot measure the phase of the impedance.

With high speed, high accuracy ADCs, some impedance measurement systems remove the high-pass filter and the rectifier, and use a sine wave for excitation [24, 59, 60]. In these systems, the voltage response from the sensor is converted into a digital signal directly by a high speed ADC, and all the signal processing is performed by the digital circuit. By using a sine wave fitting algorithm [60], both amplitude and phase information can be calculated.

An analogue sine wave can be described as following:

$$u(t) = Asin(2\pi ft) + Bcos(2\pi ft) + C \qquad [2\text{-}11]$$

There are 4 parameters in the formula: A, B, C and f. The AC amplitude and phase of sine wave can be calculated from A, B as following:

$$Amplitude = \sqrt{A^2 + B^2} \qquad [2\text{-}12]$$

$$Phase = \arctan\left(-\frac{B}{A}\right) \qquad [2\text{-}13]$$

C is the DC component, and f is the signal frequency.

If the signal frequency f is a certain ratio to the sampling frequency of the ADC, f can be set as a constant when fitting in the digital domain. Therefore a three-parameter sine wave fitting algorithm can be used for real-time processing; otherwise, a four-parameter sine-fitting should be used. This fitting is done as follows. The sample data is stored and an initial value for f is assumed to perform the first three-parameter sine wave fit. The correlation coefficient between the sample data and fitted data is determined. The value of f is slightly altered and another fit performed, providing a direction in which to increase the correlation coefficient. Subsequent iterations are made by stepwise adjustment of f to achieve a result with maximum correlation coefficient [59]. This four-parameter sine-fit is hard to use in a real-time processing application and an external data buffer is required for sample data storage.

2.5.2 Frequency based circuit

Frequency based circuits do not support full impedance measurement. This technique usually employs a Wien bridge oscillator to convert the resistance of the sensor into a frequency signal. This frequency signal is applied to a digital counter. The frequency is calculated by the number counted over a fixed measurement time, and the resistance is calculated from this frequency. A diagram of Wien bridge oscillator is shown is in figure 2-14:

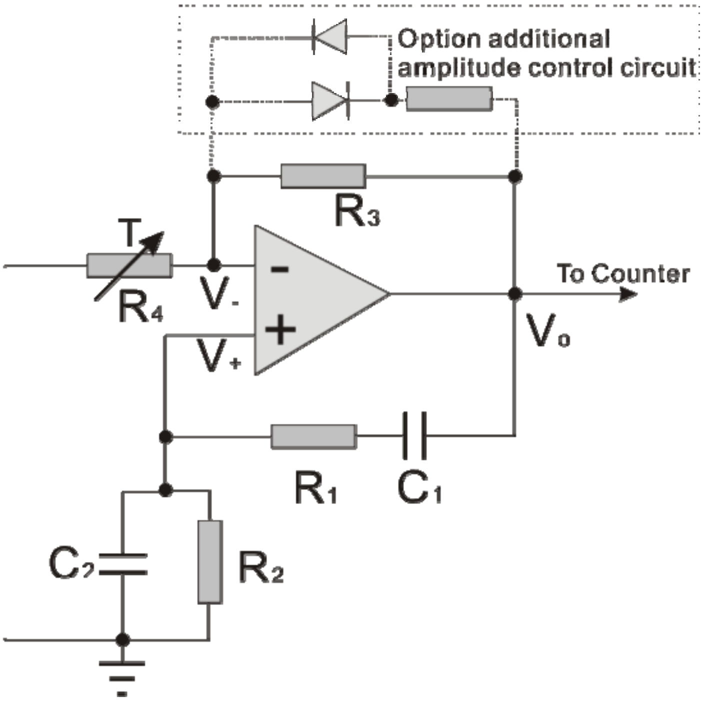

Figure 2-14 A diagram of a Wien bridge oscillator.

As shown in figure 2-14, the operational amplifier has both positive feedback and negative feedback. The voltages on positive terminal (V_+) and negative terminal (V_-) are given by:

$$V_+ = V_o \frac{\frac{1}{j\omega C_2+1/R_2}}{R_1+1/j\omega C_1+\frac{1}{j\omega C_2+1/R_2}} = \frac{V_o}{\left(1+\frac{R_1}{R_2}+\frac{C_2}{C_1}\right)+j(\omega R_1 C_2-\frac{1}{\omega R_2 C_1})} \quad [2\text{-}14]$$

$$V_- = V_o \frac{R_4}{R_3+R_4} = V_o(1-\frac{R_3}{R_3+R_4}) \quad [2\text{-}15]$$

The oscillator oscillates at the frequency ω_0 which allows V_+ and V_- to have the same phase 0. Therefore the ω_0 is given by:

$$\omega_0 R_1 C_2 - \frac{1}{\omega_0 R_2 C_1} = 0 \quad [2\text{-}16]$$

$$\omega_0 = \frac{1}{\sqrt{R_1 R_2 C_1 C_2}} \quad [2\text{-}17]$$

The oscillation amplifies if the negative terminal has smaller feedback, and attenuates if it has bigger feedback. One method to achieve an oscillation with steady amplitude is using a PTC thermistor for R_4. The thermistor has a small resistance in normal temperature. This keeps the negative feedback smaller than positive feedback at the beginning of the oscillation, amplifying the amplitude. With an increase of the amplitude, the temperature of the PTC increases, raising the resistance of R_4. Therefore negative feedback increases with amplitude until equal to the positive feedback, then the oscillating amplitude becomes stable. Another method is using the optional circuit shown in figure 2-14. This circuit uses a diode network with a small resistor to restrict the voltage drop across R_3. When the amplitude is small, the diodes are off, allowing the oscillation to amplify. When the amplitude increases to a certain level, the diodes turn on, increasing negative feedback through adding a parallel connection of a small resistor to R_3. Then the amplitude stops amplifying and becomes steady.

When using the Wien bridge oscillator for impedance measurement, one of the resistors R_1 and R_2 is replaced by the sensor, while the other is a precision resistor with known value. The values of the other precision capacitors C_1 and C_2 are also known. Therefore the resistance of the sensor can be calculated from the measured frequency ω_0, according to equation 2-17.

2.5.3 Comparison

The frequency based circuit has fewer components, and can measure resistance over a wide range. Furthermore, it doesn't need an ADC, but only a counter to convert the frequency into a digital signal. However, as a two terminal measurement, it cannot support a Wheatstone bridge measurement, and the measurement is affected by the impedance of the connection cables. In addition, it is hard to control the oscillation amplitude, which might lead to overheating of the CT sensor causing measurement error.

On the other hand, the voltage-current based circuit has four terminals for impedance measurement, and can support Wheatstone bridge. By injecting current and measuring voltage from different terminals, measurement results will not be affected by the impedance of cables or the double-layer capacitance of conductivity sensor. The measurement range is limited because accuracy will suffer if the response voltage from the sensor is too small compared with the ADC reference voltage. However, as the conductivity and temperature range is relatively narrow, current sources can be selected to make the voltage from a CT sensor always bigger than 10% of the ADC reference voltage and this disadvantage can be ignored. Furthermore, multiplexers can be used to make multi current sources, providing a number of selectable from a single circuit measurement ranges.

2.6 Literature on CTD system

Several papers have been published on CTD systems, including work by a previous PhD student, Gong [22]. Brown presented a four-electrode conductivity sensor with zero external field (US Patent 6,720,773); Hyldgard et al demonstrated a multi-sensor system [36, 37], and Broadbent et al a PCB MEMS-based CTD [38]. CTD systems are also commercially available, including Sea-bird serial CTD systems [61], Alec CTW [62], Cefas G5 DST [63] and Star-Oddi DST CTD [16]. These systems are reviewed below.

2.6.1 CT system developed by Gong

The CT system developed by Gong [22] uses two-electrode conductivity cells and a thermistor as a CT sensors. A voltage-current impedance measurement circuit is used to support the CT sensors. Figure 2-15 shows a diagram of the conductivity cell and schematics of the CT measurement circuits:

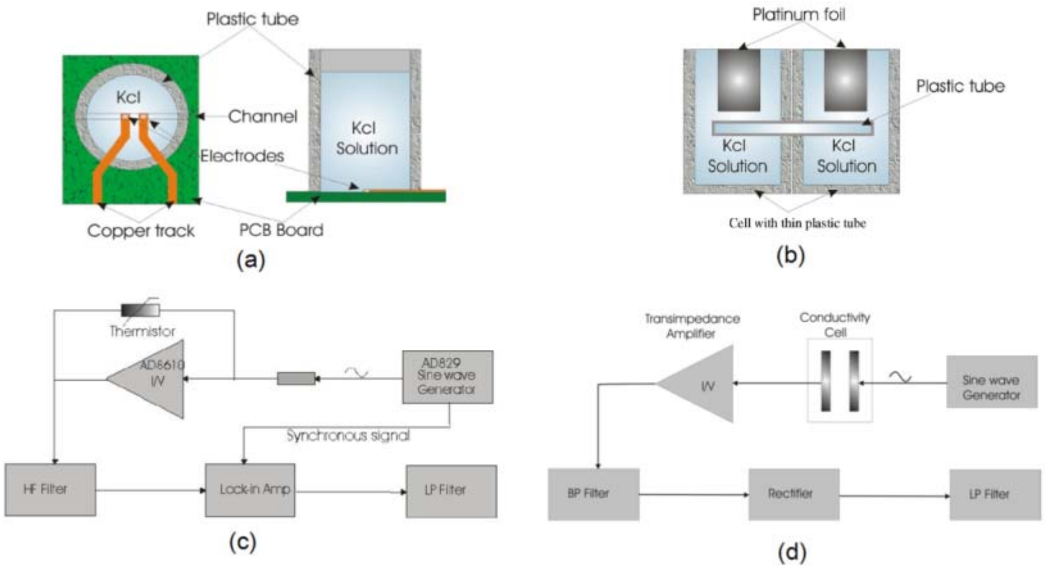

Figure 2-15 Diagrams of Gong's CT system including: (a) a two-electrode cell; (b) a two-electrode cell with a thin plastic tube to enhance cell constant; (c) schematic of a temperature measurement circuit; (d) schematic of a conductivity measurement circuit [22].

As shown in figure 2-15, there are two designs of conductivity cells. One is a common two-electrode cell which uses two electrodes to measure the impedance of the liquid inside a plastic tube. Another is a two-electrode cell where the two electrodes are placed in two separate thick plastic tubes, and another thin plastic tube is used to connect the two thick plastic tubes together. The second two electrode cell has higher cell constant, reducing the voltage drops across the electrode-electrolyte interface, and electrode polarisation effects.

Both thermistor and conductivity cells are excited by a 334 kHz sine wave. A rectifier and a low-pass filter are used to generate a DC signal whose magnitude is proportional to the magnitude of the AC voltage response of the CT sensors. This system can achieve an accuracy of $\pm0.003\ ^{o}C$ over the temperature range of $0\sim30\ ^{o}C$, and a conductivity measurement error of ±2.7%, tested using potassium chloride (KCl) in a concentration range of 0.2~1 mol/L.

Later in his thesis [64], Gong used a four-electrode conductivity cell with 5x5x50 mm water channel to replace the two-electrode cells, and improved the accuracy to ±0.2 mS/cm (±0.5%). He also proposed a five-electrode conductivity cell, where a fifth electrode is added to the four-electrode conductivity cell. The first and fifth electrodes are placed symmetrically around the axis of the fourth electrode (see figure 4-10 in chapter 4). By applying the same voltage to the first and fifth electrode, the proximity effect is reduced (this point will be discussed further in chapter 4).

2.6.2 Neil's four-electrode conductivity sensor with zero external field

Neil describes a four-electrode conductivity sensor with zero external field (US Patent 6,720,773), shown in figure 2-16:

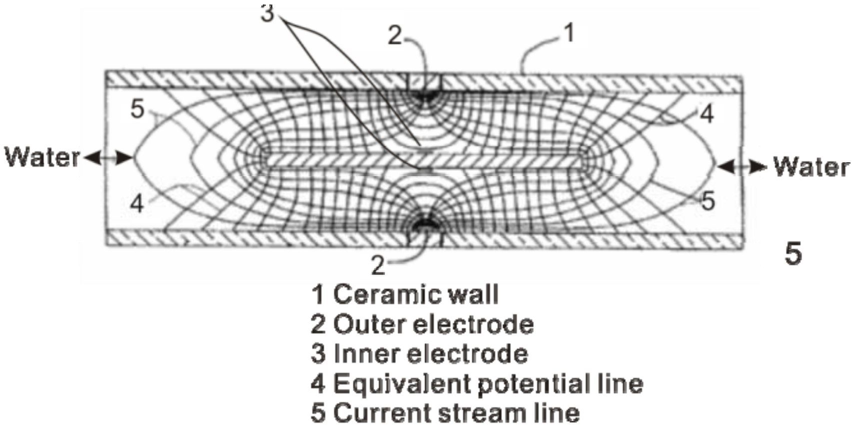

Figure 2-16 Diagrams of a four-electrode conductivity sensor with zero external field [65].

This conductivity sensor is constructed from a rectangular ceramic tube. Two outer electrodes are placed opposite each other on the wall of a tube. A ceramic plate is placed in the middle of the tube to increase the path of the current, increasing the cell constant κ. Two inner electrodes are placed on the two sides of the plate for voltage sensing. Therefore the two inner electrodes and two outer electrodes create a four-electrode conductivity sensor. The length of the tube is made longer than the plate, therefore all the electric field and current is contained inside the tube, eliminating proximity effect.

Following this principle, Schmitt et al developed a CTD system [66] using a half cell version of this conductivity sensor. This system provides better than 0.2 psu accuracy.

2.6.3 Hyldgard's multi-sensor system

Hyldgard describes a multi-sensor system called a Data Storage Tag (DST), which is used for fish tagging. Sensors are fabricated on a 4x4 mm micro-chip that can be exposed directly to the seawater [36, 37]. The sensor chip has a silicon substrate and contains a piezo-resistive pressure sensor, a RTD temperature sensor, an open four-electrode cell and a pn-junction light sensor. Figure 2-17 shows the layout of the sensor chip.

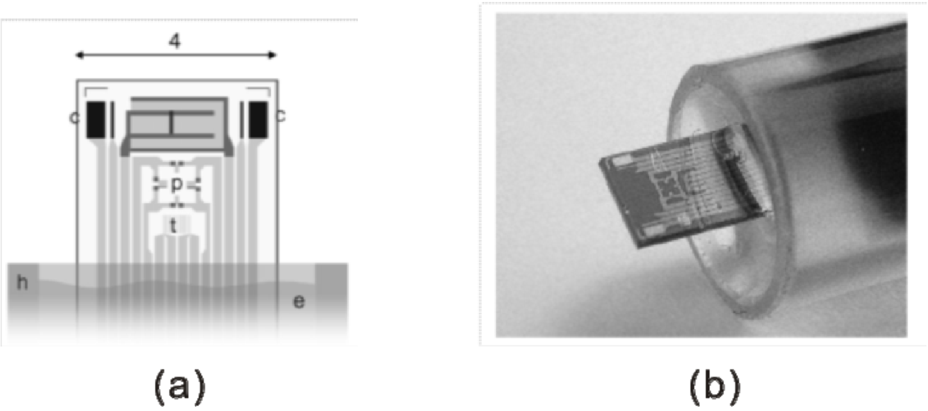

(a)

(b)

Figure 2-17 Diagrams of Hyldgard's multi-sensor chip [36]: (a) a schematic of the 4 mm wide chip layout including a pressure sensor (p), temperature sensor (t), pn-junction light sensor (l), and four-electrode open conductivity cell (c); (b) a photograph of the multi-sensor chip.

The pressure sensor is made of piezo-resistors configured as a Wheatstone bridge [55]; the RTD temperature sensor is made of titanium silicide ($TiSi_2$); the conductivity sensor is made of four platinum electrodes. In addition, a silicon nitride (Si_3N_4) film is used to insulate the whole sensor chip except for the four platinum electrodes, and the system is packaged in an epoxy potted tube.

The 4x4 mm multi-sensor enables salinity determination with an accuracy of ±0.5 psu through measurement of the conductivity, temperature and pressure with accuracies of ±0.6 mS/cm, ±0.065 ^{o}C and ±0.05 bar, respectively.

2.6.4 Broadbent's PCB MEMS-based CTD

Broadbent describes a PCB MEMS-based CTD [38]. It is a small, low cost system for measurement of salinity in coastal waters. The system incorporated three expendable sensors including a four-electrode open conductivity cell, a RTD temperature sensor, and a piezo-resistive pressure sensor. The conductivity sensor and the temperature sensor are fabricated using printed circuit board (PCB) and MEMS techniques. The substrate of the CT sensors is a new thin-film material – liquid crystal polymer (LCP). The conductivity sensor is a planar four-electrode cell consisting of electroless nickel, gold and platinum metals. The RTD temperature sensor is fabricated using copper-clad LCP material. Figure 2-18 shows the CTD sensor system.

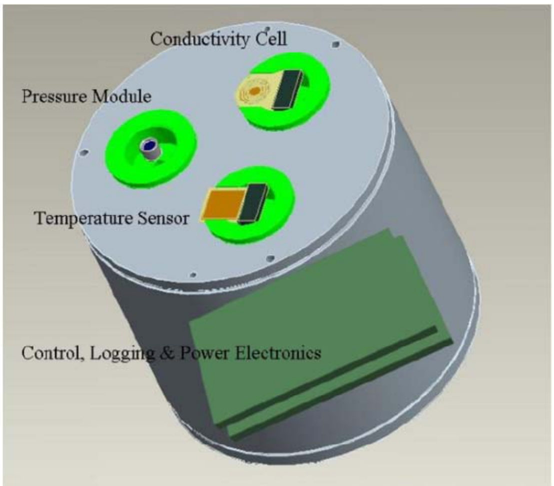

Figure 2-18 A schematic of H. A. Broadbent's Φ10x10 cm PCB MEMS-based CTD showing the independent expendable sensor plugs and environmentally protected circuit boards [38].

The overall dimension of the CTD system is approximately 10 cm in diameter and 10 cm in length. The accuracies for the CTD sensor are ±1.47% from 0~60 mS/cm, ±0.546 ^{o}C, and ±0.02 bar respectively. The system is powered by a 9 V alkaline battery, and provides 22 days of operation with a sampling rate of every 15 minutes.

2.6.5 Sea-bird serial CTD systems

Sea-bird Electronics (SBE) is a leading manufacturer of oceanographic CTD systems. Sea-Bird's 911plus CTD [17] is the primary oceanographic research tool chosen by the world's leading institutions.

As shown in figure 2-19, the system consists of an SBE 9+ Underwater Unit and SBE 11+ Deck Unit. CTD sensors are contained in the Underwater Unit, including a three-electrode conductivity sensor (figure 2-8) configured in a tube with outer electrodes held at the same potential to avoid proximity effects, an accurate and fast thermistor temperature sensor, and a precision quartz pressure sensor. A pump with constant flow is used to flush the conductivity sensor tube and provide constant response time of the CT sensors. Wien bridge oscillators are used to convert the resistance of the CT sensors into frequency outputs. The quartz pressure sensor also provides a variable frequency output. The sensor frequencies are measured using high-speed parallel counters. The resulting digital data, in the form of count totals, are transmitted serially to the Deck Unit. Then the Deck Unit reconverts the count totals to numeric representations of the original frequencies, and calculates the CTD data.

(a) (b)

Figure 2-19 Photographs of Sea-bird's 911plus CTD including: (a) SBE 9plus Underwater Unit; (b) SBE 11plus V2 Deck Unit[17].

The initial accuracy of the Sea-Bird 911plus CTD sensors are ±0.003 mS/cm in the range of 0~70 mS/cm, ±0.001 ^{o}C in the range of -5~35 ^{o}C, and ±0.015% of 10,500 m full scale (FS) respectively. The monthly drifts of the CT sensors are 0.003 mS/cm and 0.0002 ^{o}C respectively, and the yearly drift of the depth sensor is 0.018% of full scale. The Underwater Unit consumes 1 A current at 14.3 V voltage, while the Deck Unit requires an AC power supply of 130 watts at 115~ 230 V.

For long-term autonomous applications, e.g. the Argo Program [67], Sea-bird provide another version of CTD system - SBE 41/41CP [68]. Comparing this with the SBE 911plus, the stability for CT is increased to 0.001 mS/cm per year and 0.0002 ^{o}C per year respectively, while the accuracy remains the same.

2.6.6 Alec CTW

Alec CTW [62] is a conductivity and temperature sensor system aimed for long-term ocean deployment. A photo of the Alec CTW is shown in figure 2-20, and a diagram of the sensor head is shown in figure 2-9.

Figure 2-20 A photograph of Alec CTW conductivity and temperature sensor system [62].

This system uses a seven-electrode conductivity sensor and a thermistor temperature sensor. It provides accuracies of ±0.01 mS/cm and ±0.01 ^{o}C for conductivity and temperature respectively, with a dimension of Ø70 x 342 mm, weight of 1.5 kg, and consumes 110 mA current when measuring. A piston type wiper is used to clean the channel of the conductivity sensor automatically. A one year deployment has been made to prove that the system can manage bio-fouling efficiently [25, 26].

2.6.7 *Cefas G5 DST*

Cefas G5 DST [69] is one of the smallest data storage tags for fish tagging. The dimension is Ø8x33 mm, with a weight of 2.7 g. It can support temperature and depth measurement with accuracies of ±0.1 ^{o}C and ±1% of FS respectively. However it doesn't support conductivity measurement. Figure 2-21 shows a photo of the Cefas G5 DST.

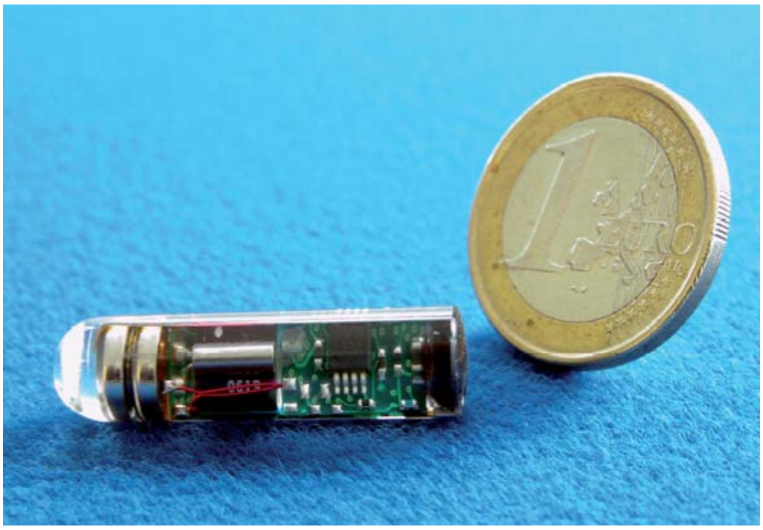

Figure 2-21 A photograph of Cefas G5 DST [69].

2.6.8 *Star-Oddi DST CTD*

The Star-Oddi DST CTD [16] shown in figure 2-22 is the smallest salinity logger current available on the market, with a dimension of Ø17x46 mm and weight of 21 g in air. It's specially designed as an archival tag for tagging fish: for analysing fish migration, distribution, feeding behaviour, vertical and horizontal movements.

Figure 2-22 A photograph of the Ø17x46 mm Star-Oddi DST CTD [16].

It uses a two-electrode conductivity sensor. The accuracies of Star-Oddi DST CTD sensors are ±0.8 mS/cm in the range of 3~37 mS/cm or 10~50mS/cm (customer specified), ±0.1 ^{o}C in the range of -1~40 ^{o}C, and ±0.4% of 200 m full scale. Therefore the accuracy of salinity measurement is about ±1 psu.

Furthermore, it provides a typical battery life of about 4 years with sampling intervals of 10 minutes or greater, and memory capacity of 87,000 measurements. The price is about £900. However, due to commercial reasons, it is hard to get any further information about the CTD sensor design.

2.6.9 Summary of the mentioned CTD systems

The different CTD systems described above are summarised in table 2-3. Their performance and main characteristics are compared. As precision systems, the Sea-bird SBE 911plus CTD and Alec CTW support salinity measurement with accuracy better than 0.01 psu. However they are large, expensive and consume a lot of power. Data storage tags and prototype systems in publications have 100 times lower salinity accuracy of about 1 psu. This limitation is due to the accuracy of the conductivity sensor.

CTD System	Conductivity accuracy	Temperature accuracy	Pressure accuracy	Power, battery life, & dimension
Gong CT System [22]	±2.7 % @ 0.2~1 mol/L KCl solution	±0.003 °C (0~30 °C)	N/A	48 hours battery life
Hyldgard multi-sensor system [36, 37]	±0.6 mS/cm	±0.065 °C	±0.05 bar	Chip dimension : 4x4 mm Package dimension: Ø8x50 mm
Broadbent PCB MEMS CTD [38]	±1.47% (0~60 mS/cm)	±0.546 °C (0~50 °C)	±0.02 bar	Battery life: 22 day @ 15 min interval Dimension: Ø100x100 mm
SBE 911plus CTD [61]	±0.003 mS/cm (0~70 mS/cm)	±0.001 °C (-5~35 °C)	±0.015% @ FS of 10500 m	(Underwater Unit only) Power: 1 A @ 14.3 V Dimension: 952x330x305 mm
Alec CTW [62]	±0.1 mS/cm (2~65 mS/cm)	±0.01 °C (0~35 °C)	N/A	Dimension: Ø70 x 342 mm Power: 100 mA
Cefas G5 DST [69]	NA	±0.1 °C (-2~40 °C)	±1% @FS of 3000 m	Dimension: Ø8x33 mm
Star-Oddi DST CTD [16]	±0.8 mS/cm (3~37 mS/cm or 10~50 mS/cm)	±0.1°C (-1~50 °C)	±0.4% @ FS of 200 m	Dimension: Ø17x46 mm Battery life: 4 years @ 10 min interval

Table 2-3 Comparison of the existing CTD systems.

Therefore, a big challenge is to develop a miniature CTD system with reduced power consumption while maintaining the high accuracy of the SBE 911plus CTD, especially for the conductivity sensor. It would be an impressive improvement even if an accuracy of 10 times lower than the Sea-bird (±0.03 mS/cm for conductivity and ±0.01 °C for temperature) can be achieved with a miniature system.

2.7 Dissolved oxygen

Dissolved Oxygen (DO) in the ocean typically varies from 100~300 µM [70]. Two types of oxygen sensors are normally used to measure dissolved oxygen in liquid, these are the electrochemical sensor and an optode sensor.

2.7.1 Electrode sensor

Electrode for DO measurement is based on electrochemical principles. Normally, two or three electrodes are immersed in an electrolyte. Voltage is applied to one of the electrodes, causing electrochemical reactions and consuming oxygen in the electrolyte. The oxygen concentration of the electrolyte is determined from the electrical current, as there is a linear relationship between them current and oxygen.

The Clark-type electrode sensor [71-73] is the most widely used oxygen sensor and a diagram of Clark-type sensor is shown in figure 2-23:

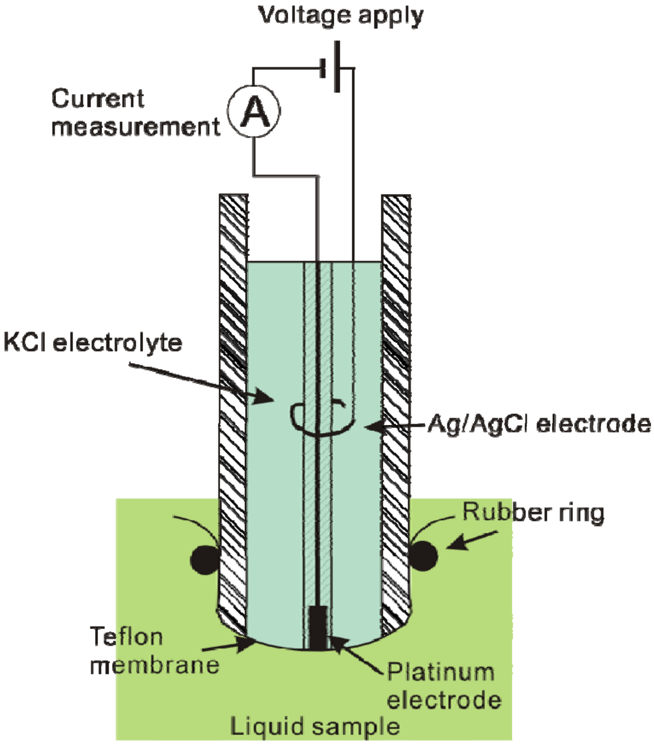

Figure 2-23 A diagram of Clark-type electrode DO sensor.

As shown in the figure, a Clark-type electrode uses platinum for the cathode and silver/sliver chloride (Ag/AgCl) for the anode. The electrodes are immersed in potassium chloride (KCl) electrolyte, which maintains the concentration of chloride ions to keep a fixed voltage between the electrolyte and the Ag/AgCl electrode. This electrolyte is separated from the liquid by a Teflon membrane, which allows the oxygen to pass through. When a voltage is applied, oxygen near the platinum electrode is totally consumed by the following reactions:

$$O_2 + 4\,e^- + 2\,H_2O \leftrightarrow 4\,OH^- \qquad [2\text{-}18]$$

$$O_2 + 2\,e^- + 2\,H_2O \leftrightarrow H_2O_2 + 2\,OH^- \qquad [2\text{-}19]$$

$$H_2O_2 + 2\,e^- \leftrightarrow 2\,OH^- \qquad [2\text{-}20]$$

The oxygen can be consumed directly by equation 2-18, or with hydrogen peroxide as intermediate equation 2-19 followed by equation 2-20, depending on the cathode material [74]. As oxygen around the electrode surface is consumed the oxygen concentration is reduced. Diffusion and consumption cause a concentration gradient across the electrolyte and in the liquid sample in the vicinity of the membrane. This diffusion gradient limits the current measured at the electrode. Further details about this diffusion are present in chapter 3. The diffusion (limited) oxygen reduction current can be measured via the electrical current at the platinum electrode, and is directly proportional to the concentration of oxygen in the liquid sample. The coefficient of this relation depends on geometry, and can be determined by calibration. The oxygen concentration in the liquid can be calculated simply from the measured current and this coefficient.

However, as the diffusion of species to and from the electrode is affected by flow, measurement error occurs when water flows with different flow rate across the electrode. In addition, the diffusion is also very sensitive to the geometry of the platinum electrode; it is very important to maintain a steady surface condition of the platinum electrode. Any changes of the surface condition will cause drift in the sensor readings.

Many Clark-type DO sensors are commercially available from YSI [75], Seabird [76], and other companies [77, 78]. The precision of these products is up to ±0.1% of FS (normally 1000 μM). However, the accuracy is much worse than the precision, about 10 μM .

The membrane and the internal KCl electrolyte make these systems difficult to miniaturise. Revsbech introduced a cylindrical miniaturised Clark-type DO sensor [79], where the Clark-type electrode is made as a needle. This needle type sensor is commercially available from Unisense [80], with needle diameter down to 1 μm. However, the volume of the internal electrolyte makes the whole sensor large, with a length of 150 mm. Therefore it is difficult to miniaturise in all the three dimensions.

As seawater has a relatively stable concentration of chloride ion, the membrane and electrolyte can be omitted for ocean applications. Recently, this was done by Sosna et al at the University of Southampton, School of Chemistry, and National Oceanography Centre, Southampton. This principle has been verified by a PC based system [81-84], shown in figure 2-24:

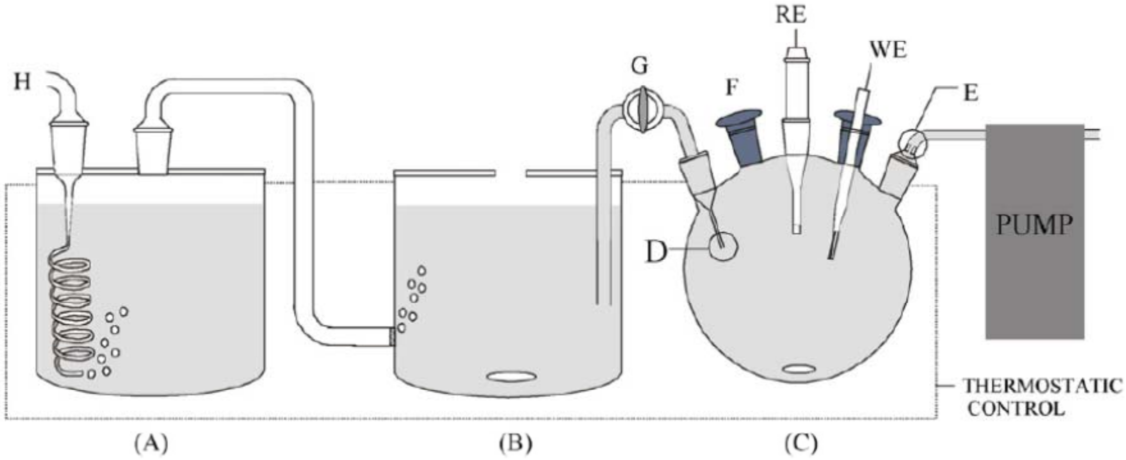

Figure 2-24 A schematic representation of the Sosna's DO calibration system. A: humidifier, B: saturated solution reservoir, C: measurement cell, D: inlet capillary, E: outlet connector, F: argon feed neck, G: valve, H: oxygen feed, WE: working electrode, and RE: reference electrode [55].

In this system, the working electrode (cathode) is made from a platinum micro-wire sealed in a soda glass pipette, and the reference electrode (anode) is a Saturated Calomel Electrode (SCE). Comparing with the Clark-type electrode system, this system does not need a membrane, and both working electrode and reference electrode are directly immersed into the liquid sample with an oxygen concentration to be measured.

Similar to the Clark-type electrode, oxygen diffusion is created from the platinum micro-wire surface to the liquid bulk. The tube of the glass pipette gives a fixed liquid dimension for this diffusion, and also minimizes the flow effect. Experiment results show that this DO system can give a precision of ±1.5% over first 24 h. However, works need to be carried to improve the durability and to reduce flow sensitivity.

2.7.2 Optode sensor

An oxygen optode is a sensor that performs an optical measurement of the oxygen concentration [85-89]. The sensor is a chemical film that is fixed to the tip of an optical cable. This film fluoresces and the property of the fluorescence changes with the oxygen concentration. Normally the fluorescence is highest when there is no oxygen, and reduces if oxygen molecules collide with the film. Therefore oxygen concentration can be calculated by measuring the fluorescence.

The relation between fluorescence and oxygen concentration is not linear, but more sensitive at low oxygen concentration. Compared with the electrode sensor, the optode is not affected by water flow. This is because oxygen is not consumed by the sensor, and therefore at steady state flow cannot change the oxygen concentration in the sensing element. However, in transient conditions stronger flow increases mass transport and therefore transport of oxygen to or from the sensing element giving rise to a quicker response time. However, as the film takes time to respond to oxygen change, the optode has the longer response time compared with an electrode. Furthermore, as the film has a finite life time (due to fluorescence attenuation by photobleaching), the sensing element needs to be replaced periodically.

Many oxygen optodes are commercially available from AADI [90], including [91-93]. These products have an accuracy of ±5% of FS, and response time (τ, 63%) of 25 s.

2.8 Summary and conclusion

This chapter introduced the definition of salinity, and the relation between salinity and the CTD; the principle of CTD measurement, and existing CTD systems. The principle of dissolved oxygen measurement was also introduced.

This thesis describes a miniature sensor system for ocean monitoring, made using an electrode conductivity sensor, PRT temperature sensor, and electrode DO sensor. All these sensors have similar requirements in terms of fabrication, and can be integrated onto a single micro chip with glass substrate and platinum electrodes. A voltage-current based circuit is used to support the CT sensors. The electrode DO sensor is also based on voltage-current measurements, and has the potential to share the same circuit as the CT sensor.

Existing small CTD systems only have about ±1 psu accuracy in salinity. To make improvements, the CT accuracy of the next generation miniature system need to be ±0.1 mS/cm and ±0.1 ^{o}C to give ±0.1 psu accuracy in salinity. A significant improvement can be achieved if the miniature system has CT accuracies of ±0.01 mS/cm and ±0.01 ^{o}C, giving similar salinity accuracy to the large precision system, of ±0.01 psu. In-situ long-term deployment applications require DO accuracy from ±2%

to ±5% [94, 95], which is about ±10 μM accordingly. However, stability and flow independence are important. Power consumption and bio-fouling issues are also important, as many autonomous applications might require a battery life of more than 1 year, and bio-fouling needs to be removed automatically during deployment.

Chapter 3 The Electrode-Electrolyte Interface

Because the conductivity and DO sensors use electrodes for measurements, it is important to understand the interface and the electrochemistry between the electrodes and the sea water. This chapter introduces the electrode-electrolyte interface and describes electrochemical reactions. It gives the equivalent electrical circuit, and discusses how to use this interfacial circuit model to analyse and design the conductivity and DO sensors.

3.1 The structure of the electrode-electrolyte interface

When an electrode is immersed into an electrolyte, a series of electrochemical reactions can occur at the electrode surface, transferring electrons between the electrode and the electrolyte, and charging the electrode. The electrode may also be charged by an outside source. These charges create an electrical potential on the electrode changing the local ion concentration. Oxidation reactions cause electrical current to flow from the electrode to the electrolyte, whilst reductions cause the current to flow in the opposite direction. When the potential and concentrations are changed to a certain level, the exchange current of oxidations and reductions reactions balance, the net current reduces to zero and an electrochemical equilibrium is established.

The electrolyte bulk has no net charge and is therefore neutral overall, however when an electrode is immersed into an electrolyte, this electrode may be charged by an outside potential or by charge transfer reactions. This charge creates an electric field, attracting anions and cations to the electrode. The charge transfer process may also produce anions and cations with different amounts of charge. Therefore the distribution of the ions in the solution is changed when an electrode is immersed into the solution. As a result of electrode charging or applied potential electrostatic attraction occurs with charged ions in the bulk electrolyte, the ion concentration near the electrode is changed, while overall the solution bulk remains neutral.

At the electrode-electrolyte interface, the ions and solvent molecules are organised into different layers. Figure 3-1 shows this structure for a metal electrode, and figure 3-2 shows the profile of the potential at the electrode-electrolyte interface:

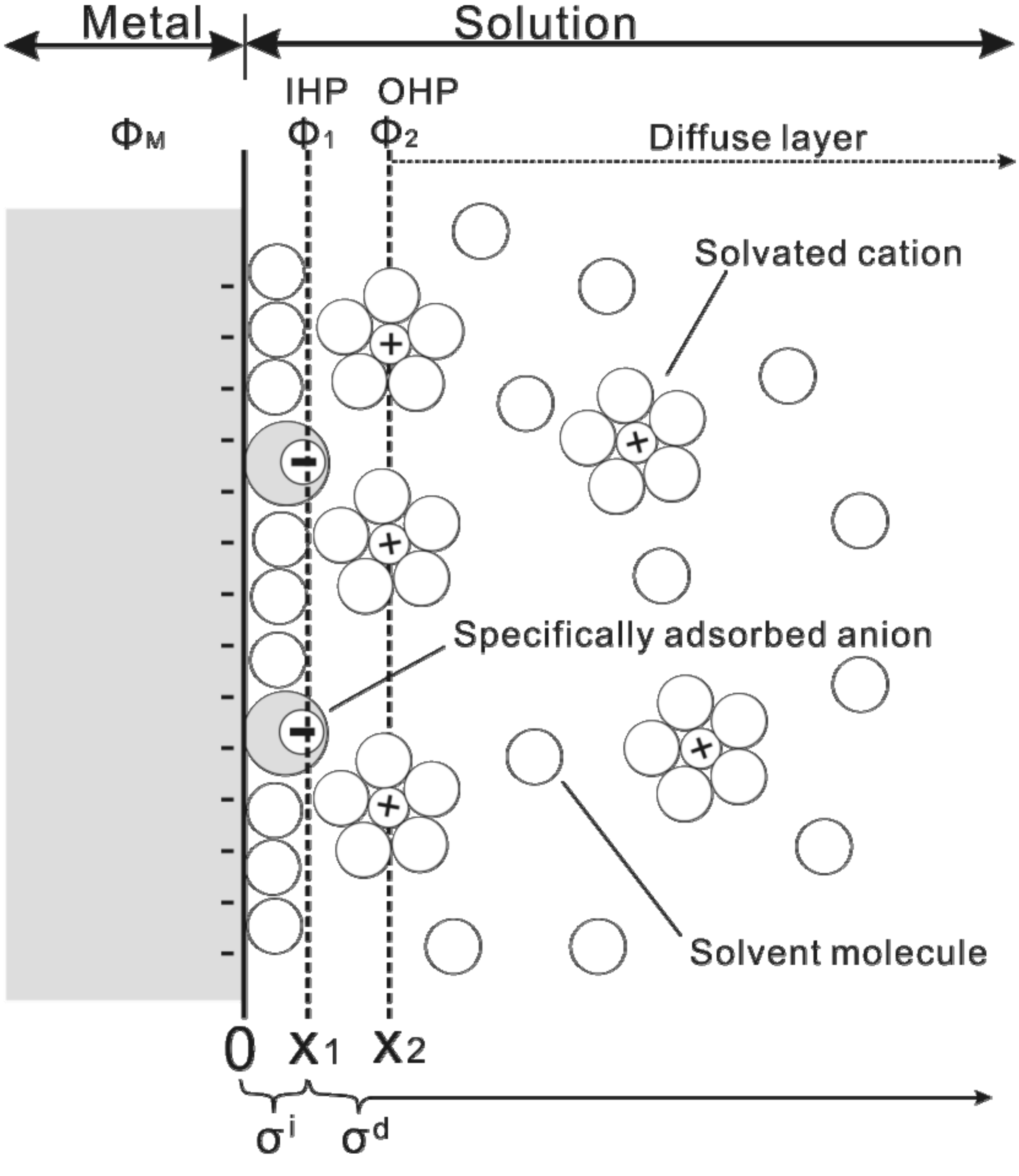

Figure 3-1 A diagram demonstrating the structure of the electrode-electrolyte interface, where x_1 is the distance between electrode surface and inner Helmholtz plane (IHP), x_2 is the distance for outer Helmholtz plane (OHP), Φ_M is the potential of the metal electrode, Φ_1 and Φ_2 are the potentials on the IHP and the OHP respectively, σ^i is the charge density in the IHP, σ^d is the charge density in the OHP and diffusion layer.

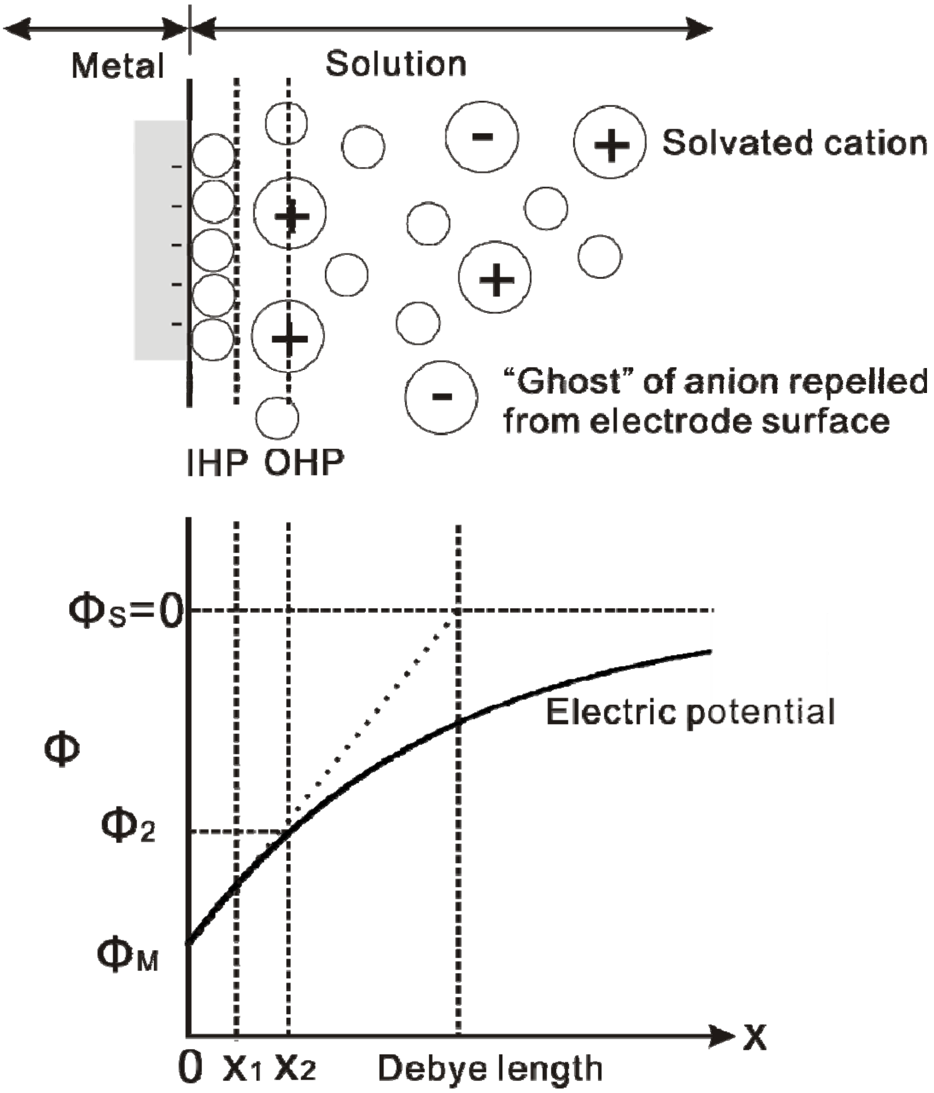

Figure 3-2 A diagram demonstrating the potential profile at the electrode-electrolyte interface. Φ_M is the potential of the metal electrode, Φ^2 is the potential on the OHP, and Φ_S is the potential of the solution bulk, which is set to 0 here.

As shown in figure 3-1, some solvent molecules and ions are specifically adsorbed close to the electrode surface and form an inner layer. This layer may also include the other ions or molecules. This is often referred to as the Stern layer. The locus of the electrical centres of these specifically adsorbed ions is called the inner Helmholtz plane (IHP), at a distance x_1, with a total charge density of σ^i. Solvated ions approach the electrode because of the electric field, and form the outer layer. The locus of centres of these nearest solvated ions is called the outer Helmholtz plane (OHP), which is at distance x_2. Also some solvated ions are not specifically adsorbed, but affected by the electric attraction and thermal motion, distributing in a region called diffuse layer. The total charge density of outer layer and diffuse layer is σ^d. The total charge density at the metal electrode σ^M is given by:

$$\sigma^M = -\sigma^S = -(\sigma^i + \sigma^d) \qquad [3\text{-}1]$$

where σ^S is the total charge density of the solution.

3.2 Double layer capacitance

For an electrode-electrolyte interface as shown in figure 3-2, the electrode and the solution around the electrode may be charged, creating a potential Φ_M on the electrode. Therefore the electrode-electrolyte interface acts as a capacitor, and the capacitance C is determined by the total charge Q and potential Φ_M as $C=Q/\Phi_M$. Helmholtz assumed the charge of solvated ions was confined within the OHP. Then the capacitance of the electrode-electrolyte interface is given by:

$$C_H = \frac{\varepsilon_0 \varepsilon_r A}{d_{OHP}} \qquad [3\text{-}2]$$

where ε_0 is the permittivity of free space, ε_r is the relative permittivity of the electrolyte media, A is the electrode area, and d_{OHP} is the distance of OHP with a typical value of 3 Å for KCl or NaCl solution [96-98]. This capacitance (C_H) is called the Helmholtz capacitance, and normally is estimated to be 10 ~ 40 μF/cm^2 [32].

The Helmholtz capacitance doesn't consider solvated ions in the diffuse layer. Therefore Gouy and Chapman considered the entire interface as a diffuse layer, and proposed that the number concentration of solvated ions (n, in ions/L) in the interface have a distribution governed by Boltzmann statistics,

$$n = n_0 \exp\left(\frac{-ze\Phi}{kT}\right) \qquad [3\text{-}3]$$

where Φ is the potential with respect to the bulk solution, n_0 the number concentration of solvated ion in the bulk solution, z the valence of the ions, e is the electron charge (1.60219×10^{-19} C), k is the Boltzmann constant, and T is the absolute temperature.

Based on equation 3-3, Gouy and Chapman deduced the capacitance (C_G, Gouy-Chapman capacitance) as follows

$$C_G = \sqrt{\frac{2z^2e^2\varepsilon_0\varepsilon_r n_0}{kT}} \cosh\left(\frac{ze\Phi_0}{2kT}\right) A \qquad [3\text{-}4]$$

where Φ_0 is the potential on the electrode surface with respect to the bulk solution.

$\cosh\left(\frac{ze\Phi_0}{2kT}\right)$ is a factor for C_G. As $\cosh(x) = \frac{1}{2}(e^x + e^{-x})$, this factor increases with Φ_0. When a small potential less than 25 mV is applied ($\Phi_0 \approx 0$), this factor becomes 1. Then C_G is given as:

$$\begin{cases} \mathrm{C_G} = \dfrac{\varepsilon_0\varepsilon_r A}{\lambda} \\ \lambda = \sqrt{\dfrac{\varepsilon_0\varepsilon_r kT}{2z^2e^2n_0}} \end{cases} \quad [3\text{-}5]$$

Comparing with equation [3-2], λ can be seen to be the characteristic thickness of the diffuse layer – the Debye length (figure 3-2). Table 3-1 gives values for λ for KCl solutions of different molarities at 25 °C:

Molar Concentration (mol/L)	1	10^{-1}	10^{-2}	10^{-3}	10^{-4}
λ (Å)	3.0	9.6	30.4	96.2	304

Table 3-1 Thickness of the diffuse layer for KCl solution of different concentrations at 25 °C [32].

Since the diffuse layer is formed because of electrostatic attraction and thermal motion, C_G is strongly dependent on potential, temperature and concentration. However, as the IHP and OHP are weakly dependent on these three parameters, error is introduced in the model of the interface if the IHP and OHP are assumed to be part of the diffuse layer (as in the Gouy and Chapman model). A better model given by Stern divides the interface into two layers: the Helmholtz layer formed by bound ions at the OHP, and the Gouy-Chapman layer formed by the diffuse layer. The capacitance of the Helmholtz layer is attributed to C_H, while the capacitance of the Gouy-Chapman layer is modelled as C_G. This model is called the Gouy-Chapman-Stern (GCS) model. Hence the total interfacial capacitance (C_{DL}, also called the double layer capacitance) is by the series combination of C_H and C_G together, where the potential on the OHP (Φ_2) should be used to replace Φ_0 for C_G:

$$\begin{cases} \dfrac{1}{C_{DL}} = \dfrac{1}{C_H} + \dfrac{1}{C_G} \\ C_G = \dfrac{\varepsilon_0\varepsilon_r A}{\lambda}\cosh\left(\dfrac{ze\Phi_2}{2kT}\right) \\ C_H = \dfrac{\varepsilon_0\varepsilon_r A}{d_{OHP}} \end{cases} \quad [3\text{-}6]$$

Figure 3-3 is a plot of C_{DL} for solutions with different concentrations:

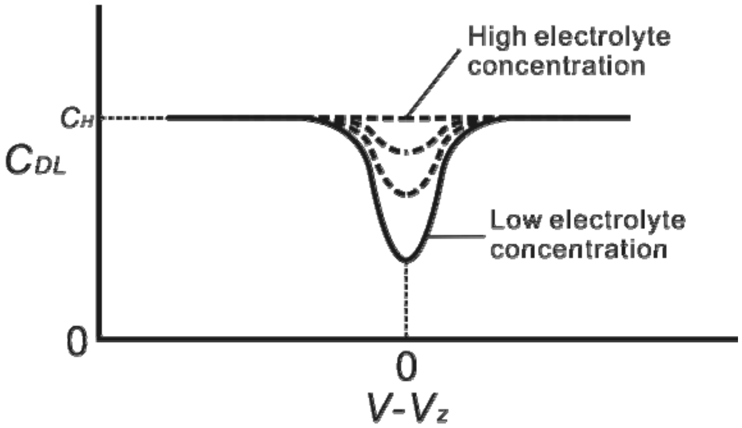

Figure 3-3 Plot of the expected behaviour of C_{DL} according to GCS theory as the electrolyte concentration changes, where V_z is the voltage on the electrode at the point of zero charge.

As shown in figure 3.3, an electrolyte with a higher salt concentration has a larger C_{DL} when the applied voltage (V-V_z) is small. However, if this voltage is large, the concentration makes no difference to C_{DL}, which is very close to C_H.

The reason for this is that as a series connection, the value of C_{DL} depends on the smaller of the either C_H or C_G. If $C_H >> C_G$, $C_{DL} \approx C_G$. Otherwise, if $C_G >> C_H$, $C_{DL} \approx C_H$. From table 3-1 we see that, normally d_{OHP} (3 Å) is smaller than λ, except when the electrolyte concentration is greater than 1 M. Therefore, as shown in the figure, for small excitation voltages, C_H is bigger than C_G. Therefore, the value of C_{DL} is governed by C_G, and increases with concentration. However, as C_G also increases with applied voltage, for high excitation voltage, C_G is bigger than C_H and C_{DL} becomes close to C_H.

3.3 Faradaic impedance

An electrode, at which no charge transfer occurs, regardless of the potential imposed by an outside source of voltage, is called an ideal polarized electrode (IPE). Although no real electrodes behave as an IPE, some can approach IPE behaviour over limited potential ranges [32].

The double layer capacitance provides a model for the electrode-electrolyte interface when there is no charge transfer. Charge transfer occurs when a chemical reaction happens at the electrode surface, transferring electrons between the electrolyte and electrode. This charge transfer behaves like a leakage current through the double layer capacitance. Therefore impedance in parallel with the double layer capacitance is used to describe this behaviour, called Faradaic impedance.

As mentioned previously, electrochemical equilibrium is established when the potential on the electrode and the ion concentration in the electrolyte are changed to certain levels. A reaction is given as following:

$$O+ne \underset{Oxidation}{\overset{Reduction}{\rightleftharpoons}} R \qquad [3\text{-}7]$$

where O is the oxidised form of the chemical species, R is the reduced form, and n is the number of electrons transferred in this reaction. Two electric currents are created in this reaction: oxidation (following the equation from right to left) makes electric current flow from electrode to the electrolyte (i.e. electrons are generated at the electrode), while reduction (following the equation from left to right) makes the electric current flow in the opposite way. At equilibrium, these two currents maintain a net current of zero.

When there is no net current, the potential of the electrode with respect to the surrounding solution (equilibrium voltage within the diffusion layer, V_{eq}) is given by the Nernst equation:

$$V_{eq} = \Phi^0 + \frac{RT}{nF} \ln \frac{C_O(x=0)}{C_R(x=0)} \qquad [3\text{-}8]$$

Where Φ^0 is the standard electrode potential, which is the equilibrium voltage measured at standard state against a Standard Hydrogen Electrode. (SHE, also called Normal Hydrogen Electrode, NHE). The standard state is 1 mol/L for solutes and 1 bar for gases. R is the universal gas constant equal to 8.3144621(75) J K^{-1} mol^{-1} [99]. T is the absolute temperature. F is the Faraday constant, equals to 96485.3365 (21) C mol^{-1} [100]. C_O and C_R are the concentrations of the oxidant and reductant respectively, and $(x=0)$ means these concentrations are taken around the electrode surface. At 25 °C, this equation can also be written as:

$$V_{eq} = \Phi^0 + \frac{0.05916}{n} \log_{10} \frac{C_O(x=0)}{C_R(x=0)} \qquad [3\text{-}9]$$

As discussed in section 3.1, the concentrations at the electrode ($C_O(x=0)$, $C_R(x=0)$) may be slightly different from the concentrations of the solution bulk (C_O^*, C_R^*) due to charge transfer effects and electrostatic attraction. However, when the interface is at equilibrium, these differences can normally be ignored. Therefore V_{eq} at equilibrium is the same as the equilibrium voltage of the solution bulk V_{eq}^*:

$$V_{eq}^* = \Phi^0 + \frac{RT}{nF} \ln \frac{C_O^*}{C_R^*} \qquad [3\text{-}10]$$

However, if an external voltage/current source is used to generate a current flowing through the electrode, the equilibrium is perturbed, making the equilibrium voltage within the diffusion layer V_{eq} different from the equilibrium voltage of the solution bulk V_{eq}^{*}.

The voltage on the electrode increases the oxidation energy potential, and decreases the reduction energy potential. The potential energy of oxidation and reduction is the same when V_{eq} is applied to the electrode. Therefore the oxidation current and reduction current are the same, creating a net current of zero. This energy balance will cease if a voltage (V) different from V_{eq} is applied to the electrode. A voltage higher than V_{eq} increases the oxidation current and reduces the reduction current, making a net current flow from the electrode to the solution.

If the net current is non-zero, the concentration of the reaction products will be elevated (and reaction constituents (substrates) diminished) within the diffuse layer. These concentration gaps in the diffuse layer make V_{eq} different from V_{eq}^{*}. Mass transfer via fluid motion (e.g. convection) in the bulk solution is much faster and of greater flux than diffusive mass transport from the electrode. The size of this effect is dependent on the thickness of the diffuse layer, which itself is dependent on the properties of hydrodynamic boundary layer in the vicinity of the electrode and hence on flow within the bulk solution. Regardless of the magnitude of the effect, when a voltage different to V_{eq} is applied to the electrode the elevated concentration of reaction products (and reduced concentration of substrates) within the vicinity of the electrode will decrease the magnitude of the reaction current. This effect is observed in amperometric (current measuring) analytical systems, and changes V_{eq} in polarographic (measuring V_{eq}) systems with electrodes that are not ideally polarized.

The volume of the solution is usually considered to be large enough to avoid any changes in C_O^{*} and C_R^{*}. Therefore V_{eq}^{*} is a constant. The original (undisturbed by induced concentration variation at the electrode) equilibrium voltage (V_{eq}^{*}) can be considered as a DC bias. Therefore the voltage applied to the electrode for charge transfer can be divided into two parts:

$$V - V_{eq}^{*} = \left(V - V_{eq}\right) + \left(V_{eq} - V_{eq}^{*}\right) \qquad [3\text{-}11]$$

The first part (V-V_{eq}) of the voltage is consumed in breaking the energy potential balance and generating a net current at the electrode surface, and the second part (V_{eq}-V_{eq}^{*}) is consumed by transferring the reaction products from electrode surface to the solution bulk. To describe these two voltage consumptions, the Faradaic impedance can be divided into two series components. When an extremely small AC voltage is applied, these two impedance elements are modelled as charge transfer resistance and Warburg impedance respectively.

3.3.1 Charge transfer resistance

When a voltage (*V*) different from V_{eq} is applied to the electrode, equilibrium is broken and a net current is generated by this voltage difference. The relation between the voltage difference (V-V_{eq}) and the net current (from electrode to solution) is given by the Butler-Volmer equation:

$$I = I_0[\exp\left(\frac{(1-\alpha)nF(V-V_{eq})}{RT}\right) - \exp\left(\frac{(-\alpha)nF(V-V_{eq})}{RT}\right)] \quad [3\text{-}12]$$

Here I_0 is the exchange current at equilibrium. α is the charge transfer coefficient, ranging from 0 to 1. The value of α depends on the slopes of standard free energy (Gibbs's theory [32]) vs. reaction coordinate [32] for both oxidant and reductant, with a typical value of 0.5.

The exchange current I_0 can be given by:

$$I_0 = nFAk_0C_O(x=0)^{1-\alpha}C_R(x=0)^{\alpha} \quad [3\text{-}13]$$

where k_0 is the standard rate constant, which takes different values depending on the type of the reactions. As shown in the equation, the exchange current I_0 is in direct proportion to the electrode area *A*. The Nernst equation shows that, the ratio of $C_O(x=0)$ to $C_R(x=0)$ is fixed for a certain V_{eq} at equilibrium. Therefore, as the power coefficients of $C_O(x=0)$ and $C_R(x=0)$ sum to 1, I_0 can also be considered directly proportional to either $C_O(x=0)$ or $C_R(x=0)$.

The net current *I* can be further divided into I_1 and I_2, given as follows:

$$\begin{cases} I = I_1 - I_2 \\ I_1 = I_0 \exp\left(\frac{(1-\alpha)nF(V-V_{eq})}{RT}\right) \\ I_2 = I_0 \exp\left(\frac{(-\alpha)nF(V-V_{eq})}{RT}\right) \end{cases} \quad [3\text{-}14]$$

I_1 is the oxidation current, giving a positive contribution to *I*, while I_2 is the reduction current, giving a negative contribution to *I*. If *V* is bigger than V_{eq}, I_1 is bigger than I_2. Then *I* has a positive value, which means that net current flows from the electrode into the solution. If *V* is smaller than V_{eq}, I_1 is smaller than I_2. Then *I* has a negative value, which means that net current flows from the solution into the electrode.

The ratio between V- V_{eq} to *I* is considered the charge transfer resistance (R_{ct}), given by:

$$R_{ct} = \frac{V-V_{eq}}{I} = 1/\{I_0[\frac{\exp\left(\frac{(1-\alpha)nF(V-V_{eq})}{RT}\right)}{V-V_{eq}} - \frac{\exp\left(\frac{(-\alpha)nF(V-V_{eq})}{RT}\right)}{V-V_{eq}}]\} \qquad [3\text{-}15]$$

As shown in the equation, R_{ct} is not an ideal resistance as it increases steeply with the absolute applied voltage ($|V\text{-}\ V_{eq}|$). However, if an extremely small voltage is used to make ($|V\text{-}\ V_{eq}| \rightarrow 0$), then R_{ct} is similar to an ideal resistance, with a value as:

$$R_{ct} = \frac{RT}{nFI_0}, \quad when\ |V - V_{eq}| \rightarrow 0 \qquad [3\text{-}16]$$

3.3.2 Warburg impedance

As mentioned before, the differences in the mass transport and diffusive fluxes into the bulk solution, coupled with the charge transfer current, changes the concentrations of oxidant and reductant close to the electrode, creating a diffusion gradient from the electrode surface to the solution bulk. The concentrations of oxidant and reductant are functions of time t and distance x from the electrode, and can be written as $C_O(x,t)$ and $C_R(x,t)$ respectively. The dimension of the electrolyte bath is usually large compared with the diffusion length, and the concentration of the solution bulk can be considered unchanged. Therefore the boundary condition of the diffusion is:

$$\lim_{x\rightarrow\infty} C_O(x,t) = {C_O}^* \qquad [3\text{-}17]$$

$$\lim_{x\rightarrow\infty} C_R(x,t) = {C_R}^*$$

This boundary condition is called a semi-infinite boundary condition.

According to equation 3-16, when using an extremely small excitation voltage, the charge transfer current I is:

$$I = \frac{nFI_0(V - V_{eq})}{RT}, \quad when\ |V - V_{eq}| \rightarrow 0 \qquad [3\text{-}18]$$

Because I_0 is in direct proportion to either $C_O(x=0)$ or $C_R(x=0)$, according to equation 3-13, the charge transfer current I can be considered directly proportional to $C_O(x=0)$ or $C_R(x=0)$.

When a large (>> the diffusion length, $2\sqrt{Dt}$ (see chapter 4)) planar electrode is used, the diffusion can be assumed to be perpendicular to the electrode surface (one dimensional diffusion in unstirred liquid). Diffusion for planar electrodes using extremely small excitation voltages and under semi-infinite boundary condition is called semi-infinite linear diffusion. The V/I relations of this diffusion can be described by Warburg impedance (Z_W):

$$Z_W = \frac{V_{eq} - V_{eq}^*}{I} = \frac{A_W}{\sqrt{\omega}} + \frac{A_W}{j\sqrt{\omega}} = \frac{\sqrt{2}A_W}{(j\omega)^{0.5}} \qquad [3\text{-}19]$$

where j is the imaginary number, ω is the angular frequency of the excitation voltage, and A_w is called Warburg coefficient or Warburg constant, which is given as:

$$A_W = \frac{RT}{\sqrt{2}F^2 A}\left(\frac{1}{{D_O}^{0.5}{C_O}^*} + \frac{1}{{D_R}^{0.5}{C_R}^*}\right) \qquad [3\text{-}20]$$

where D_O and D_R are the diffusion coefficient (in cm^2/s) of the oxidant and reductant respectively.

The Warburg impedance is a constant phase element with a fixed phase of -45^o. The amplitude of this impedance depends on the diffusion coefficients of oxidant and reductant, and can be reduced by increasing the excitation frequency.

For some electrode and electrolyte system, e.g. Ag/AgCl electrode in KCl solution, the diffusion coefficients are very large, which means the Warburg impedance can be ignored. When extremely small currents pass though the electrode-electrolyte interfaces, the voltage drop across the Faradaic impedance can be ignored, and a fixed voltage drop of ${V_{eq}}^*$ is created across the interface. On the other hand, some interfaces have very small diffusion coefficients, e.g. the mercury electrode in KCl solution. This interface has very large Faradaic impedance, and can be considered as an IPE.

3.4 Randles model for AC excitation

To model the behaviour of the electrode-electrolyte interface for extremely small AC excitations, Randles gave an equivalent circuit that combines the double-layer capacitance and Faradaic impedance together. Figure 3-4 shows this equivalent circuit:

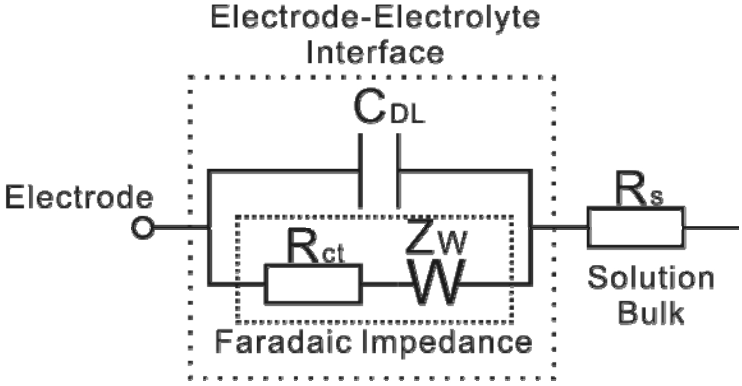

Figure 3-4 Randles equivalent circuit for electrode-electrolyte interface.

In addition to the Faradaic impedance and the double-layer capacitance, a resistor R_s is included in the equivalent circuit, representing the resistance of the bulk electrolyte. This equivalent circuit is commonly used in Electrochemical Impedance Spectroscopy (EIS) for interpretation of impedance spectra. However, we should be aware that this equivalent circuit only works for extremely small AC excitation signals. All the components in this circuit are not ideal electronic component when the excitation signal is not small, except R_s. We should also be aware that both C_{DL} and the Faradaic impedance have a DC voltage bias. This DC bias is V_z for C_{DL}, and V_{eq}^* for the Faradaic impedance.

3.5 Model for DC excitation

As mentioned before, the concentration of oxidant or reductant on the electrode surface is the same as in the bulk solution at equilibrium ($C_O(x=0) = C_O^*$, $C_R(x=0) = C_R^*$), and a floating electrode has a potential of V_{eq}^* with respect to the solution bulk. If a voltage V different from V_{eq}^* is applied to the electrode, this voltage will create a charge transfer current given by equation 3-12, causing concentrations on the electrode surface ($C_O(x=0)$, $C_R(x=0)$) to differ from the solution bulk (C_O^*, C_R^*). The difference of concentrations creates diffusion current as follows:

$$|I_O| = nFAm_O|C_O(x=0) - C_O^*| \qquad [3\text{-}21]$$

$$|I_R| = nFAm_R|C_R(x=0) - C_R^*| \qquad [3\text{-}22]$$

m_O is the mass-transfer coefficient of oxidant, which can be affected by solution dimensions, thickness of the diffusion, water flow and temperature. If a transient measurement is applied, the mass-transfer coefficient is also time dependent as the diffusion thickness changes with time (see section 4.4). m_R is the mass-transfer coefficient of reductant. $|I_O|$ and $|I_R|$ are the unsigned diffusion current.

When a DC voltage is applied on the electrode, equilibrium is broken and the charge transfer current I is bigger than the diffusion current $|I_O|$ and $|I_R|$ because the concentration differences are smaller. Then the difference from I to $|I_O|$ and $|I_R|$ creates a concentration difference. This accumulation reduces I by decreasing $|V-V_{eq}|$, and enhances $|I_O|$ and $|I_R|$ by increasing the concentration differences. Finally I, $|I_O|$ and $|I_R|$ reach the same values as $I = |I_O| = |I_R|$, assuming the bulk concentration does not change. Then the charge transfer current I is stabilized.

The relation between the DC voltage V and stabilized current I can be found as follows:

Consider that the positive direction of current is from the electrode to the electrolyte, then the diffusion current is:

$$I_O = nFAm_O(C_O(x=0) - {C_O}^*) \quad [3\text{-}23]$$

$$I_R = nFAm_R({C_R}^* - C_R(x=0)) \quad [3\text{-}24]$$

If V is bigger than ${V_{eq}}^*$, the reduced species (reductant) is consumed, therefore I has an upper limit (I_{ul}) when $C_R(x=0) = 0$:

$$I_{ul} = nFAm_R{C_R}^* \quad [3\text{-}25]$$

If the reaction has more than one reductant, the upper limit of current will be determined by the reductant which has smallest product of m_R and ${C_R}^*$. If one of the reductants has an initial concentration of 0, this reaction will have I_{ul} of 0.

Conversely if V is smaller than ${V_{eq}}^*$, then oxidised species (oxidant) is consumed, therefore I has a lower limit (I_{ll}) when $C_O(x=0) = 0$:

$$I_{ll} = -nFAm_O{C_O}^* \quad [3\text{-}26]$$

Therefore the relations between the concentrations on the electrode surface and in the solution bulk when stabilized are given as:

$$C_O(x=0) = \frac{I - I_{ll}}{nFAm_O} \quad [3\text{-}27]$$

$$C_R(x=0) = \frac{I_{ul} - I}{nFAm_R} \quad [3\text{-}28]$$

Using equation 3-27 and 3-28 into equation 3-8, we see that:

$$V = \eta + V_{eq} = \eta + \Phi^0 - \frac{RT}{nF}\ln\frac{m_O}{m_R} + \frac{RT}{nF}\ln\frac{I - I_{ll}}{I_{ul} - I} \quad [3\text{-}29]$$

Where η is the voltage difference between V and V_{eq} ($\eta = V - V_{eq}$). Normally η is very small, therefore it is not necessary to distinguish between V and V_{eq}. By ignoring this difference, the relation between V and I is shown in figure 3-5:

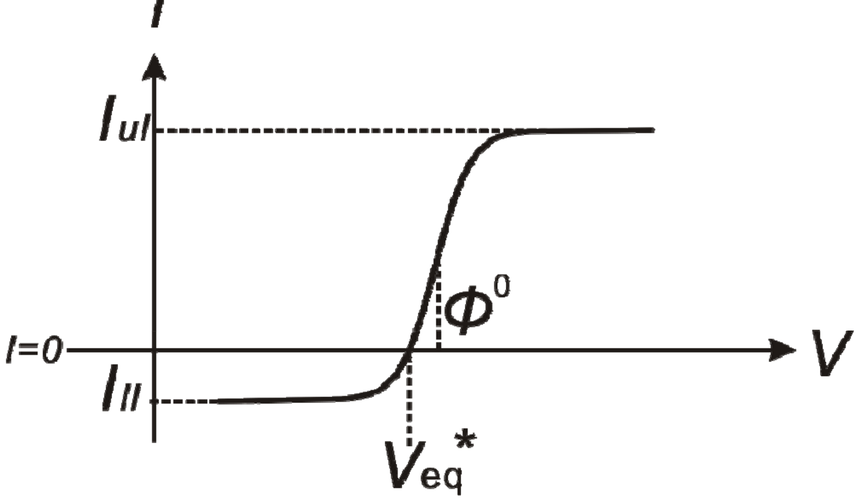

Figure 3-5 Plot of the V-I relation. V is the applied DC voltage on the electrode-electrolyte interface, while I is the stabilized current.

As shown in the figure, the stabilized current I is very close to I_{ll} if V is much smaller than the standard equilibrium voltage Φ^0. This current increases rapidly from I_{ll} to I_{ul} in the region of Φ^0, then is close to I_{ul} when V is bigger than Φ^0.

The concentration of the solution (C_O^* and C_R^*) is important to the shape of this V/I figure. As I_{ul} and I_{ll} are in direct proportion to C_O^* and C_R^* respectively, they determine the range of the stabilized current I. This range is in direct proportion to the width of the increasing slope. However, no matter where the equilibrium voltage V_{eq}^* is, the centre position of the slope is Φ^0, and has no relation to C_O^* and C_R^*.

3.6 Electrochemical reactions in sea water

Sea water is a complex mixture of dissolved salts. As table 3-2 shows, many kinds of ions are dissolved in sea water. Furthermore, gas molecules, such N_2 and O_2, are also dissolved in sea water, e.g. O_2 has a concentration of about 0.0003 mol/kg at one atmosphere. Electrodes are normally made from Pt or Ag/AgCl, therefore we need to consider reactions concerning these ions, molecules, and the electrodes. Table 3-3 gives these reactions, with their standard equilibrium voltage Φ^0.

Component	**Concentration (mol/kg)**
H_2O	53.6
Cl^-	0.546
Na^+	0.469
Mg_2^+	0.0528
SO_4^{2-}	0.0282
Ca^{2+}	0.0103
K^+	0.0102
C_T $([CO_2*] + [HCO_3^-] + [CO_3^{2-}])$	0.00206
Br^-	0.000844
B_T $([H_2BO_3^-] + [H_3BO_3])$	0.000416
Sr^{2+}	0.000091
F^-	0.000068

Table 3-2 Concentrations of major species present in seawater @ Salinity = 35 psu [101].

Number	Reactions	Φ^0 (V)
1	$\frac{3}{2}N_2(g) + H^+ + e^- \leftrightarrow HN_3(aq)$	−3.09 [102]
2	$K^+ + e^- \leftrightarrow K(s)$	−2.931 [103]
3	$Sr^{2+} + 2e^- \leftrightarrow Sr(s)$	−2.899 [103]
4	$Ca^{2+} + 2e^- \leftrightarrow Ca(s)$	−2.868 [103]
5	$Na^+ + e^- \leftrightarrow Na(s)$	−2.71 [103]
6	$Mg^{2+} + 2e^- \leftrightarrow Mg(s)$	−2.372 [103]
7	$2H_2O + 2e^- \leftrightarrow H_2(g) + 2OH^-$	−0.8277 [103]
8	$2CO_2(g) + 2H^+ + 2e^- \leftrightarrow HOOCCOOH(aq)$	−0.43
9	$O_2(g) + H^+ + e^- \leftrightarrow HO_2\bullet(aq)$	−0.13
10	$CO_2(g) + 2H^+ + 2e^- \leftrightarrow CO(g) + H_2O$	−0.11
11	$N_2(g) + 2H_2O + 6H^+ + 6e^- \leftrightarrow 2NH_4OH(aq)$	+0.092
12	$SO_4^{2-} + 4H^+ + 2e^- \leftrightarrow SO_2(aq) + 2H_2O$	+0.17
13	$AgCl(s) + e^- \leftrightarrow Ag(s) + Cl^-$	+0.22233 [103]
14	$O_2(g) + 2H_2O + 4e^- \leftrightarrow 4OH^-(aq)$	+0.40 [104]
15	$O_2(g) + 2H^+ + 2e^- \leftrightarrow H_2O_2(aq)$	+0.70
16	$Br_2(aq) + 2e^- \leftrightarrow 2Br^-$	+1.0873 [103]
17	$Ag_2O(s) + 2H^+ + 2e^- \leftrightarrow 2Ag(s) + H_2O$	+1.17
18	$Pt^{2+} + 2e^- \leftrightarrow Pt(s)$	+1.188 [32]
19	$O_2(g) + 4H^+ + 4e^- \leftrightarrow 2H_2O$	+1.229 [104]
20	$Cl_2(g) + 2e^- \leftrightarrow 2Cl^-$	+1.36 [104]
21	$AgO(s) + 2H^+ + e^- \leftrightarrow Ag^+ + H_2O$	+1.77
22	$H_2O_2(aq) + 2H^+ + 2e^- \leftrightarrow 2H_2O$	+1.78
23	$Ag^{2+} + e^- \leftrightarrow Ag^+$	+1.98 [105]
24	$O_3(g) + 2H^+ + 2e^- \leftrightarrow O_2(g) + H_2O$	+2.075 [32]
25	$F_2(g) + 2e^- \leftrightarrow 2F^-$	+2.87[106]

Table 3-3 List of electrochemical reactions for sea water, ordered by their standard electrode potential from low to high. The legends behind the reagents' names indicate the reagents' form: *(s)* – solid, *(l)* – liquid, *(g)* – gas, *(aq)* – aqueous. Reagents in red text are rare in sea water, in blue text are provide by the electrode, in black are in sea with certain concentrations.

As discussed above, a reaction will have I_{ul} or I_{ll} equal to 0, if at least one of the reductants or oxidants is rare in the seawater. Therefore reaction 8~12, 15, 20, and 23 in the table can be ignored because both I_{ul} and I_{ll} are 0. Also, reactions 1~7, and 14 have I_{ul} equal to 0, while reactions 16~20, 22, 24, and 25 have I_{ll} equal to 0.

3.6.1 Ag/AgCl electrode

When a Ag/AgCl electrode is used, reaction 13 is the only reaction which has neither rare oxidant nor rare reductant. The oxidant of the reaction is AgCl and can be considered infinite as it is the material of the electrode. Therefore the I_{ll} of this reaction can be considered infinite. For the reductant, Ag is the electrode material, and Cl^- is the ion of largest concentration (0.546 M) in seawater. Therefore I_{ul} of this reaction is also large. Because reaction 13 allows large currents to pass though it in both directions, other reactions are not going to happen, and the Ag/AgCl electrode has a narrow range of excitation voltages around the Φ^0 (0.222 V). The equilibrium voltage of Ag/AgCl electrode for seawater at 25 ^{o}C is 0.237 V calculated from equation 3-9. Therefore it can be considered as a non-polarisable electrode, as long as the excitation current is small, and does not impact the Cl^- concentration around the electrode.

3.6.2 Platinum Electrode

When a platinum electrode is used, equation 13 and 17 can be ignored as no silver is present. The equilibrium voltage of a platinum electrode is difficult to determine, and depends on the concentration of the rare ions. However, this equilibrium voltage is in the range between Φ^0_{14} and Φ^0_{16} (0.40~1.0873 V, Φ^0_i is Φ^0 of equation i), because equation 1~14 have I_{ul} equal to 0, and equation 16~24 have I_{ll} equal to 0.

Water (H_2O) has a positive standard electrolysis potential of 1.229 V (Φ^0_{19}), and negative standard electrolysis potential of -0.8277 V (Φ^0_7). If seawater is neutral (pH=7), both H^+ and OH^- have concentrations of 10^{-7} M, therefore the potentials where electrolysis starts (at 25 ^{o}C) can be calculated as Φ^{0*}_{19}=0.814 V and Φ^{0*}_7=-0.413 V. As a solvent, H_2O can provide a very large electrolysis current when the potential increase above its standard electrolysis potential. These electrolysis potentials confine the applied voltage on the electrode, prohibiting it from being either much higher than Φ^0_{19} or much lower than Φ^0_7. Therefore any reduction with a Φ^0 much lower than Φ^0_7 is not going to happen (reactions 1~6, from left to right). As they also have I_{ul} equal to 0, reactions 1~6 are not going to happen in either directions, and can be ignored. Similarly, reactions 21~25 have Φ^0 much higher than Φ^0_{19}, and I_{ll} equal to 0. Therefore they are not going to happen either.

Reactions 16, 18, 19, and 20 are competing reactions with similar standard electrode potentials. Reaction 16 can be ignored because Br^- has a much lower concentration compared to Pt, H_2O, and Cl^- in equation 18~20 respectively. In neutral or alkaline solvent, reaction 18 happens in another form as:

$$PtO(s) + 2H^+ + 2e^- \leftrightarrow Pt + H_2O \qquad \Phi^0 = 0.980\ \text{V}\ [107]$$

In this reaction, the oxidation product PtO is in solid state. It covers the electrode surface, preventing the remaining Pt to be oxidised. Due to this kinetics reason, reaction 18 has I_{ul} of 0. In the remaining 2 reactions, experiments [108, 109] show that reaction 20 will happen, prohibiting reaction 19, if the applied potential is bigger than Φ^0_{20}.

Hence only reactions 7, 14, 19 and 20 need to be considered. The combined effect of these results can be seen in figure 3-6 which gives the V-I profile of sea water for a platinum electrode. The dominant electrochemical reactions over specific potential bands are indicated.

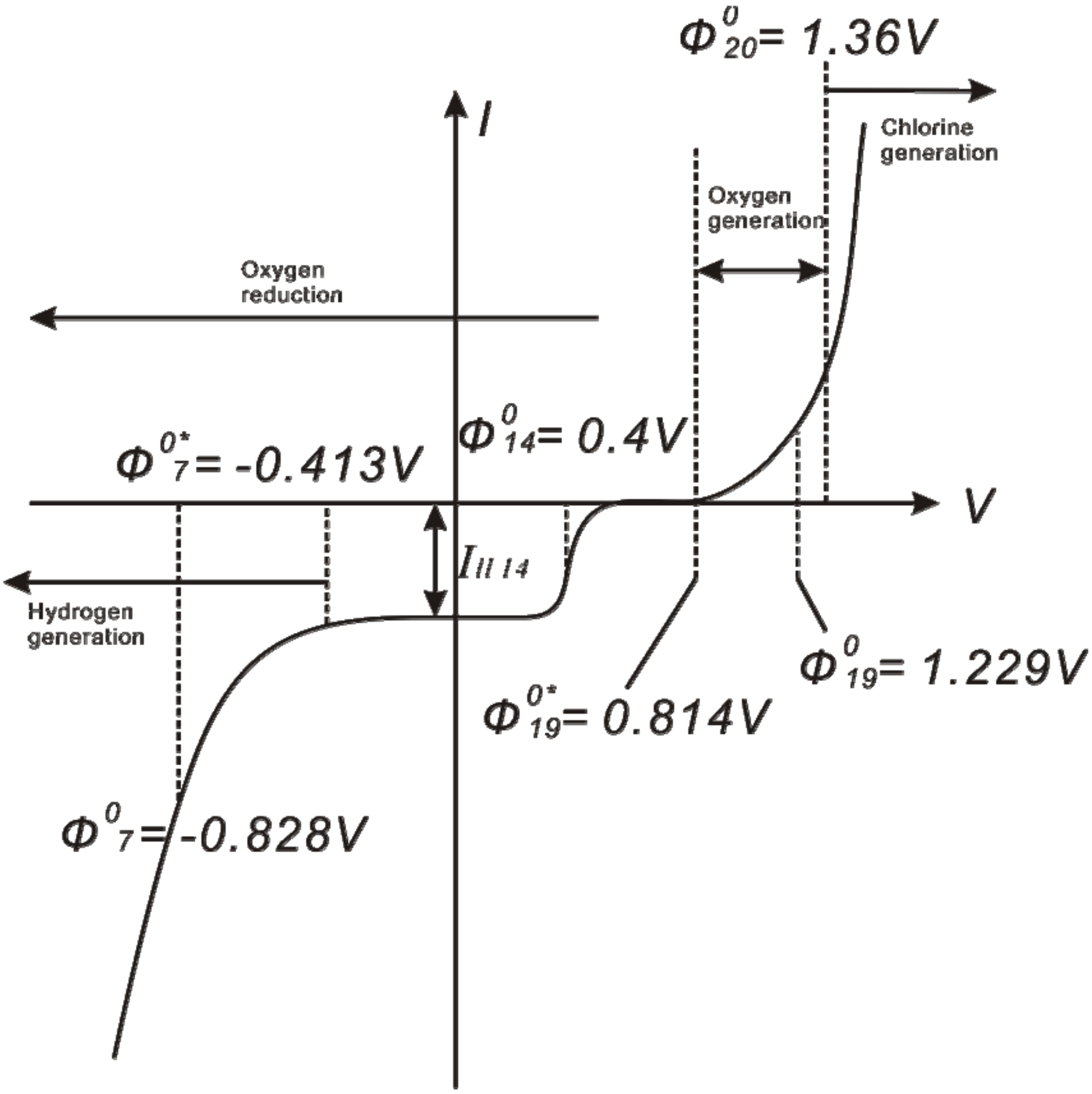

Figure 3-6 V-I profile of the platinum electrode-sea water interface. *V* is the DC voltage applied on the electrode-electrolyte interface, while *I* is the stabilized current.

3.7 Discussions

This chapter introduced the theories of the electrode-electrolyte interface and electrochemical reactions of the sea water. These theories underpin the measurement of the conductivity and dissolved oxygen in water. Furthermore, as chlorine is toxic for organism, these theories can also be used to generate chlorine gas around the sensor cell as mitigation against bio-fouling.

In order to use these theories, some specific points need to be made as follows.

3.7.1 Conductivity sensor

As shown by equation 2-2, the water conductivity σ is determined from the water resistance R_s, together with the cell constant. R_s is present in the Randles equivalent circuit as the only linear component, and can be measured using an AC signal.

A two-electrode conductivity cell has measurement error caused by the interface impedance, including the double-layer capacitance and the Faradaic impedance. The value of these interface impedances are not fixed but are affected by temperature and water flow rate. Therefore this error varies, and cannot be removed by calibration with piecewise fitting. Furthermore, these interface impedances are not linear components. Lock-in method is usually used to improve the AC measurement accuracy, where a signal with a known carrier wave is extracted from a noisy environment. When using a single frequency excitation, other frequency components will be included in response signal by the non-linear components affecting the lock-in measurement accuracy. Hence a two-electrode conductivity cell is not suitable for high accuracy measurement.

A four-electrode cell with an AC excitation can be used for high accuracy measurement. When a current source is used to apply current through the two outer current terminals, it does not matter how non-linear the applied voltage at the interface is, a linear voltage response can be measured across R_s using the two voltage terminals. Therefore a lock-in measurement method can be used.

Concerning electrode selection, the Ag/AgCl electrode has an almost fixed voltage referenced against the solution bulk and can be considered as non-polarized electrode. However this electrode will take part in any chemical reaction when current passes through it, changing its surface properties. Also the electrode can be consumed during the deployment as AgCl has solubility of 1.9 mg/L in water. As the cell constant κ is sensitive to surface conditions and dimensions, this change will cause a measurement error in the conductivity cell. Conversely a platinum electrode is a polarized electrode. However it is much more stable than Ag/AgCl, therefore is more suitable for conductivity measurement.

The charge transfer reactions for a platinum electrode will generate gases, such as O_2, H_2, and Cl_2, affecting the water dimension and κ, causing measurement error. Gases are generated only when the interface voltage is outside the range ±0.4V. Therefore this measurement error can be eliminated by constraining the interface voltage within this range. AC frequencies can also be used, which increases the current passing through the double-layer capacitance, and increasing the allowed current within this excitation voltage range.

3.7.2 Dissolved oxygen sensor

In ideal conditions, where an ideal diffusion gradient is created from the electrode to the semi-infinite and static bulk, dissolved oxygen can be measured using DC excitation, with a platinum electrode as a working electrode. As figure 3-6 shows, when applying a DC voltage in the range -0.4~0.3 V on a platinum electrode, the input current has an almost constant value of I_{ll14}. This current is in direct proportion to the concentration of dissolved oxygen, from equation 3-26. Therefore the DO concentration (C) is calculated as:

$$C_{O2}{}^{*} = -\frac{I_{ll7}}{4FAm_{O2}} \qquad [3\text{-}30]$$

A voltage in the range of -0.4~+0.3 V can be used as the measurement voltage. Applying a voltage range of +0.5~0.8 V gives an output current of 0. Therefore the equilibrium voltage is in this range, and a voltage in this range can be used as a resting voltage (i.e. a voltage at which no net chemical changes will occur).

The range and boundaries of the measurement voltage and the rest voltage are weakly affected by temperature, according to equation 3-8. However, as the ranges are relatively wide, if the voltages are set in the middle of these ranges, the measurement will not be affected by these weakly changing boundaries.

m_{O2} is the mass-transfer coefficient of the oxygen, and this can be affected by the dimensions of the electrode and water, the flow rate and temperature. The working electrode can be placed in the bottom of a blind hole, which defines the “water dimension”, and minimizes the influence of flow. For affect of the temperature, m_{O2} is considered a function of temperature. This function can be determined by calibration with fixed DO concentrations, changing the temperature from -2~30 °C. Because m_{O2} is an independent factor in equation 3-30, this calibrated function can be used for all DO concentrations.

To establish the voltage between the working electrode and solution bulk, a reference potential needs to be applied to the solution bulk. In a three electrode system [110], a reference electrode and an auxiliary electrode are used for this as shown in figure 3-7.

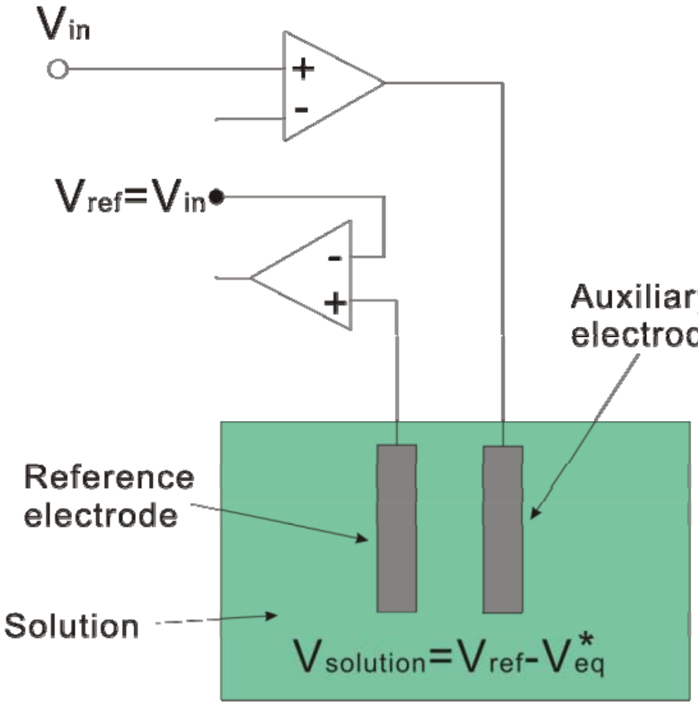

Figure 3-7 Diagram of a reference electrode – auxiliary electrode system.

The reference electrode is normally made from Ag/AgCl or Saturated Calomel Electrode (SCE), which has a fixed and stable equilibrium voltage (V_{eq}^*). This equilibrium voltage can be changed if large current passes through the reference electrode. To solve this problem, as shown in the figure, the auxiliary electrode is used to apply current, and the reference electrode is used as a voltage sensing electrode, passing no current. As the amplifiers keep the two input terminals at the same voltage, the voltage of the solution ($V_{solution}$) is set as:

$$V_{solution} = V_{in} - V_{eq}^* \qquad [3\text{-}31]$$

where V_{in} is the input voltage.

However, if the reference electrode has a much larger area than the working electrode, we can remove the auxiliary electrode and use the reference electrode to apply the current directly. In this case, the reference electrode should have an extremely small current density, causing an insignificant change in the voltage.

3.7.3 Electrochemical cleaning

Ocean sensors are affected by bio-fouling during deployment. Most of the existing sensors need periodic manual cleaning. Some sensors use wipers or toxic chemicals to automatically remove bio-fouling. However these mechanisms require power hungry machinery, including pumps and motors, and are not suitable for low power in-situ systems [111].

Chlorination has long been used in industrial applications to protect systems from bio-fouling [111]. Recently electrolysis chlorination method has been used for bio-fouling protection of in-situ oceanographic instruments [111-114]. As figure 3-6 shows, application of a voltage greater than 1.36 V on a platinum electrode causes chlorine gas to be generated [115]. This mechanism can be used in the CT-DO device to remove bio-fouling, and is ideally suited to a low power in-situ CT-DO system, where the platinum electrodes of conductivity sensor can be used as working electrode, and the Ag/AgCl electrode of DO sensor can be used as reference electrode (see chapter 6).

Chapter 4 Sensor Chip Design

4.1 Overview of sensor design

As discussed in chapter 2 and 3, the electrode conductivity cell has advantages in minimizing the proximity effect and has smaller dimensions. Therefore it was chosen as the conductivity sensor. The PRT was chosen as the temperature sensor because it has better stability and is more suitable for precision applications. For the DO sensor, the membrane-less electrode sensor was chosen as it has a fast time response, and is easy to miniaturize.

The CT-DO sensors use micro-fabrication techniques similar to those used to manufacture integrated circuits. The sensor chips are manufactured on a 500 μm thick glass substrate. Platinum is coated on the substrate to make electrodes, wires, and soldering pads. Insulating material is then coated to protect the platinum which should be insulated from the water. Appendix B shows a figure of the fabrication process flow. Figure 4-1 shows the structure of the sensor chips.

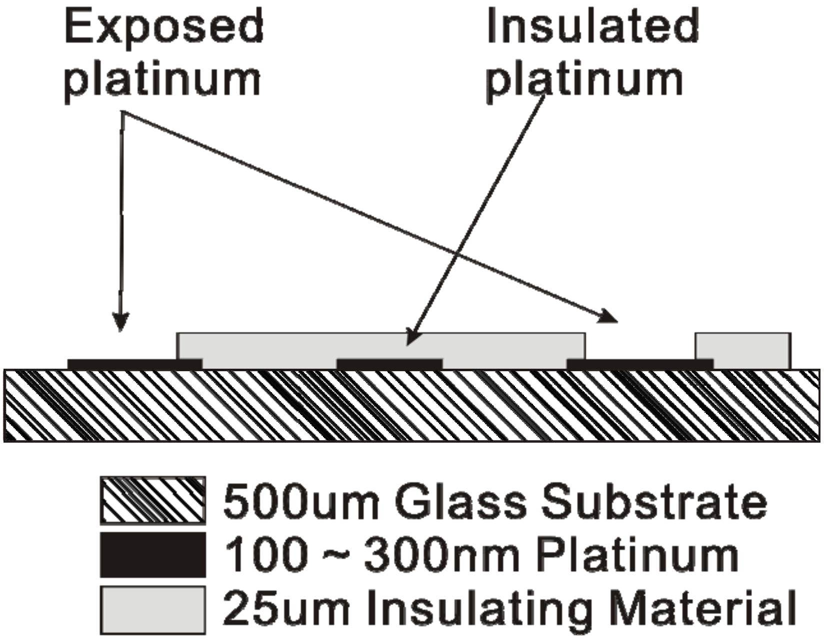

Figure 4-1 A diagram of sensor chip structure with a 500 μm thick glass substrate, a platinum layer, and an insulating material layer.

The CT-DO sensors were manufactured on a glass wafer, and then the wafer was scribed to give many sensor chips. Three different designs of the CT-DO sensors were made. Design 1 has only CT sensors and is manufactured on a 4-inch glass wafer. The electrodes are insulated with a 20 μm thick epoxy laminate (SY320). The thickness of the platinum layer in this design is 100 nm.

Design 1 was manufactured in order to test the seven-electrode channel conductivity cell (chip design 1-A). A four-electrode open cell (chip design 1-B) was also implemented into this design for evaluation purposes. A PRT electrical-bridge was implemented for temperature sensing. The CT sensors are integrated into a single chip. Therefore there are two types of CT sensor chips with different combinations of the PRT temperature sensor and the two different conductivity sensors. Figure 4-2 shows the mask of the CT sensor chips in design 1, figure 4-3 shows a photograph of the sensor chips, and figure 4-4 shows the mask for the whole glass wafer.

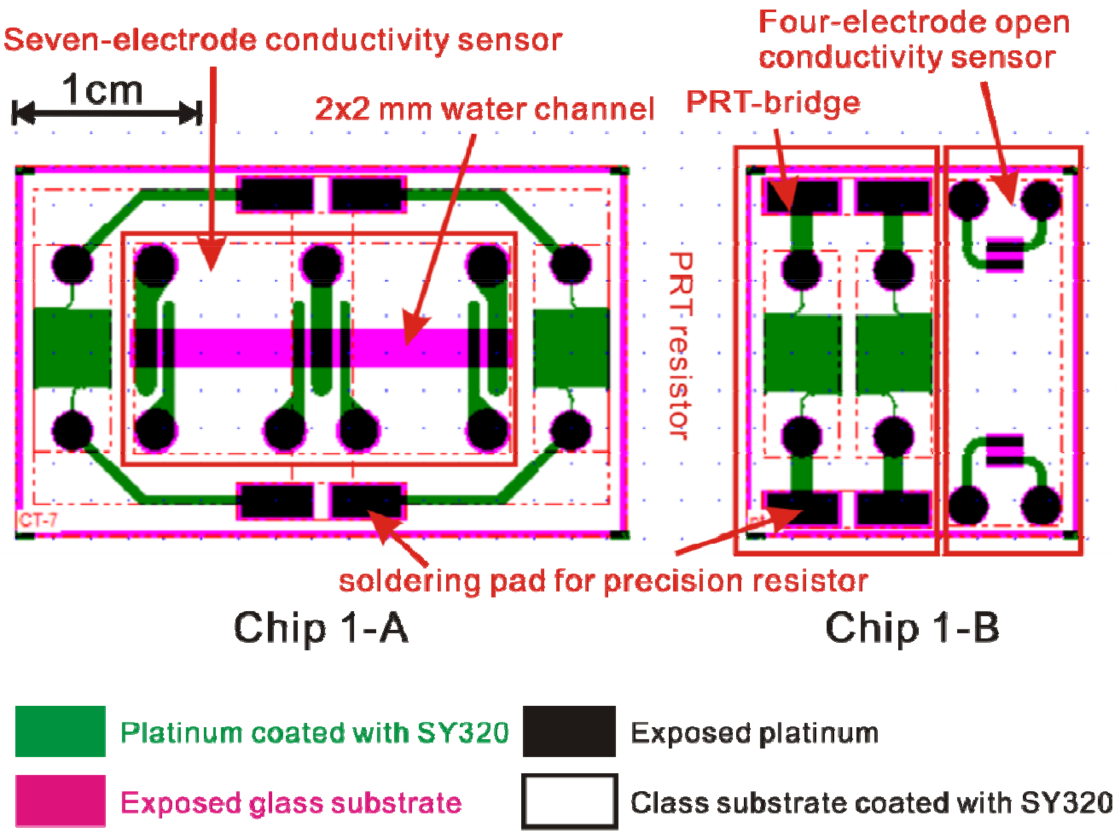

Figure 4-2 A diagram showing the masks of the CT sensor chips in design 1, including chip 1-A – a seven-electrode conductivity sensor with a PRT electric-bridge temperature sensor and chip 1-B – a four-electrode conductivity sensor with a PRT electric-bridge temperature sensor.

Figure 4-3 A Photograph of the CT sensor chips in design 1, including chip 1-A (left) and chip 1-B (right).

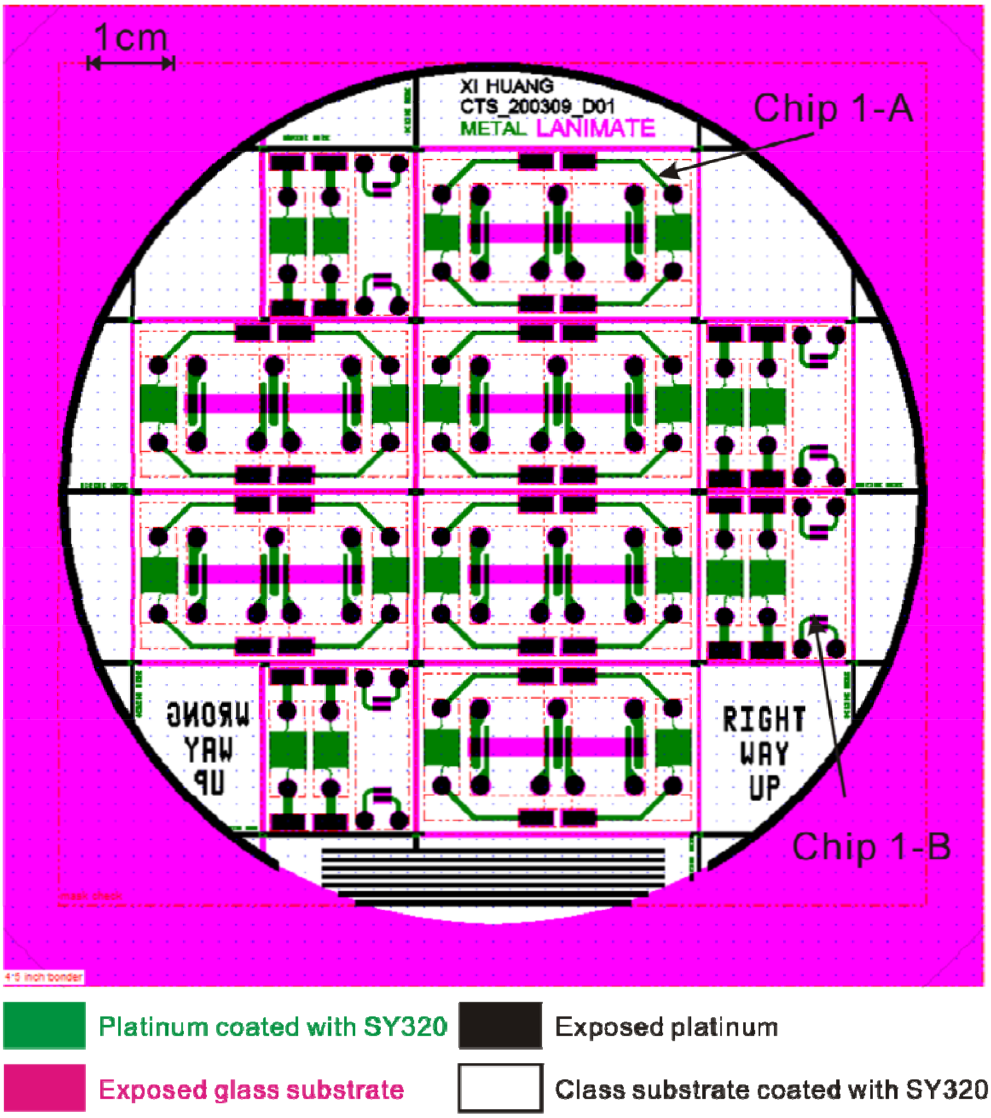

Figure 4-4 A diagram of the 4-inch mask of design 1. Two types of chips are implemented in this mask including chip 1-A and chip 1-B.

Design 2 was manufactured on a 6-inch glass wafer, and includes both CT and DO sensors. Improvements were made based on the test results from design 1 sensors, including: the thickness of the platinum layer was increased to 300 nm; the SY320 epoxy laminate was replaced by 300 nm silicon nitride (low stress SiN) covering the platinum, and a 25 μm thick SU8 epoxy laminate covered the SiN.

From the test result of design 1 sensors (chapter 6), the open cell conductivity sensor has better reliability. Therefore a four-ring-electrode open conductivity sensor is used in design 2 (chip 2-A). This sensor can also be used as a DO sensor, as there are 5 micro holes in insulation covering the centre electrode which defines 5 bare platinum disc microelectrodes at the base of small pits which can be used for DO measurement.

The temperature sensor in this design is implemented on a separate chip (chip 2-B). As an alternative concept, another two conductivity sensor designs are also included in the mask set for design 2. These are a seven-electrode conductivity cell with a 2x2 mm water channel (chip 2-C), and a seven-electrode open conductivity cell (chip 2-D). Therefore, there are four kinds of sensor chips in design 2. Figure 4-5 shows the masks of these four sensor chips, figure 4-6 shows a photograph of chips 2-A and 2-B, and figure 4-7 shows the mask of the whole glass wafer.

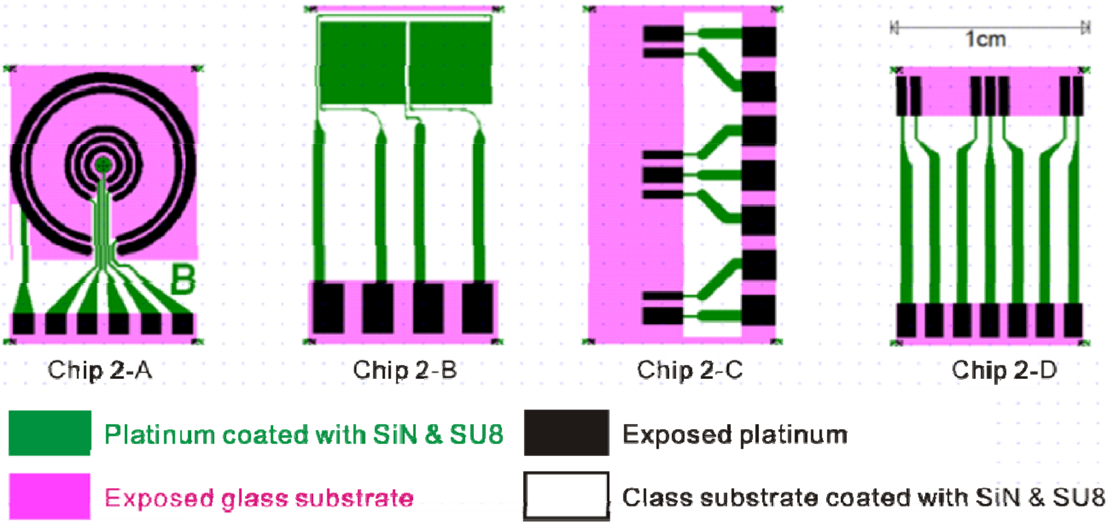

Figure 4-5 A diagram showing the masks of the CT sensor chips in design 2, including chip 2-A – four-ring-electrode open conductivity and DO sensor, chip 2-B – a PRT-bridge temperature sensor, chip 2-C – a seven-electrode conductivity sensor chip to couple with a 2x2 mm water channel, and chip 2-D – a seven-electrode open conductivity sensor.

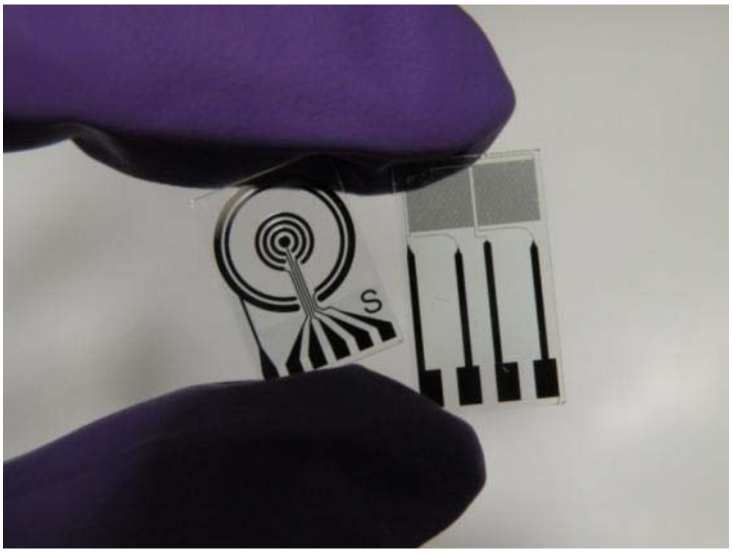

Figure 4-6 A Photograph of the sensor chips in design 2, including chip 2-A (left) and chip 2-B (right).

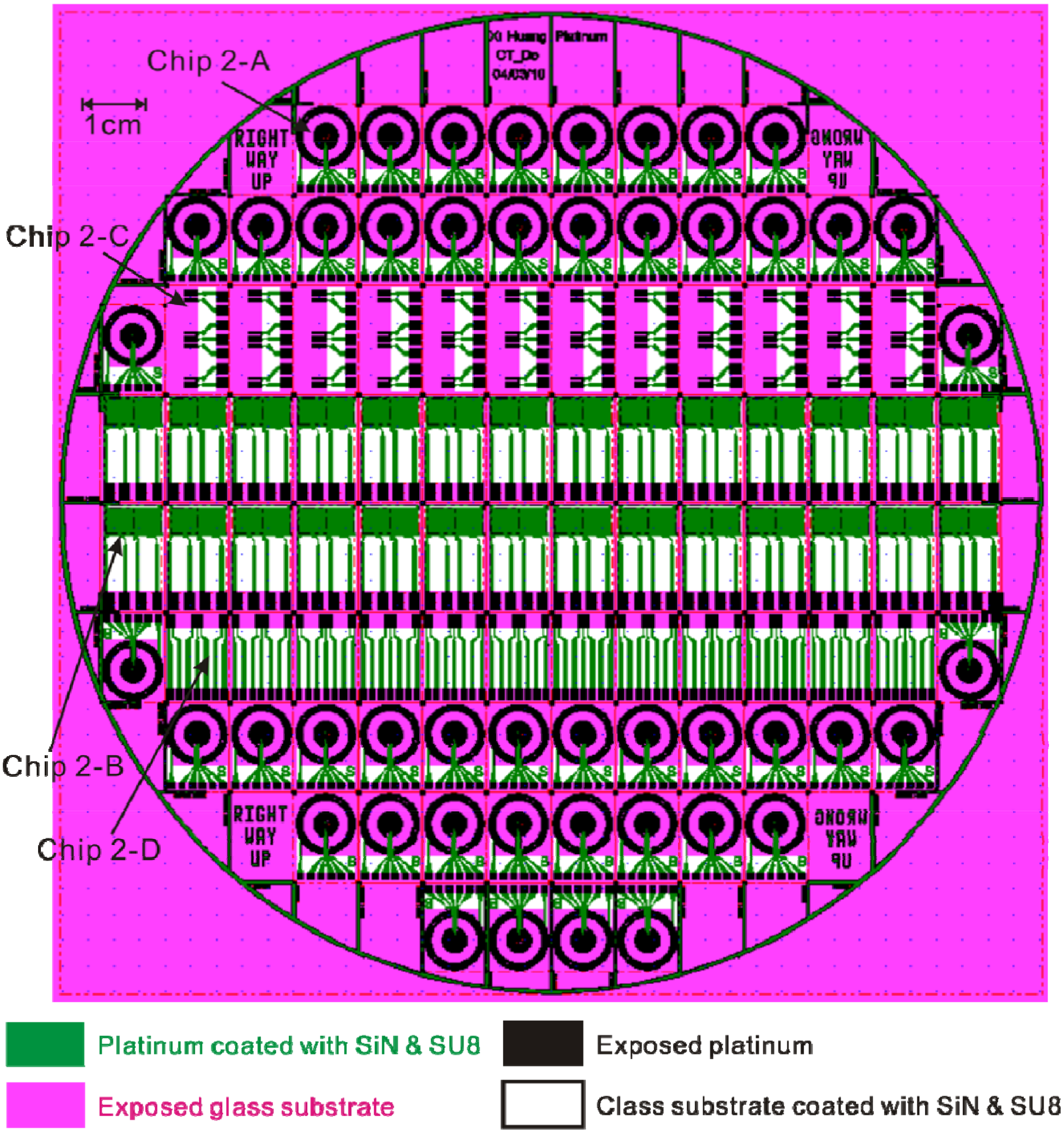

Figure 4-7 A diagram of the 6-inch mask of design 2. Four types of chips are implemented in this mask, including chip 2-A, chip 2-B, chip 2-C, and chip 2-D.

Sensors of design 2 worked well in the tests, but the conductivity and temperature sensor are on separated chips. Also chip 2-A can only be configured as either conductivity or DO sensor at one time unless an external multiplexer is used. A complete integrated CT-DO sensor system therefore requires three sensor chips, based on design 2. To further miniaturize the system, design 3 integrates the entire CT-DO into a single sensor chip.

Design 3 is manufactured on a 6-inch glass wafer in the same materials as design 2. However the platinum and SU8 is now on the both sides of the glass substrate. One side of the sensor chip is used for conductivity sensing, while the other side is used for DO sensing. Each side has a PRT resistor. Therefore two PRT resistors are on the sensor chip. These can be used as a PRT bridge temperature sensor. Design 3 is not yet fabricated and the results are not included in this thesis. Figure 4-8 shows the mask for the two sides of the sensor chip, figure 4-9 shows the mask of the whole glass wafer.

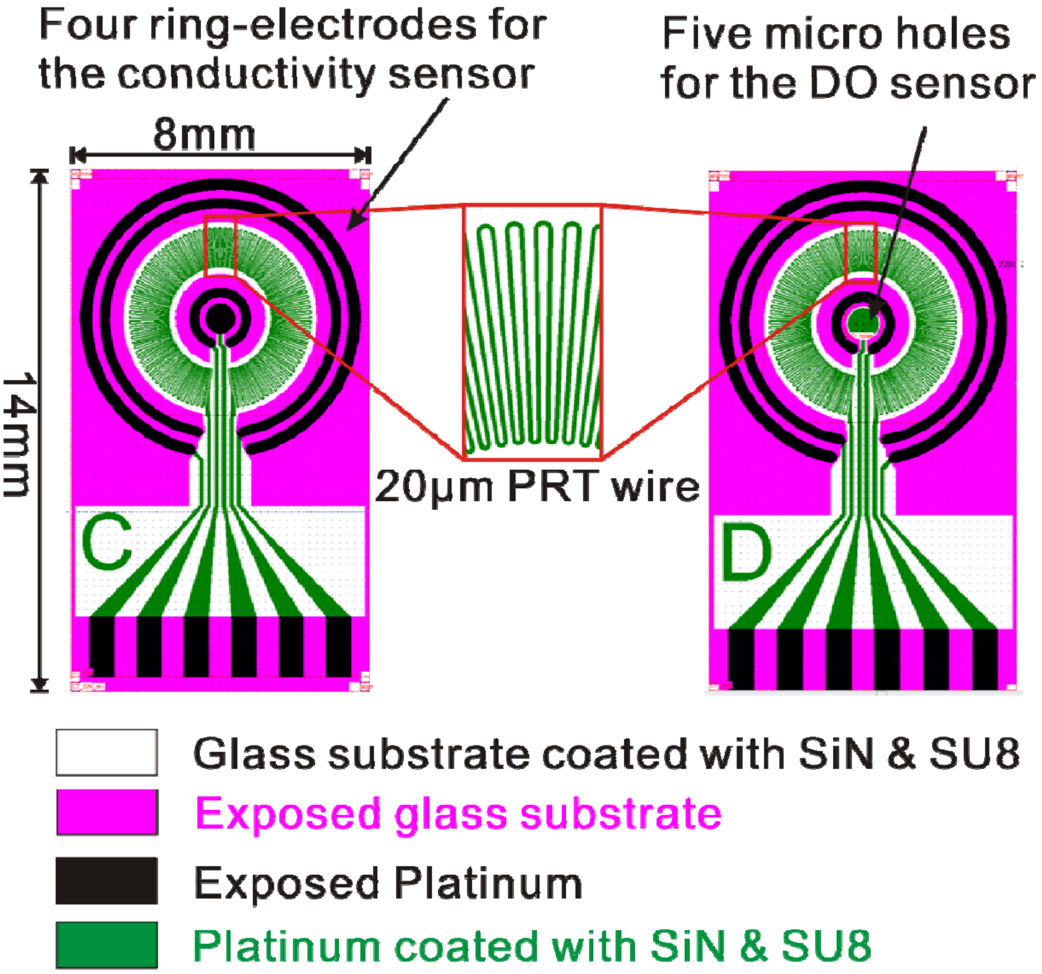

Figure 4-8 A diagram showing the mask of the double-side CT sensor chip in design 3: (left) conductivity side; (right) DO side.

As shown in figure 4-8, both sides of the chip, i.e. the conductivity and DO sensors both use symmetric platinum patterns. The only other difference is that the side containing the conductivity sensor has the central electrode completely exposed, whilst on the side with the DO sensor this is covered with an insulator except for 5 x 25 μm micro holes.

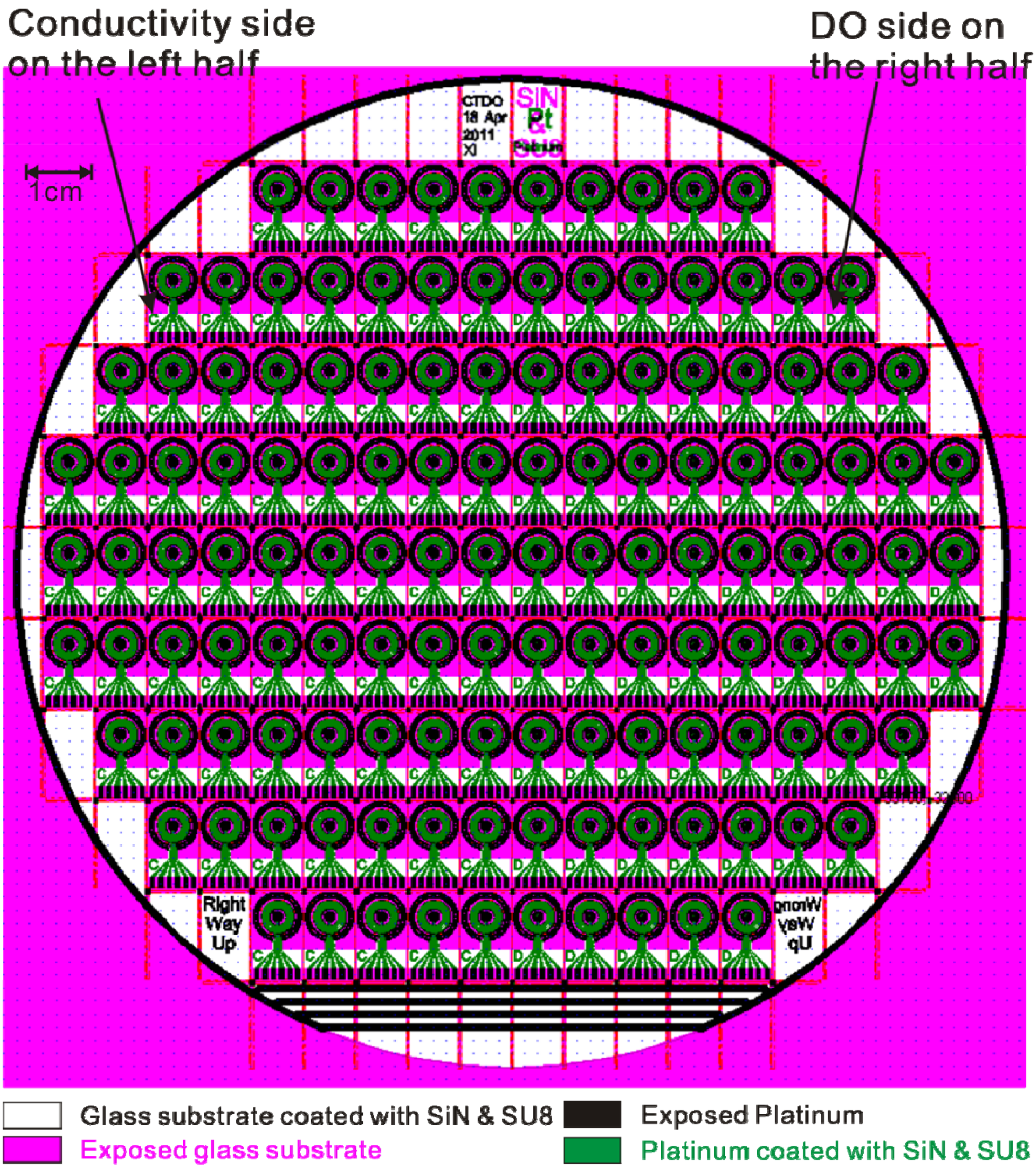

Figure 4-9 A diagram of the 6-inch mask of design 3. Two types of chips are implemented in this mask, with conductivity chips on the left half, and DO chips on the right half.

As shown in figure 4-9, the mask is symmetrical along the centre, with conductivity chips on the left half, and DO chips on the right half. Using double sided lithography, each sensor chip will have one side for measuring conductivity and the reverse side for DO. Sensor chips on the left half of the wafer will have conductivity side on the top, and DO side on the bottom, while the sensor chip on the right half will have DO side on the top, and conductivity side on the bottom.

4.2 Conductivity sensor

4.2.1 Channel conductivity sensor

Proximity effect simulation

As discussed in section 2.2.1, to prevent proximity effects, the external electric field can be reduced by adding a counter electrode to the water channel. Intuitively it would seem sensible to create a geometrically symmetric design with this 5th electrode at the same distance from the outer current drive electrode as is the furthest electrode at the other end of the channel (as in Figure. 4-10). However, because the voltage sensing electrodes have a significant length and high conductivity, this cell is not symmetric in resistance, and hence current distribution. A simulation was made to demonstrate this point. Figure 4-10 is a diagram showing the signal excitation method and the dimension of a five-electrode conductivity cell. Figure 4-11 is an equivalent circuit drawn in ORCAD [116] with estimated components values of the five-electrode conductivity cell using 50 mS/cm seawater. The simulation results are shown in Figure 4-12.

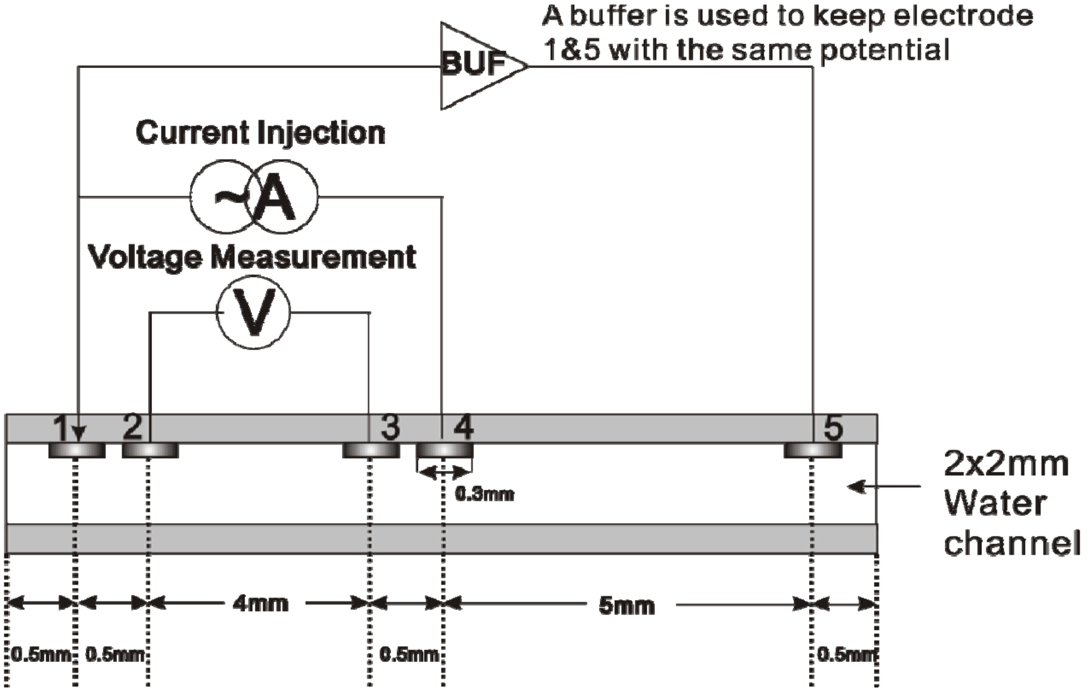

Figure 4-10 A diagram showing the dimension and signal exciting method of a five-electrode cell.

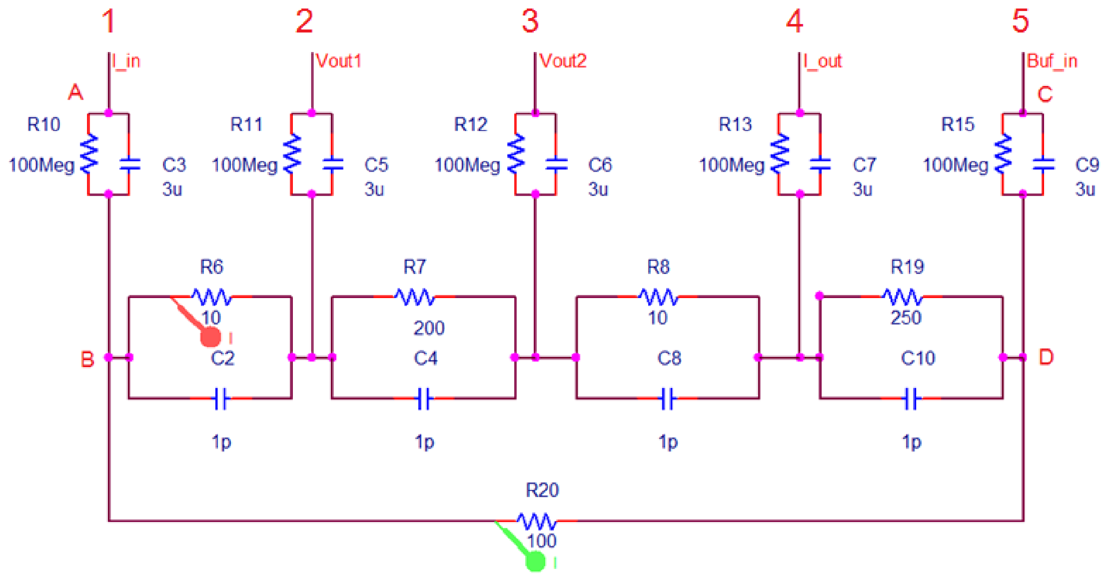

Figure 4-11 An equivalent circuit built in ORCAD of the five-electrode conductivity cell with 50 mS/cm seawater. The sum of resistances R_6, R_7 and R_8 is less than R_{19} because of the conductivity and non zero dimension of electrodes 2 and 3.

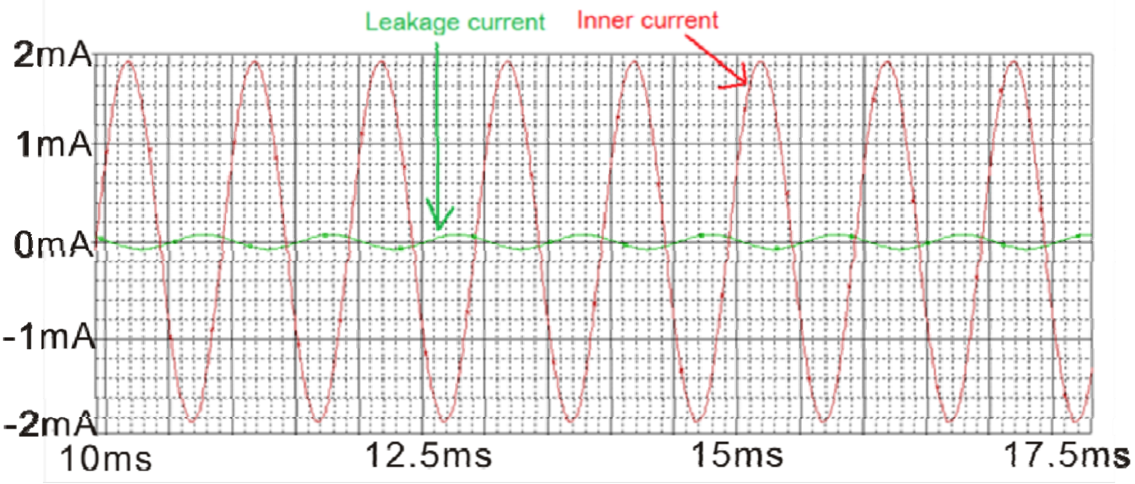

Figure 4-12 ORCAD simulation result of the inner current and leakage current of the five-electrode conductivity cell.

In a five-electrode cell, electrodes 1~4 are used to provide a conventional four-electrode cell, whilst electrode 5 is driven with the same voltage as electrode 1. If electrode 4 is in the middle of electrode 1 and 5 geometrically and electrodes 2 and 3 have non zero length, the resistance between electrode 1 and 4 (R_6+R_7+R_8 in figure 4-11) will be smaller than the resistance between electrode 4 and 5 (R_{19} in figure 4-11). This imbalance coupled with polarisation effects, means that although electrode 1 and 5 (points A and C in figure 4-11) are at the same potential, the surrounding water (points

B and D in figure 4-11) will not have the sample potential. Hence there is still some leakage current, which causes proximity effects. In the simulation, the resistance between electrode 1 and 4 is set to 220 Ω, while the resistance between electrode 4 and 5 is set as 250 Ω. This gives about 5% leakage current because of the 15% difference in the resistances.

The difference in the resistances can be reduced by shortening the distance between electrode 4 and 5. However, this method cannot totally eliminate this difference for water with different conductivities. The resistance between electrode 4 and 5 (R_{19} in figure 4-11) is directly proportional to water resistivity, but the resistance between electrode 1 and 4 refers to not only the water resistivity, but also the impedance of the electrode-electrolyte interface at electrode 2 and 3, which is not directly proportional to the water resistivity. Therefore, water conductivity has different effects on these two resistances. Even we can eliminate this difference for certain conductivity, this balance will be broken once the conductivity changes. Alternatively both geometric and electrical symmetry can be achieved with a seven-electrode conductivity cell. Such a design is presented in figure 4-13 together with an electric field simulation:

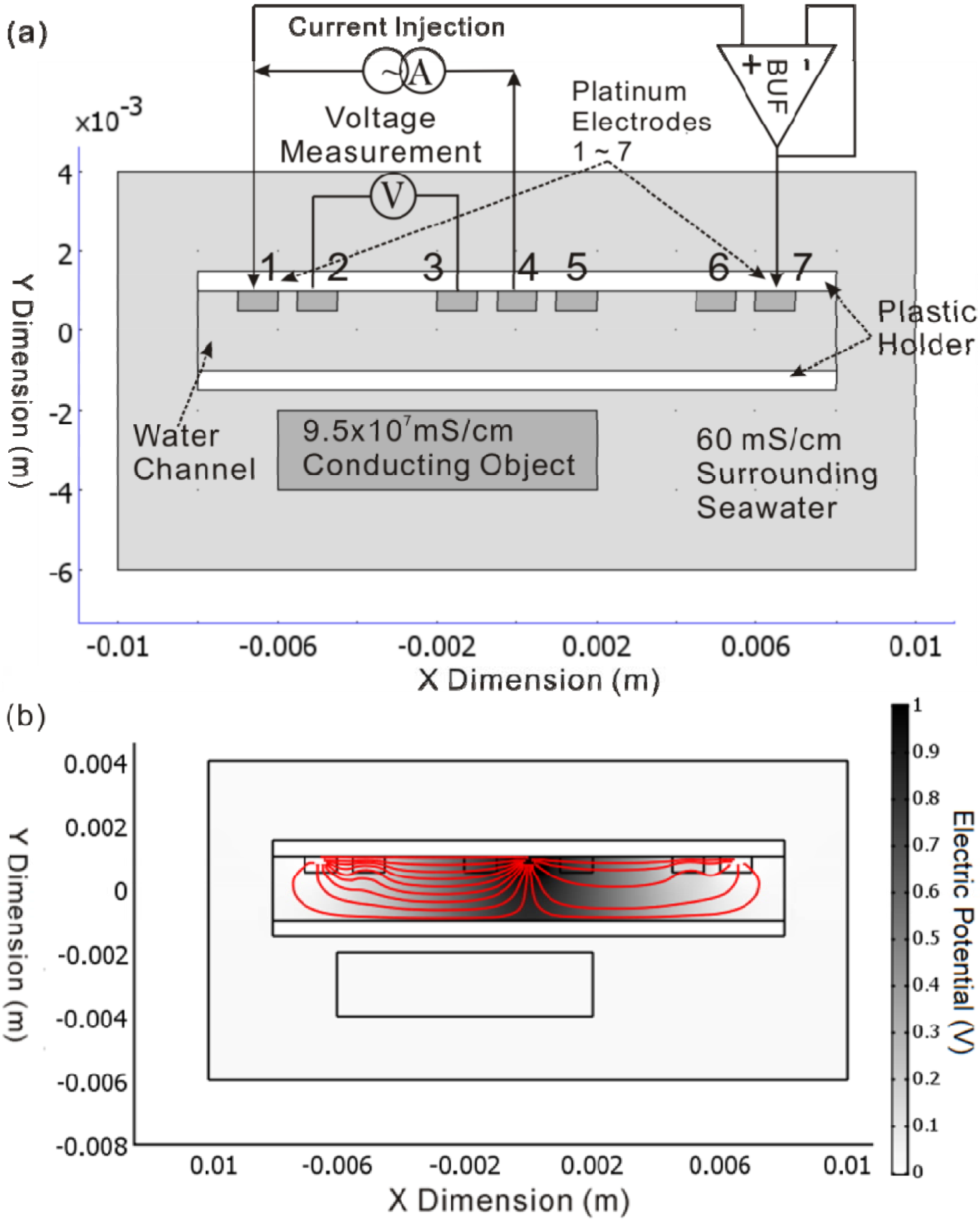

Figure 4-13 (a) A diagram showing the signal excitation scheme for the seven-electrode cell, and 2D drawing in COMSOL. Electrode 4 is set to 1 V, and electrodes 1 and 7 are set to 0 V; (b) FEM simulation result for the seven-electrode conductivity cell, where the gray scale is the electrical potential and the streamlines are current density.

Electrodes 1 to 4 and 7 of the seven-electrode cell are used as a five-electrode cell, while electrode 5 and 6 keep the sensor resistances symmetrical. As shown in figure 4-13, the current is totally constrained inside the water channel. Compared with the four-electrode cell (figure 2-7), the conducting object does not affect the distribution of the electric field. Therefore the seven-electrode sensor reduces the proximity effects almost completely.

However, even if the design of the seven-electrode cell is symmetric, the real sensor will not be perfectly symmetric due to manufacturing errors. Slight asymmetries in the electrodes or the water channel will cause proximity effects, creating an extremely small error. To reduce the extremely small error, we can detect the voltage between electrode 5 and 6. By comparing this with the voltage response between electrode 2 and 3, the amount of leakage current can be calculated to remove the error. However this method requires two ADCs working together, and makes the conductivity calculation more complex. Furthermore, other errors might be caused by the durability and thermal expansion of the electrodes and the channel. Depending on manufacture, if these errors are larger than the extremely small error caused by the proximity effects, then the method based on sensing the voltage between electrode 5 and 6 is not required.

Design specifications

The seven-electrode cell should be as small as possible for a miniature system. However, if the water channel is too narrow, it is hard for water to enter. Adding a pump is a solution, but it will make the system complex and larger. In order to omit the pump, the channel size was set at 2x2 mm.

Although the seven-electrode cell is not affected by electrode polarisation, to achieve a significant voltage drop between electrode 2 and 3, the voltage across the double-layer capacitances of electrode 1, 2, 7 needs to be kept as small as possible. Therefore, the impedance of the double-layer capacitance should not be greater than the water resistance.

There is approximately 300 nF of double-layer capacitance for every mm^2 of electrode area, according to chapter 3. If there is no leakage current, the water resistance between two electrodes can be estimated by [117]:

$$R = \frac{L}{WH\sigma}$$

where L is the distance between the two electrodes, W and H is the width and height of the water channel and σ is the conductivity of water.

The dimension of the seven-electrode conductivity cells is shown in figure 4-14:

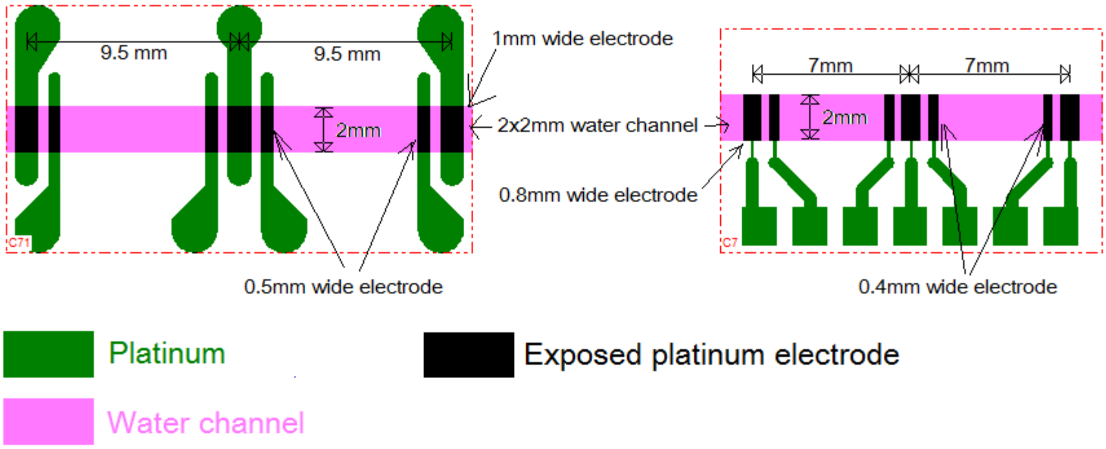

Figure 4-14 A diagram of the seven-electrode cells with 2x2mm water channel: (left) the conductivity cell using chip 1-A; (right) the conductivity cell using chip 2-C.

The distance between electrode 1 and 4 is 9.5 mm on chip 1-A, and 7 mm on chip 2-C. The widths of electrode 1, 4 and 7 are 1 mm on chip 1-A, and 0.8mm on chip 2-C. If the water conductivity is 50 mS/cm, the water resistance between electrode 1 and 4 is about 475 Ω and 350 Ω for chips 1-A and 2-C respectively, and the impedance of the double-layer capacitance for electrode 1, 4 and 7 is about 180 Ω and 225 Ω at 1.5 kHz. Therefore the water resistance is higher than the impedance of the double-layer capacitance. In addition, the widths of electrode 2, 3, 5, and 6 are 0.5 mm on chip 1-A, and 0.4 mm on chip 2-C.

4.2.2 Open conductivity cell

As discussed in section 2.2.1, proximity effects can also be reduced by constraining most of the electric field within a very small volume. For this method, the water channel is removed to make the distribution of electric field smaller. The distribution of the electric field depends on the geometry of the electrodes, and is proportional to the dimension of sensor cell.

To find the best geometry for constraining the electric field and reducing proximity effects, four kinds of geometries of open conductivity cells were simulated. Figure 4-15 shows the four open cells:

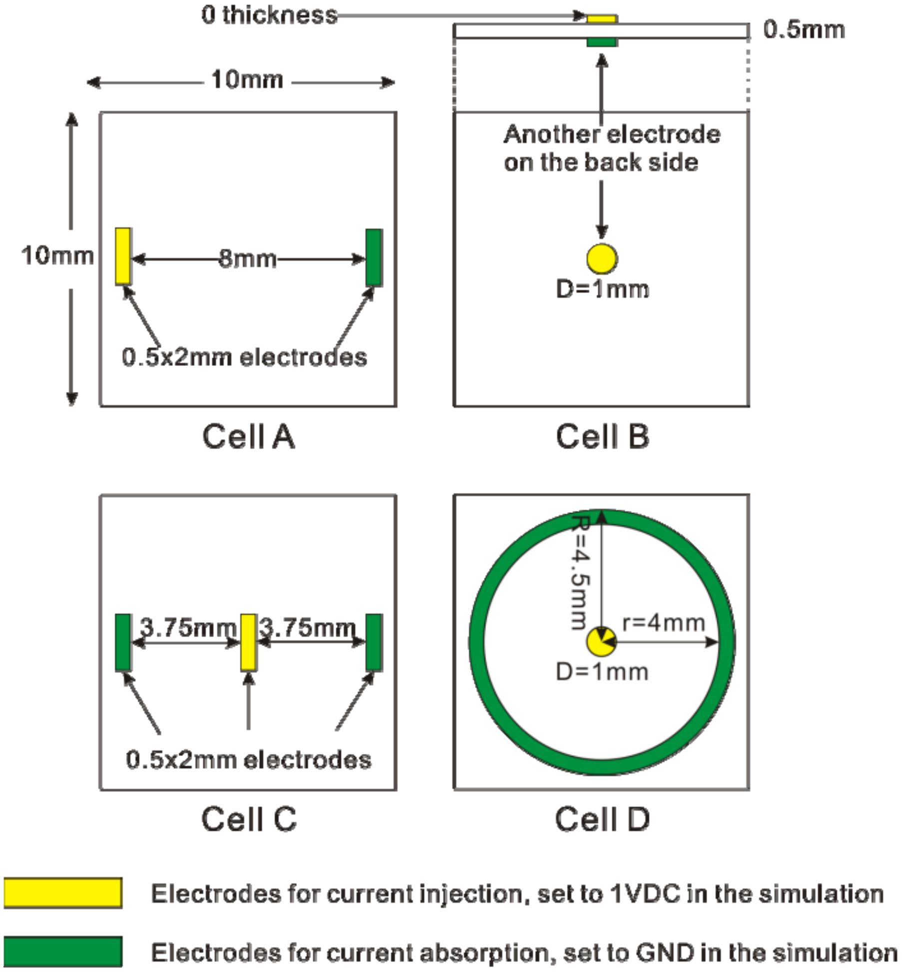

Figure 4-15 Diagrams of four kinds of geometries of open conductivity cells, including: (Cell A) two electrodes on the same side of the substrate; (Cell B) two electrodes on the opposite sides of the substrate; (Cell C) three electrodes on the same side of the substrate; (Cell D) a round electrode and a ring electrode on the same side of the substrate.

In the simulation, the substrates for the four cells are modelled as insulated cubes with the same dimension, which is 10x10x0.5 mm. The surrounding water was modelled as a sphere with a variable diameter from 10 mm to 200 mm. By comparing changes in the cell resistance as a function of the diameter of the water sphere, we can estimate the performance of the system in terms of sensitivity to proximity effects. Less resistance change for a given change in the diameter of the water sphere means that the system has smaller proximity effects, and has better performance.

However, the FEM simulation results are affected by the mesh density. To minimise this, the water sphere is not put around the cell directly. Instead, the surrounding medium is divided in to several parts by spherical shells with diameters of 10, 20, 40, 100, and 200 mm. To simulate a water sphere with a certain diameter, for example 20 mm, the medium inside the 20 mm spherical shell is modelled as water with conductivity of 60 mS/cm, while the medium outside is set as an insulator. So that for one cell, all the simulations share the same mesh. Therefore the effect of different meshes is removed.

The electric potential distribution for the four cells (calculated by FEM simulation) is shown in figure 4-16, and the resistance of the cells is presented in table 4-1：

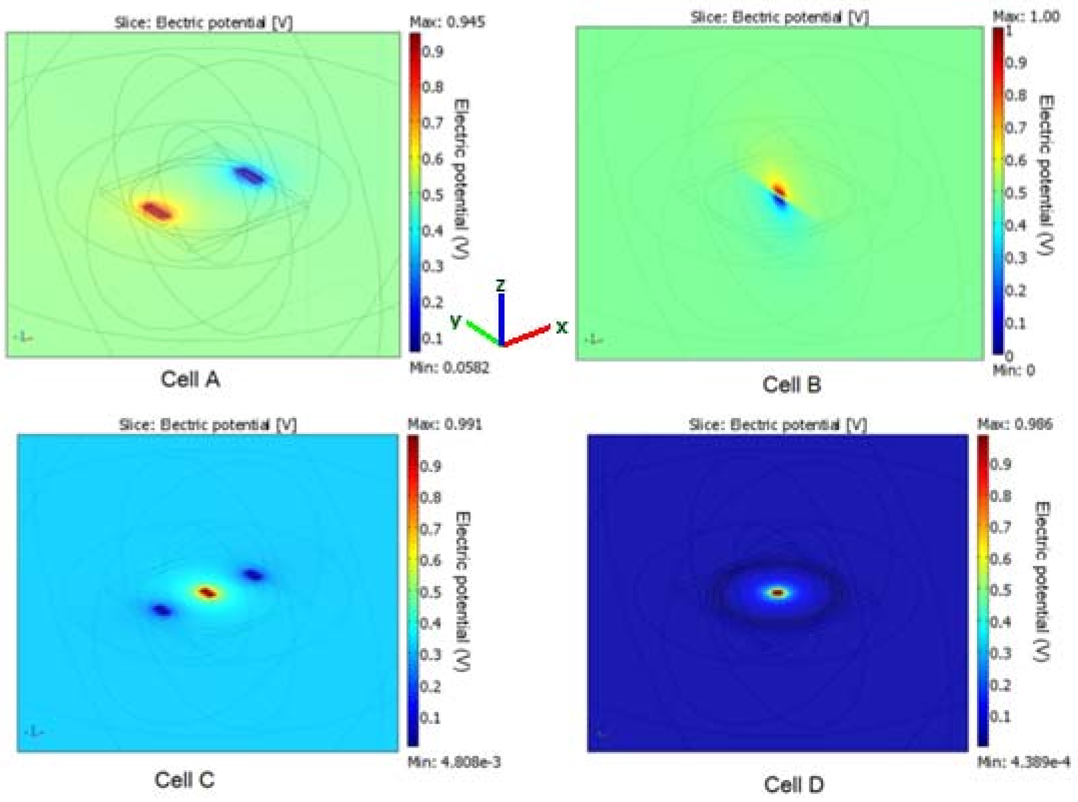

Figure 4-16 Diagrams of the electric potential distributions of the four open conductivity cells by FEM simulation.

Diameter (mm)		10	20	40	100	200
Resistance (Ω) (error compared with diameter = 200 mm)	Cell A	709.6 (43.3%)	504.4 (1.88%)	496.1 (0.20%)	495.1 (0.00%)	495.1 (0%)
	Cell B	Infinite	1593.6 (0.95%)	1580.3 (0.11%)	1578.7 (0.01%)	1578.6 (0.00%)
	Cell C	662.3 (4.44%)	634.9 (0.13%)	634.1 (0.00%)	634.1 (0.00%)	634.1 (0.00%)
	Cell D	677.5 (1.42%)	668.4 (0.07%)	668.0 (0.00%)	668.0 (0.00%)	668.0 (0.00%)

Table 4-1 FEM simulation results for the resistances of the open cells with different diameters of surrounding water.

As shown in table 4-1, cell D has the best performance. This is because it confines the electrical potential within a symmetric design. When the dimension of the surrounding water is bigger than 40 mm, 4 times the cell dimension, the resistance of cell D is almost unchanged within a tolerance of 0.01%. This means that cell D is up to 99.99% accurate if an insulating object is 20 mm or more away from the centre of the chip. Furthermore, even if the diameter of the surrounding water is only 10mm, which just covers the electrodes, the error is only 1.42%.

Cell C (an axial symmetric design) is the second best, with error about 2 times bigger than that for cell D.

Cell A and cell B have much bigger proximity effects. Cell B with electrodes on the opposite sides of the substrate, does not work if the water sphere is smaller than the substrate. However, if the water sphere is bigger than the substrate, the performance of cell B is slightly better than cell A.

In these simulations, media outside the certain diameter is set to be an insulator. By setting this media as a conductor, it gives the opposite effect (the same amount).

Although the cell A has the worst performance, as it’s the simplest design, an open conductivity cell (chip 1-B) following the principle of cell A was implemented in design 1 for evaluation. Figure 4-17 shows the design of this open conductivity cell:

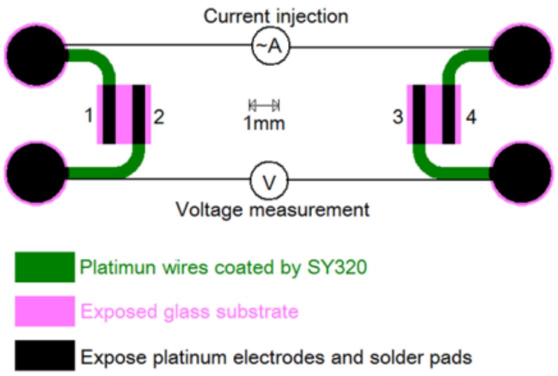

Figure 4-17 A diagram of the four-electrode open conductivity cell on chip 1-B.

Figure 4-17 shows the four-electrode open conductivity cell on chip 1-B. The current is injected from the electrode 1 and 4 following the principle of cell A. Electrode 2 and 3 are added to measure the voltage.

Chip 2-A in figure 4-5 is a multi-sensor chip implemented in design 2, with 10x14 mm dimension. As shown in figure 4-18, it integrates an open conductivity cell with ring-type electrodes (following the principle of cell D), and a dissolved oxygen (DO) sensor. A four-ring-electrode open cell is in design 3 with reduced dimension (8x14 mm, figure 4-8, left).

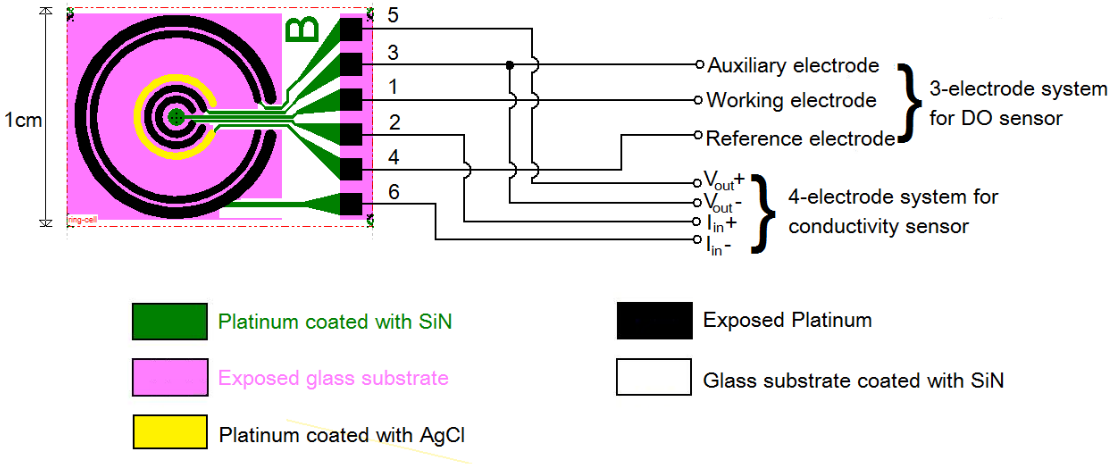

Figure 4-18 A diagram showing the configuration of chip 2-A: the conductivity and DO multi-sensor chip.

As shown in figure 4-18, six electrodes on the chip are numbered from inside to outside. For conductivity measurement, electrode 2 and 6 are used for current injection following the principle of cell D, while electrode 3 and 5 are used to measure the voltage response. The design specification of DO sensor will be introduced in following sections in this chapter.

In addition, chip 2-D in figure 4-5 is an alternative conductivity cell implemented in design 2. Electrode 1, 4, and 7 (left to right) are used for current injection following the principle of cell C. Electrode 2 and 3 are used for voltage measurement, while electrode 5 and 6 are used to maintain an axial symmetric design.

4.3 Temperature sensor

4.3.1 PRT-bridge

As discussed in chapter 2, the PRT is a better choice than a thermistor for a precision system. Our micro-fabrication techniques allow manufacture of a film PRT by coating a glass substrate with an extremely thin (down to 100 nm) platinum foil. Thin film PRTs are relatively low cost and have a fast response, although the different thermal expansion rates for the glass substrate and platinum might give strain gauge effects [118] and stability problems. It is hard to estimate the strain gauge effects. However, as glass is a solid material while platinum is extremely thin, the thermal expansion of the glass will dominate, and this will be proportional to temperature. The strain gauge effect can therefore be ignored with little penalty, especially if the sensor is calibrated. However, strain gauge effects may still be observed if the source of strain is mechanical loading.

To enhance the sensitivity of the PRT, an electric bridge consisting of two PRT resistors and two precision resistors is used as the temperature sensor. The PRT resistors are made from platinum wires. These platinum wires are 30 μm wide in both designs 1 and 2, and 20 μm wide in design 3 (figure 4-8). Figure 4-19 shows the PRT-bridges in both designs 1 and 2.

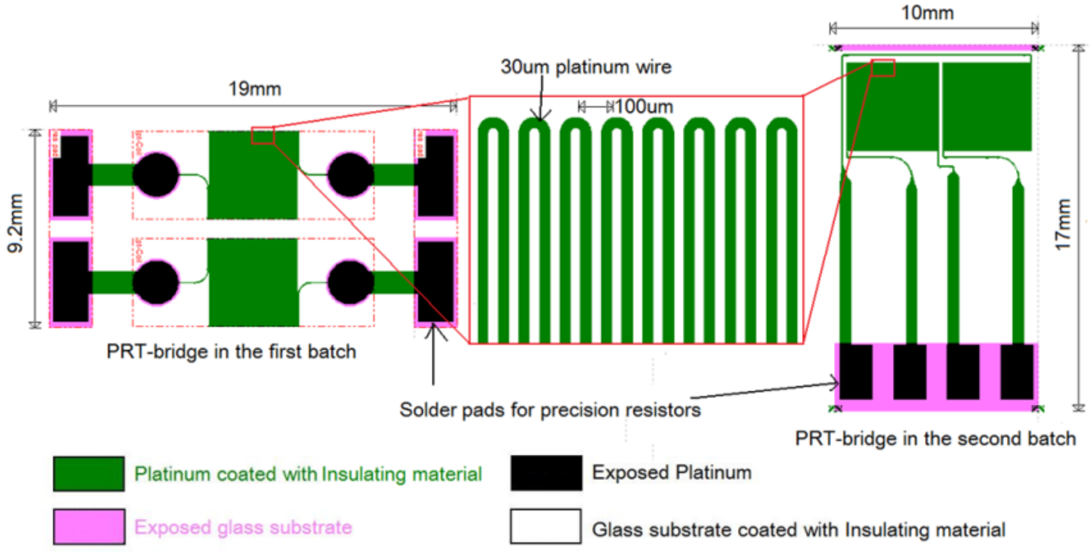

Figure 4-19 A diagram of the PRT-bridge temperature sensor chips in both wafer designs 1 and 2.

There are two platinum resistors and two pairs of solder pads on each sensor chip. Two precision resistors can be soldered onto the pads, to give a temperature bridge. Figure 4-20 shows a schematic of the PRT-bridge temperature sensor:

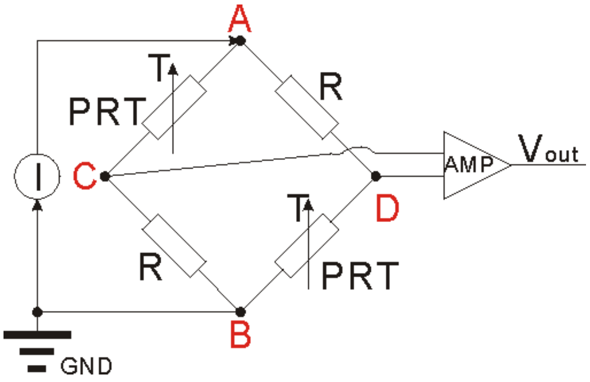

Figure 4-20 A schematic of the PRT-bridge temperature sensor.

As shown in figure 4.20, a current source is used to inject current from point A, and remove current from point B. Because of the symmetrical design, half of the current will pass through point C, and half of the current passes through point D. Therefore, the voltages at point C and D will change due to the different temperature coefficients of the PRT resistors and the precision resistors. With the aid of a differential amplifier, a temperature sensitive voltage signal can be amplified and collected from the C, D points.

In designs 1 and 3, the CT sensors are on one chip. However, in order to evaluate and improve the response time, the CT sensors are placed in separate chips in design 2.

Furthermore, the two platinum resistors are placed symmetrically on the two sides of the chip in design 3. If a mechanically or thermally induced bend causes a strain gauge effect to occur, one resistor has increased resistance by stretching on the glass substrate, whilst the other resistor will have a decreased resistance as it is compressed on the other side. As the sensors are arranged in a compensating bridge network this arrangement reduces such strain gauge error.

4.3.2 Response time and sensor package

The response time of the temperature sensor not only depends on the sensor chip, but also depends on the package of the sensor system, and water flow rate. Simulations were made by FEM to explore this point. A 3D drawing of the sensor package in shown in figure 4-21:

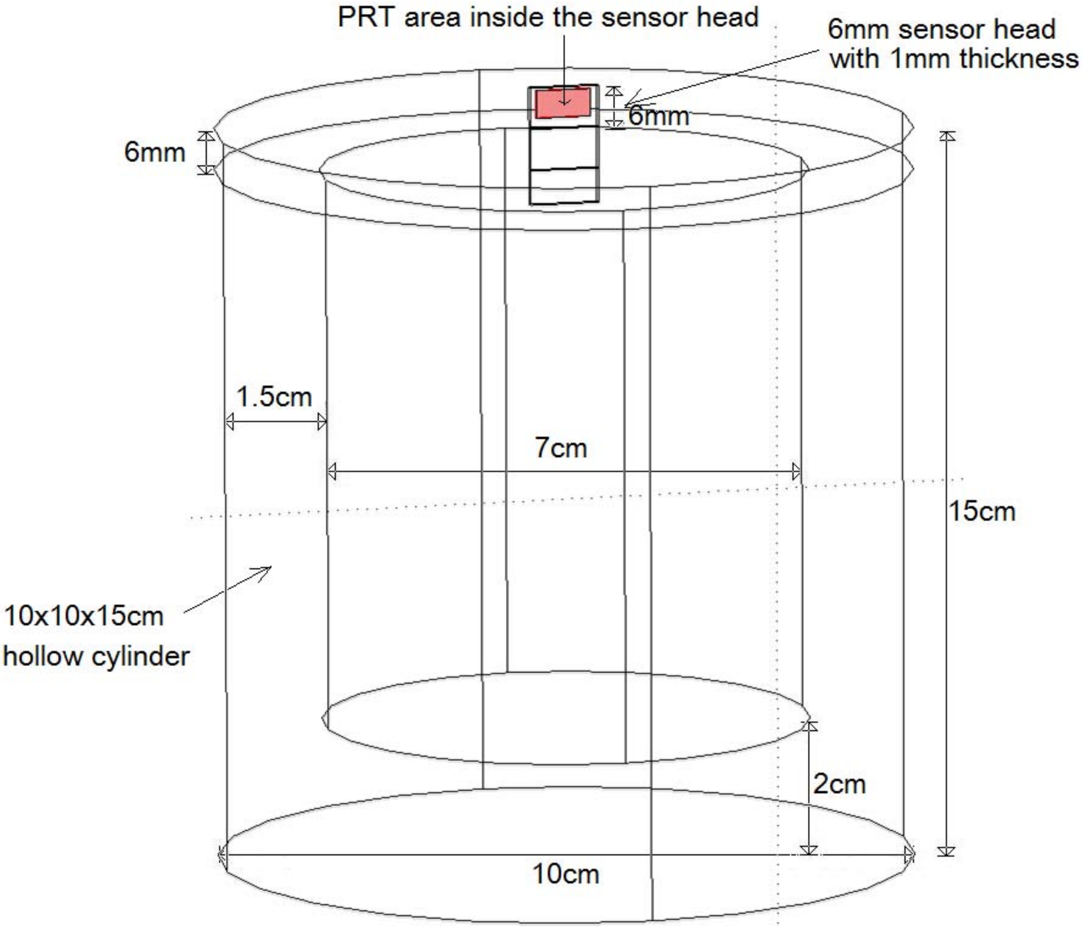

Figure 4-21 A diagram demonstrating the 3D drawing of a Ø10x15cm sensor package.

As shown in figure 4-21, the sensor is packaged in a Ø10x15 cm hollow plastic cylinder. The temperature sensor head is fixed vertically on top of the cylinder. The thickness of the temperature sensor head is 1 mm. The PRT area is in the middle of the sensor head.

To simulate the behaviour of water, a water sphere of 50 cm diameter at an initial temperature of 290 K surrounds the sensor. The boundary condition of the water sphere surface is set to constant 290 K. The initial temperature of the sensor head and the packaging is set as 289 K, 1 K lower than the surrounding water. The response time in static water can be determined by analyzing how the temperature of the PRT changes with time.

In the first simulation, the PRT area is set a distance of 6 mm from the cylinder as shown in figure 4-21. The simulation results are shown in Figure 4-22:

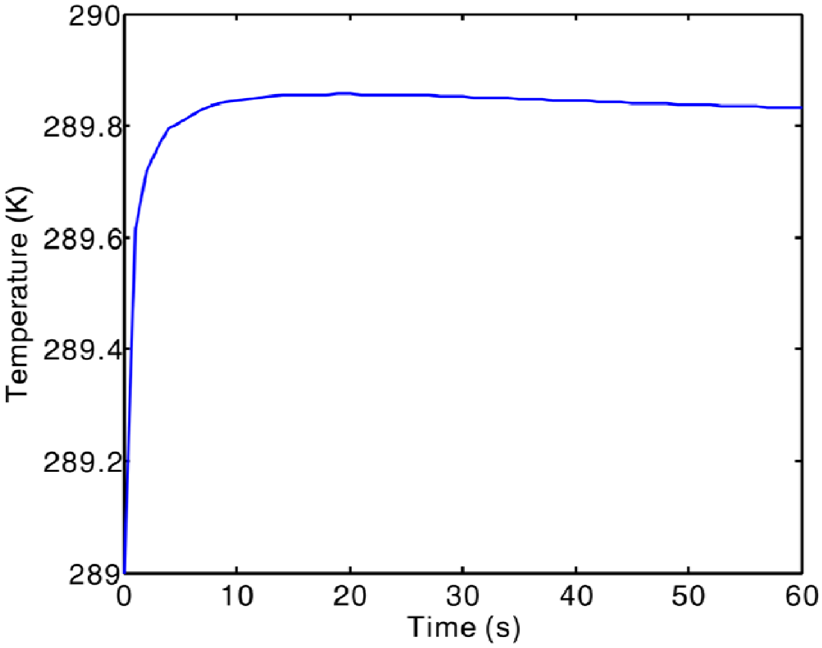

Figure 4-22 FEM simulation result of the average temperature change of the PRT in static water, when water temperature is 1 K higher and sensor head is 6 mm high.

As shown in figure 4-22, the average temperature of the PRT increases from 289 K to 289.85 K within 15 s. However, it then starts decreasing. The reason why the temperature does not increase to 290 K directly is that the surrounding water is cooled by the sensor package.

The surrounding water heats the sensor package, and is also cooled by the sensor package at the same time. At the very beginning, both sensor head and the package are heated by the water, but the temperature of the sensor head grows faster, due to the higher thermal conductance of the glass, lower thermal mass and the relativity larger contact area. Later, because of its bulk and the lower temperature of the package, it makes the temperature of surrounding water lower than the sensor head. So the sensor head starts cooling.

Because the simulation is in static water, the cooled surrounding water is not refreshed by water with a higher temperature. Therefore the cooled surrounding water only receives heat from the outside by thermal conduction. Due to the relatively low thermal conductance of the water, it takes a very long time to reach steady state.

Moving the sensor head farther away from the package will improve the speed of temperature change, but the cooling behaviour will not be improved as this is an artefact of the boundary conditions of the simulation. In the second simulation, the sensor head is set 11 mm from the cylinder. As Figure 4-23 shows, the ratio improves from 85% to 92% at 15 s.

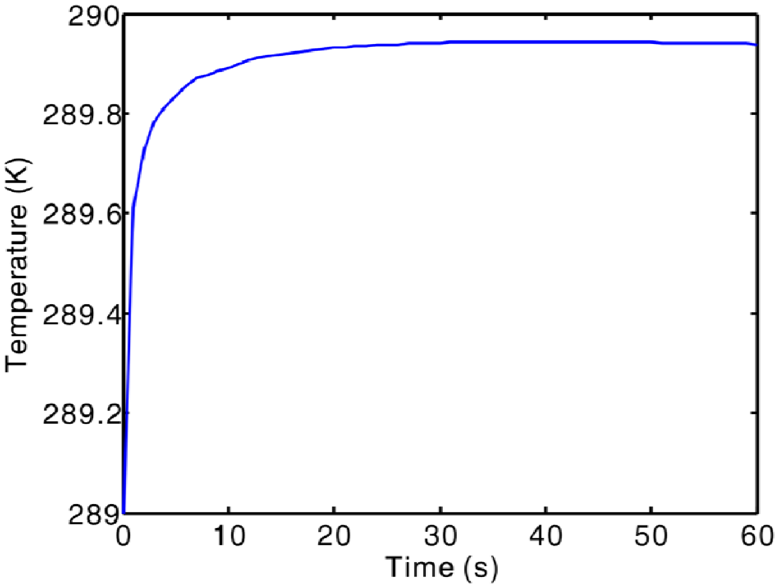

Figure 4-23 FEM simulation result of the average temperature change of the PRT in static water, when water temperature is 1 K higher and sensor head is 11 mm high.

However, if the water flows, the cooled surrounding water is heated by convection, so that the surrounding water temperature remains static. To simulate this situation, the temperature of the package boundary is set to a constant 290 K, and the sensor head is set to 6 mm, as in the first simulation. Figure 4-24 shows the simulation result.

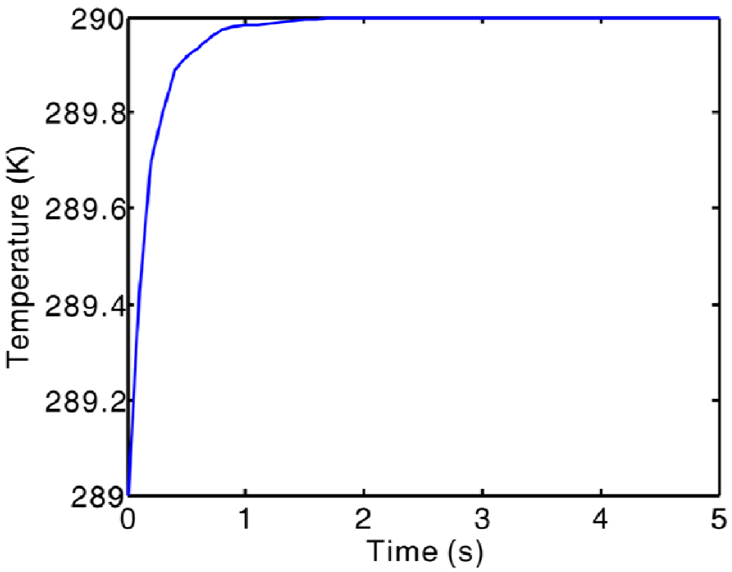

Figure 4-24 FEM simulation result of the average temperature change of the PRT in flowing water, when water temperature is 1 K higher and sensor head is 6 mm high

As shown in the figure, the sensor head only takes 0.5 s for an 85% change, and 2 s to achieve a 99% change. Furthermore, no cooling occurs.

To conclude, water flow is essential to provide a fast response time for the temperature sensor. Also making the sensor system smaller improves the response time as does keeping the sensor head further away from the package. For this reason in design 2, the temperature sensor is put in a separate chip with the solder pads far away from the PRT.

4.4 Dissolved oxygen sensor

As discussed in chapters 2 and 3, the electrical current I measured between a platinum electrode and a reference electrode can be used to measure dissolved oxygen provided the correct voltage is applied between these two electrodes. During this measurement oxygen is consumed at the electrode surface and an oxygen diffusion gradient is established from zero oxygen on the electrode surface to oxygen with a concentration C^* in the solution bulk, leading to an oxygen flux. The relation between the electric current I and the oxygen current J is described as:

$$I = nFJ \qquad [4\text{-}1]$$

where F is the Faraday constant, and n is the number of electrons transferred in the reaction. As mentioned in chapter 2, oxygen is consumed either directly by equation 2-18, or with hydrogen peroxide as intermediate (equation 2-19 followed by equation 2-

20). Equation 2-18 gives an electron number of 4, whilst equation 2-19 gives an electron number of 2. However, if the peroxide generated by equation 2-19 doesn't diffuse away, another 2 electrons are also transferred to the electrode by equation 2-20. Therefore, the value of n (the apparent number of electrons) is between 2 and 4, depending on the reaction pathways and the peroxide diffusion.

The process for creating the oxygen diffusion depends on the geometry of the sensor cell, and can be affected by temperature and flow. The diffusion equation [119] can be used to calculate the relation between I and C^*. It also helps us to understand the temperature and flow effects, and to optimize the geometry of designs.

4.4.1 Diffusion modelling

Static water with uniform temperature has a uniform and non-directional diffusion coefficient D. For diffusion in this kind of water, the diffusion equation is given as[119]:

$$\frac{\partial C(\vec{r},t)}{\partial t} = D\nabla^2 C(\vec{r},t) \qquad [4\text{-}2]$$

where ∇^2 is the Laplace operator, and $C(\vec{r},t)$ is the oxygen concentration at location $\vec{r}$ and time t. Furthermore, the oxygen flux $\vec{j}$ is given as:

$$\vec{j} = D\nabla C(\vec{r},t) \qquad [4\text{-}3]$$

The sensor cell consists of an electrode and wall (laminate material). The geometry of the sensor cell gives the boundary conditions of the diffusion, which is:

1. $C(\vec{r},t)$=0, when $\vec{r}$ is on the electrode.
2. $C(\vec{r},t)$=C^*, when $\vec{r}$ is infinite far away from the electrode.
3. $\vec{j}$ is parallel with the wall of the cell, when $\vec{r}$ is on the wall.

while the initial conduction of this diffusion is $C(\vec{r},0)$=C^*.

The solutions of the diffusion equation for several ideal boundary conditions have been given in textbooks. These ideal boundary conditions include one dimensional diffusion, semi-infinite spherical/hemispherical diffusion, and semi-infinite diffusion with disc electrode.

One dimensional diffusion

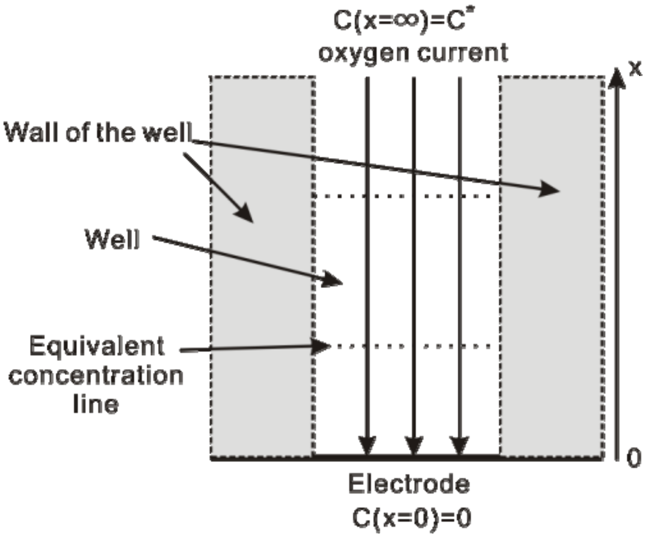

Figure 4-25 A diagram demonstrating the one dimensional diffusion for planar electrode.

As shown in figure 4-25, if an infinite planar electrode is used, or a planar electrode in a well with infinite height is used, and there is no water flow, diffusion is only on the *x* direction (due to symmetry), and liquid with the same *x* coordinate has the same concentration. Therefore the oxygen concentration $C(\vec{r},t)$ can be written as *C(x,t)*.

The solution of this one dimensional diffusion is given by [119, 120] as:

$$C(x,t) = C^{*}\text{erf}\,(\frac{x}{2\sqrt{Dt}}) \qquad [4\text{-}4]$$

where *erf(x)* is the error function given as:

$$\text{erf}(x) = \frac{2}{\sqrt{\pi}}\int_0^x e^{-y^2}dy \qquad [4\text{-}5]$$

The electric current *I* is given as:

$$I(t) = nFAC^{*}\sqrt{\frac{D}{\pi t}} \qquad [4\text{-}6]$$

where *A* is the area of the electrode.

The concentration profile of the diffusion is shown in figure 4-26:

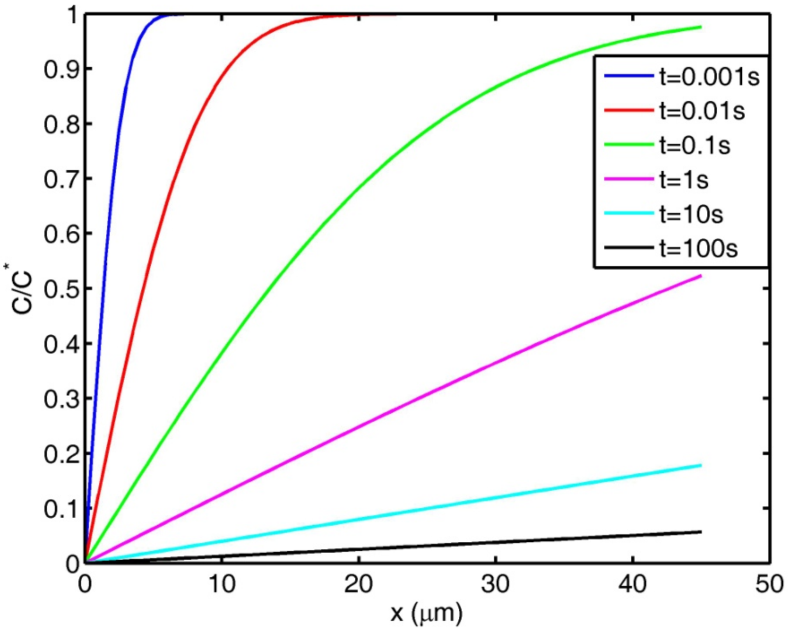

Figure 4-26 Concentration profiles of one dimension diffusion with several times after oxygen diffusion starting. Diffusion constant D is set to $2\text{x}10^{-5}$ cm^2/s here.

By examining equation 4-4, we see that the diffusion boundary is directly proportional to $\sqrt{Dt}$. For estimation with less than 1% error, the diffusion boundary δ can be considered as:

$$\delta = 4\sqrt{Dt} \qquad [4\text{-}7]$$

where the concentration at this boundary is 99.5% of the bulk concentration (*erf*(2)=0.9953). A more conservative estimate can be made by increasing the number 4 in equation 4-7. E.g. increasing the number to 6 moves the boundary concentration to 99. 998% of the bulk concentration.

Semi-infinite spherical/hemispherical diffusion

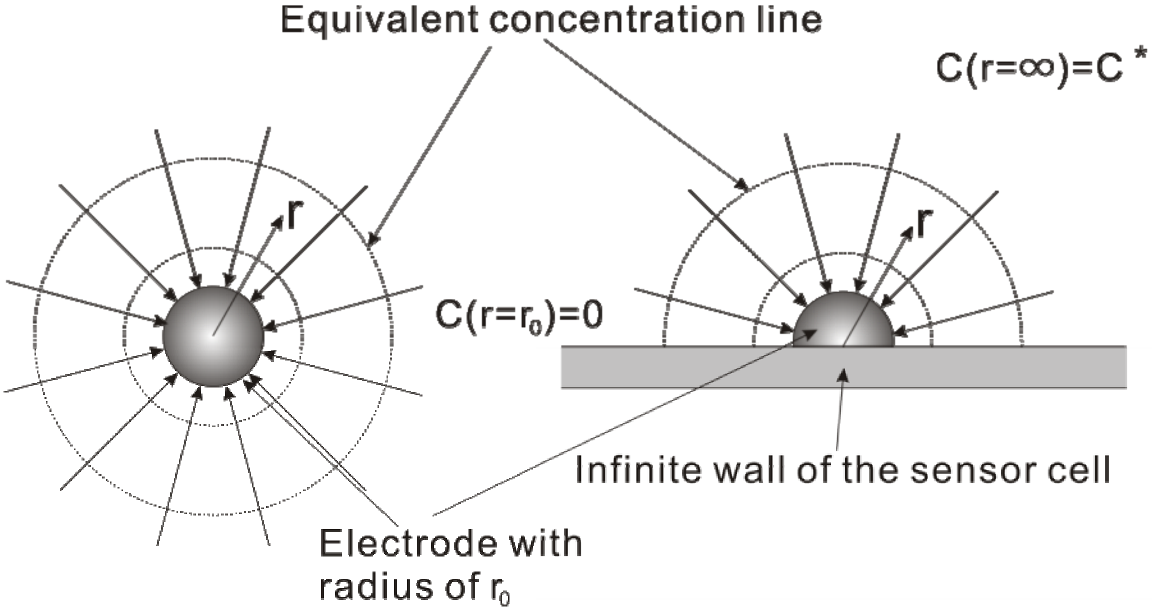

Figure 4-27 A diagram demonstrating semi-infinite spherical diffusion (left), and the semi-infinite hemispherical diffusion (right), in spherical coordinates, with the stream lines showing the oxygen flux.

As shown in figure 4-27, if a spherical electrode is used, or a hemispherical electrode on an infinite plate wall is used, and there is no water flow, diffusion is created only in the direction of *r*, and liquid with the same *r* coordinate has the same concentration. Therefore the oxygen concentration $C(\vec{r},t)$ can be write as $C(r,t)$.

The solution of this semi-infinite spherical/hemispherical diffusion is given by [119-121] as:

$$C(r,t) = C^{*}[1 - \frac{r_0}{r}\,\mathrm{erfc}\left(\frac{r-r_0}{2\sqrt{Dt}}\right)] \qquad [4\text{-}8]$$

where r_0 is the radius of the electrode, *erfc(x)* is another error function:

$$\mathrm{erfc}(x) = 1 - \mathrm{erf}(x) = \frac{2}{\sqrt{\pi}}\int_{x}^{\infty} e^{-y^2}dy \qquad [4\text{-}9]$$

The electric current *I* is given as:

$$I(t) = nFADC^{*}(\frac{1}{\sqrt{\pi Dt}} + \frac{1}{r_0}) \qquad [4\text{-}10]$$

where *A* is the area of the electrode.

To compare the spherical/hemispherical diffusion with one dimensional diffusion, we consider a distance $x=r-r_0$, which is the distance from the liquid to the electrode surface in both conditions. When *r* is close to r_0, equation 4-8 is the same as equation 4-4, with $\frac{r_0}{r} = 1$. This means that diffusion close to the electrode surface is similar to the one dimensional case. However, when diffusion reaches to the point where $\frac{r_0}{r} \ll 1$, the spherical/hemispherical diffusion is higher than that for one dimension diffusion. Figure 4-28 shows the concentration profile of a semi-infinite spherical/hemispherical diffusion with 5 μm radius electrode:

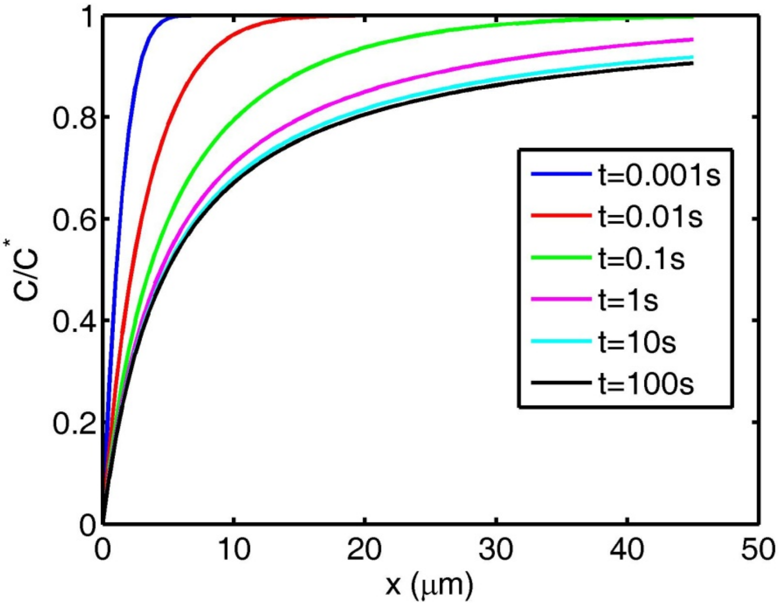

Figure 4-28 Concentration profiles of a semi-infinite spherical/hemispherical diffusion with 5 μm radius electrode. Diffusion constant D is set to 2×10^{-5} cm^2/s here.

Comparing with figure 4-26, we see that one dimensional diffusion never reaches a steady state. The concentration profile always decreases to 0 with time, and increasing to C^* with distance. However, for a semi-infinite spherical/hemispherical diffusion, the concentration attenuation tends to self limit. As shown in figure 4-28, the difference between the profiles at t = 1 s and t = 100 s is only 10%, and this difference reduces to 1% between t = 10 s and t = 100 s. Therefore considering a 1% tolerance, 100 s is time required to reach near steady state for the hemispherical electrode with 5 μm diameter. The limiting oxygen reduction current ($I(t)=\frac{nFADC^*}{r_0}$ when $t \rightarrow \infty$) through the electrode is proportional to the oxygen concentration at this time. As a comparison, the one dimensional diffusion for the planar electrode never has a steady concentration profile and the current is not stable, with a limitation current of 0, which cannot be used for oxygen measurement.

The electric current I for the spherical/hemispherical diffusion can be divided into two parts as:

$$I(t) = I_t(t) + I_s \qquad [4\text{-}11]$$

$$I_t(t) = nFAC^*\sqrt{\frac{D}{\pi t}} \qquad [4\text{-}12]$$

$$I_s = \frac{nFADC^*}{r_0} \qquad [4\text{-}13]$$

where I_t is the transient current which attenuates to 0 with time t, and I_s is the steady state current which does not change with time, and is the current when diffusion profile reaches steady state. From equation 4-1, the oxygen current J_s at steady state is derived as:

$$J_s = \frac{ADC^*}{r_0} \qquad [4\text{-}14]$$

while the oxygen concentration profile at steady state is:

$$C_s(r) = C^*(1 - \frac{r}{r_0}) \qquad [4\text{-}15]$$

Diffusion never reaches an ideal steady state. In order to calculate the time to steady state, we set a tolerance e for the ratio of I_t to I_s. e.g. if we consider a 1% tolerance, the waiting time t_w is when this ratio is equal to 1%.

As:

$$e = \frac{I_t(t)}{I_s} = \frac{r_0}{\sqrt{\pi D t_w}} \qquad [4\text{-}16]$$

for a certain tolerance, the waiting time t_w for steady state is calculated as:

$$t_w = \frac{{r_0}^2}{\pi D e^2} \qquad [4\text{-}17]$$

As shown in equation 4-17, the waiting time increases with ${r_0}^2$, therefore a smaller electrode has a shorter waiting time but a lower current. The diffusion coefficient of oxygen in water is about $2\text{x}10^{-5}$ cm^2/s at 20 ^{o}C [122]. With 1% tolerance, the waiting time is 40 s for an electrode with 5µm radius. This waiting time increases to 160 s if the radius is 10 µm.

Semi-infinite spherical/hemispherical diffusion reaches steady state because the diffusion distributes into three dimensions. A real oxygen cell may not fulfil the ideal semi-infinite spherical/hemispherical condition, however as long as the diffusion can distribute into a three dimension volume without disturbance, it will reach steady state.

Semi-infinite diffusion with disc electrode

It is difficult to make an oxygen sensor cell that fulfils the one dimensional diffusion or spherical/hemispherical diffusion conditions. Instead, a micro-disc electrode is widely used in analytical chemistry [123], and for oxygen measurement in [81-84]. Figure 4-29 shows a micro-disc electrode:

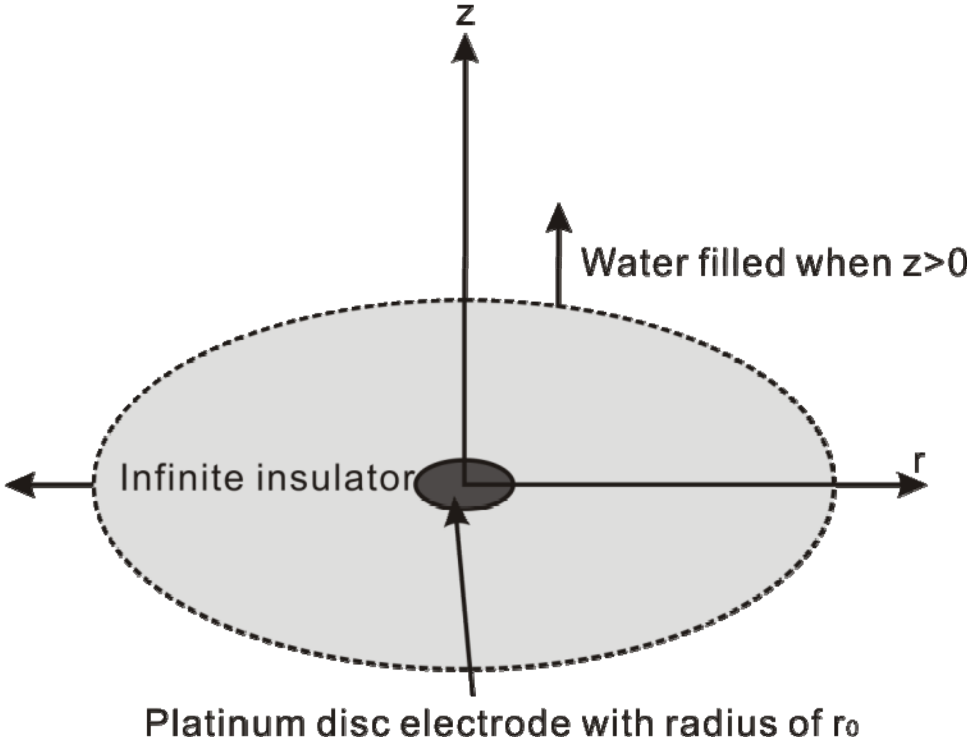

Figure 4-29 A diagram demonstrating a micro-disc electrode oxygen cell in a cylindrical coordinates.

The micro electrode normally has a radius less than 25μm [32]. Compared with the electrode dimension, the dimensions of the holder and the water can be considered as infinite. As shown in figure 4-29, a micro-disc electrode is placed on a flat infinite insulator, and water is placed on top of the electrode and insulating substrate. For this semi-infinite boundary conduction, the electric current consumed by the electrode is given by Aoki and Osteryoung in [121, 124-126] as:

$$I(\tau) = \frac{4nFADC^*}{\pi r_0} \mathrm{f}(\tau) \qquad [4\text{-}18]$$

where τ is a dimensionless time parameter defined as:

$$\tau = \frac{4Dt}{{r_0}^2} \qquad [4\text{-}19]$$

There is no exact analytical solution for the function *f(τ)*. But it can be approximated by two equations in different domains of τ. At short times, when $\tau < 1$,

$$f(\tau) = 0.88623\tau^{-0.5} + 0.78540 + 0.094\tau^{0.5} \qquad [4\text{-}20]$$

At long times, when $\tau > 1$,

$$f(\tau) = 1 + 0.71835\tau^{-0.5} + 0.05626\tau^{-1.5} + 0.00646\tau^{-2.5} \qquad [4\text{-}21]$$

The two versions of *f(τ)* overlap for $0.82 < \tau < 1.44$, which shows that the dividing point 1 is convenient and appropriate.

As $lim_{\tau\to\infty}\,\mathrm{f}(\tau) = 1$, the electric current at steady state is:

$$I_s = \frac{4nFADC^*}{\pi r_0} = 4nFDC^*r_0 \qquad [4\text{-}22]$$

Again, if we set a tolerance of 1% ($f(\tau) = 1.01$ when $\tau = 5160$), the waiting time for steady state is 65s for an electrode of 5μm radius. This waiting time increases to 260s if the radius is 10μm. Compared with the spherical/hemispherical diffusion, this waiting time is increased by 62.5%. This is because the disc electrode has less surface area than the spherical/hemispherical for the same radius, which makes the diffusion distribute slower.

4.4.2 Measurement method and other factors

The electric current from an oxygen sensor cell can be divided into two parts: transient current and steady state current. As shown in the equations in section 4.4.1, both transient current and steady state current are directly proportional to the bulk concentration C^*, and can be utilized for oxygen measurement. The relation between the steady state current I_s or transient current at fixed measurement time I_t can be given as:

$$I_s \; or \; I_t = K_T\mathrm{C}^* \qquad [4\text{-}23]$$

where K_T is the ratio of electric current to oxygen concentration.

Temperature has an influence on this current-concentration relation, because K_T and diffusion coefficient D are temperature dependent. Furthermore, the electric current for each model is deduced with the flowing assumptions, and will be affected if any assumption is not fulfilled:

1. Water has a uniform temperature.
2. Water is not stirred.
3. The oxygen concentration has an initial state of C^*.

Therefore the oxygen measurement can be affected by changes in water temperature, water flow, and the initial concentration state. Furthermore, for a transient measurement, part of the measured electric current does not come from the oxygen, but from charging of the double-layer capacitor on the electrode (and any other stray capacitance in the system), which also lead to error in the measurement.

Temperature effects

Temperature influences the current because the diffusion coefficient is temperature dependent. The diffusion coefficient of oxygen D is given by the Einstein–Stokes equation [103, 119] as:

$$D = \frac{kT}{6\pi\eta r_{O2}} \qquad [4\text{-}24]$$

where k is the Boltzmann constant, T is the absolute temperature, η is the water viscosity, and r_{O2} is the hydrodynamic radius of the oxygen molecule. Among these parameters, η is temperature dependent parameter, given as [127]:

$$\eta = A \times 10^{B/(T-C)} \qquad [4\text{-}25]$$

where A=2.414 × 10^{-5} Pa·s, B = 247.8 K, and C = 140 K.

If we ignore the change of r_{O2} with temperature, the coefficient D can be deduced as:

$$D = D_{T0} \times \frac{T}{T_0} \times 10^{B\left(\frac{1}{T-C} - \frac{1}{T_0-C}\right)} \qquad [4\text{-}26]$$

where D_{T0} is the diffusion coefficient at temperature T_0.

For steady state measurement, the electric current is directly proportional to D. Therefore, if we calibrate the oxygen sensor at a temperature T_0 as $I = K_{T0}C^*$, this calibration can also be applied at any temperature T by modifying the ratio K_{T0} as:

$$K_T = K_{T0} \times \frac{T}{T_0} \times 10^{B\left(\frac{1}{T-C} - \frac{1}{T_0-C}\right)} \qquad [4\text{-}27]$$

For transient measurement, the transient current attenuates with time. The change in D not only affects the amplitude of the current attenuation profile, but also stretches the attenuation profile. For a fixed measurement time, it is hard to get an analytical solution to determine K_T, as in equation 4-27 for steady state. Nevertheless, if we can make a calibration at a fixed oxygen concentration C^*_0, and change the temperature through all required temperatures, recording the electric current $I(T)$, then K_T for transient measurement is:

$$K_T = {C^*}_0/I(T) \qquad [4\text{-}28]$$

Flow effects

Flow enhances the measurement current as it shifts the diffusion profile, bringing more oxygen from solution bulk to the electrode surface by convection. The oxygen current brought by water flow can be estimated by the following method.

Using the simplifying assumptions that S is the boundary of the diffusion, that the liquid outside S has oxygen concentration C^*, and liquid inside S has zero oxygen concentration, a simple mathematical model describing flow induced oxygen flux can be created. $\overrightarrow{dS}$ is a small area on *S*, with direction from outside to inside and $\vec{v}$ is the velocity of flow on $\overrightarrow{dS}$. In a small time *dt*, the liquid volume passing through $\overrightarrow{dS}$ can be calculated as $(\vec{v} \cdot \overrightarrow{dS})dt$. By consuming the oxygen inside this liquid volume, the electric current is increased by:

$$dI = nF\frac{C^*(\vec{v} \cdot \overrightarrow{dS})dt}{dt} = nFC^*(\vec{v} \cdot \overrightarrow{dS}) \qquad [4\text{-}29]$$

Note that if $\vec{v}$ is from inside to outside (where $\left(\vec{v} \cdot \overrightarrow{dS}\right) < 0$), the contribution to the electric current is 0 rather than a negative value. Therefore the total electric current brought by the flow is:

$$I_{flow} = nFC^* \iint_{on\ S\ when\ (\vec{v} \cdot \overrightarrow{dS})>0} (\vec{v} \cdot \overrightarrow{dS}) \qquad [4\text{-}30]$$

This estimation is pessimistic as the oxygen concentration is assumed to be 0 inside the diffusion boundary. The actual flow induced current may be much smaller as the average concentration inside the boundary is higher than 0.

Water flow and an object in the water has a relative velocity of 0 on the object surface due to frictional force [128, 129]. Therefore there is a profile of flow from velocity of zero on the electrode to a maximum velocity v_{max} in the bulk. An actual flow profile is created by washing the sensor cell using water with flow of v_{max}. However an analytical solution is difficult to derive for this profile. Instead, the velocity profile for a laminar flow in a rectangular channel was used, [129] as used to calculate the flow effect previously [130], see figure 4-30. This model was used to estimate flow effects by setting the width of the channel comparable to the chip dimension.

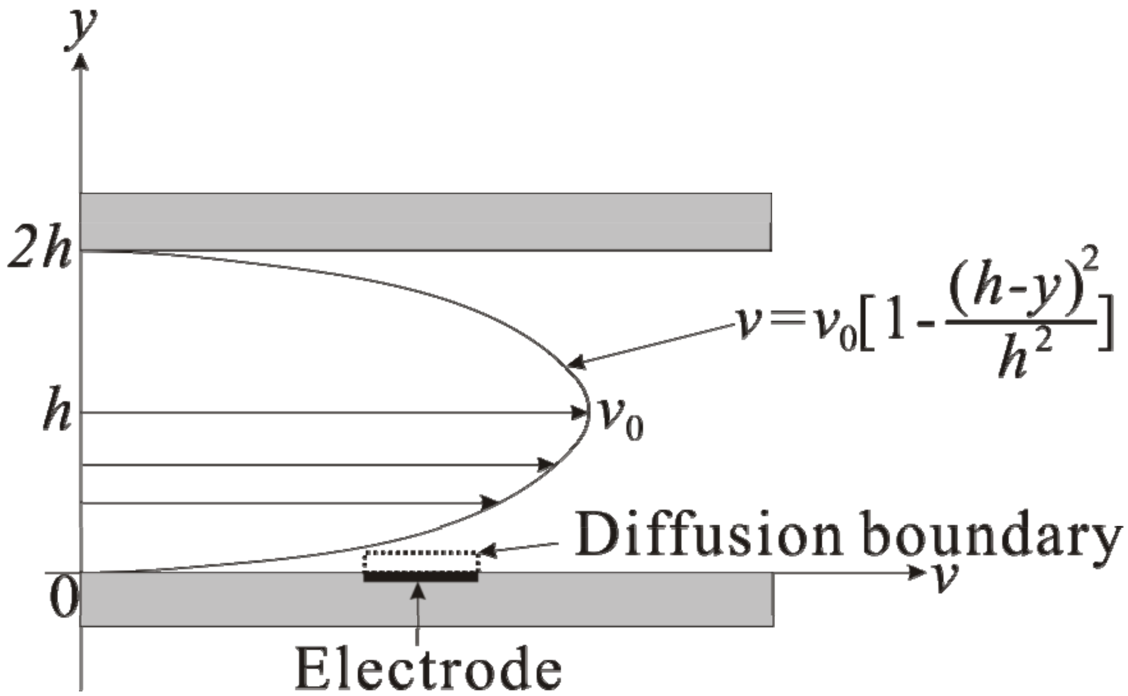

Figure 4-30 Velocity profile of water flow in a rectangular channel, where the maximum flow rate is v_0, and the width of the channel is $2h$.

As figure 4-30 shows, when a plate electrode is placed at the bottom of the channel, there is zero velocity on the electrode surface, and the velocity increases with distance y to the centre of the channel. Obviously, the steady state current is affected by water flow. However, for transient measurement, at the very beginning, the diffusion is close to electrode surface, where there is nearly zero flow. Therefore early transient measurements are less affected by flow. Then as the diffusion thickness increases with time, the flow rate on the diffusion boundary increases, affecting the measurements.

To determine the maximum waiting time for a transient measurement that is not affected by flow, a disc electrode with radius r_0 is used; the width of channel is set to 2 cm (h=1 cm) as a typical dimension of the sensor chip is 1cm; and the maximum flow rate v_0 is set to 100 cm/s. At early times, the diffusion thickness is much smaller than the electrode dimension. Therefore diffusion in this state can be considered as one dimensional diffusion. Again, 1% error tolerance is used. As we only discuss the situation when the flow causes less than the 1% change in current, the shift of diffusion boundary induced by flow can be ignored. Ignoring this shift means that the thickness of the diffusion layer δ can be calculated using equation 4-7. As the diffusion boundary has a cross section of $2r_0\delta$ against the water flow, the current brought by water flow is estimated as:

$$I_{flow} = nFC^{*}2r_0\delta v(\delta) \qquad [4\text{-}31]$$

where $v(\delta)$ is the flow velocity at the top of the diffusion boundary. This is a pessimistic estimation as $v(\delta)$ is the maximum flow velocity on the whole diffusion boundary. Figure 4-31 compares the electric current at no flow rate and electric current induced by the flow at r_0=10 µm:

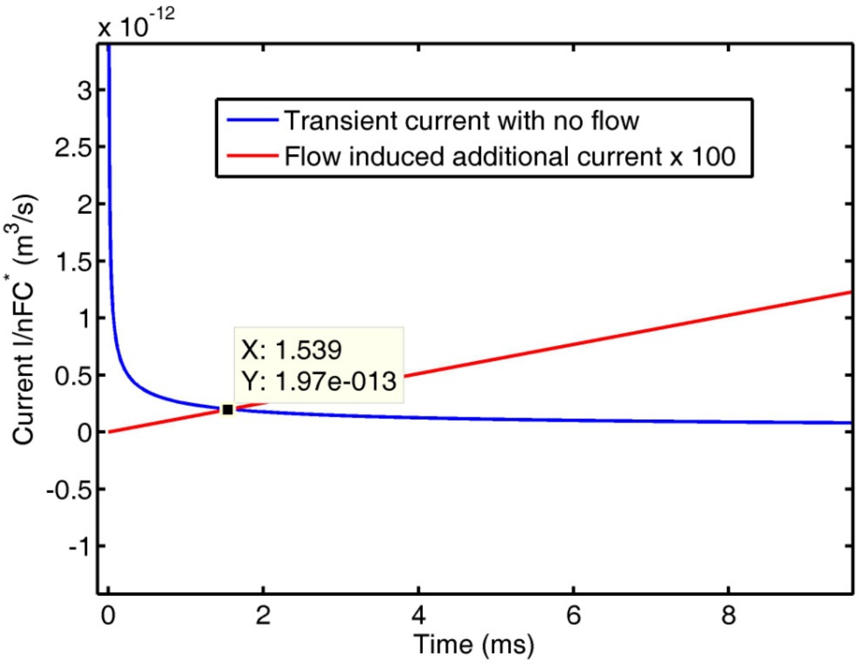

Figure 4-31 Plot of the transient current and the additional current induced by flow versus time for a disc electrode with 10 µm radius. The plotted additional current induced by the flow is magnified by 100 to estimate when the flow changes the current by 1% (point identified on plot). The diffusion coefficient is set to 2x10^{-5} cm^2/s, with a maximum flow velocity of 100 cm/s in a 2 cm wide rectangular channel.

As shown in the figure, the current induced by flow reaches 1% of the transient current at about 1.5 ms. Therefore 1.5 ms is the maximum measurement time for a transient measurement from a disc electrode of 10 µm radius. The transient current is in direct proportion to electrode area, which is πr_0^2, whilst the flow induced current is in direct proportion to r_0. Therefore the ratio of transient current to flow induced current changes with r_0. This means that the maximum waiting time can be increased by increasing r_0, e.g. the maximum waiting time increases to 2.5 ms if r_0 is increased to 20 µm.

RC charging Effects

For a transient measurement, the total electric current is not only from the oxygen, but also from the current charging the double-layer capacitor of the electrode and any stray capacitance in the system. Therefore error is induced by including this capacitive charging current into the electric current for oxygen consumption.

The stray capacitance depends on the connecting cable, and is usually less than 10 pF. However, the double-layer capacitance of a 25 μm diameter disc electrode is about 15~60 pF (from an estimate of 10~40 $\mu F/cm^2$), which is larger than the stray capacitance. Therefore for an approximate calculation, the stray capacitance can be ignored. According to the Randles model, an RC charging circuit can be used to calculate this charging current, where R is the water resistance, and C is the double-layer capacitance. As the RC charging effect changes with water conductivity, therefore it cannot be considered as a DC bias. For a measurement with 1% accuracy, we need to wait until the charging current attenuate to 1% of the transient current.

The RC charging circuit has a time constant τ_c:

$$\tau_c = R_s C_{dl} \qquad [4\text{-}32]$$

where R_s is the water resistance and C_{dl} is the double-layer capacitance. The charging current is:

$$I_{RC} = \frac{V}{R_s}\exp(-\frac{\mathrm{t}}{\tau_c}) \qquad [4\text{-}33]$$

where V is the oxygen measurement voltage.

As discussed in chapter 3, the measurement voltage is about 0.6 V, the double-layer capacitance is estimated as 10 $\mu F/cm^2$. The relation between electric current density $\overrightarrow{J_E}$ and electric potential field V_E is:

$$\overrightarrow{J_E} = \sigma \nabla V_E \qquad [4\text{-}34]$$

This equation is very similar to the diffusion equation (equation 4-3), the only difference is the diffusion coefficient is replaced by water conductivity σ. Therefore the static electric field has a similar equation as the concentration equation in steady state. According to equation 4-22, the water resistivity for a disc electrode is:

$$R_s = \frac{1}{4\sigma r_0} \qquad [4\text{-}35]$$

The charging current attenuation has an exponential form ($exp(-\frac{t}{\tau_c})$), which is much quicker than the oxygen transient current attenuation ($1/\sqrt{t}$). For a disc electrode with 10 μm radius, the time constant τ_c can be calculated to be 1 μs at 10 mS/cm. Calculation shows that after 10 μs, the charging current is less than 1% of the transient current for oxygen consumption. 10 μs is much smaller than the maximum waiting time of 1.5 ms for flow effects. As 10 mS/cm is the lowest conductivity in seawater, giving the maximum time constant, the charging current can be ignored for seawater oxygen measurement. However if we extend the application to fresh water, the waiting time will become a problem, e.g. for fresh water with 10 µS/cm conductivity, the waiting time increases to 5 ms for less than 1% RC charging effect.

Discussions

Dissolved oxygen can be measured in either the steady state or during the transient. A steady state measurement has several advantages in that the temperature coefficient can be easily determined by equation 4-27, and the measurement result is not affected by double-layer capacitance or initial state. The steady state measurement is very suitable for Clark-type electrodes as it has a membrane to protect the electrode against flow. However, for a membraneless sensor, the steady state current has serious flow effects. Furthermore the waiting time to get to steady state is in minutes. Therefore the sensor has a slow response time.

Conversely, a transient measurement has a complex temperature coefficient. However this coefficient can be determined from calibration. The flow effects for transient measurements can be reduced by reducing the waiting time. Therefore it is more suitable for a membraneless oxygen sensor. Typically this waiting time can be up to 1.5 ms for a disc electrode with 10 µm radius. The minimum waiting time at which the RC charging effect can be ignored is about 10 µs for seawater. As there is a substantial time between 10 µs and 1.5 ms, both flow effects and RC charging effects can be removed by taking measurement within this time gap. However, if the application is extended to fresh water, the minimum waiting for RC charging effects increases to 5 ms. There is no time gap to remove both effects for a disc electrode. Furthermore, transient current measurement using a long waiting time is influenced more by the oxygen concentration in the solution bulk, whilst transient current with shorter waiting time depends on the initial oxygen concentration around the electrode. Therefore measurement with longer waiting time depends less on the initial concentration. If the geometry of the sensor is modified to extend the maximum waiting time for flow effects and the measurement waiting time increased, the system could be extended to the fresh water field, and the initial effects could be reduced.

4.4.3 Sensor design

In order to minimise flow effects and increase the maximum waiting time, the sensor is fabricated within a well as shown in figure 4-32. The diffusion inside the well will be unaffected by water flow. Therefore the time for the diffusion boundary to reach the top of the well gives the maximum wait time for no flow effects. Figure 4-32 shows the oxygen sensor design with a well:

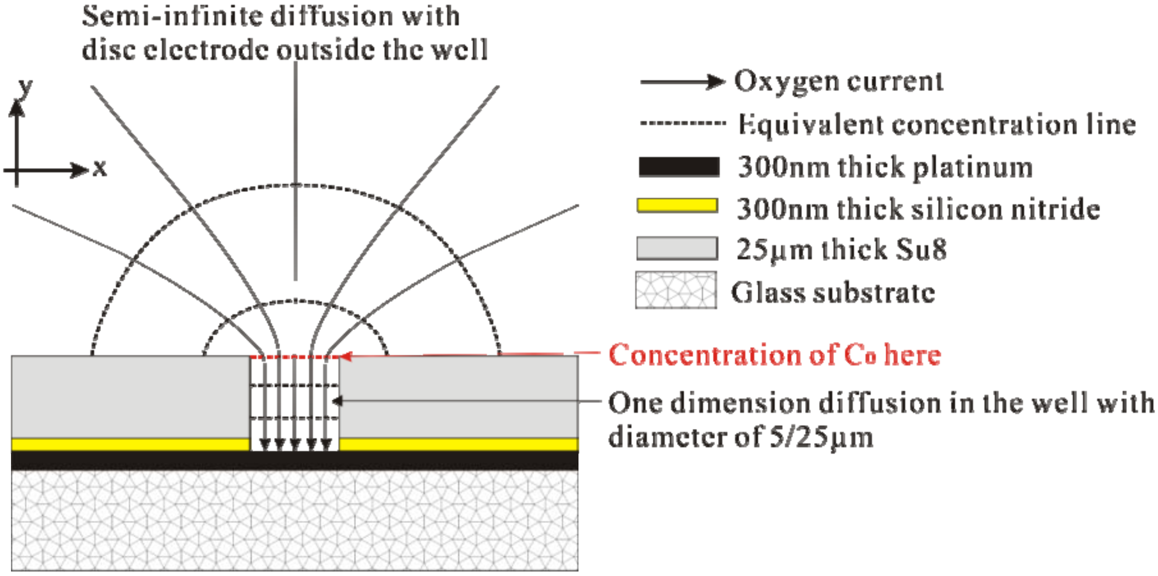

Figure 4-32 A diagram of oxygen sensor cell with a disc platinum electrode in a well, using micro fabrication technique.

As shown in figure 4-32, diffusion for a disc electrode in a well can be divided into two parts: one dimensional diffusion in the well and semi-infinite diffusion as for a disc electrode outside the well [131-133]. In order to estimate the steady state current and water resistance, we assume that the oxygen concentration at the outlet of the well (red line in figure 4-32) is the same, and has a value of C_0. Therefore, for one dimensional diffusion in the well, the steady state oxygen current J_s is:

$$J_s = \frac{ADC_0}{H} \qquad [4\text{-}36]$$

where A is the area of the electrode, equals to πr_0^2 (r_0 is the radius), H is the height of the well. The semi-infinite diffusion for a disc electrode outside the well has steady state oxygen current J_s :

$$J_s = 4Dr_0(C^* - C_0) \qquad [4\text{-}37]$$

As the two equations share the same oxygen current, equations 4-36 and 4-37 can be combined and solved to give C_0 and J_s:

$$C_0 = \frac{4HC^*}{\pi r_0 + 4H} \qquad [4\text{-}38]$$

$$J_s = \frac{4ADC^*}{\pi r_0 + 4H} \qquad [4\text{-}39]$$

The water resistivity is:

$$R_s = \frac{\pi r_0 + 4H}{4A\sigma} \qquad [4\text{-}40]$$

In the early (transient) state, the diffusion boundary is inside the well. The diffusion in this stage is only in the y direction as figure 4-32 shows, therefore, only the y velocity of flow will affect the current. A FEM simulation is made to estimate the flow velocity in the well. Figure 4-33 shows the boundary conditions of the flow:

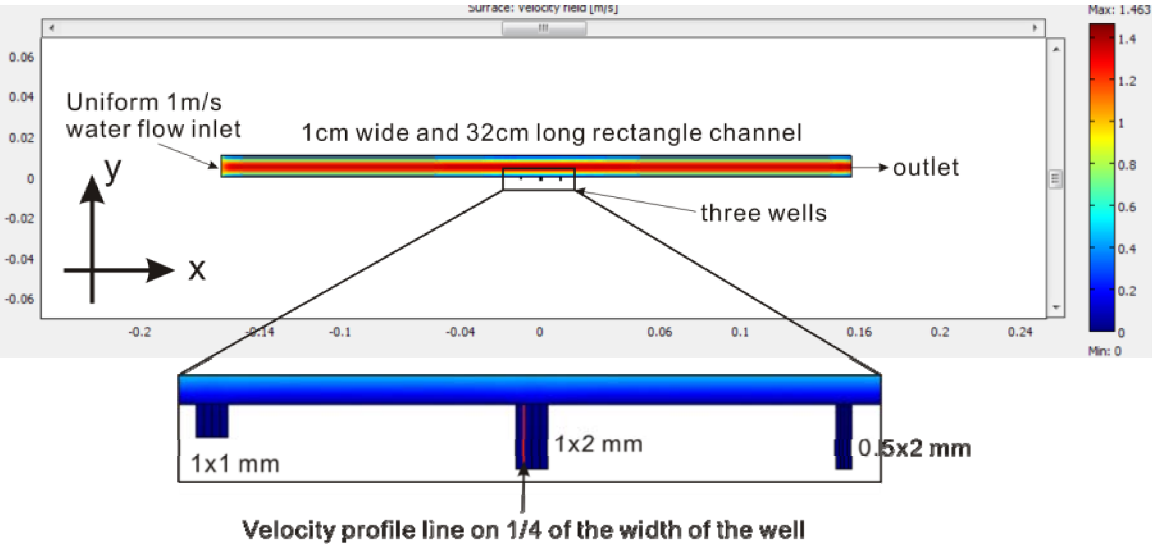

Figure 4-33 FEM simulation in COMSOL for flow velocity field of a rectangular water channel with 3 wells, where the colour shows the velocity field. The mesh dimension is about 0.1 mm in the wells.

In this simulation, a rectangular 1x32 cm water channel is used to define the velocity field above the sensor cell. The inlet of the channel has a uniform 100 cm/s flow velocity and 3 wells with different dimensions are placed in the middle of the channel. There is 15 cm from the inlet to the well, which acts as a buffer, changing the y direction profile of the flow from a uniform 100 cm/s at the inlet to the distribution shown in figure 4-30, with a maximum velocity of 140 cm/s in the centre. The three wells have dimensions of 1x1 mm, 1x2 mm, and 0.5x2 mm. Due to symmetry, the flow in the half width of the well has no y velocity. Therefore the profile of the y velocity is made along the line on the ¼ of the width of the well. Figure 4-34 shows the profiles:

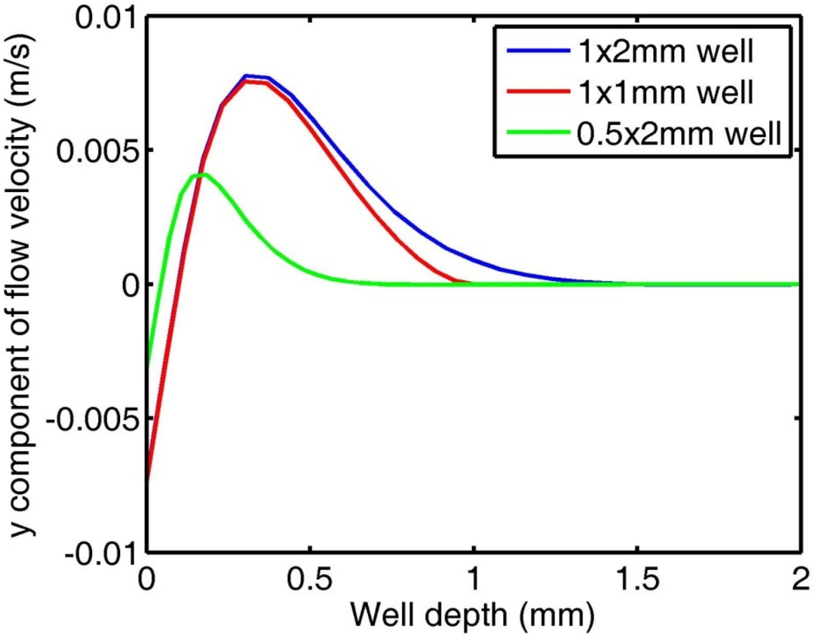

Figure 4-34 Plot of FEM simulated flow velocity in the wells along the *y*-direction.

As shown in the figure, all the three wells have a maximum *y* velocity at the top of the well (depth = 0). We see that the maximum *y* velocity depends on the width of the well, because the 1x2 mm well and 1x1mm well have the same maximum *y* velocity of 7.3 mm/s, and the 0.5x2 mm well has a smaller maximum y velocity of 3.5 mm/s. The attenuation speed is primarily determined by the width of the well, because the 0.5x2 mm well has twice the attenuation speed. However, the depth of the well also affects the attenuation, as the 1x1 mm well has slightly quicker flow attenuation with depth because it has a smaller depth.

Furthermore, when the well depth is longer than diameter (1x2 mm and 0.5x2 mm), the *y* velocity attenuates to 10% of the maximum value when the depth equals the diameter, and 1% when the depth equals 1.3 times the diameter.

In the sensor chip, the height of the well is set to 25 µm. This height is defined by the thickness of SU8. Two designs with different diameters are implemented on chip 2-A in design 2: one with a diameter of 5 µm, and the other with a diameter of 25 µm. According to equation 4-7, the diffusion boundary takes 20 ms to come out of the 25 µm deep well. FEM simulations were made to calculate the velocity, and the result show that the *y* velocity is 20 µm/s at the top of the 5 µm diameter well, when the flow is in a 1 cm wide rectangle channel with maximum flow velocity of 100 cm/s. For the well with 25 µm diameter, this *y* velocity is 100 µm/s.

For the 5 μm diameter well, the ratio coefficient K_T is calculated to be 1.35 pA/μM at 20 ms, from equation 4-6 (n=4). The flow-induced current at 20 ms is calculated to be 0.075 pA/μM, which is 5.6% of the transient current. However, the actual flow effects may be smaller as the estimate of the flow-induced current is pessimistic. Furthermore, as the y velocity attenuates to 10% of the maximum value when the depth equals the diameter when the diffusion thickness is smaller than 20μm (25 μm depth – 5 μm diameter electrode well), the flow effect is smaller than 0.56%. The diffusion takes 12.5 ms to reach the 20 μm thickness, therefore in the first 12.5 ms, the flow effect is smaller than 1%.

For the RC charging effects, calculations show that the minimum waiting time is 22 μs for 10 mS/cm seawater, and 11 ms for 10 μS/cm fresh water. Therefore, the transient measurement at a time between 11 ms and 12.5 ms removes both flow effects and RC charging effects.

For the well of 25 μm diameter, K_T is calculated as 35 pA/μM at 20 ms. The flow-induced current is 9.5 pA/μM, which is about 28%. Therefore the 25 μm diameter well cannot totally remove the flow effects. However, as this is a pessimistic estimate, and 100 cm/s is a large flow, the actual flow effects at 20 ms may be much smaller than estimated, especially when a slower flow is applied, e.g. 10 cm/s.

The minimum waiting time to remove the RC charging effects is 22 μs for 10 mS/cm seawater and 15 ms for 10 μS/cm fresh water. Therefore if experimentally the flow effects are not found to be a serious problem using a 20 ms measurement delay the preferred waiting time should be about 15~20 ms.

The DO sensor and the conductivity sensor are implemented on chip 2-A in design 2 as shown in figure 4-18. Instead of one well, five wells are placed on the platinum electrode to achieve an average effect and increase the total current. As shown in the figure, five ring-type platinum electrodes are placed around the working electrode. These electrodes can either be used as counter electrode in a three-electrode system, or be plated for Ag/AgCl for reference electrode.

The micro fabrication technique cannot etch micro holes with a diameter smaller than their depth. Therefore the sensor chips with five 5 μm diameter wells were not successfully manufactured. However, the sensor chips with five 25 μm diameter wells were manufactured successfully, and had good performance (chapter 6). Therefore, this design is also implemented in design 3 as shown in figure 4-8.

Chapter 5 Electronics Design

Electronic circuitry is required for the CT-DO sensors. Both CT sensors are impedance sensor, and can share a single impedance measurement circuit with multiplexers. However, the DO sensor is an electrochemical sensor, and requires separate circuit for the two/three-electrode electrochemical system.

5.1 Impedance measurement circuit for CT sensor

An impedance measurement circuit was designed for the CT sensors – the schematic diagram is presented in figure 5-1. The circuit can be divided into the analogue part and the digital part, which are introduced in the follow sections.

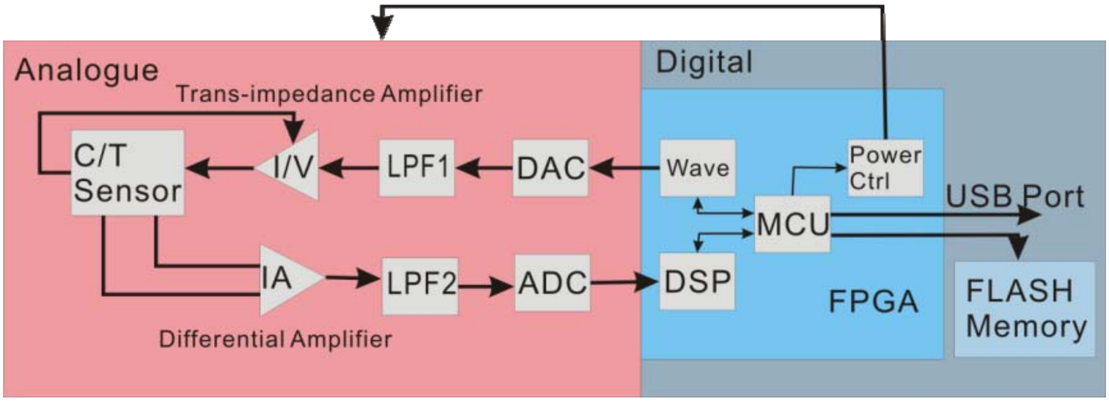

Figure 5-1 A block diagram of CT sensor system, including CT sensors and supporting circuit for impedance measurement.

5.1.1 Analogue circuit

Figure 5-2 shows a photograph of the PCB of the analogue circuit:

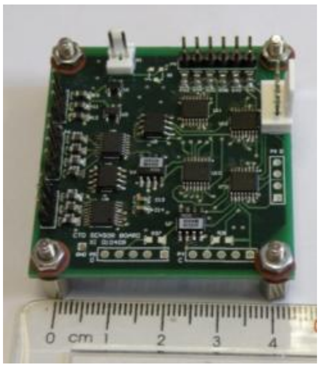

Figure 5-2 A photograph of the analogue circuit PCB for the impedance measurement system.

As shown in figure 5-1, there are seven modules in the analogue circuit: a digital-to-analogue converter (DAC) is used to convert the digital waveform into an analogue signal; a low-pass filter (LPF1) is used to smooth the analogue signal from the DAC; a trans-impedance Amplifier (I/V) converts the voltage signal from the LPF1 into a current signal, to drive the C/T sensor, and a differential amplifier (IA) amplifies the voltage signal from the C/T sensor; another low-pass filter (LPF2) is used to remove the high frequency noise from the sensor; after filtering, the analogue signal is converted into digital signal by an analogue-to- digital converter (ADC).

DAC, ADC and low-pass filters

The analogue circuit is similar to the square wave excitation system (chapter 2, figure 2-13). However, there are two main differences. First, instead of a signal generator, a digital-to-analogue converter (DAC) and a low-pass filter (LPF1) are used to generate the signal. Second, the high-pass filter and the synchronous rectifier are removed to reduce ripple noise. Instead a low-pass filter (LPF2) an ADC with 100 ksps sample rate is used to convert the analogue signal into a digital signal, allowing all the signal processing work to be done by the digital circuit.

One advantage of using a DAC rather than a signal generator is that it can generate many kinds of signals, so that the analogue board can support both sine wave and square wave excitation. Furthermore, the DAC and ADC can be driven by the same controller. Therefore, the frequency of the excitation signal and the ADC sample rate can be kept to a fixed ratio, making the digital signal processing (DSP) much easier. For example, with sine wave excitation, the frequency of the sensor response signal is exactly known. Therefore only a three-parameter fitting algorithm is required rather than a four-parameter fitting.

Trans-impedance amplifier and differential amplifier

The trans-impedance amplifier (AD822 [134]) is used to convert the voltage signal into a current signal, and injects this current into the sensor via the two current terminals. The differential amplifier (AD623 [135]) measures the voltage response from the sensor via the two voltage terminals. This four-terminal interface can support many kinds of impedance measurement. For a four-electrode conductivity cell, by injecting current via two of the electrodes and measuring voltage from the other two electrodes, electrode polarization effects can be removed. A Wheatstone resistor bridge has four terminals connected to this interface. Therefore, this interface can also support a PRT-bridge temperature sensor and piezo-resistor bridge pressure sensor, as they are based on a Wheatstone bridge. Furthermore, it can also be configured as two-terminal interface by connecting the current terminal and voltage terminal together. Therefore two-terminal components, such as resistors, capacitors, and thermistors, can be supported by this interface.

A common design for the trans-impedance amplifier is shown in figure 5-3:

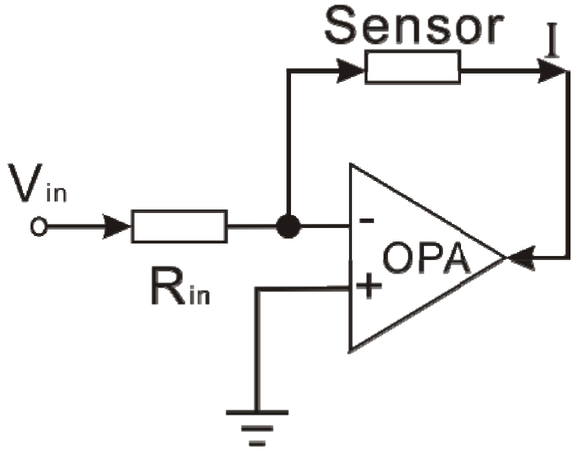

Figure 5-3 Schematic of a common design for the trans-impedance amplifier.

It is based on an operational amplifier (OPA) with negative feedback from the sensor. R_{in} is the V/I (voltage to current) gain resistor which is used to define the transfer ratio between the input voltage V_{in} and the injection current I by $I = \frac{V_{in}}{R_{in}}$.

However, because of the double-layer capacitance, the impedance of the conductivity cell at DC signal is infinite (in the absence of Faradaic reactions). Therefore, there is no negative feedback for the DC signal, and the static voltage response of the OPA is uncertain and easily saturates, increasing the signal setup time and inducing overflow error.

To solve this problem, an improved design is implemented in the analogue circuit – figure 5-4:

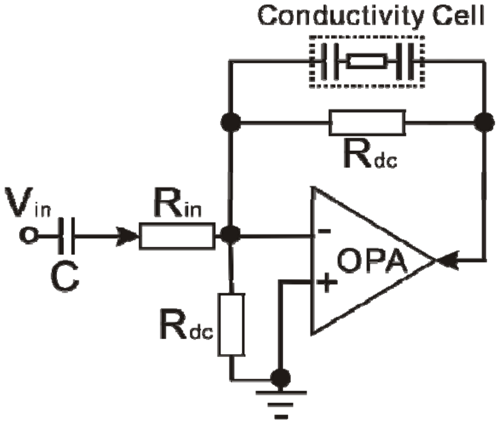

Figure 5-4 Schematic of the improved trans-impedance amplifier design for the conductivity cell.

As shown in the figure, a capacitor (*C*) and two resistors with the same impedance (R_{dc}) are added in to this design. The R_{dc} has a resistance more than 100 times bigger than R_{in} and the resistance of seawater in the conductivity cell. For a DC signal, because of the infinite impedance of the capacitor and the conductivity cell, the equivalent circuit can be simplified as shown in figure 5-5(a). Therefore there is only a small static voltage response from the OPA, due to the extremely small leakage current (I_{leak}) of the OPA. For AC signals, because R_{dc} is very big, the equivalent circuit can be simplified as shown in figure 5-5(b). Therefore the injection current can be calculated as: $I = \frac{V_{in}}{R_{in}+{}^{1}/_{j\omega C}}$.

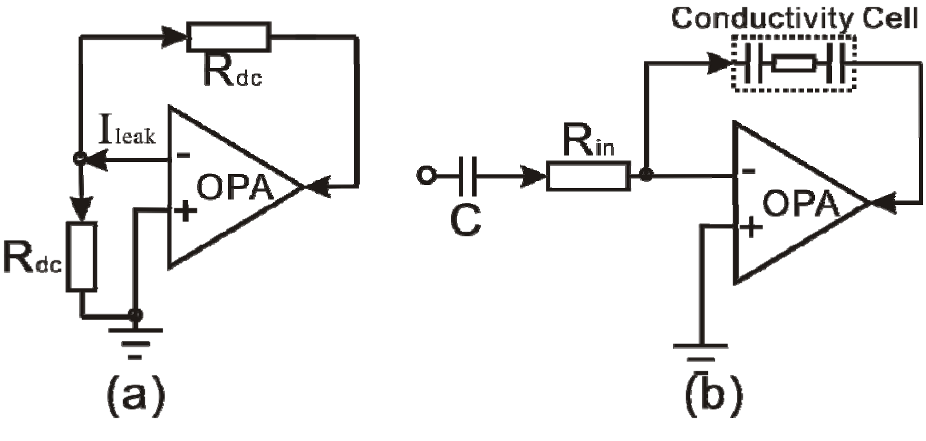

Figure 5-5 Schematic of the simplified equivalent circuits for the trans-impedance amplifier: (a) for DC signal; (b) for AC signal.

C/T Sensor model and multiplexers

The four-way multiplexers are used in the C/T sensor model to support four-channel impedance measurement. Figure 5-6 shows the multiplexing used for the trans-impedance amplifier:

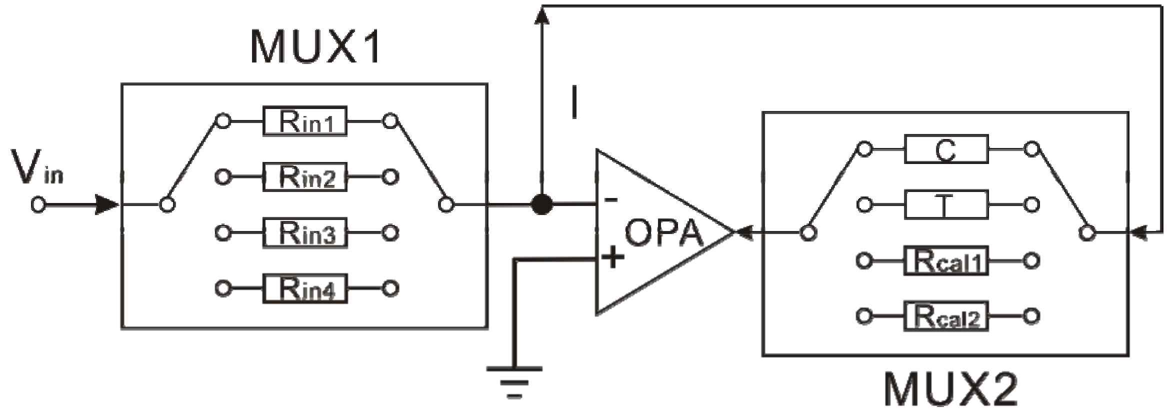

Figure 5-6 A schematic of the trans-impedance amplifier with multiplexers.

As shown in the figure, two multiplexers (MUX1 and MUX2) are used. MUX1 is used to select the V/I gain resistors and determine the magnitude of the injection current *I*. MUX2 is used to select the C/T sensors or calibration resistors for current injection. The CT sensors will take two of the channels. The other two channels can be used for the calibration resistors (R_{cal1}, R_{cal2}) or the other sensor, for example, the depth sensor.

Another two multiplexers are used for the differential amplifier. One is used to select the voltage response from the sensors or calibration resistors, while the other is used to determine the gain of the amplifier by selecting different feedback resistor.

The measured impedance of the C/T sensor $|Z_{C/T}|$ can be calculated as:

$$|Z_{C/T}| = \frac{U}{GI} \qquad [5\text{-}1]$$

where *I* is the injection current, *U* is the AC amplitude sampled by ADC, and *G* is the gain of the differential amplifier. Both *I* and *G* are controlled by multiplexing the resistors of the trans-impedance amplifier and the instrumentation amplifier respectively.

Both the gain of the amplifiers and the value of the resistors drift with temperature and time, affecting *G* and *I*. To minimize this error, calibration resistors with extremely low temperature coefficient (0.6 ppm/^{o}C) and excellent load life stability (0.005% drift after 2000 hours under load) are embedded in the C/T sensor block. Sequentially measuring the AC amplitude of the C/T sensor voltage ($U_{C/T}$) or the calibration resistor voltage (U_R) using the same G and I, the impedance of C/T sensor ($|Z|$) becomes:

$$|Z_{C/T}| = \frac{U_{C/T}}{U_R} R_{cal} \quad [5\text{-}2]$$

where R_{cal} is the resistance of the calibration resistor.

Because G and I are eliminated in equation 5-2, the system error depends on the stability of the calibration resistor with temperature and with time. Because the temperature of the environment varies between -2 and 30 °C, the maximum change in the calibration resistor due to temperature is 0.0018%. Typically the system takes 100 ms for a single channel measurement with a 10 s measurement interval. At this 1% duty cycle the calibration resistor drifts by a maximum of 0.0002% per year. Therefore the annual system drift is very low and any inaccuracy is determined by the temperature of the resistor.

5.1.2 Digital circuit design

The micro-controller unit (MCU) is usually used for analogue circuit control in a square wave excitation system. However, due to the limited calculation ability, it is not suitable for controlling the high speed ADC and DAC, and implementing the DSP algorithms such as sine wave fitting. Instead a low power field programmable gate array (FPGA) with system-on-a-chip (SOC) solution is used in the digital part.

As shown in figure 5-1, four major modules are implemented inside the FPGA, including MCU module, DSP (Digital Signal Processing) module, waveform module, and the power control module. The impedance measurement uses sine wave excitation. The waveform module controls the DAC to generate a sine wave. The DSP model calculates the amplitude and phase of the sine wave sampled by the ADC, and this amplitude and phase information is used for C/T calculation. The power control module is used to control the system working mode, eliminating unnecessary power consumption when the system is not measuring. The MCU controls the other modules, records the data from DSP module into a 512 Mbit external FLASH memory, and communicates with a PC through a USB interface.

Figure 5-7(a) shows the PCB of the digital circuit, while 5-7(b) shows the optional USB communication board for connecting the digital circuit to a PC:

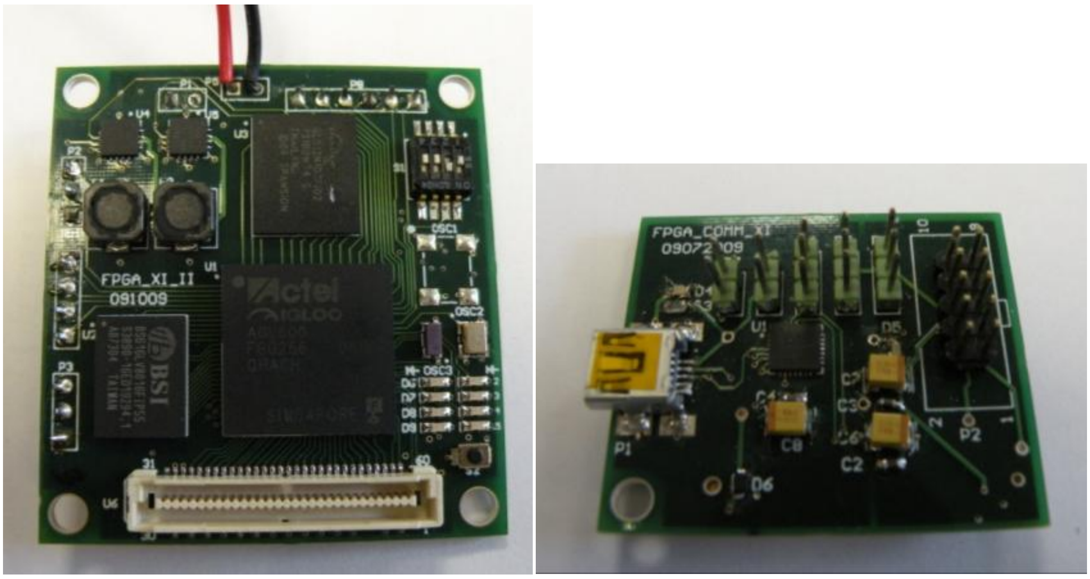

(a) (b)

Figure 5-7 Photographs of the digital circuit PCBs for the impedance measurement system: (a) FPGA board; (b) optional USB communication board.

MCU

The MCU module is modified from the CQPIC [136], which is a free synthesizable VHDL [137]/ Verilog HDL [138] description of the PIC16F84A processor [139]. The original CQPIC can only support 68 bytes RAM and 1.75 kB program memory. After modification, the MCU module can support 512 bytes RAM space, and 4 kB program memory.

For the software development, because the MCU module has the same instruction set as a PIC16 serial processor, we can use the same compiler as for a PIC16 for compiling, for example, the CCS C compiler [140]. Software coupled with a program downloader module was also developed for downloading the compiled program. Figure 5-8(a) shows the CCS C compiler, and Figure 5-8(b) shows the downloading software:

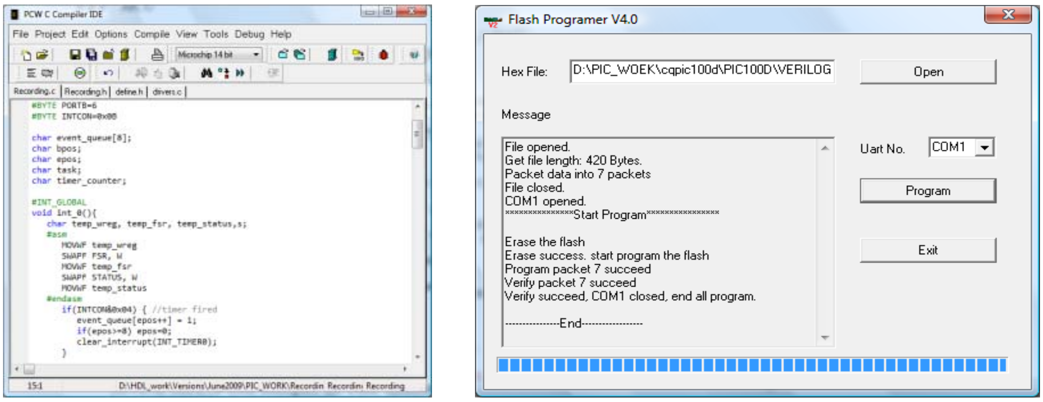

```
#BYTE PORTB=6
#BYTE INTCON=0x0B

char event_queue[8];
char bpos;
char epos;
char task;
char timer_counter;

#INT_GLOBAL
void Int_0(){
   char temp_wreg, temp_fsr, temp_status,s;
   #asm
      MOVWF temp_wreg
      SWAPF FSR, W
      MOVWF temp_fsr
      SWAPF STATUS, W
      MOVWF temp_status
   #endasm
      if(INTCON&0x04) { //timer fired
         event_queue[epos++] = 1;
         if(epos>=8) epos=0;
         clear_interrupt(INT_TIMER0);
      }
```

Hex File: D:\PIC_WOEK\cqpic100d\PIC100D\VERILOG

Uart No. COM1

Message

```
File opened.
Get file length: 420 Bytes.
Packet data into 7 packets
File closed.
COM1 opened.
***************Start Program***************

Erase the flash
Erase success. start program the flash
Program packet 7 succeed
Verify packet 7 succeed
Verify succeed, COM1 closed, end all program.

-------------End-------------
```

(a) (b)

Figure 5-8 Diagrams showing the software development kits: (a) CCS C compiler; (b) program downloading software.

The MCU module is used to configure the other modules, set the multiplexers in the analogue circuit, control the data storage of the FLASH memory, and communicate with a PC. Therefore, the parameters of the sensor system can be configured for applications by programming, including:

(1) The sensors/calibration resistors selection, injection current volume, and the gain of the differential amplifier.
(2) The signal setup time and fitting time for each measurement.
(3) The measurement interval (the sleep/wake-up period).

Waveform and DSP

The waveform module and DSP module is used to couple to the high speed DAC and ADC, and to process the digital signal. With different designs of the waveform and DSP modules, the system can support both sine wave and square wave excitations.

In the current implementation the system is configured for the sine wave excitation. The waveform module stores a 64-point digital sine wave. By controlling the DAC with 100 ksps sample rate, it can generate an analogue sine wave with a frequency of 1.5625 kHz (100/64 kHz).

The DSP module controls the ADC to work with exactly the same sample rate as the DAC. Therefore the digital signal x_i sampled from ADC can be described as following formula:

$$x_i = A\sin\left(\frac{2\pi i}{64}\right) + B\cos\left(\frac{2\pi i}{64}\right) + C + n_i, \qquad i = 0,1,2,3 \ldots\ldots \qquad [5\text{-}3]$$

$$\xrightarrow{\textit{sine wave}} \quad \xrightarrow{\textit{noise}}$$

x_i consists of the induced noise n_i and the sine wave with three unknown parameters A, B and C. A is the magnitude of the in phase (or sine) component of the response, B is the magnitude of the cosine (quadrature) component, and C is the DC component. The amplitude and phase of the resultant response can be calculated as:

$$Amplitude = \sqrt{A^2 + B^2} \quad [5\text{-}4]$$

$$Phase = \tan^{-1}\frac{B}{A} \quad [5\text{-}5]$$

A three-parameter sine fitting algorithm is implemented in the DSP module for the calculations of A, B, and C using the following equations:

$$A' = \frac{1}{32m}\sum_{i=0}^{64m} x_i \sin\left(\frac{2\pi i}{64}\right) \quad [5\text{-}6]$$

$$B' = \frac{1}{32m}\sum_{i=0}^{64m} x_i \cos\left(\frac{2\pi i}{64}\right) \quad [5\text{-}7]$$

$$C' = \frac{1}{64m}\sum_{i=0}^{64m} x_i \quad [5\text{-}8]$$

$$e_A = A' - A = \frac{1}{32m}\sum_{i=0}^{64m} n_i \sin\left(\frac{2\pi i}{64}\right) \quad [5\text{-}9]$$

$$e_B = B' - B = \frac{1}{32m}\sum_{i=0}^{64m} n_i \cos\left(\frac{2\pi i}{64}\right) \quad [5\text{-}10]$$

$$e_C = C' - C = \frac{1}{64m}\sum_{i=0}^{64m} n_i \quad [5\text{-}11]$$

where A', B', and C' are the fitted parameters for A, B, and C, while e_A, e_B, and e_C are the fitting errors respectively. m is the period number of the sine wave. It can be configured by the MCU as the sampling time for each measurement.

Normally n_i is White Gaussian Noise whose average value approaches zero by extending the sampling length to infinity, e_C is the average (mean) of this noise with a length of *64m*. In e_A and e_B this noise is first multiplied by $2\sin\left(\frac{2\pi i}{64}\right)$ and $2\cos\left(\frac{2\pi i}{64}\right)$ respectively, and then averaged with a length of *64m*. Multiplying a signal with a sine/cosine wave performs a frequency shift of the field of the original signal in both directions by the frequency of the sine/cosine wave ($\pi/32$), followed by combining them together. White Gaussian Noise is a noise model which has a uniform frequency component. Therefore this shifting and combining does not change the uniformity of the frequency component, and the noise produced by the multiplication is still White Gaussian Noise. Hence all the fitting errors can be reduced by increasing the sampling length (*64m*), meaning that the measurement precision of the system can be improved by increasing the sampling length (time), until it reaches the limitation of 16-bit precision.

Power control module

The power control module is used for supporting the ‘wake-up’ and ‘sleep’ modes, eliminating unnecessary power consumption when the system is not measuring.

There are two oscillators in the digital circuit. One with 24 MHz frequency is used for driving most of the modules in the FPGA, while the other with 32 kHz frequency is used for a timer in the power control module.

When measuring, the analogue circuit and the 24 MHz frequency is powered on by the power control module, and the system operates in the ‘wake-up’ mode. Subsequently, the power control module turns off the power of the analogue circuit and the 24 MHz oscillator following the instruction MCU. The system will be kept in this ‘sleep’ mode until a system state change is triggered by the timer. The power control module then turns on the power to resume the ‘wake-up’ mode. The time interval between timer controlled wake up and sleep triggers can be configured by the MCU to define the measurement time interval of the system.

5.2 Electronics for DO sensor

The design of the electronic circuit supporting two/three electrode electrochemical system for the DO sensor is shown in figure 5-9:

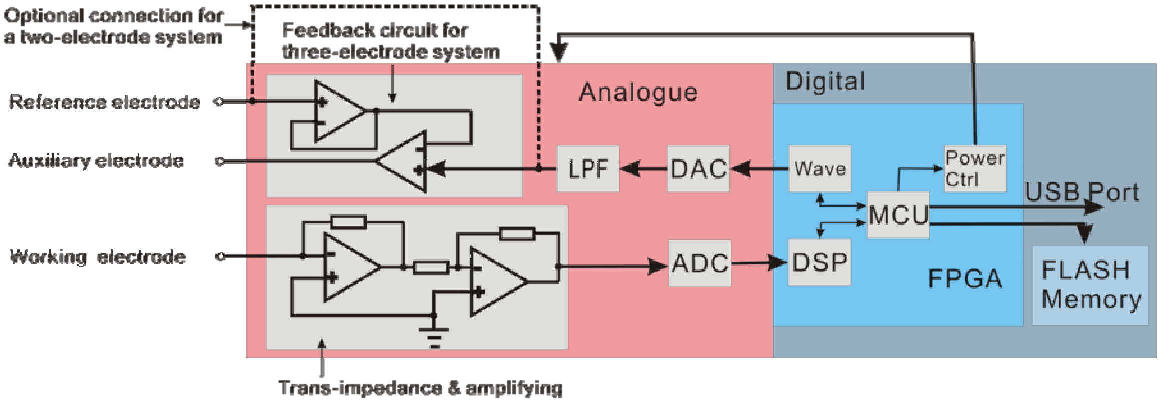

Figure 5-9 Block diagram of two/three electrode electrochemical sensor system, supporting DO measurement.

As shown in the figure, this system is similar to the CT sensor system. The digital circuit uses the same hardware as the CT sensor system. However, the waveform and DSP module are not used for sine wave fitting, but for a waveform designed for DO measurement.

In common with the impedance measurement system (see section 5.1), the excitation voltage signal in the analogue circuit is generated by a DAC and a low-pass filter (LPF). For a three electrode system this excitation voltage signal is applied to the solution bulk using a reference electrode and an auxiliary electrode with a feedback circuit. For a two electrode system, the feedback circuit can be removed, and the excitation voltage signal can be directly applied to the reference electrode (using an optional connection included within the circuit design as shown in figure 5-9).

A trans-impedance and amplifying model is used to set the working electrode at 0V, and convert the current on the working electrode into a voltage signal. This voltage signal is sampled by an ADC, converted into a digital signal, and processed by the DSP module for DO calculation. Figure 5-10 shows a photograph of the PCB for the analogue circuit of DO sensor and USB connection. Figure 5-11 shows a photograph of the complete CT-DO system with 3 PCBs connecting together:

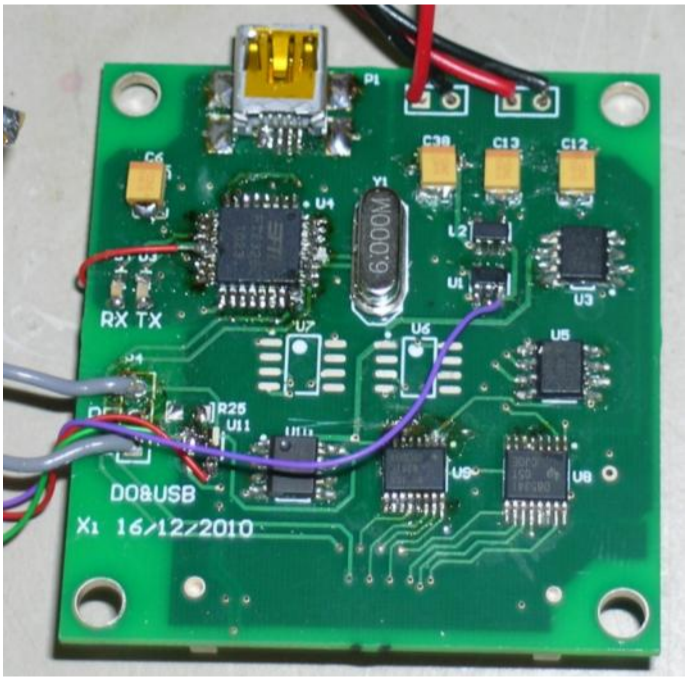

Figure 5-10 A photograph of the PCB for the DO analogue circuit and USB communication. Two amplifiers (U6 and U7) for the feedback module are unsoldered here as this PCB is configured as for two-electrode electrochemical system.

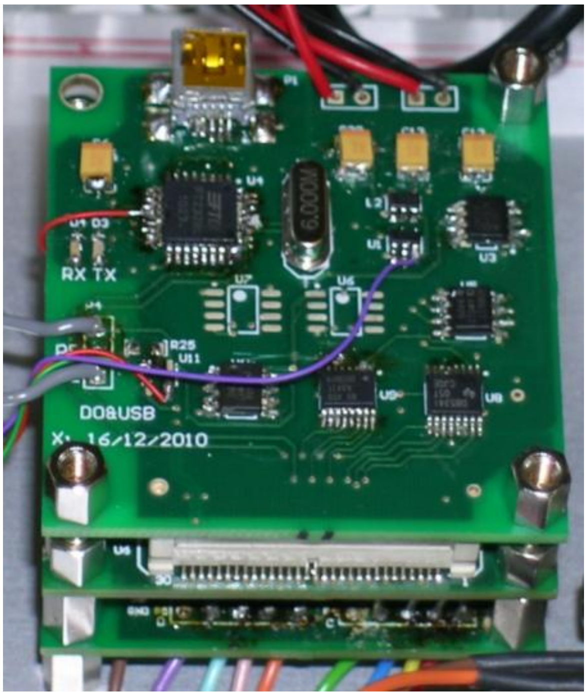

Figure 5-11 A photograph of the complete CT-DO electronics with three layers of PCBs, where the CT analogue circuit PCB is on the bottom, the digital circuit PCB is in the middle, and the PCB of DO analogue circuit and USB connection is on the top.

5.2.1 *Analogue circuit for two/three electrode system*

In an electrochemical system, the voltage in the solution bulk $V_{solution}$ can be set by either applying a voltage V_{in} to the reference electrode directly (two electrode system), or applying V_{in} through a feedback circuit using reference electrode and auxiliary electrode together (three electrode system). The feedback circuit has been introduced in chapter 3, figure 3-7. The relation between $V_{solution}$ and V_{in} is:

$$V_{solution} = V_{in} - V_{eq} \qquad [5\text{-}12]$$

where V_{eq} is the equilibrium voltage of the reference electrode.

A trans-impedance amplifier is usually used to set the voltage of the working electrode to 0V, and convert the current on the working electrode into a voltage signal. Therefore the voltage applied on the working electrode against the solution $V_{reaction}$ is:

$$V_{reaction} = 0 - V_{solution} = V_{eq} - V_{in} \qquad [5\text{-}13]$$

Figure 5-12 shows the trans-impedance and amplifying circuit for the working electrode:

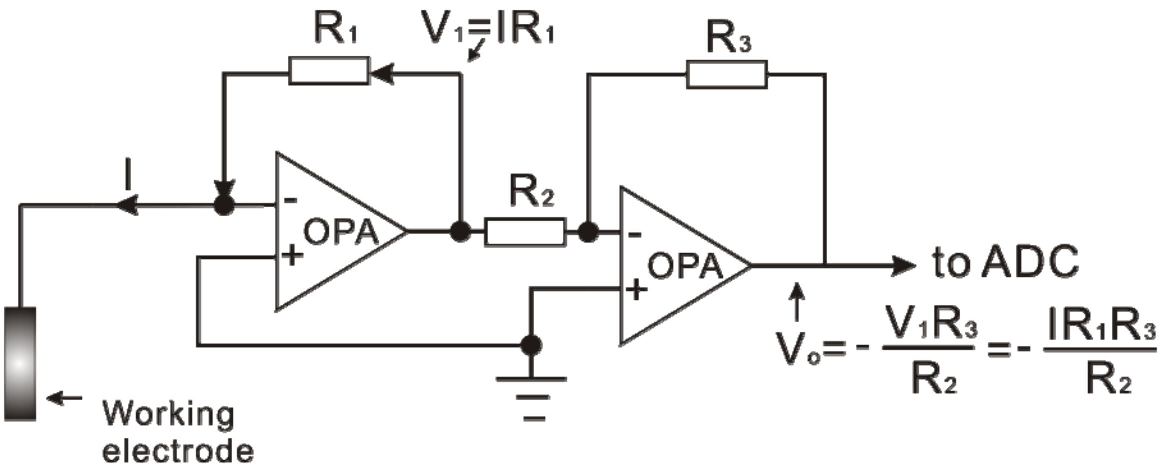

Figure 5-12 A schematic of the circuit design for the trans-impedance and amplifying module, where the voltage of working electrode is set to 0V, and the current passing through the working electrode is converted into a voltage output for ADC.

There are two amplifiers in this design. The first amplifier (left in the figure, LMP7721 [159]) acts as a trans-impedance amplifier, which sets the voltage on the working electrode to 0 V, and converts the current passing through the working electrode (I) into a voltage output V_1 by a resistor R_1 as $V_1 = IR_1$. The second amplifier (AD822 [134]) is used to further enhance this voltage signal for ADC sampling.

The reason we need the second amplifier is that the initial current for oxygen measurement is large due to charging of the double-layer capacitance. R_1 needs to be kept small to make sure the first amplifier does not saturate during this initial state. Otherwise if this occurs, the voltage on the working electrode will not be 0 V, causing measurement error. After the charging of the double layer, V_1 becomes too small for the ADC to measure directly. Therefore the second amplifier is used to increase the input voltage for the ADC and enables measurement. Of course the second amplifier will saturate at the initial state. However this overflow will not affect the voltage set to the working electrode, and will not cause measurement error.

5.2.2 Waveform and measurement

As described in chapter 3, the Ag/AgCl reference electrode has a V_{eq} of 0.237 V for 35 psu seawater at 25 ^{o}C. The data in Figure 3-6 suggest that $V_{reaction}$ should be set between -0.4 V and 0.3 V for oxygen reduction, and 0.5~0.8 V for no oxygen consumption or generation. The optimum $V_{reaction}$ for oxygen reduction was found by experiment (figure 6-36 in chapter 6) to be -0.069 V, while $V_{reaction}$ for no oxygen consumption/generation is 0.531 V.

The $V_{reaction}$ waveform for DO measurement is a 2 s periodic signal. Figure 5-13 shows the waveform in one period:

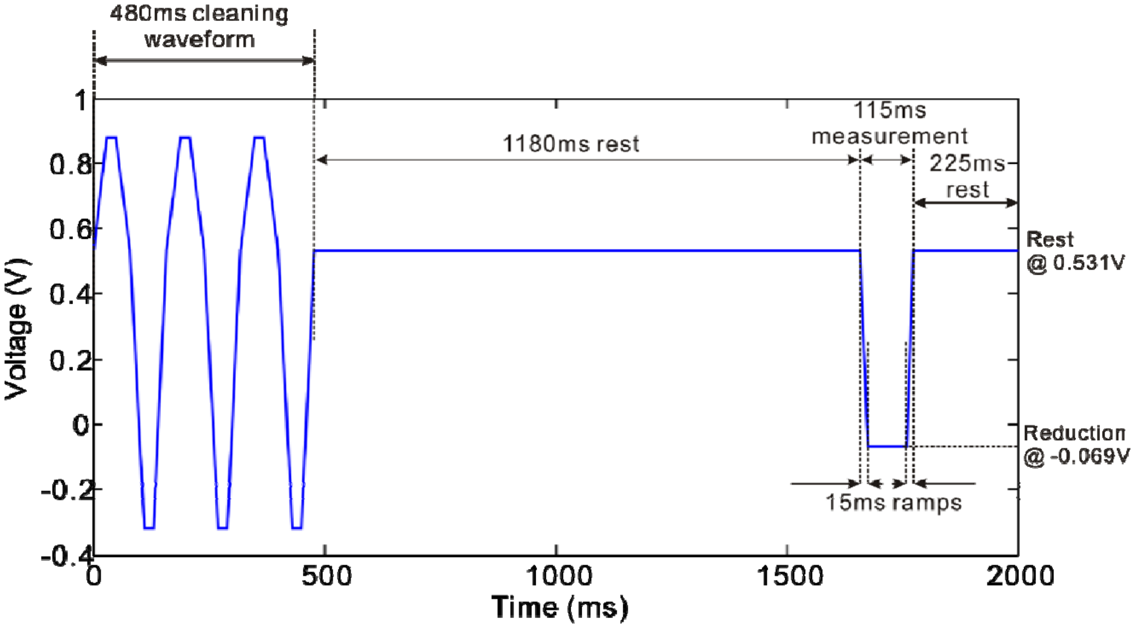

Figure 5-13 Plot of the voltage waveform applied on working electrode against solution bulk for DO measurement.

As shown in the figure, in the first 480 ms, the applied $V_{reaction}$ sweeps from -0.32 to 0.88 V three times. Platinum electrodes held at a constant potential are known to lose their activity towards oxygen reduction [141, 142]. In addition electroplating can occur on the platinum cathode, affecting the oxygen measurement. This sweep performs electrode reconditioning, which maintains the activity of the electrode, and removes any electroplated materials [142].

The electrode reconditioning interferes with the oxygen concentration around the working electrode. Therefore $V_{reaction}$ is kept in 0.531 V for 1180 ms after reconditioning and the oxygen concentration returns to the solution bulk value.

After the 1180 ms rest, $V_{reaction}$ reduces to -0.069 V for oxygen reduction. Instead of changing $V_{reaction}$ immediately, a 15 ms ramp is used to avoid overflow of the trans-impedance amplifier. After 85 ms of oxygen reduction, $V_{reaction}$ goes back to 0.531 V for another 225 ms rest, then electrode reconditioning is repeated in the following period.

The waveform module in the digital circuit stores the waveform for V_{in}. According to equation 5-13, V_{in} is calculated, see figure 5-14:

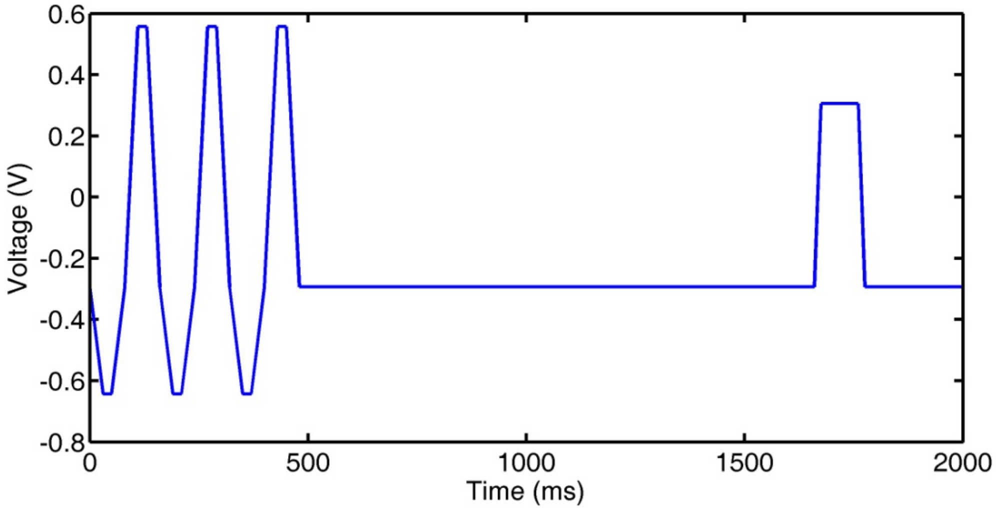

Figure 5-14 Plot of the voltage waveform in the waveform module for DO measurement.

The DSP module samples the voltage output of the trans-impedance and amplifying module at the time slots of 10, 15, 25, and 35 ms after the $V_{reaction}$ ramp for oxygen reduction. Each time slot is 1.28 ms wide, which allows 128 samples to be taken at 100 ksps sample rate. The 128 samples in one slot are averaged to provide one value for oxygen calculation, and recorded in FLASH memory. The four time slots help in understanding any flow and initial electrode state effects, and thence enable choice of an optimized measurement time with smallest measurement error.

Chapter 6 Experimental results

Three versions of sensor systems have been developed, including version 1 CT system using chips in design 1, version 2 CT system using chips in design 2, and a complete CT-DO system. These systems have tested through several calibration runs and various deployments. This chapter presents these experimental results, including testing of the impedance measurement circuit, calibration and deployments of the two versions of CT sensor systems, testing of the DO sensor, and a deployment of the complete CT-DO system on a rowing boat in the Indian Ocean. Preliminary experiments were carried out to explore the possibility of using an electrochemical method to remove bio-fouling, and extending the use of the CT system into freshwater area. These experimental results are also presented in this chapter.

6.1 Test of impedance measurement circuit

The impedance measurement circuit was tested using resistors and capacitors, to find the optimum measurement time, power consumption, and accuracy.

6.1.1 Measurement time

When applying a current excitation signal to the CT sensor or the calibration resistor, the circuit needs to wait some time before reaching a stable voltage response. This time is the signal setup time. After this setup time, the stabilized voltage signal can be sampled for impedance calculation. The measurement time for a single impedance channel can be separated into the signal setup time and the sampling time. In order to determine the signal setup time, the transient voltage response of the impedance measurement circuit was measured, shown in figure 6-1:

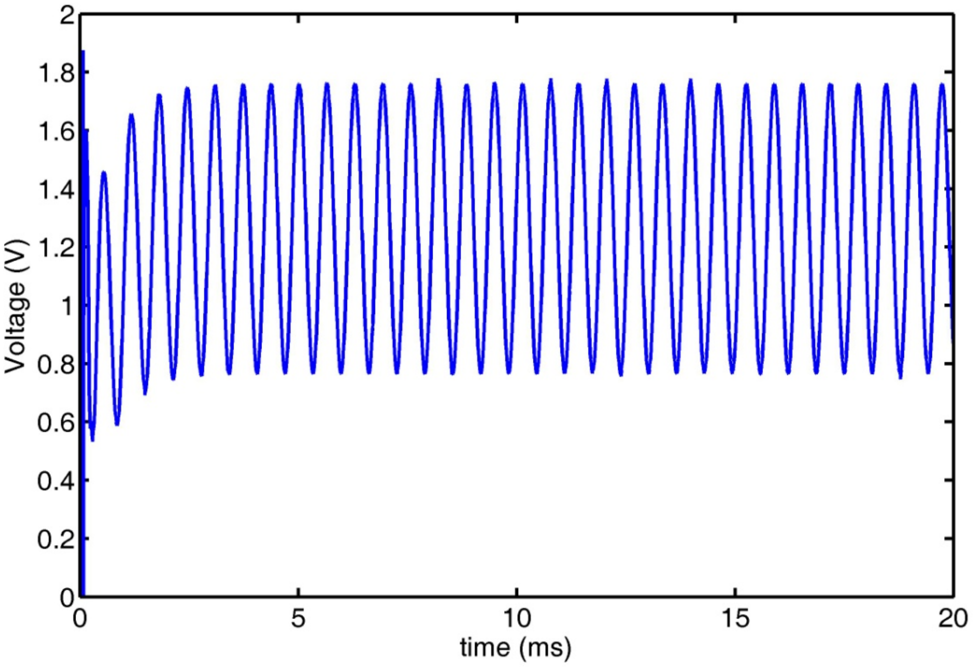

Figure 6-1 Plot of the transient voltage response sampled by the ADC of the impedance measurement circuit, when measuring a 500 Ω resistor using a 1 kΩ gain resistor.

As shown in the figure, the analogue circuit takes about 5ms to produce a stable sine wave. Therefore, a pessimistic estimate shows that the signal setup time is 20 ms.

The sampling time for sine wave fitting should be an integral multiple of the period of the 1.5625 kHz signal. Furthermore, coupling noise will be induced by any 50 Hz AC sources present in laboratory or calibration setups. Setting the fitting time as an integer multiple of 20 ms (which is the period of the 50 Hz power supply) reduces the coupling noise. Hence, the measurement time is set to 80 ms, which is 125 times the 1.5625 kHz signal period, and 4 times the 50 Hz signal period.

6.1.2 Power consumption

The circuit was powered by a PP3 battery. With this 9 V power supply, it consumes 9.2 mA when measuring, and 200 µA when quiescent. The battery life time can be calculated from these measurements and the measured time interval.

Because the measurement time is set to 100 ms (20 ms + 80 ms), assuming there are 4 channels to be measured each time, the system takes 400 ms for a complete CT measurement. The relation between battery life (9 V/600 mAh PP3 battery) and the measurement time interval is calculated and shown in figure 6-2:

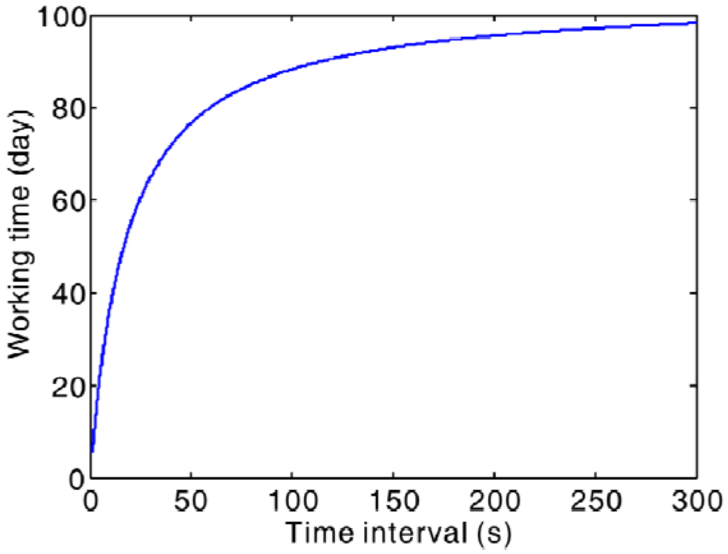

Figure 6-2 Plot of the battery life of the CT sensor system versus measurement time interval.

A system with a longer measurement interval has a lower duty cycle, and consumes less average current. Therefore, as shown in figure 6-2, the battery life increases with measurement time interval; the maximum battery life is about 100 days. This increases quickly when the interval is smaller than 50 s, because the battery life is governed by the 9.2 mA measuring current in this stage. However, the battery life increases slowly when the interval is bigger than 50 s. This is because when the duty cycle is already very small, and the battery life is determined by the quiescent current. Reducing the measuring current at this stage does not affect the battery life very much.

The calculated battery life is 35 days for a 10 s interval. An experiment was carried out to verify this calculation. The system worked for 30 days with 10 s sampling interval; the battery voltage dropped from 9.2 V to 7.6 V, which shows that the battery life calculation is correct within the accuracy of the datasheet and measurement data.

6.1.3 Measurement accuracy

Four resistors and one capacitor were used to test the measurement accuracy without the use of calibrating resistors (following equation 5-1). The factor resistor (resistor R_{in} as described in chapter 5) was set to 500 Ω, which sets the impedance measurement range to 100~600 Ω.

The 4 resistors varied from 100 Ω to 560 Ω. First the resistors were measured with a multimeter with 0.1 Ω resolution to provide reference values. Then every resistor was measured by the impedance measurement circuit more than 100 times. The error in the impedance measurement circuit is determined from the difference between the measured values and the reference values from the multimeter, figure 6-3.

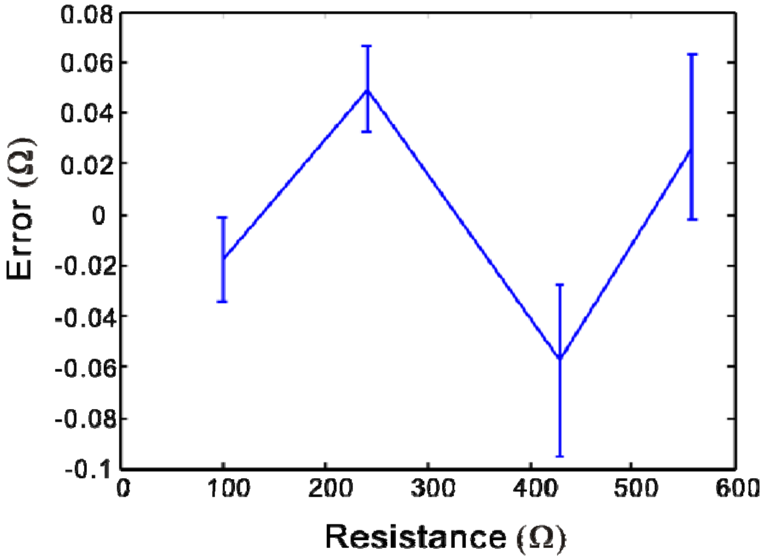

Figure 6-3 Plot of the measurement error of the impedance measurement circuit for four resistors, X-axis is the resistor value read from a multimeter, curve shows the average error (i.e. the difference between the value measured with a multimeter (accuracy 0.1 Ω) and the mean of 100 measurements made with the impedance circuit), and error bar shows the distribution (range) of this difference.

The standard deviation of the amplitude is 0.01 Ω (0.002% of the full measurement range, SNR = 92 DB), and the standard deviation of phase is about 0.02°. As shown in figure 6-3, the biggest error is less than 0.1 Ω, which is even smaller than the resolution of the multi-meter. It is probable that the measurement bias shown in the figure comes from the measurement error in the multi-meter. Each error bar shows the distribution of 100 measurement results for one resistor. The largest distribution is about 0.07 Ω for the 420 Ω resistor. This distribution is probably due to temperature drift.

A capacitor of nominal value of 680 nF with 10% tolerance was also tested. The measured value was 718.3 nF, with a phase of 89.68 °, which is very close to the expected value of 90°. This proves that the impedance measurement circuit can support full impedance measurement.

Calibration resistors are used to remove the temperature drift, following equation 5-2. To test the system accuracy with calibration resistors, two calibration resistors with 0.6 ppm/°C temperature coefficient were measured alternately. The voltage response from the two resistors is shown in figure 6-4:

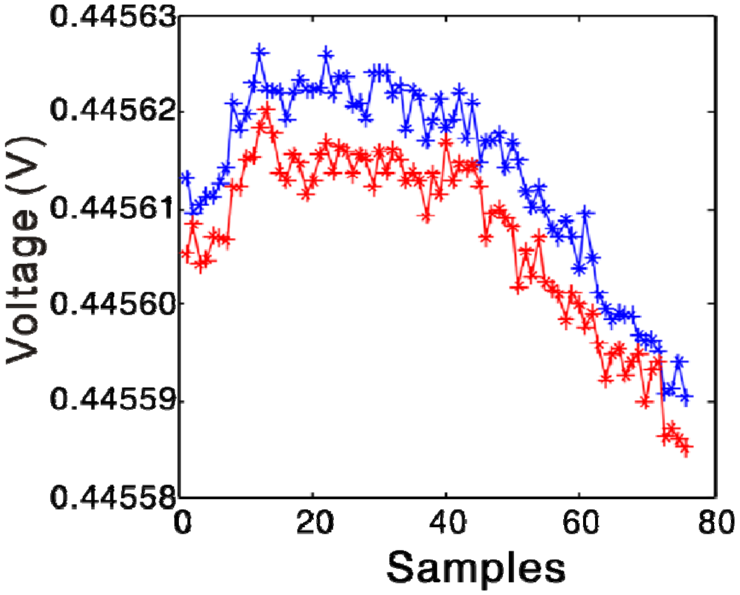

Figure 6-4 Plot of voltage responses from two calibration resistors, when the temperature of the analogue circuit was changed by touching the PCB.

The gain resistors in the trans-impedance amplifier have temperature coefficients of 20 ppm/°C, which translates into a 0.002% measurement error per degree. Figure 6-4, show the measured voltage response from each calibration resistor for a 3 °C temperature change giving a deviation of about 0.005% (86 dB SNR), which is close to the 0.006% estimated value. However the ratio of the two voltage responses had a lower deviation of 0.001% (100 dB in SNR). This means that if we use equation 5-1 for impedance calculation, the temperature drift is 0.005%. However, with calibration resistors and equation 5-2, measurement noise is reduced to 0.001%, and most of this noise comes from the 0.002% quantization noise, rather than the 0.00018% (0.6 ppm/°C x 3 °C) temperature drift in the calibration resistor.

The temperature in the ocean has a span of about 30 °C, and we can expect that the temperature drift using equation 5-1 will increase to 0.05%, if the temperature change covers this range. However, with a temperature coefficient of 0.6 ppm/°C, the calibration resistors only change by 0.002% over this 30 °C temperature range. Therefore the temperature drift is reduced to 0.002% by using equation 5-2.

The quantization noise of the 16-bit ADC/DAC is about 0.002% of full scale, which is the limit on the system accuracy. Although this noise can also be improved by averaging, this is not as efficient as for other noise sources [143]. With 80 ms sampling time (average of 8,000 samples) and a calibration resistor, the measurement has a 0.001% noise. Therefore, this measurement is already greater than the limit accuracy, and the system accuracy should be considered as 0.002% rather than 0.001% (imaging a 1-bit system, 0 for 0 V, 1 for 1 V. A 0.49 V DC signal with no noise will always be sampled as 0 V, with a noise of 0 V, however the measurement accuracy is still 0.5 V). With this 0.002% accuracy, the impedance measurement circuit can support 1 μS/cm accuracy for conductivities in the range 10~70 mS/cm, and 0.6 m^{o}C accuracy for temperature in the range -2~30 ^{o}C. Of course, the final accuracy of the CT measurement also depends on the sensor design.

6.2 Calibration and deployment of the CT sensors in design 1

The CT sensors in design 1 include the seven-electrode conductivity cell with a 2x2 mm water channel (on chip 1-A), four-electrode open conductivity cell (on chip 1-B), and a PRT-bridge temperature sensor (on both chip 1-A and 1-B). Several calibrations were carried out to evaluate the performance of these sensors. Figure 6-5 shows the sensor system using chip 1-A:

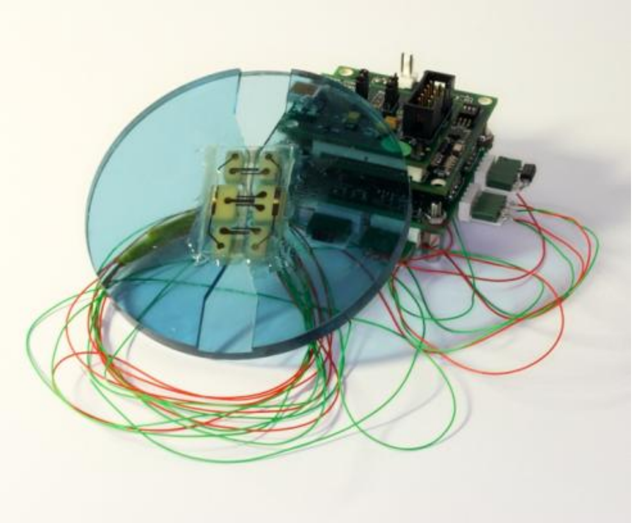

Figure 6-5 A photograph of the unpackaged CT sensor system using chip 1-A as the CT sensor.

6.2.1 PRT-bridge temperature sensor calibration

The PRT-bridge temperature sensor was calibrated using a FLUKE Hart 7012 calibration bath [144]. This provides a fixed temperature with a stability of ±0.0008 °C and uniformity of ±0.002 °C at 25 °C. The water inside the bath is mixed rapidly by propellers, providing a stable temperature and large flow rate. The temperature was changed from 4 ^{o}C to 29 ^{o}C in 5^{o}C increments, and 100 repeat measurements were taken with 10 s intervals. This calibration procedure was run three times. The interval between each calibration was 24 hours, and the sensor was always kept immersed in water between calibrations. A Sea-Bird SBE-35 temperature probe [145] was used to provide a reference temperature with an accuracy of ±0.001 ^{o}C.

The relationship between the reference temperature and the PRT-bridge voltage was fitted to a 3rd order polynomial using the data from the third calibration run. The PRT-bridge voltages were converted into temperature data using this polynomial. The difference between reference temperature and PRT-bridge temperature reading is the measurement error, and is plotted in figure 6-6:

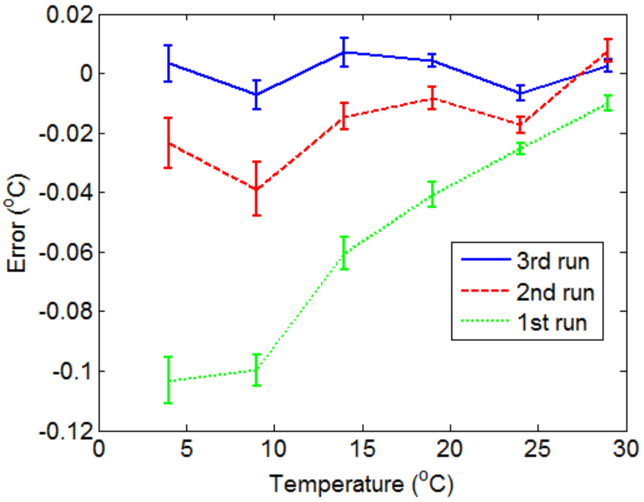

Figure 6-6 Plot of the measurement error of PRT-bridge temperature sensor, with error bar showing the standard deviation of the 100 repeated measurements on each temperature point.

The error bar is the standard deviation of 100 repeat measurements at each temperature. As shown the maximum standard deviation of the error for the 3rd run is ±0.004 ^{o}C. This sets the limit on the resolution of the temperature sensor. The mean error for all temperatures was ±0.005 ^{o}C, hence the error (for the 3rd run) for a spot measurement compared with the Sea-Bird probe is ±0.01^{o}C. The drift observed during the first two runs leads to a maximum error of about 0.1 ^{o}C (at low temperatures). However, compared with the third run, drifts are seen in the first and second runs, especially for the low temperature part giving an error of more than 0.1 ^{o}C.

This drift is probably due to water absorption into the SY320 insulating material and epoxy glue used to package the chip. Uptake of water causes expansion of the insulator and reduces its resistance. The expansion also induces a small strain gauge effect which changes the resistance of the PRT, causing drift. During calibration the sensor was continuously immersed. Because the water was absorbed in the first 24 hours, the drift was greatest between the first and second run. It is assumed that the rate of absorption reached a plateau after the second run. The sensor chip was bonded at room temperature of about 25 °C. Therefore any strain gauge effect is induced by thermal expansion when the temperature deviates from 25°C. As water absorption changes the expansion coefficient of SY320 and the epoxy glue, a larger temperature drift is seen in figure 6-6 when the temperature is lower than 25 °C.

6.2.2 Thermistor calibration

Because the PRT-bridge temperature is affected by water absorption into the SY320 laminate, a thermistor temperature sensor (EPCON NTC thermistor B57863S0302+040 [146]) was used as a replacement. The calibration result for this thermistor is shown in figure 6-7:

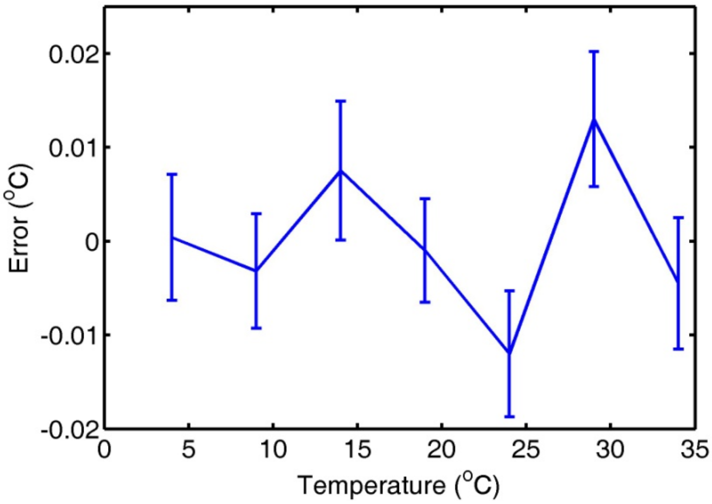

Figure 6-7 Plot of the thermistor calibration results, where the curve shows the average bias errors, and the error bar shows the standard deviation errors.

This thermistor has a bigger measurement error (about ±0.02 °C) than a PRT-bridge. However it is a commercial temperature sensor with reliability proved by tests in several harsh conditions. In version 1 CT system, there was concern about the reliability of the PRT-bridge temperature sensor when covered with SY320 laminate. Therefore this thermistor was used to replace the PRT-bridge.

6.2.3 *Temperature response time test*

A temperature sensor in the FLUKE Hart 7012 calibration bath has a very fast response time as there is very rapid water flow in the bath. However, if water flow is slow, the response time will become an issue as introduced in chapter 4.

A thermistor is physically separated from the conductivity cell, and can be placed at different distances from the package to evaluate the time response. Figure 6-8 shows the sensor system in a Ø10x15 cm (diameter x height) cylinder:

Figure 6-8 A photograph of the version 1 CT system with a Ø10x15 cm cylinder package.

In order to provide a constant temperature environment with slow water flow, another precision water bath was used (Grant GD100 [147]). This bath pumps water constantly and slowly through the sensor, and maintains water temperature within ±0.02 °C stability. The temperature of the seawater was changed stepwise from 4 °C to 34 °C in 5 °C increments. A temperature probe (ASL F250 MKII Precision Thermometer [148]) with ±0.002 °C accuracy was used to provide the reference temperature at 10 s sample intervals. Each temperature was held for 1 hour.

Two designs were tried: one with the thermistor set on top of the cylinder package, and another with the thermistor set 3 mm higher. Figure 6-9 shows the recorded temperature:

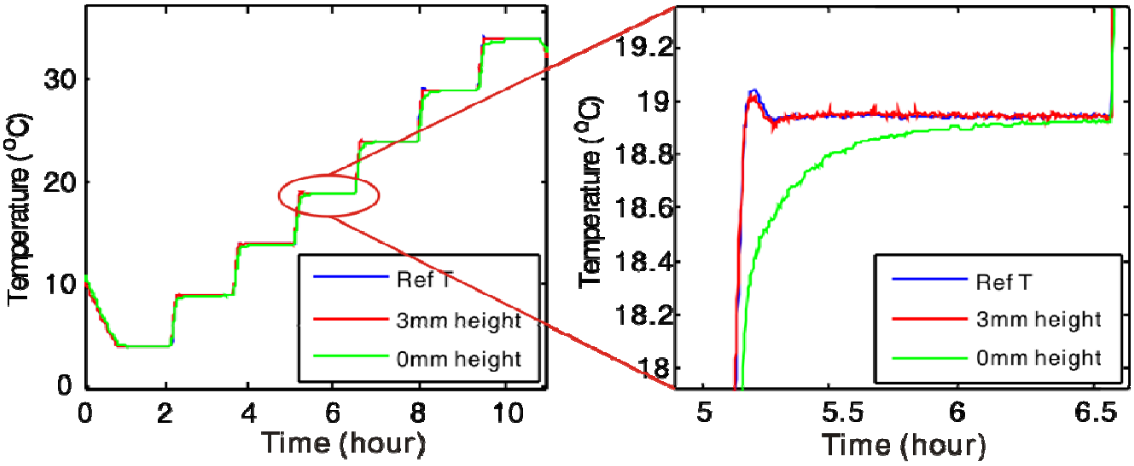

Figure 6-9 Plot of the temperature data from the thermistors with heights of 0 mm and 3 mm, response time is estimated by comparing the temperature data from the thermistors and the reference temperature probe.

The thermistor set on the top took about 0.5 hour to achieve a measurement accuracy of 0.1 °C. However, by moving the thermistor 3 mm higher, the response time is much improved. As figure 6-9 shows, the response of the thermistor set 3 mm away follows the reference temperature, and the response time is estimated to be less than the 10 second measurement interval.

6.2.4 Conductivity sensor calibrations

The FLUKE Hart 7012 calibration bath produces many bubbles from the propellers, and cannot be use to calibrate the conductivity sensor. Therefore both the seven-electrode conductivity cell with channel (chip 1-A) and the four-electrode open conductivity cell (chip 1-B) were calibrated using the same temperature bath, as for the response time test. The Grant temperature bath was filled with seawater at a salinity of 30 psu. The salinity of this water was measured using a salinometer (Guildline 8410A Portasal [149]) with an accuracy of ±0.003 psu.

The temperature of the seawater was changed stepwise from 4 °C to 34 °C in 5 °C increments, and each temperature step took 1 hour. Spot calibration was performed to determine the relationship between the measured cell conductance and the water conductivity for 7 different temperatures, following the formula given in [10]. The conductivity of the seawater was calculated at each temperature based on the measured salinity of the sea water. At each temperature, a total of 360 conductance ($1/R_s$) measurements were taken (over one hour), and the last 100 values were averaged to give the mean cell conductance at this temperature. The relationship between measured conductance and calculated seawater conductivity gives the cell constant κ of the sensor. Normally κ is constant, independent of the measured conductivity. However, in order to improve the accuracy of the sensor (for example, due to small non-linearity in the circuits), κ was calculated from a 3rd order polynomial fit between measured conductance and seawater conductivity. The calibration results are shown in figure 6-10:

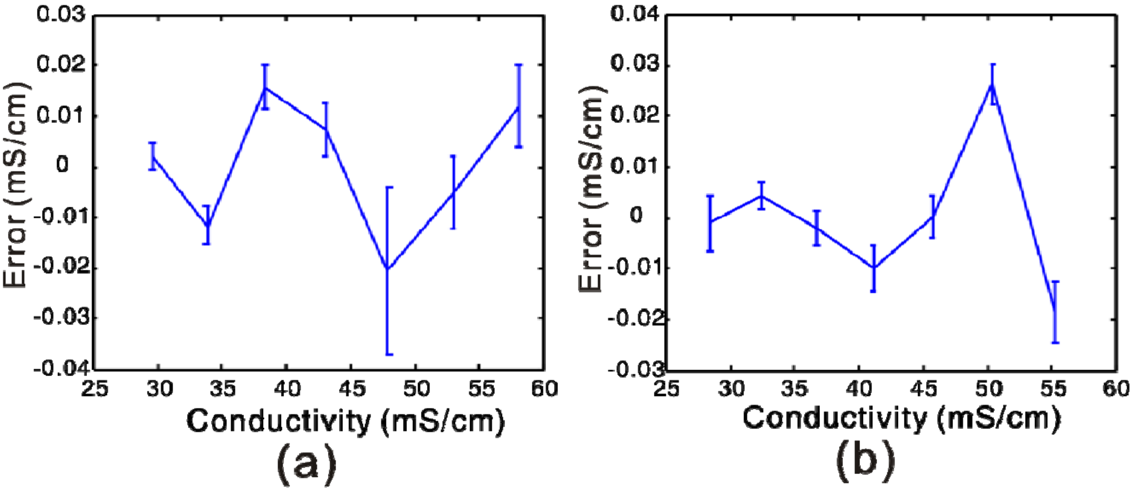

Figure 6-10 Plot of the conductivity sensor calibration results, where the curves show the average bias errors, and the error bars show the standard deviation errors: (a) four-electrode open cell; (b) seven-electrode cell with channel.

Both the four-electrode open cell and the seven-electrode cell have similar measurement errors of about ±0.03 mS/cm. However the seven-electrode cell has a slightly smaller standard deviation of about ±0.005 mS/cm, which can be considered the resolution of the system.

The seven-electrode conductivity cell is expected to have no proximity effects. To experimentally determine the proximity effects, conductivity measurements were taken both with and without a conducting metal rod placed close (1 mm or less) to the seven-electrode conductivity cell. The position of this rod was varied, and made no difference to the measurements; the difference between the two measurements was less than the ±0.03 mS/cm precision. The effect of an insulating object was evaluated by placing the sensor in air with the channel full of seawater. Again the reading was unaffected, within the precision of measurement.

6.2.5 Repeatability testing of the conductivity sensor

To test the stability and repeatability of the conductivity sensor, the seven-electrode cell was spot calibrated in the Grant temperature bath with three seawater samples. The calibration results are shown in figure 6-11:

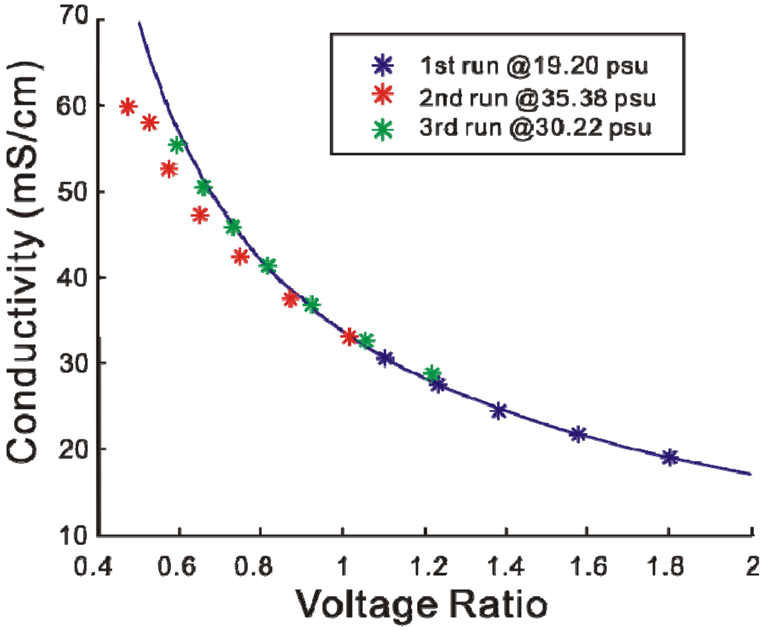

Figure 6-11 Plot of the calibration results of the seven-electrode cell with channel (chip 1-A) in three seawater samples.

The fitted curve is based on the data from the first calibration. The second calibration was affected by an air bubble inside the water channel, so that the measured conductivity (fitting curve) deviates from the actual value, especially for data at higher temperature, which makes the air bubble bigger. However the data for the third calibration still differs from the first calibration, with an average difference (measurement error) of about 1 mS/cm. This error is due to water absorption by the SY320 laminate, which changes the geometry of the water channel. In addition, the Araldite 2020 epoxy [150], which was used to glue the sensor chip and plastic water channel, also absorbs water.

Testing was also carried out on the four-electrode open cell. It was tested with two seawater samples in the temperature bath, and the results are shown in figure 6-12:

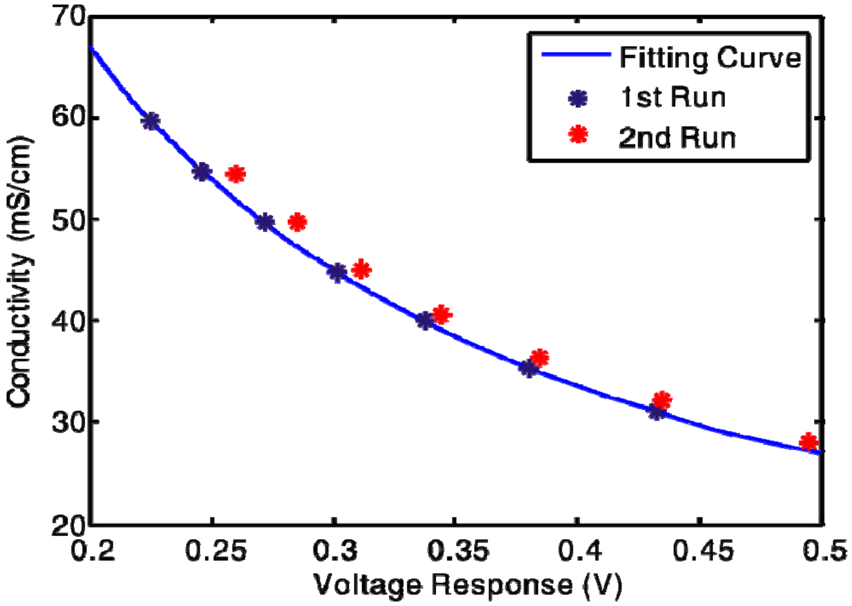

Figure 6-12 Plot of the four-electrode open cell (chip 1-B) calibration results in two seawater samples.

The four-electrode open cell has a bigger drift of about 2 mS/cm. This is also because of the water absorption into the SY320 laminate, which cover the middle of the electrodes. The laminate expanded and became uneven after immersion in water for 48 hours, so that drift occurred.

6.2.6 Deployment of version 1 CT system

Eight version 1 CT sensor systems with the seven-electrode cell on chip 1-A and a thermistor (figure 6-8), were tested on an Atlantic cruise from 4th Jan, 2010 to 19th Feb, 2010 in the North Atlantic (24.5N, -62.55W). The systems were packaged into Ø10x15 cm pressure pots, shown in figure 6-8, and deployed from a floating buoy. The depth of a particular sensor was adjusted by configuring the length of rope. Figure 6-13 shows photographs of the deployment, and figure 6-14 shows temperature (*T*) and salinity (*S*) data collected by the sensor in 0.4 meter deep seawater:

Figure 6-13 Photographs of the deployment of the version 1 CT system in the Atlantic.

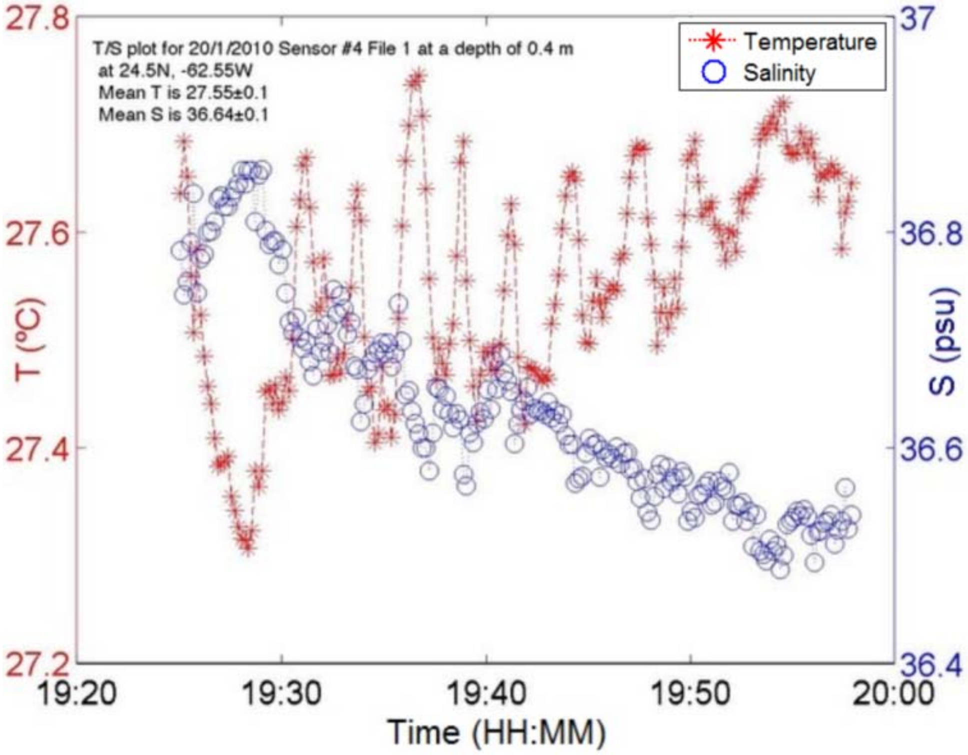

Figure 6-14 Plot of temperature and salinity data collected at 24.5N, -62.55W, at a depth of 0.4 m, with sampling interval of 10 s. Data shown is from a 40 minute deployment.

A typical deployment was one hour. During measurement, the sensor was held just below the surface of the water but was not immobile. Owing to wave action the water depth changed periodically. As water temperature varies with depth, this periodic change is reflected in the temperature profiles seen in figure 6-14. In this example the average temperature showed a gradual increase with time whilst the salinity showed the opposite trend.

The salinity measured by the CT sensor varied from 36.5 to 36.8 psu. As a reference, a water sample was taken close to the sensor, and measured by a handheld commercial CT probe (YSI Model 30 [151]) with ±0.1 psu accuracy. The reference reading obtained was 36.6 psu, which is within the range measured by the sensor.

The CT sensor was used periodically during the first 5 weeks of the cruise without losing calibration. It slowly drifted by about 3 psu over weeks 5 to 7. Re-calibration was performed after the cruise, and the data is present in figure 6-15. It indicated that the conductivity cell constant changed by 8%. Also the response of the conductivity sensor became unstable, with standard deviation error increasing from ±0.03 mS/cm to ±0.5 mS/cm as shown in figure 6-16. Again, we presume that this was due to water absorption into the epoxy laminate and glue that was used as an insulator and packaging. Examination of the sensor after deployment showed that some of the epoxy glue had detached from the channel. This caused errors due to a change in the geometry of the sensor cell. Re-calibration also indicated that the thermistor temperature sensor had drifted by 0.1 ^oC, with standard deviation unchanged. This drift is presumably due to water absorption into the insulating material, reducing its resistance.

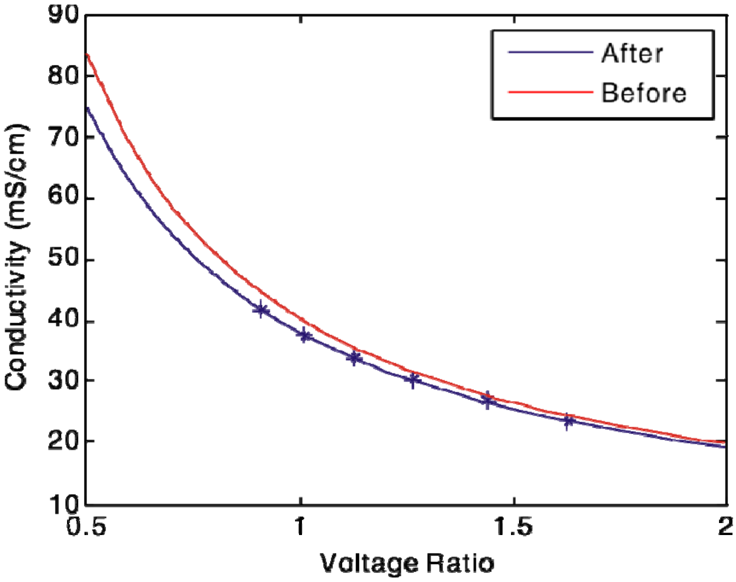

Figure 6-15 Plot of the conductivity calibration results of a version 1 CT system, before and after the Atlantic cruise.

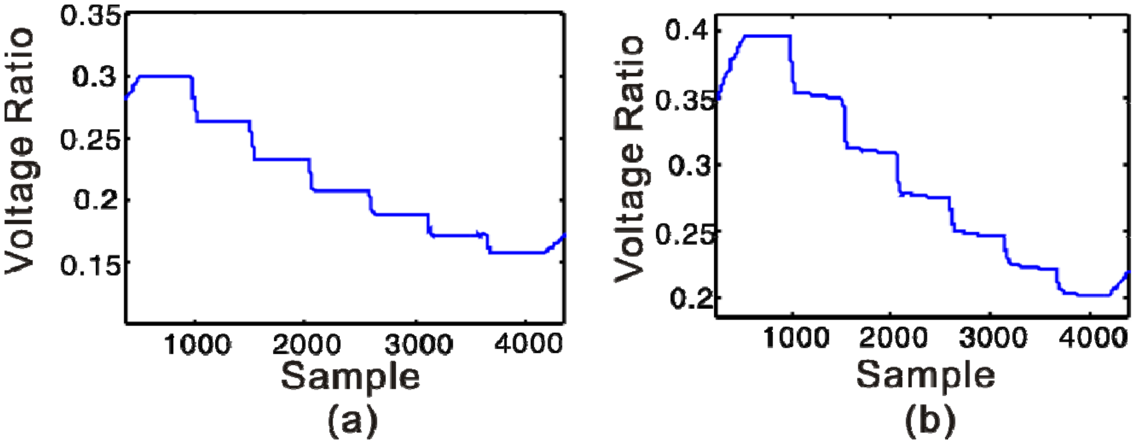

Figure 6-16 Plots of the conductivity sensor voltage of a version 1 CT system during the calibrations: (a) before the Atlantic cruise; (b) after the Atlantic cruise.

6.3 Calibration and deployment of the CT sensors in design 2

The CT sensor in design 1 has good initial accuracy of ±0.03 mS/cm over the range 25~55 mS/cm, and ±0.01 ^{o}C over the range 4~34 ^{o}C. However, the repeatability and stability is poor due to water absorption into the SY320 laminate and poor durability of the Araldite 2020 epoxy glue.

Design 2 aimed to solve the repeatability and stability problem. It includes a four-ring-electrode open cell conductivity sensor (chip 2-A) and a PRT-bridge temperature sensor (chip 2-B). As introduced in chapter 4, a 300 nm thick silicon nitride layer and 25 μm thick SU8 were used to replace the SY320 laminate. The Epo-Tek 302-3M epoxy glue [152] is used to replace the Araldite 2020 for a better durability. A silane pre-treatment technique [153] using (3-glycidoxypropyl) trimethoxysilane [154] was used to improve the adhesion between the glass chip and epoxy glue. Furthermore, the open channel design of the conductivity sensor is less dependent on the durability of the epoxy glue.

Figure 6-17 shows version 2 CT system in the Ø10x15 cm package, with the CT sensor of design 2 placed horizontally:

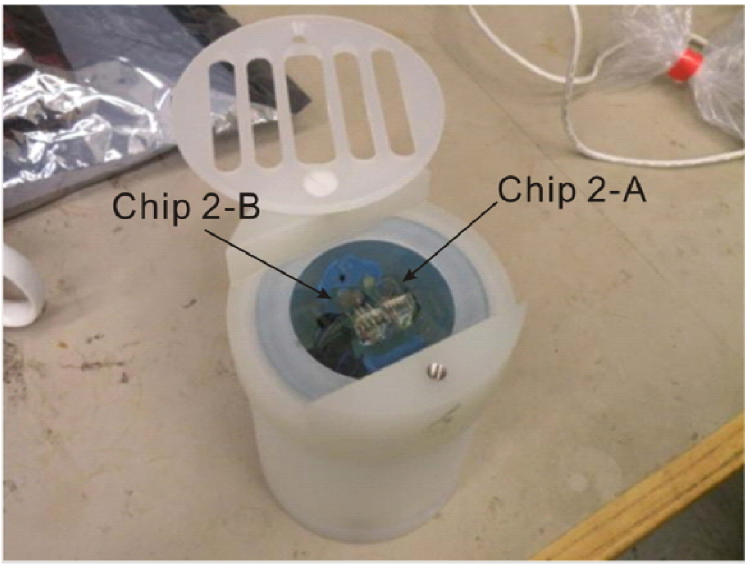

Figure 6-17 Photograph of a version 2 CT system in the Ø10X15cm package, where the chip 2-A and chip 2-B are placed horizontally on the top of the package.

6.3.1 CT sensor calibration

Chips 2-A and 2-B were calibrated together three times in the Grant temperature bath. The salinity of the seawater was set to around 30 psu. Water samples were taken before and after each calibration for salinity measurement, and the measured salinity was used to calculate the conductivity at each temperature step.

Again the temperature was changed from 4 to 34 ^{o}C, in 5 ^{o}C increments. The last 100 measured values at each temperature step were averaged to give the mean cell conductance at this temperature. A 3rd order polynomial was used to fit the spot calibrations. Figure 6-18 shows calibration result for the conductivity sensor on chip 2-A, and figure 6-19 shows the calibration result for the temperature sensor on chip 2-B.

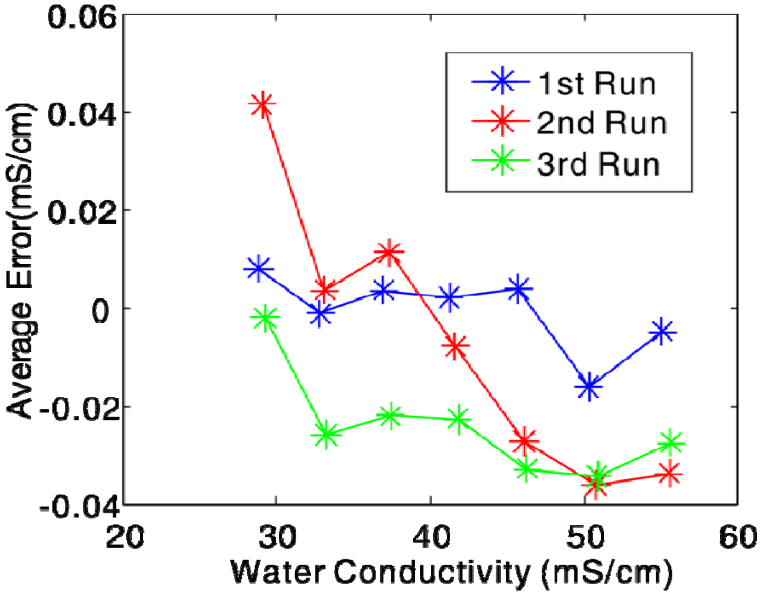

Figure 6-18 Plot of calibration results for the four-ring-electrode open conductivity sensor on chip 2-A. The sensor was placed in 30 psu seawater, with temperature changed from 4 to 34 °C in 5 °C increments for each calibration. The calibration was performed for three times.

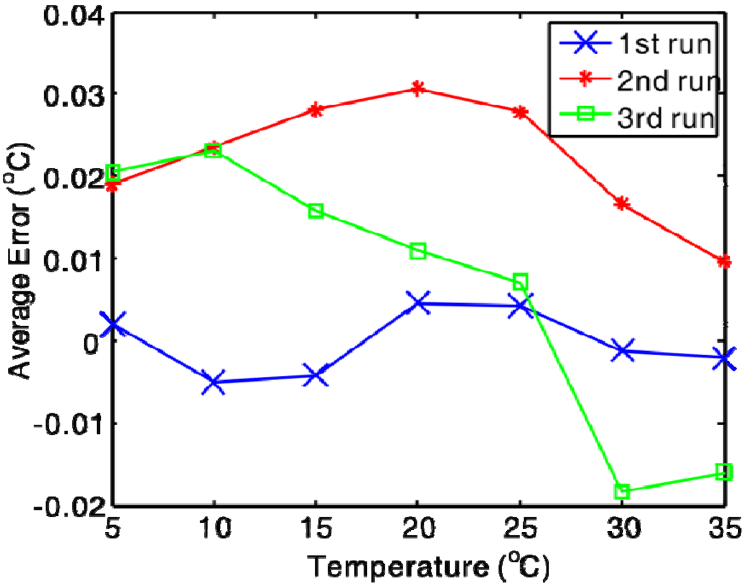

Figure 6-19 Plot of calibration results for the PRT-bridge temperature sensor on chip 2-B. The surrounding water temperature was changed from 4 to 34 °C in 5 °C increments for each calibration. The calibration was performed for three times.

The standard deviations of the CT sensors in design 2 are ±0.003 °C and ±0.003 mS/cm respectively, which is similar to the sensors in design 1. However, the initial accuracy and repeatability error is much improved.

As shown in figure 6-18, the initial conductivity accuracy of chip 2-A in design 2 sensor improves to ±0.02 mS/cm (1st run). The repeatability error also improves to

±0.04 mS/cm, which is much better than the 1 mS/cm repeatability error of the seven-electrode channel sensor (chip 1-A in design 1). The repeatability error might be due to water absorption of the epoxy glue or the SU8 laminate. However the errors in 2nd and 3rd run did not show a trend that looks like a gradual drift. Another reason for this repeatability error is water evaporation, which changes the salinity of the seawater. As seawater samples are only taken before and after each calibration, the salinity during each temperature step can only be determined by estimation using the salinities from the two seawater samples. The two samples normally have a salinity difference of about 0.1 psu, which may cause a maximum estimated error of 0.1 mS/cm in conductivity, inducing the repeatability error.

The PRT-bridge temperature sensor on chip 2-B has an initial accuracy of ±0.01 ^{o}C, as shown in the 1st run of figure 6-19. The three repeat calibrations show a repeatability error of ±0.03 ^{o}C. This is a big improvement compared with the 0.1 ^{o}C repeatability error for design 1. This improvement can be attributed to less water absorption of the SU8 laminate, and the silicon nitride layer which removes error caused by the resistance change in the SU8 laminate.

6.3.2 Proximity effects of conductivity sensor

Experiments were carried out to test the proximity effect of the four-ring-electrode open conductivity sensor on chip 2-A. In this experiment, the CT sensor was placed in the Grant temperature bath, with a fixed water temperature of 20 ^{o}C. The salinity of the seawater inside the bath was 30 psu. A plastic pen of 6 mm diameter was used as an insulating object. One end of the pen was placed 1 mm above the surface of the glass chip, and the pen was moved horizontally. The distance between the end of the pen and the centre of the ring electrode was recorded. The proximity effects can be estimated by comparing the change in the measured conductivity for different distances. Figure 6-20 shows a photography of this experiment, where the pen is placed on the edge of the conductivity chip (5 mm away from the centre):

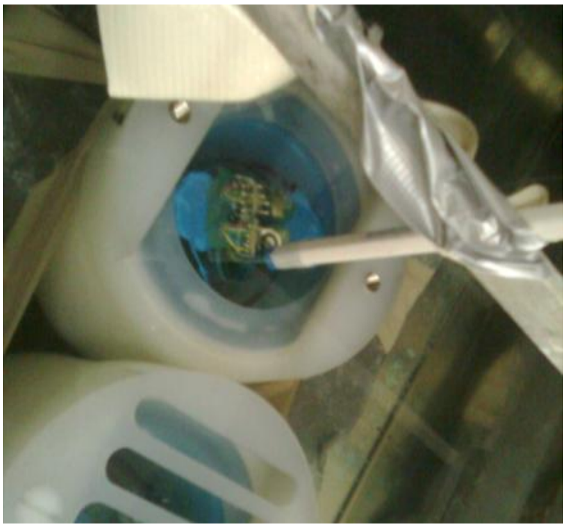

Figure 6-20 A photograph of the experiment setup for the proximity effect test of chip 2-A, where plastic pen is place 5 mm away from the centre of the ring-electrode.

Experiments show that when the plastic pen is on top of the centre of the ring electrode, the measured conductivity reduces by 2.5%. This reduces to 0.6% when the distance increases to 3 mm (horizontally), and disappears when the distance is 7 mm.

An aluminium probe was used as a conducing object. However, instead of increasing, it also reduces the measured conductivity by the same amount as the plastic pen. The reason is that the surface of the aluminium probe is oxidised, making it appear as an insulating object to the conductivity sensor.

Proximity effects were also tested by moving the plastic pen vertically; results show that the proximity effects disappears when the pen is 7 mm away from the surface of the glass chip.

6.3.3 Dock deployment of version 2 CT sensor system

In order to test durability in a real environment, a version 2 CT sensor system with the Ø10x15 cm package was deployed in Southampton docks for 6 weeks. The system was fixed to a float to give a fixed deployment depth of about 20 cm. The measured temperature and salinity data of the first two weeks deployment is shown in figure 6-21:

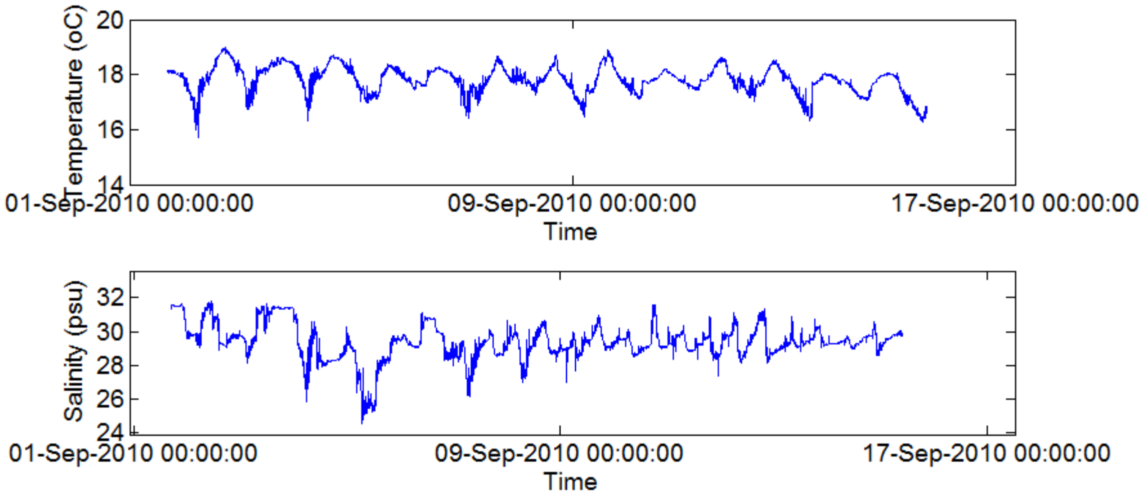

Figure 6-21 Plot of temperature and salinity data from the version 2 CT system during the first two weeks dock deployment.

We can see that the water temperature has a daily periodic change, with an average value of about 17.5 ^{o}C. The salinity of the dock water is around 30 psu. However the salinity varies from 25 to 32 psu, with a period of about 12 hours. This periodic change in salinity is caused by the tide. Figure 6-22 compares the measured salinity from the CT sensor and the recorded water depth:

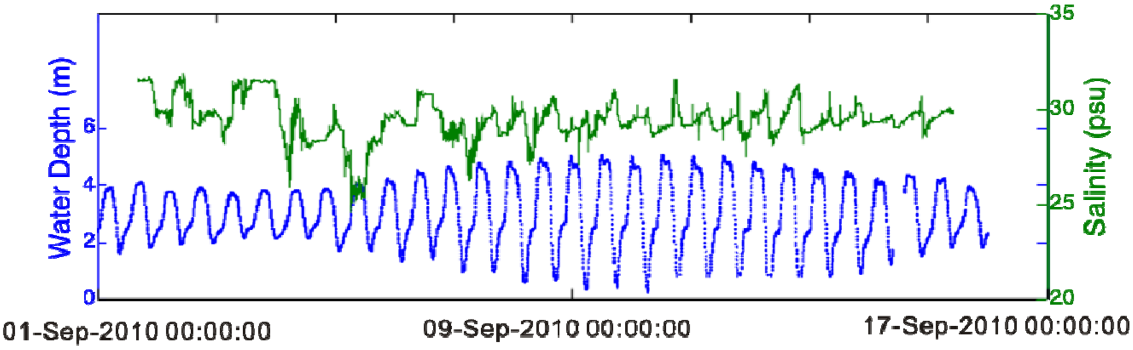

Figure 6-22 Plot of salinity data from the version 2 CT system and recorded water depth during the first two weeks dock deployment.

The tide in Southampton has a period of about 12 hours. A river is beside the dock. When there is an ebb tide, the fresh water in the river comes into the dock. The fresh water is on top of the dock water, reducing the salinity around the CT sensor to about 28 psu. When there is a flood tide, the unmixed fresh water goes back to the river, and deeper dock water with higher salinity comes to the top. Therefore the salinity around the CT sensor rises up to about 32 psu.

Figure 6-23 A photograph of the version 2 CT system after first two weeks dock deployment.

The CT sensor had heavy bio-fouling after the first two weeks of deployment - figure 6-23. However, as figure 6-21 shows, the salinity data was not significantly affected by this bio-fouling. The CT sensor was cleaned after the first two weeks deployment, and then deployed again. A commercial CTD probe (Idronaut Ocean Seven 320+ [155]) with ±0.001 mS/cm and ±0.001 ^{o}C CT accuracies was deployed close to the CT sensor to verify the performance. Figure 6-24 shows the recorded temperature data, while figure 6-25 shows the salinity data.

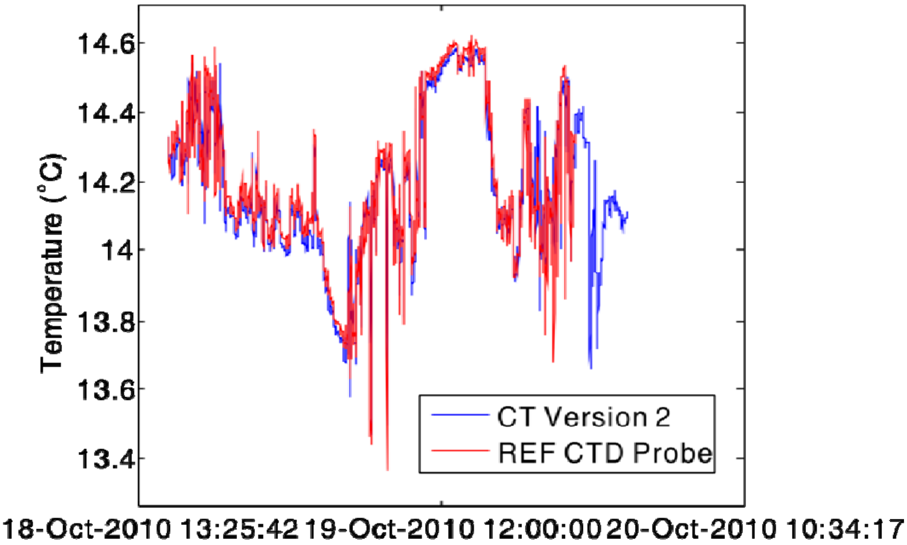

Figure 6-24 Plot of the temperature data sampled from the version 2 CT system (blue curve) and the Idronaut CTD probe (red curve) in a dock deployment.

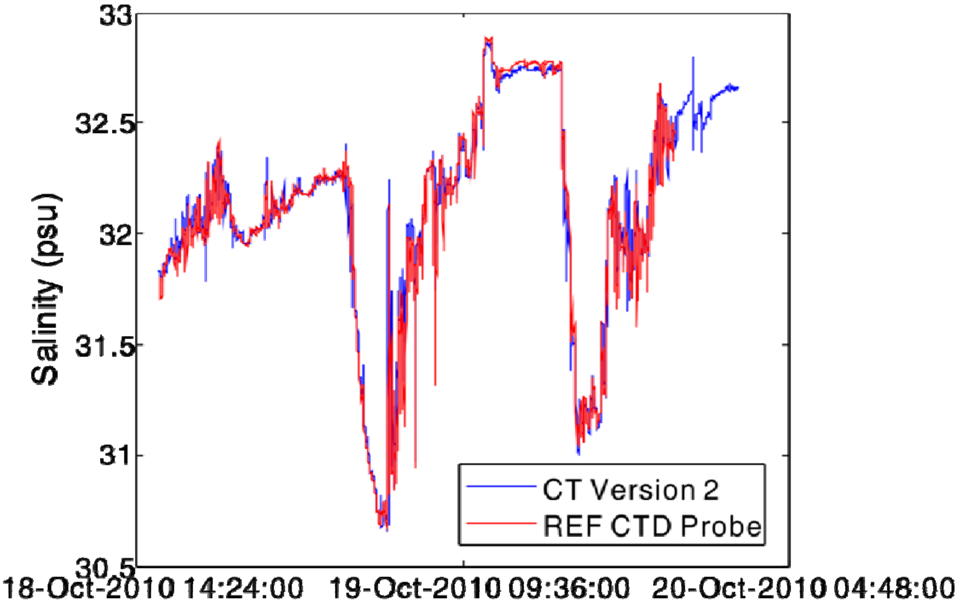

Figure 6-25 Plot of the salinity data sampled from the version 2 CT sensor system (blue curve) and the Idronaut CTD probe (red curve) in a dock deployment.

As shown in figure 6-24 and 6-25, the data from the version 2 CT system and the reference CTD probe are in excellent agreement, with a maximum difference of 0.03 °C for temperature, and 0.03 psu for salinity. These differences are within the repeatability accuracy, and may be caused by the non-uniform temperature and salinity distributions in the dock.

The CT sensor was kept in the dock for 6 weeks in total. Then another calibration was performed to determine the drift error. The conductivity sensor did not have any drift error bigger than the ±0.04 mS/cm repeatability error. However, the PRT-bridge temperature sensor drifted by 0.1 °C, probably due to water absorption in the SU8, causing a strain-gauge error in the temperature measurement.

6.4 Improvements in the CT sensors in design 2

6.4.1 Summary of existing problems

Experiments show that the CT sensors in design 2 have big improvements in accuracy, repeatability and stability, compared to that in design 1. However, the major problem is that the temperature still drifted by 0.1 °C during the dock deployment, due to the water absorption into the SU8, causing a strain gauge effect. In addition, the calibration method needs to be improved to support higher accuracy calibration, so that the drift of the conductivity sensor can be determined.

For temperature calibration, we discovered that the temperature in the water bath used for calibration was not uniform because the flow rate was not high enough. Therefore if the temperature sensor is too far away from the reference temperature probe, there will be a temperature difference causing a calibration error. For each calibration, this temperature difference may be different for different positions, leading to a repeatability error. Conductivity calibration is also affected by the non-uniform temperature profile in the water bath. Furthermore, water evaporation also causes problems in estimating water salinity, introducing a calibration error.

The Ø10x15 cm package has a big thermal mass, causing temperature around the package to be different from the environment temperature, and slows the sensor response time. Furthermore, if the temperature around the temperature sensor and conductivity sensor are different, error will be induced in salinity calculation by this difference. To reduce this effect and achieve the maximum performance of the CT sensor, chips 2-A and 2-B were packaged as probes as shown in figure 6-26:

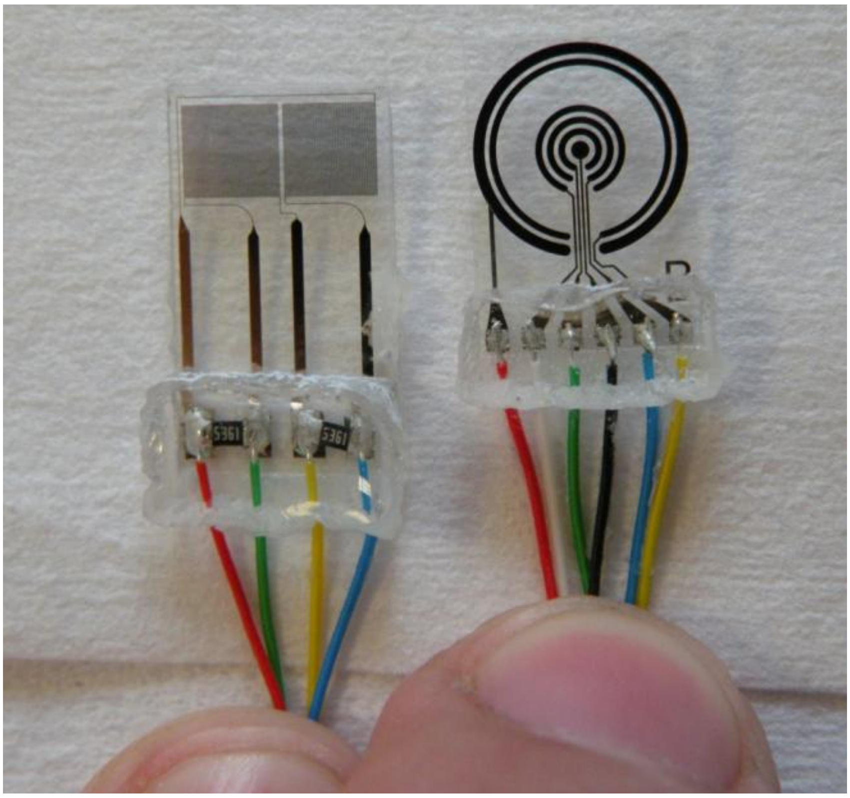

Figure 6-26 Photograph of the CT sensor probe, where the temperature sensor probe (chip 2-B) is on the left, and conductivity sensor probe (chip 2-A) is on the right.

The CT sensor probe consists of the sensor chip, wires, and epoxy glue for potting the soldering pads. In the following experiments, only these probes are immersed into the water. Electronics are kept outside the bath, with wires connected to the probes. Because of the small thermal mass of the probe, we expected that these probes should have better accuracy, repeatability, and faster response time.

6.4.2 PRT-bridge temperature sensor probe coated with ECG-2702

The drift problem of the PRT-bridge temperature sensor on chip 2-B is due to the water absorption of the SU8. A metal sleeve was used to insulate the temperature sensor from contact with water to solve the drift problem. However this leads to a large response time (10 min for 0.1 °C accuracy). Figure 6-27 shows the CT sensor with an aluminium sleeve to cover the temperature sensor:

Figure 6-27 Photograph of a version 2 CT sensor system, where the conductivity sensor chip is placed vertically on the left, and temperature sensor chip is coated inside a aluminium sleeve on the right.

In order to insulate the SU8 from water, whilst keeping a good time response, the 3M ECG-2072 [156] coating material was used. This is a fluoro-polymer, which is anti-wetting, and protects the SU8 from contact with water. The temperature sensor probe was coated with this material to a thickness of about 20 µm, and tied to the reference temperature probe to reduce the error from the space between the two devices. The sensor was calibrated in the Grant temperature bath three times, with a cycle from 5 to 35 °C in 5 °C increments. The calibration result is shown in figure 6-28:

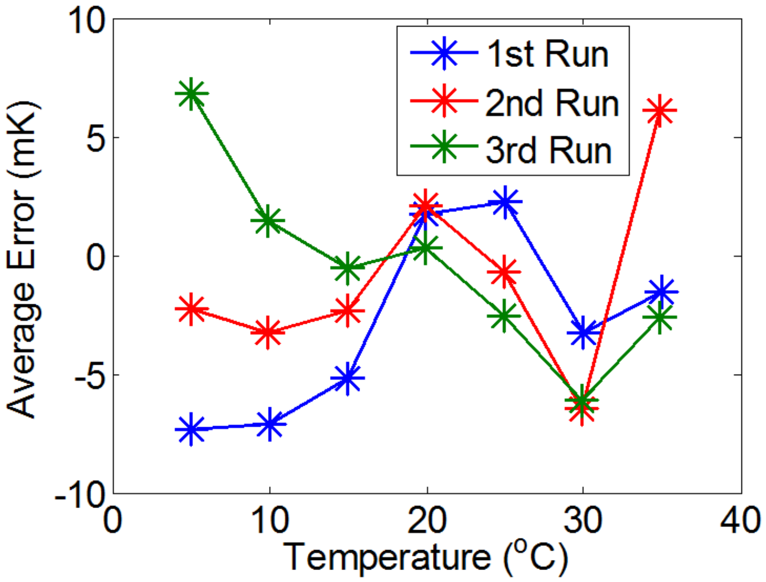

Figure 6-28 Calibration results for the temperature sensor probe of chip 2-B coated with ECG-2702. The surrounding water temperature was changed from 5 to 35 °C in 5 °C increments for each calibration. The calibration was performed for three times.

As shown in the figure, the ECG-2702 coating improves both the initial accuracy and repeatability error to ±0.008 °C. Furthermore, the smallest error of ±0.002 °C is found at 20 °C, which is close to room temperature; temperatures furthers from room temperature have highest repeatability error. This is because the reference temperature probe is part exposed out of the water. If the room temperature differs from the water temperature, the accuracy of the reference temperature will be affected and becomes worse than the declared accuracy (±0.002 °C). Therefore the ±0.008 °C repeatability error may not come from our temperature sensor, but from the reference temperature probe. Potentially the maximum accuracy of the temperature sensor may be achieved in a single run calibration.

Figure 6-29 shows the experimental result for a single run calibration, where 7 data points are fitted by a 3rd order polynomial with 4 unknown parameters. The maximum error of this fit is ±0.003 °C, which is the initial accuracy of the temperature sensor.

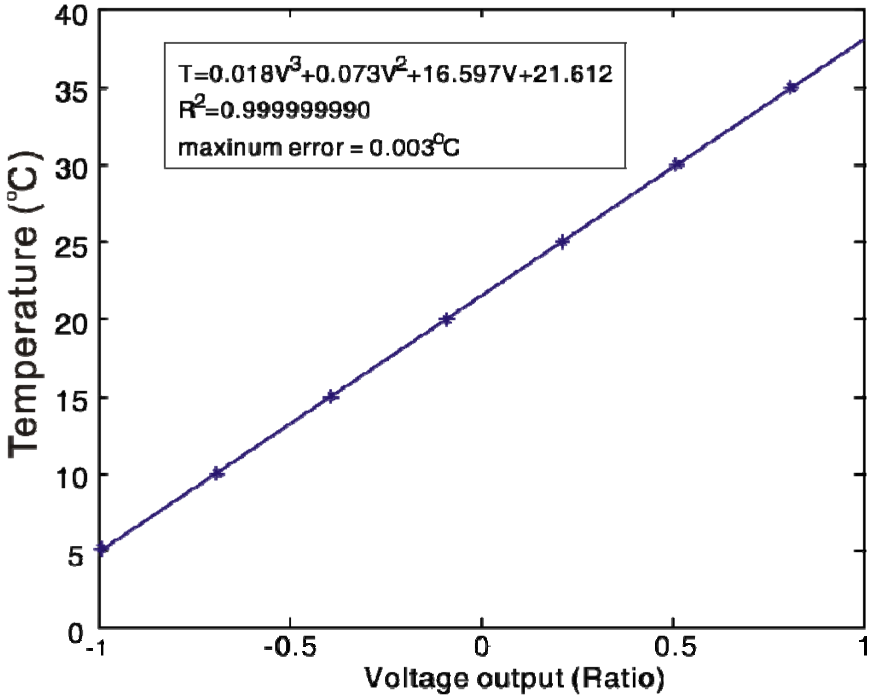

Figure 6-29 Plot of calibration result for the temperature sensor probe of chip 2-B coated with ECG-2702. The surrounding water temperature was changed from 5 to 35 ^{o}C in 5 ^{o}C increments for each calibration.

To test the long term stability of the ECG-2702 coated temperature sensor, the sensor probe was tested in the Grant temperature bath for 5 weeks. The temperature is changed from 5 to 30 ^{o}C periodically, with 5 ^{o}C increments. Each temperature step is kept for 1 hour. The temperature reading from the temperature sensor and F250 reference probe are recorded, and averaged for each temperature. The difference between the two averaged temperature data sets is present in figure 6-30:

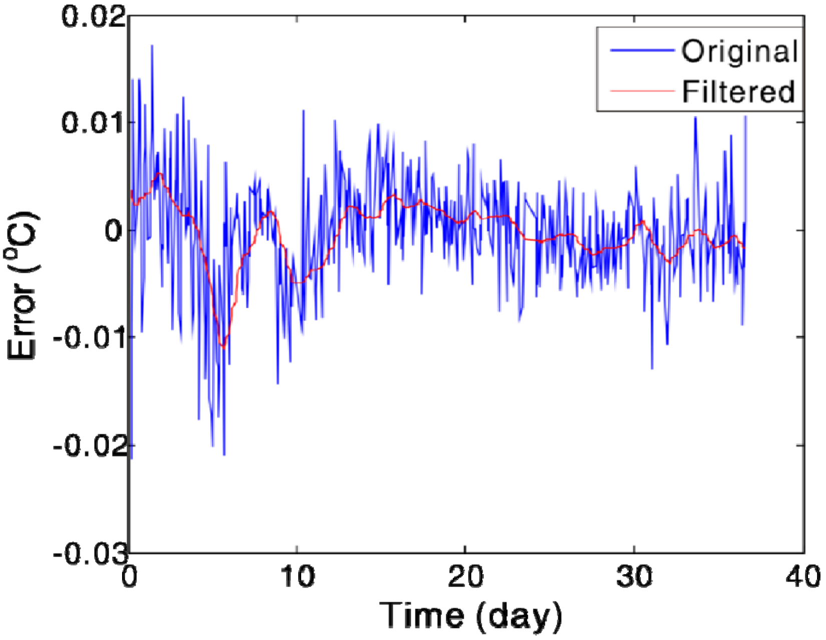

Figure 6-30 Plot of the measurement error of the ECG-2702 coated temperature sensor probe in a 5-week test. The surrounding water temperature was changed periodically from 5 to 35 ^{o}C in 5 ^{o}C increments.

As shown in the figure, the maximum error during the test is ±0.02 ^{o}C. However part of this error may come from the reference probe when the water temperature is different from room temperature. The error from the reference probe is removed by filtering this data with a low-pass filter. The filtered data indicates that the maximum error is ±0.01 ^{o}C. Furthermore, no significant drift is observed. Therefore the long term stability of the coated temperature sensor is up to ±0.01 ^{o}C

In order to estimate the response time, a dip test was performed. The temperature probe was kept in air at room temperature (about 20.5 ^{o}C), and then quickly immersed into the Grant temperature bath at a temperature of 14.89 ^{o}C. The temperature data was sampled at 1 s interval – the results are shown in figure 6-31. We see that the sensor takes 7 s to reach the 0.01 ^{o}C accuracy, and the time constant τ of this temperature probe is 1 s for a 63.2% change.

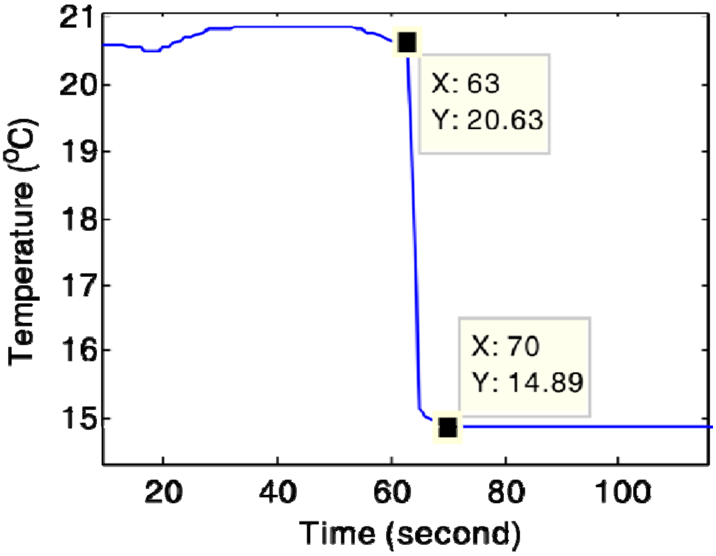

Figure 6-31 Plot of the data for the dip in test of the temperature sensor probe. The probe was firstly kept in the air of about 20.5 ^{o}C, and then immersed into water with temperature of 14.89 ^{o}C at 63 s.

6.4.3 Calibration of conductivity sensor probe in water buckets

Both version 1 and version 2 CT systems were calibrated in the temperature bath as described previously. The seawater in the bath has a fixed salinity, and the conductivity was changed by changing the water temperature. This method gives many conductivity values, as the temperature can be set to an arbitrary value. However, the major disadvantage is water evaporation, which changes the salinity and introduces calibration error.

Another method for conductivity calibration, which avoids evaporation error, is to measure the conductivity of water samples with different salinities over a short time. The volume of the water sample must be large enough to avoid evaporation error, with a relatively stable temperature.

The calibration lab in the National Oceanography Centre has four seawater samples, with salinities in the range from 10 to 40 psu. Each sample is contained in a 300 L bucket, giving a large volume. The water sample is mixed by a pump to provide a uniform salinity distribution. However, normally the water sample has a temperature about 2 ^{o}C lower than room temperature, and the surface water has a higher temperature. By stirring the water with pump, the temperature around the conductivity sensor is not constant, but fluctuates by ±0.1 ^{o}C. This temperature fluctuation introduces errors into the reference conductivity calculation unless a temperature probe with fast response time can be used to track the temperature change.

The time response of the packaged CT sensor is not fast enough, therefore this method was not used for the previous calibrations. However, as the temperature sensor probe of chip 2-B now has a very fast time response (1 s) and good accuracy (0.01 ^{o}C), we used the calibrated temperature sensor probe to measure the temperature profile, and calibrate the conductivity probe of chip 2-A in water buckets.

During calibration, the CT sensor probes were placed close together to avoid any large temperature change between them. The probes were immersed into each bucket for 10 minutes and with a 5 s sampling interval this provides 120 samples. The salinity of the water sample was measured by the Guildline 8410A Portasal salinometer. The conductivity of the water sample was calculated from the measured salinity and the averaged temperature of the 120 temperature samples. As there are only four conductivities, a linear fitting was used to define the relation between water resistivity and cell resistance (instead of a 3rd order polynomial). Figure 6-32 shows this calibration result:

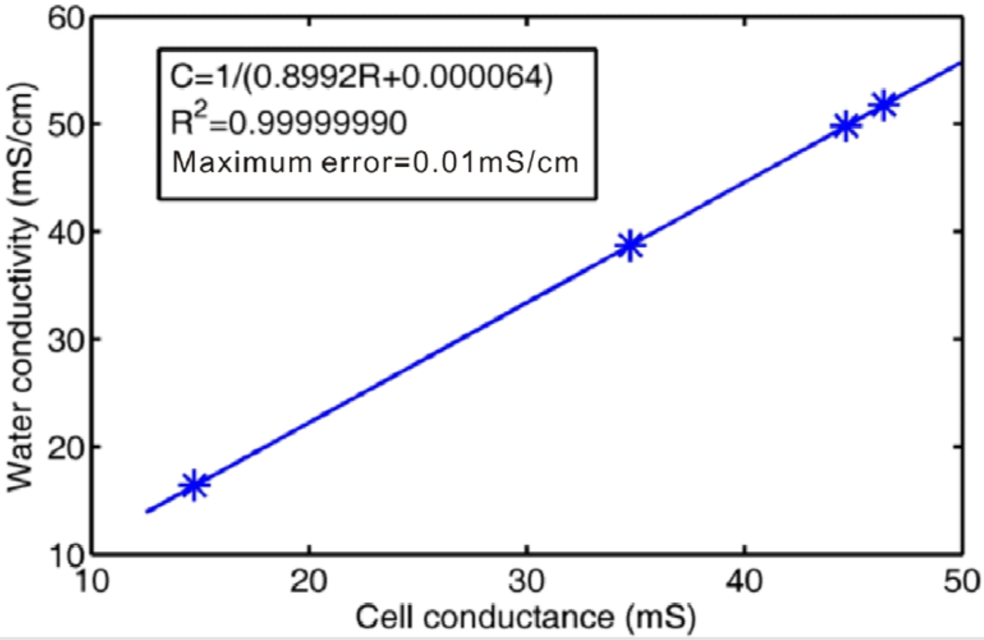

Figure 6-32 Plot of the calibration result for the conductivity probe of chip 2-A in four seawater samples. *R* in the equation is cell resistance, and *C* is water conductivity.

Although there are only four points in the calibration, the linear fit gives a maximum fitting error of ±0.01 mS/cm. This means that the conductivity has an excellent linearity (correlation $R^2 = 0.99999990$) and initial accuracy of ±0.01 mS/cm.

The fit also gives the cell constant κ = 1.112 cm^{-1} (1/0.8992). Furthermore, the temperature reading from the sensor fluctuated by ±0.1 ^{o}C during calibration, which reduces to ±0.01 ^{o}C by averaging 120 samples. As the temperature sensor has better accuracy, the total uncertainty of temperature can be considered to be ±0.01 ^{o}C, which leads to an uncertainty in conductivity of ±0.01 mS/cm. Therefore the fitting error may come from the temperature effect, and the initial accuracy of the conductivity sensor may be further improved if the temperature fluctuation can be reduced.

Pervious calibration with the Grant temperature bath used seven points and a 3rd polynomial fit, giving a fit error of ±0.02 mS/cm. Therefore the calibration in the buckets has smaller error even though a linear fit was used. This means that the nonlinear performance with higher error in the previous calibration is due to an error in estimating the salinity, and the non-uniform temperature distribution in the grant temperature bath.

As this calibration can distinguish drifts higher than ±0.01 mS/cm, another long term drift test was carried out to estimate drift error of the conductivity sensor. The conductivity sensor probe was kept in the Grant temperature bath for 8 weeks, the same as for the long term test of the temperature sensor. The bath temperature was changed periodically from 5 to 30 ^{o}C to mimic a harsh environment. Calibration was carried out before this test. After the test, four seawater samples were measured using the calibration result before this test. The difference between the reading from the conductivity sensor and the Guildline 8410A Portasal salinometer is considered as the drift error, and presented in figure 6-33:

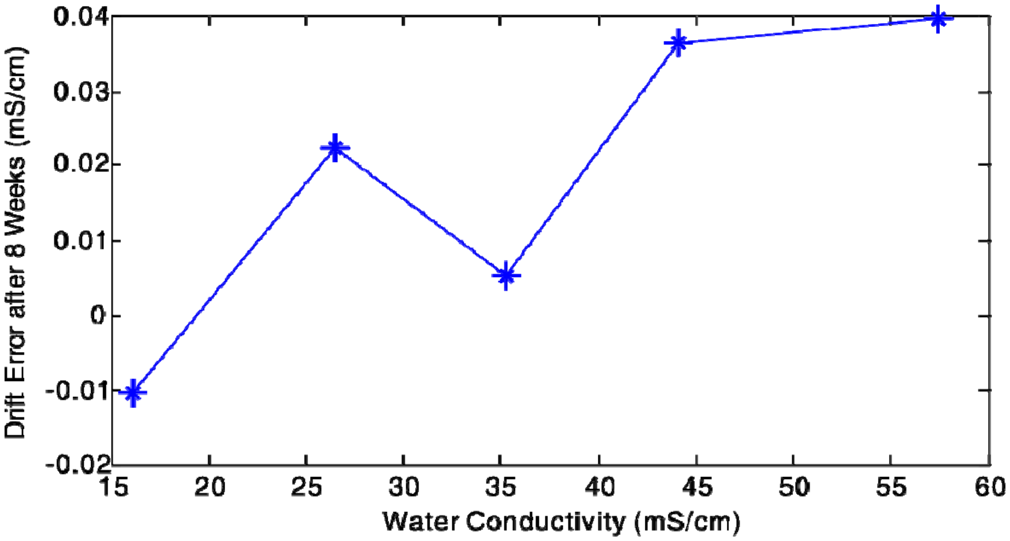

Figure 6-33 Plot of the drift error for the conductivity sensor probe of chip 2-A after 8 weeks in water, with temperature changing from 5 to 30 ^{o}C periodically.

As shown in the figure, the conductivity sensor has a maximum drift of 0.04 mS/cm at a water conductivity of 58 mS/cm. Therefore the monthly drift of the sensor can be considered to be 0.02 mS/cm, which will lead to a maximum error of 0.02 psu in salinity measurement. The sensor chip has a small amount of SU8 in the ring electrode area to cover the platinum wires. This drift is assumed to come from expansion of this SU8 after water absorption, changing the cell geometry; this can be improved by coating this part of the SU8 with ECG-2702.

6.5 Dissolved oxygen sensor

6.5.1 Experimental setup

The DO sensor was tested in both a three-electrode system and a two-electrode system. The DC bias of the three-electrode system fluctuated with time, increasing the system error, while the two-electrode system has a stable DC bias. Therefore we used the two-electrode system to test the DO sensor.

In the two-electrode system, the working electrode consists of five microelectrodes formed by holes in the insulation covering the central electrode in the sensor chip. Although the ring-electrodes can be used as reference electrodes by coating them with Ag/AgCl, this method might cause some uncertainty in the system because either the coating may not be mechanically sound, or the thin Ag/AgCl layer may be totally consumed. Therefore in the first test, an external Ag/AgCl electrode is used as the reference electrode. Figure 6-34 shows the DO sensor cell with a sensor chip and an external Ag/AgCl electrode:

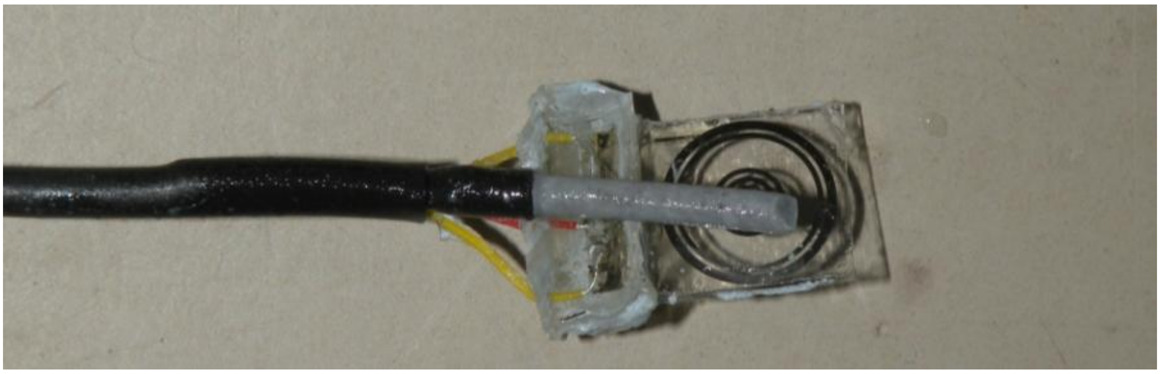

Figure 6-34 A photograph of the DO sensor probe, which consists of a DO sensor chip and an external Ag/AgCl electrode in front of the sensor chip.

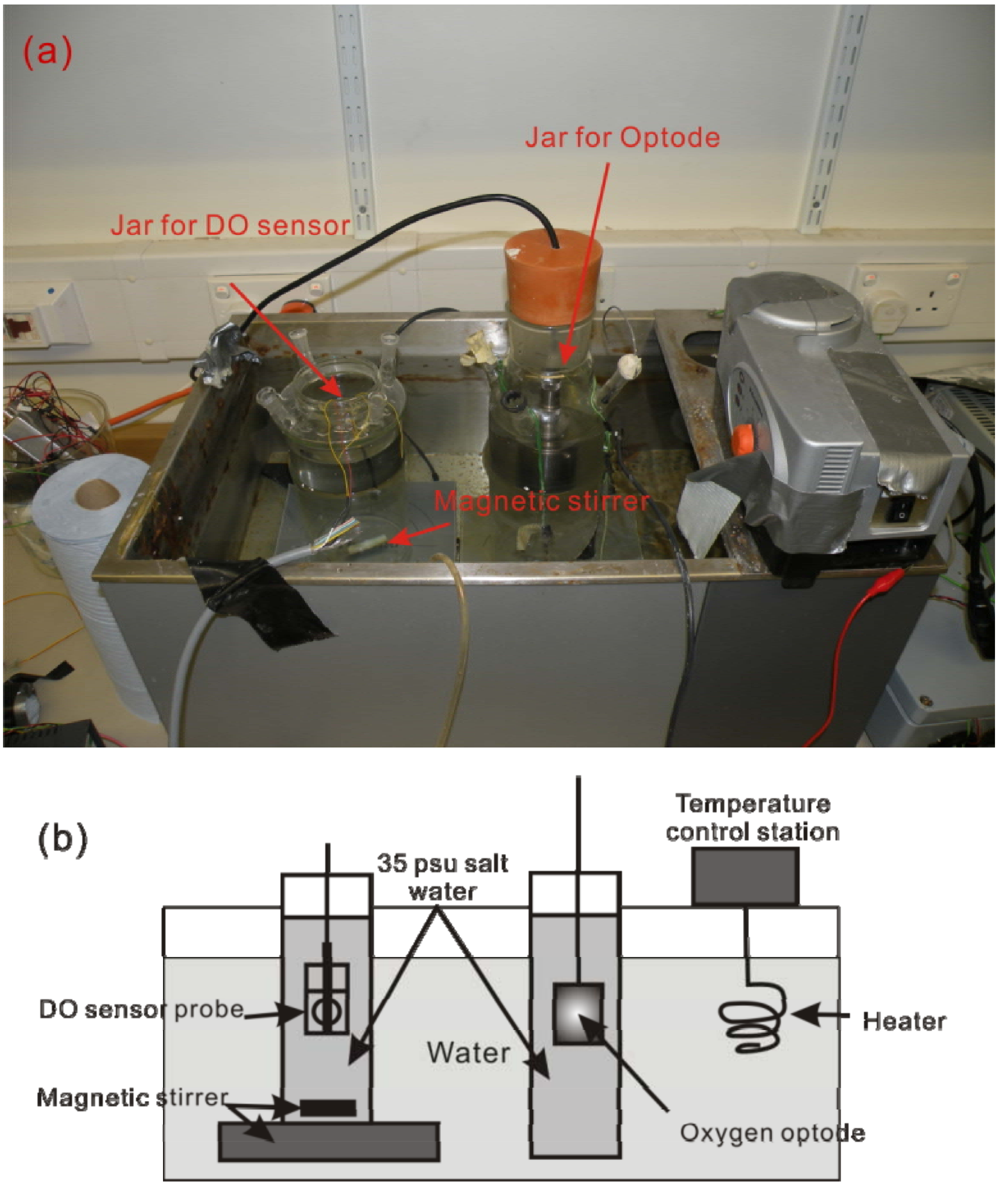

Figure 6-35 (a) Photograph of the experimental apparatus used to test the DO sensor. (b) Schematic of the experimental apparatus used to test the DO sensor.

As shown in figure 6-35, the DO sensor probe was immersed in a glass jar. A magnetic stirrer was put in the bottom of the jar to generate flow. The glass jar is filled with seawater at 35 psu, and kept in a water tank. The large volume of the water in the tank is used to provide a relatively constant temperature for the DO sensor. An AADI 3830 oxygen optode with 5% accuracy [91] was used to provide the reference oxygen calibration. This oxygen optode was kept in another jar. When the reference oxygen concentration is required, the optode is move to the jar containing the microelectrode based DO sensor to make a measurement. The reason that the optode and the microelectrode DO sensor are not kept together in the same jar is that the presence of the optode induces a significant increase in the noise in the electrochemical DO sensor readings when they are in close proximity.

6.5.2 Cyclic voltammetry of the DO sensor

As introduced in chapter 3, the current voltage relationship for a platinum working electrode will have a profile shown in figure 3-6. To verify the function of the DO sensor, a Cyclic Voltammetry (CV) method [32] was used, where the measurement voltage was periodically increased from -0.663 V to 1.137 V and then decreased back in 0.05 V steps. 10 current measurements were taken on each step and averaged to generate each data point.

Two seawater samples were used to generate two different cyclic voltamogrammes. One had air continuously bubbled through it to provide an oxygen concentration of about 270 µM, while the other one was purged with nitrogen to provide an oxygen concentration near to zero. Transient current measurements were taken at 10 ms, 15 ms, 25 ms, and 35 ms as introduced in chapter 5. The relation between the measurement voltage and measured current is shown in figure 6-36:

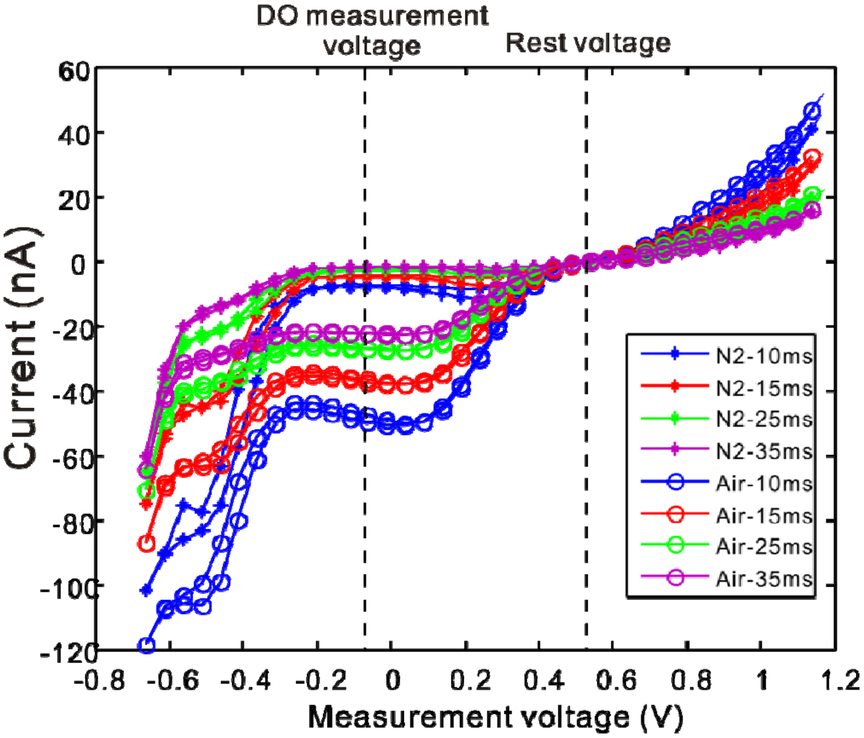

Figure 6-36 Plot of current-voltage relationship of the DO sensor during the CV test. The CV was performed in two water samples. One was purged with N_2 resulting in a near zero oxygen concentration, and the other was bubbled with air and had an oxygen concentration of about 270 µM. The transient current was measured at 10ms, 15ms, 25ms, and 35ms after the ramp of the measurement voltage.

As shown in the figure, the DO sensor immersed in the air-saturated sample has a profile very similar to that described in figure 3-6. There is significant difference between the oxygenated and deoxygenated CV profiles between -0.4~0.2 V, which is the voltage range for oxygen reduction. The N_2-saturated sample has zero oxygen; therefore it has a current close to zero in this region. The air-saturated sample has an oxygen concentration of about 270 μM, therefore it has relatively high and constant current in this range.

Using the data from these CVs the DO measurement voltage was set to -0.069 V. Seawater in real environment may have a salinity different from 35 psu, causing equilibrium voltage change in the Ag/AgCl reference electrode, and shifting the CV profile. However, because the current is mostly constant near -0.069 V, error induced by this voltage shift can be minimised by setting it as the measurement voltage. The rest voltage was set to 0.531 V, where the current is close to zero. This CV proves that the analysis in chapter 3 is correct, and the oxygen sensor is most sensitive to oxygen concentration at a measurement voltage of -0.069 V.

Furthermore, the CV profile is cyclic and enables hysteresis effects to be observed as can be seen in the figure. There are two current values at the same measurement voltage one measured when the voltage is increasing, and the other when it is decreasing. The transient current for shorter waiting time has a large hysteresis because measurements with short waiting times are influenced more by the initial state. Measurements following the CV from left to right and right to left have different initial states, causing the hysteresis.

6.5.3 Calibration of DO sensor

The DO sensor probe was calibrated with three water samples with the same salinity of 35 psu but different oxygen concentrations. The temperature of the three water samples is 20 ^{o}C. One water sample was purged with nitrogen to give an oxygen concentration of 55 μM (measured from the AADI 3830 oxygen optode); one water sample was saturated with air, and had an oxygen concentration of 270 μM; and the other one was purged with oxygen to give an oxygen concentration of 340 μM.

The DO sensor probe was placed in each sample twice, and the water was flowed slowly across the sensor (about 1 cm/s) using a magnetic stirrer. The DO sensor was recording continuously at a data rate of 0.5 Hz. 50 measurements were taken to provide an average current value. The relationship between the current and the oxygen concentration was fitted to a 2nd order polynomial, shown in figure 6-37:

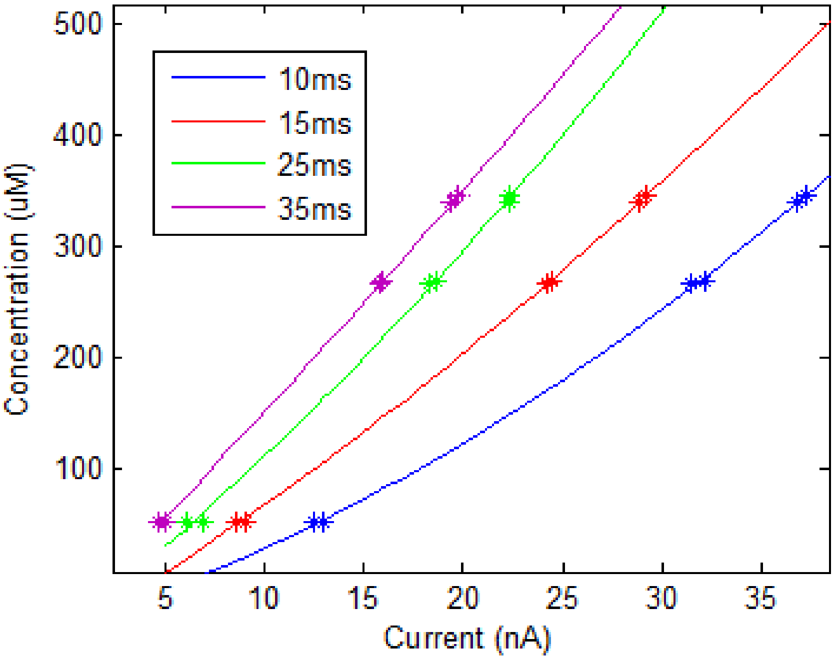

Figure 6-37 Plot of the calibration result of the DO sensor. Transient current was measured at 10 ms, 15 ms, 25 ms, and 35 ms after the ramp of the measurement voltage, and is plotted versus the oxygen concentration.

As shown in the figure, the oxygen sensor has good repeatability with a maximum error of 5 μM. The linearity of the current-concentration increases with the wait time; data with 35 ms wait time has the best linearity, probably due to the initial state effects.

Although the 0.531 V rest voltage has a current output near 0, it still slightly modifies the oxygen concentration around the working electrode. Therefore, during the initial state, the oxygen concentration is not exactly the same as the solution bulk, but determined by both the bulk concentration and the resting voltage. This initial difference in oxygen concentration makes the current-concentration relation non-linear. A transient current with a longer wait time is influenced less by the initial state effects, therefore the 35 ms data has the best linearity.

6.5.4 Flow effects

The effect of flow on the oxygen concentration was tested with a stop-start-stop flow experiment. In the experiment, a water sample at 285 µM oxygen concentration and 35 psu salinity was used. The oxygen probe was running continuously in this water sample for 30 minutes with 0.5 Hz data rate. The magnetic stirrer was stopped during the first 10 minutes to provide a no flow environment, and then run at full speed for 10 minutes to generate a rapid water flow (estimated as about 30 cm/s). After 10 minutes, the magnetic stirrer was stopped for 10 minutes.

The current from the DO sensor was converted into oxygen concentration using the calibration data. Figure 6-38 compares DO data with 15 ms and 35 ms wait time:

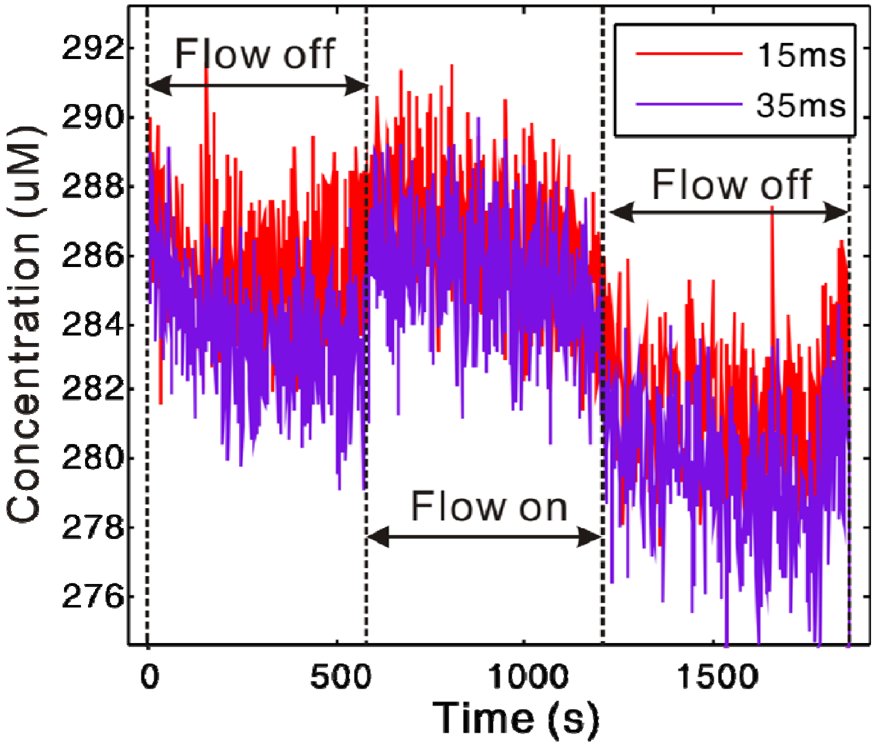

Figure 6-38 Plot of the flow test data of the DO sensor probe. Transient current was measured at 15 ms and 35 ms after the ramp of the measurement voltage. Water flow was applied between 600 and 1200 s.

As shown in the figure, the current increases at 600 s and decreases at 1200 s due to the flow. The wait time of 35 ms has a slightly higher increase of 3 µM at 600 s when the flow starts. However this flow effect is only about 1% and is much smaller than estimated in chapter 4 (28% at 20 ms).

There are two reasons for this difference. One is that the flow rate in the test (30 cm/s) is about one third of that used in the estimation (100 cm/s). The other reason is that the estimate is pessimistic; all the oxygen brought into the diffusion boundary is considered consumed by the electrode, ignoring the fact that some of the oxygen is also removed by the water flow. The experimental test result has 10 times smaller flow effect than the estimate.

Figure 6-37 also shows the measurement noise of the DO sensor. The standard deviation of the measurement noise is about ±2 μM, which can be considered the system resolution.

Over the read time, the DO value reduced from 286 μM to 282 μM. This attenuation may be due to the temperature change of the sample or loss of the activity of the working electrode. The calibration set up used could not provide a completely constant temperature and oxygen concentration, and the AADI 3830 oxygen optode does not provide an accurate reading within the 20 mins waiting time. Therefore it is difficult to determine the exact reason for this attenuation. Calibration method needs to be improved to provide water samples with constant oxygen concentration and temperature so that the long term stability test and temperature profile test can be carried out.

6.6 Deployment of a complete CT-DO system

The CT sensors and the DO sensor in design 2 are combined together to make a complete CT-DO system. Figure 5-11 (chapter 5) shows the electronics for this system. A photo of the sensor head is shown in figure 6-39, and the whole system is shown in figure 6-40:

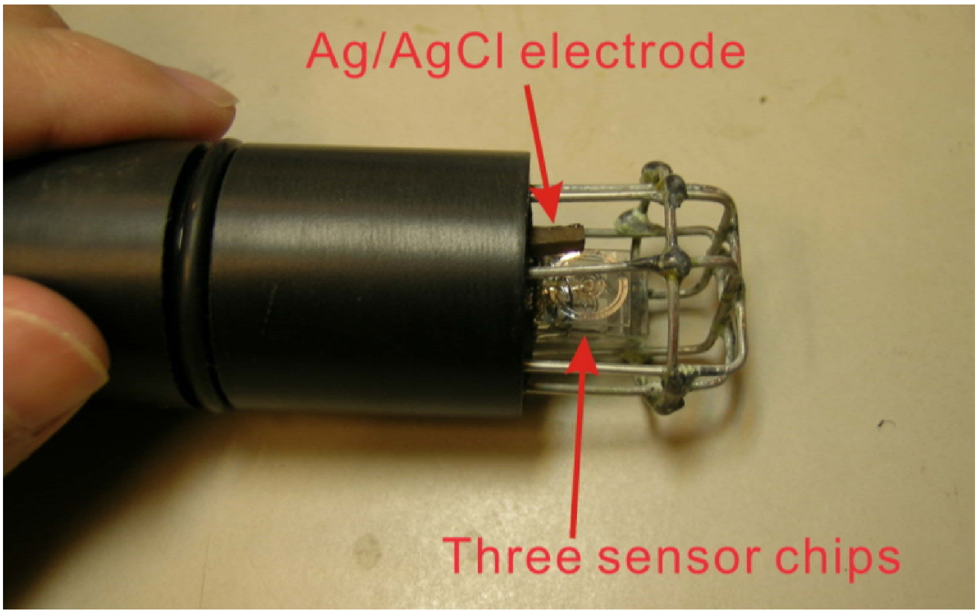

Figure 6-39 A photograph of the CT-DO sensor head.

Figure 6-40 A photograph of the complete CT-DO system, including the main electronics box with USB connection cable, and two CT-DO sensor heads.

As shown in figure 6-39, three sensor chips are installed in each sensor head. A 2-B temperature sensor chip is in the middle. Two 2-A conductivity/DO sensor chips are beside the temperature sensor chip. One is for conductivity measurement, and one is for DO measurement. An external Ag/AgCl electrode is placed in front of the DO sensor chip as the reference electrode. These sensors are protected by a metal cage. The sensor head is coupled with a standard yacht / boat log (distance and speed) sensor skin fitting [157], and can be installed into a boat or ship, with the head exposed to the water.

This system was installed on a rowing boat [1] that travelled in the Indian Ocean from Geraldton, Australia to Mauritius, Africa. The journey started on 21st April, 2011 and ended on 6th July, 2011 - the route is shown in figure 6-41:

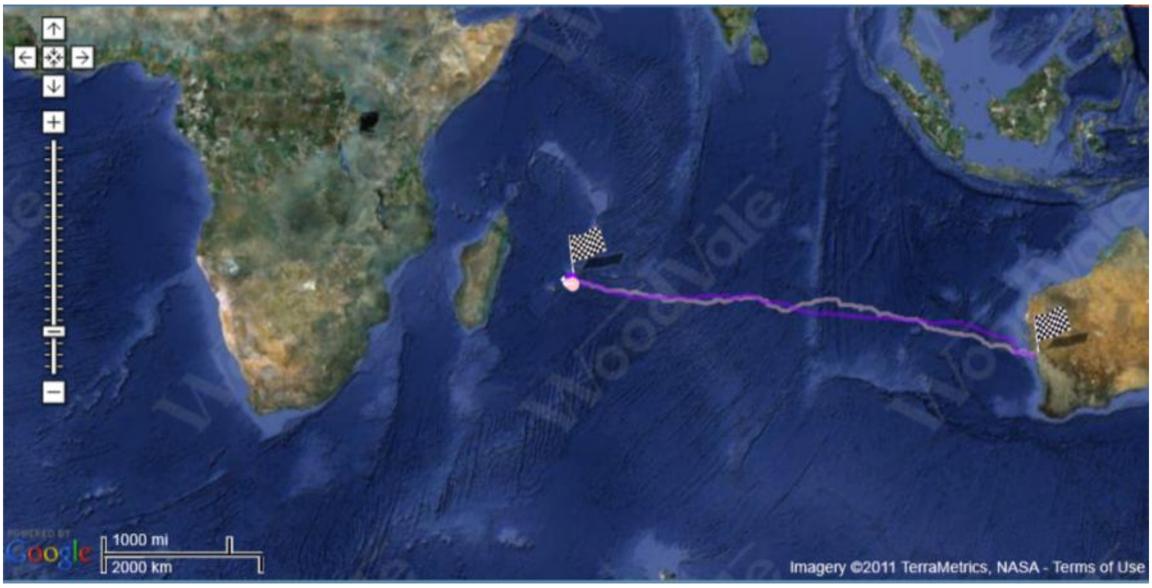

Figure 6-41 A diagram demonstrating the routing of the Indian Ocean rowing boats. The CT-DO system was installed in the boat which followed the route shown by a dark purple trace.

Figures 6-42 and 6-43 show historical satellite derived salinity and temperature data for the Indian Ocean (provided by the satellite group of the National Oceanography Centre), where the average salinity is about 35 psu, and temperature is about 25 °C. Figures 6-44 ~ 6-46 show the recorded data from the CT-DO sensor system.

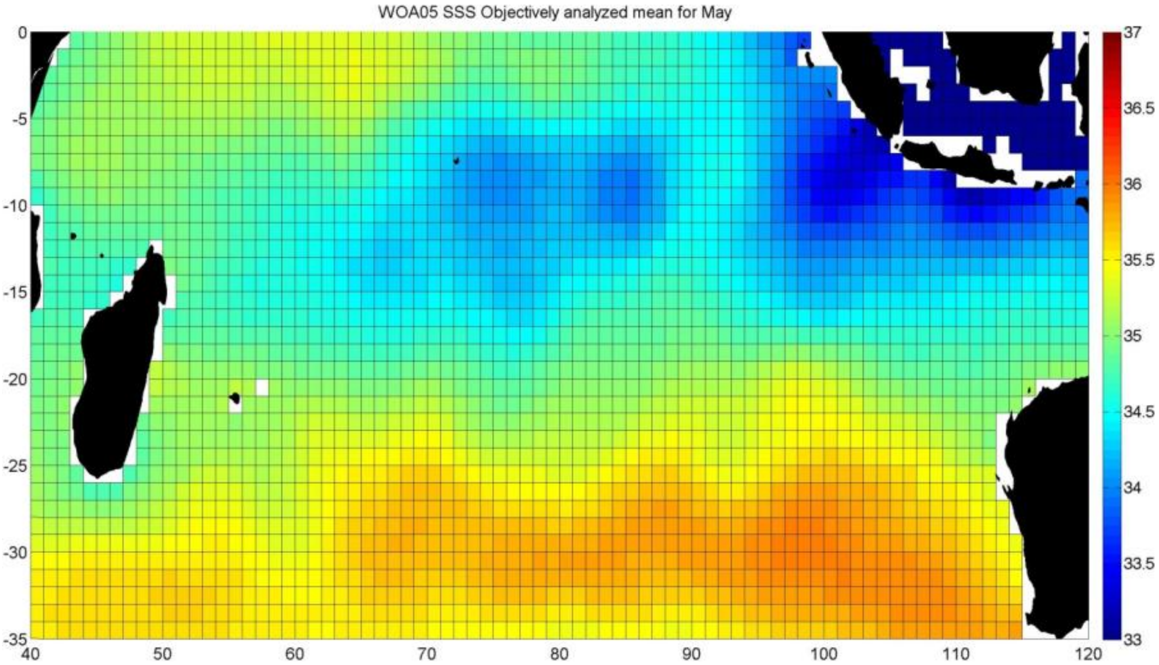

Figure 6-42 Plot of the recorded salinity data for the Indian Ocean of May, 2005.

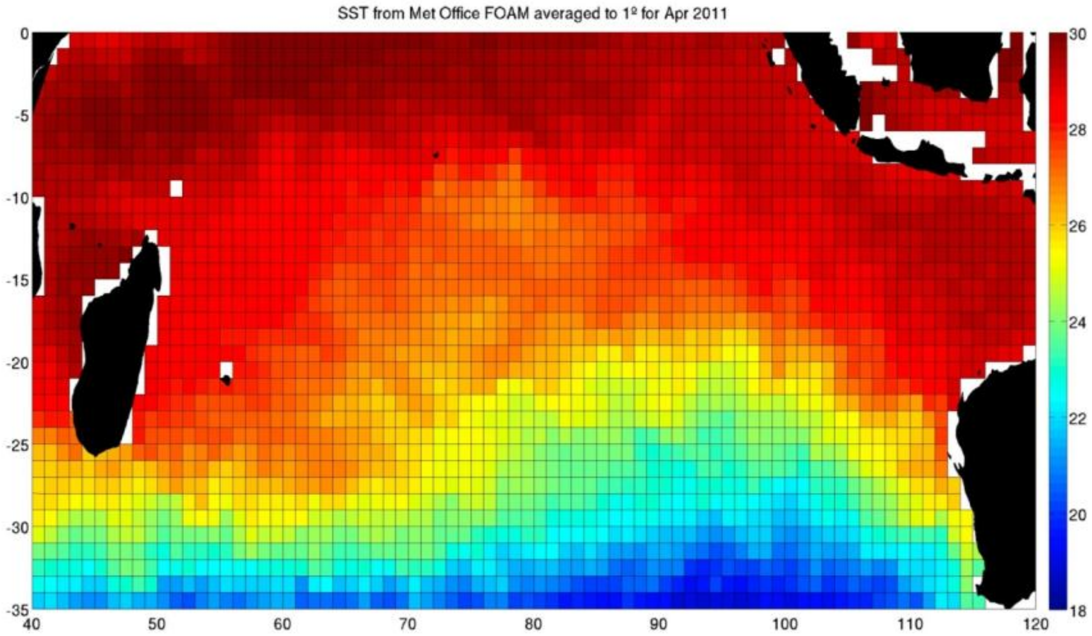

Figure 6-43 Plot of the recorded temperature data for the Indian Ocean of April, 2011.

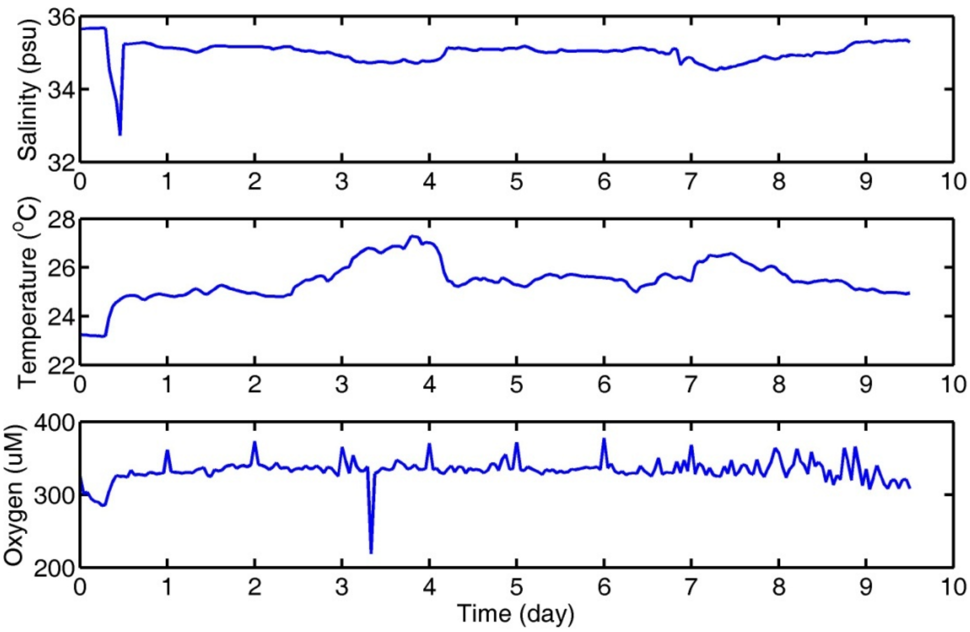

Figure 6-44 Plot of the salinity, temperature, and oxygen data from the CT-DO system of the Indian Ocean rowing boat. The data is from 21st April, 2011 to 1st May, 2011.

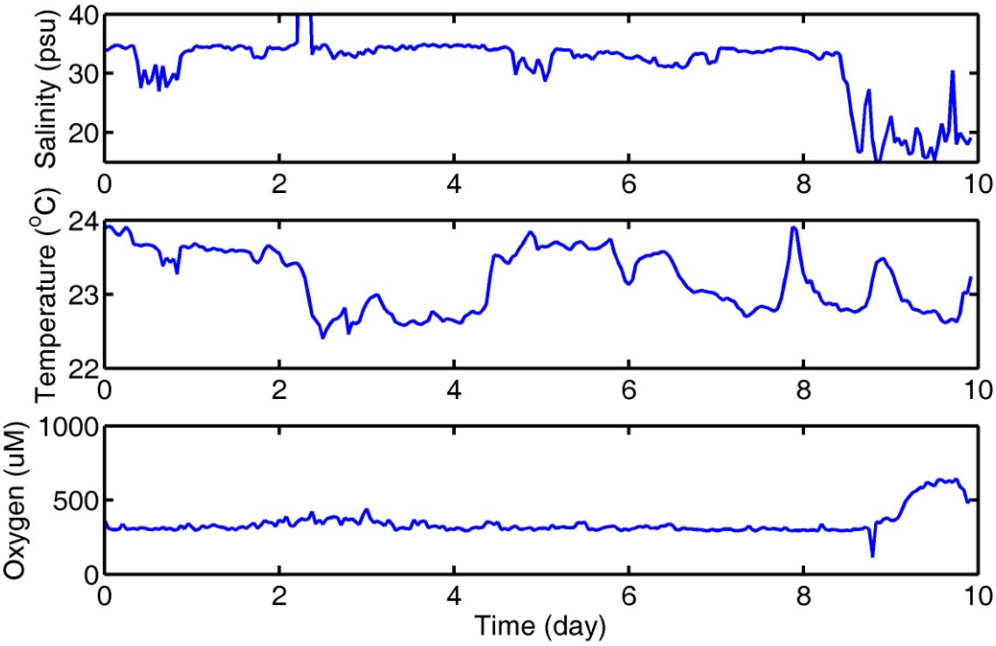

Figure 6-45 Plot of the salinity, temperature, and oxygen data from the CT-DO system on the Indian Ocean rowing boat. The data is from 7th May, 2011 to 17th May, 2011.

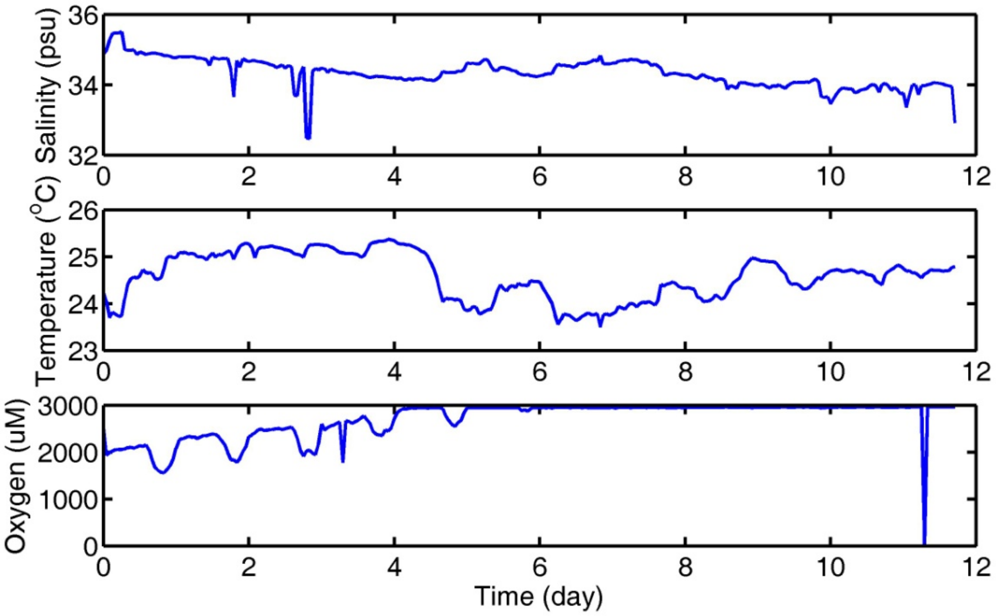

Figure 6-46 Plot of the salinity, temperature, and oxygen data from the CT-DO system of the Indian Ocean rowing boat. The data is from 6th June, 2011 to 18th June, 2011.

The boat departed the dock on 21st April, 2011 and the CT-DO sensor system was deployed two weeks before the departure. Figure 6-44 shows a salinity drop from 36 psu to 32 psu when the boat departed, due to the boat passing a river outlet. The salinity value is about 35 psu, which is very close to the historical data.

The temperature and oxygen sensor also worked well, see figure 6-44. The temperature reading is about 26 °C, close to historical data. The oxygen reading is about 270 µM, which is close to the oxygen concentration of air saturated water. The oxygen reading has periodic peaks every 24 hours. This is because the oxygen was set to run a CV every day. These CVs clean the working electrode and maintain its activity. The measured current is higher than normal after the working electrode has a CV, therefore peaks are generated every 24 hours.

The conductivity and DO sensor worked until 15th May, 2011. As shown in figure 6-45, the salinity data dropped to 18 psu, while the oxygen data rose to 500 µM on 15th May, 2011 (8th day in the figure). One sailor on the boat examined the sensor head and found that it was covered by barnacles. These barnacles prevented seawater reaching the sensor chip; therefore the conductivity and oxygen sensor stopped working. However the barnacles are thermally conducting and the temperature sensor continued to work.

The barnacles were cleaned off and the conductivity sensor resumed working, as shown in figure 6-46. However the DO sensor did not work, the reading was higher than 1000 μM. The barnacles probably broke the laminate on the sensor chip, enlarging the contact area of the platinum and causing a much higher and unstable reading.

6.7 Bio-fouling cleaning experiment

Bio-fouling is a serious problem for long term autonomous deployment of a CT-DO sensor. The DO sensor circuit can be used to electrochemically generate chlorine at the platinum electrode which should remove or inhibit bio-fouling. An experiment was carried out to test this.

A ring-electrode sensor on chip 2-A was used. The connections to the exposed electrodes were changed to enable all electrodes to be held at a chlorine generation voltage. This could be achieved with switching circuits in a new version of the control electronics. In this test all the ring-electrodes were connected to the trans-impedance amplifier of the DO circuit as working electrodes. The resistor in the trans-impedance amplifier was set to a short circuit to allow a large current to pass. Using the same setup as the DO sensor, an external Ag/AgCl electrode was used to create a two-electrode system. A voltage waveform was applied to the ring-electrodes against this electrode and hence the solution bulk, with a voltage periodically changing from -1.36 V to 2.24 V as shown in figure 6-47.

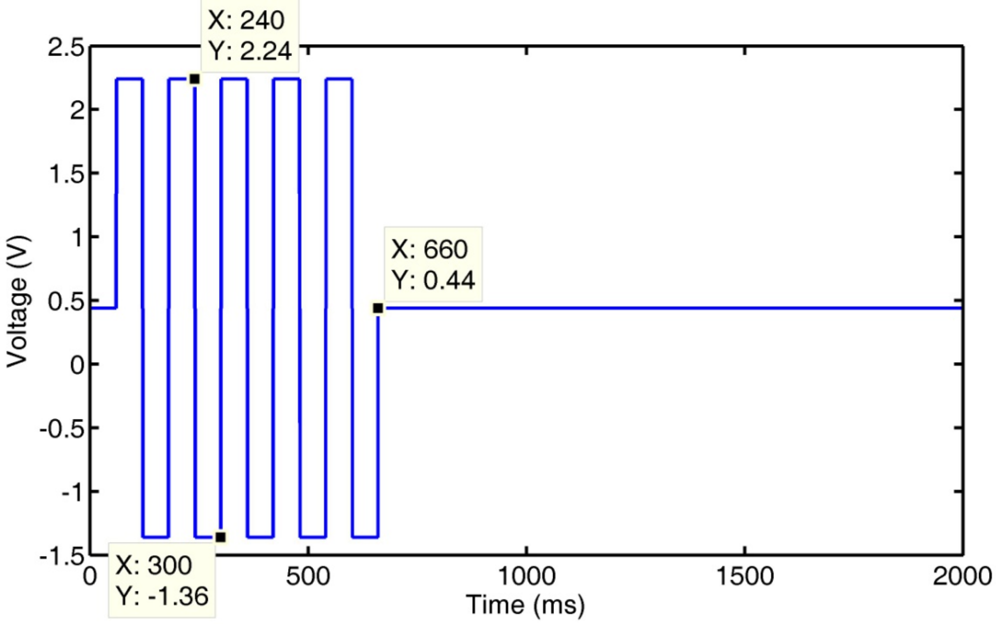

Figure 6-47 Plot of the 2 s periodical waveform for chlorine generation.

As discussed in chapter 3, chlorine is generated if the voltage is higher than 1.36 V. Therefore a voltage of 2.24 V has sufficient over potential to generate chlorine.

Measurement showed that the current at this voltage is about 1 mA. The Ag of the Ag/AgCl electrode is converted to AgCl during chlorine generation. Therefore the -1.36 V voltage is used to convert the AgCl back to Ag, preventing the reference electrode from being consumed.

Another sensor chip was used for comparison. This did not have the cleaning wave form applied to its electrodes. The two sensor chips were deployed in the dock for two weeks. Figure 6-48 shows the sensor chips before deployment, and figure 6-49 shows the sensor chips after deployment:

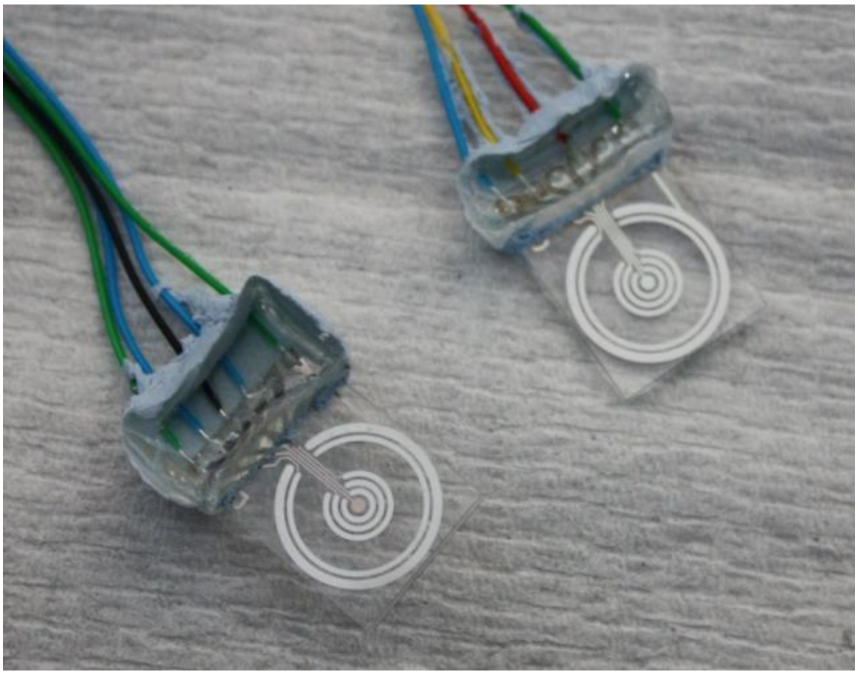

Figure 6-48 Photograph of the two 2-A sensor chips before a 2 weeks dock deployment for bio-fouling test. The chip on the left is applied with the cleaning wave form, while the chip on the right is not.

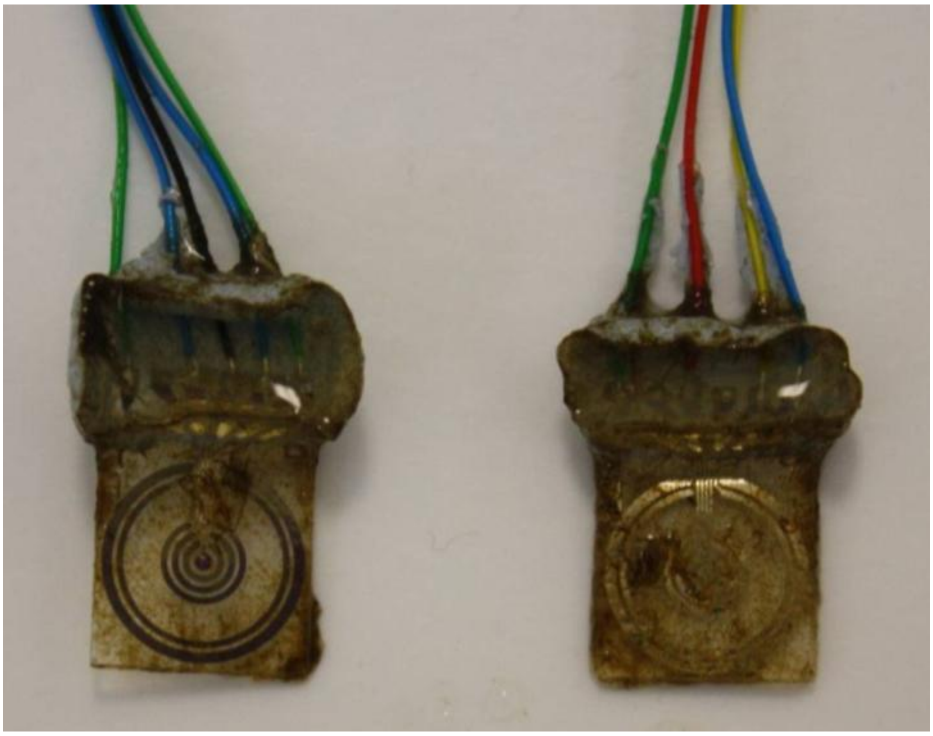

Figure 6-49 Photograph of the two sensor chips after a 2-week deployment in Empress Dock Southampton for bio-fouling test. The chip on the left had the cleaning wave form applied to it, while the chip on the right did not. Note that the electrodes are only present on one side of the chip and the chip is transparent. The bio-fouling seen on the chip with the waveform applied is predominantly on the side without electrodes.

As shown in figure 6-49, heavy bio-fouling was found on both sensor chips. The chip without the cleaning waveform has bio-fouling on both sides. However, the chip with the cleaning waveform only has bio-fouling on the back side - the electrode is very clean. This indicates that the cleaning waveform works well and prevents growth on the electrodes.

6.8 Calibration in fresh water

An experiment was used to discover the possibility of using the conductivity sensor in fresh water. A version 2 CT system (figure 6-17) was calibrated in fresh water samples with conductivities in the range from 8~94 μS/cm. A YSI 3100 conductivity meter [158] was used for reference. The calibration result is presented in figure 6-50:

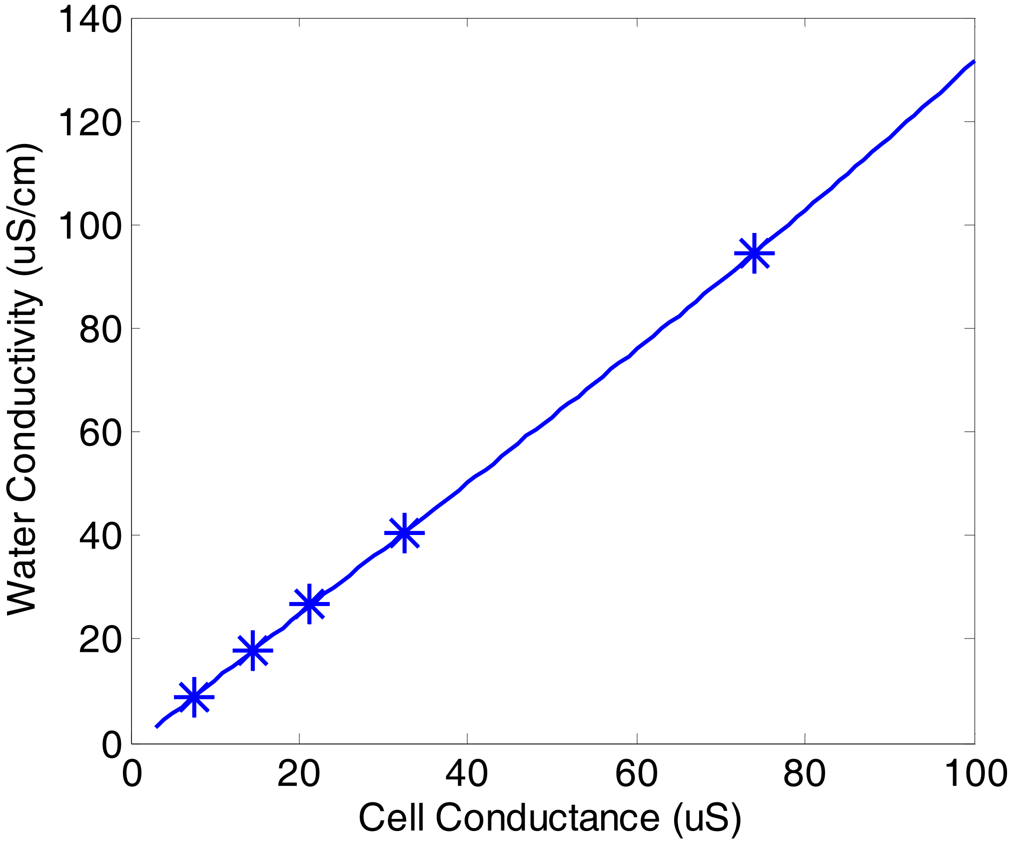

Figure 6-50 Plot of the conductivity calibration result for the version 2 CT system, in the conductivity range of 8~94 μS/cm for fresh water application.

The cell constant of the version 2 CT system calibrated in fresh water is about 1.2 cm^{-1}, which is very close to the 1.12 cm^{-1} cell constant of the conductivity sensor probe calibrated in seawater. The slight difference in the two cell constants is not due to the different conductivity ranges, but because of the inaccurate reading from the reference conductivity value. The reference conductivity probe is a two-electrode cell, and is calibrated in small tubes. When using this probe in bigger containers, the reference reading may be larger than the actual conductivity, inducing a positive error in the calibrated cell constant.

The CT sensor calibrated in fresh water was deployed in ice water of Greenland. The sensor worked well in the harsh environment at a temperature near to 0 ^{o}C, and gave conductivity readings of about 6 μS/cm. This deployment shows that the CT sensor can work for not only in ocean applications, but also fresh water applications in harsh environmental conditions.

Chapter 7 Conclusions and Further Work

7.1 Conclusions

In this thesis, 3 different designs of sensor chips have been presented. Design 1 uses seven-electrodes within a channel for conductivity and a PRT-bridge temperature sensor, all integrated into one sensor chip. Design 2 has a four-ring-electrode open conductivity sensor and a PRT-bridge temperature sensor in separate chips. The four-ring-electrode chip can also be used as DO sensor. Design 3 has a four-ring-electrode open conductivity sensor, a PRT-bridge temperature sensor, and a DO sensor all integrated into one double-sided sensor chip.

An impedance measurement circuit was built to support the CT sensor with 16-bit resolution. With averaging of 8000 samples (obtained at 100 ksps) 16-bit resolution is obtained. To compensate for drift in the impedance measurement electronics, the system measures the voltage response for both CT sensors together with that for two calibrations resistors. This 4-channel measurement takes 400 ms in total. With a 9.2 mA working current and 200 µA quiescent current, this circuit has a battery life of one month for a 10 s sampling interval when powered by a 9 V/500 mAh PP3 battery. This circuit does not support one year battery life with 9 V/ 500 mAh battery, because the 200 µA quiescent current is too large. However, if two serially connected lithium batteries with 7.2 V/3000 mAh capacity were used, and the sampling interval is increased to 30 s, the battery life will be one year.

A separate circuit was designed for the DO sensor, supporting both two-electrode and three-electrode electrochemical measurements. This circuit has a working current of 7 mA and a quiescent current of 200 µA. It shares the same digital circuit as the impedance measurement circuit. Therefore these two circuits can be combined together to make the electronics for a complete CT-DO system.

The sensors of designs 1 and 2 were manufactured and tested; The sensors of design 3 is currently being manufactured. In design 1, the temperature sensor has an initial accuracy of ±0.01 ^{o}C, with a standard deviation of ±0.004 ^{o}C. However the temperature sensor was not stable and drifted by 0.1 ^{o}C after 72 hours of immersion in water. The conductivity sensor has an initial accuracy of ±0.04 mS/cm, with a standard deviation of ±0.005 mS/cm. A deployment on an Atlantic cruise discovered that the conductivity sensor had a problem with durability due to water absorption into the insulating laminate material and epoxy glue.

The drift and durability problems were solved in design 2 by replacing the laminate and using an open cell conductivity sensor. CT sensors from design 2 together with the electronics were packaged in a Ø10x15cm plastic pot, and calibrated in a temperature bath. The initial accuracies and standard deviations of the CT sensors are ±0.02 mS/cm and ±0.01 ^{o}C, and ±0.003 mS/cm and ±0.003 ^{o}C respectively. The CT calibration was affected by the thermal mass of the plastic package, non-uniform temperature distribution of the water bath, and the water evaporation. 3 repeat calibrations show maximum errors of ±0.04 mS/cm and ±0.03 ^{o}C.

The CT sensor was made into a probe to reduce the thermal mass of the package. The temperature sensor probe was tied to the reference temperature sensor to reduce the effect of the non-uniform temperature distribution, giving a much better initial accuracy of ±0.003 ^{o}C. The conductivity sensor was calibrated in water buckets containing different water salinities to remove the effect of water evaporation, giving an accuracy of ±0.01 mS/cm.

During long term stability testing, the temperature sensor drifted less than ±0.01 ^{o}C during 5 weeks immersion in water, and the conductivity sensor had a monthly drift of 0.02 mS/cm after an 8-week test. Experiments were also carried to estimate the proximity effects for the four-ring-electrode open conductivity sensor. The results show that no proximity effect was found if the object is 7 mm (or more) away from the centre of the sensor chip.

Table 7-1 compares our system with other commercial and published systems, showing that only the Seabird system has better accuracy. However, it is much larger and has significant power consumption. Comparing systems with equivalent dimension

(PCB MEMS CTD) or smaller dimension (multi-sensor system and Star-Oddi DST), our system has an order of magnitude or more better accuracy.

CTD System	Conductivity accuracy	Temperature accuracy	Pressure accuracy	Power, battery life, & dimension
Our System	±0.01 mS/cm (10~70 mS/cm)	±0.003 °C (0~35 °C)	N/A	Battery life: 1month @ 10s interval Dimension: Ø100x150 mm
Gong CT System [22]	±2.7% @ 0.2~1 mol/L KCl solution	±0.003 °C (0~30 °C)	N/A	48 hours battery life
Hyldgard multi-sensor system [36, 37]	±0.6 mS/cm	±0.065 °C	±0.05 bar	Chip dimension : 4x4 mm Package dimension: About Ø8x50 mm
Broadbent PCB MEMS CTD [38]	±1.47% (0~60 mS/cm)	±0.546 °C (0~50 °C)	±0.02 bar	Battery life: 22 day @ 15 min interval Dimension: Ø100x100 mm
Sea-bird SBE 911plus CTD [61]	±0.003 mS/cm (0~70 mS/cm)	±0.001 °C (-5~35 °C)	±0.015% @ FS of 10500 m	(Underwater Unit only) Power: 1 A @ 14.3 V Dimension: 952x330x305 mm
Star-Oddi DST CTD [16]	±0.8 mS/cm (3~37 mS/cm or 10~50 mS/cm)	±0.1 °C (-1~50 °C)	±0.4% @ FS of 200 m	Dimension: 17x17x46mm Battery life: 4 years @ 10min interval

Table 7-1 Comparison of our sensor system and other salinity sensor systems.

A novel DO sensor was implemented in design 2, with a platinum electrode covered with laminate in which there are five wells of 25 µm diameter and 25 µm depth used as a working electrode. The voltage-current relation of the platinum working electrode was analysed, and a conservative estimate made of the maximum flow effect on the DO sensor. The DO sensor was tested as a two electrode system with an external Ag/AgCl electrode as a reference electrode. CV test shows that the voltage-current relations was very close to theoretical predictions, and flow tests showed a 1% change in sensor readings in flow, which is 10 times smaller than estimated by a simple theoretical model.

The DO sensor was calibrated using three different water samples of 35 psu salinity at room temperature (20 ^{o}C). It has ±5 μM initial accuracy, with ±3 μM standard deviation error. More experiments need to be carried out to determine the effect of temperature and its long term stability. Greater control of oxygen concentration, temperature and flow during calibration would be afforded by using the apparatus described by Sosna et al [83].

A complete CT-DO sensor system was deployed in a rowing boat for 75 days in the Indian Ocean. The CT sensor survived and gave reasonable readings during this deployment. The DO sensor worked for 25 days, and then it was destroyed by bio-fouling.

An electrochemical method for reducing bio-fouling was tested using the electronics of the DO sensor. Dock deployment result shows that this method has a remarkable effect on bio-fouling reduction, and can be implemented in the CT sensor in the future by incorporating a relatively small change in the sensor electronics. Furthermore, the version 2 CT system was also calibrated in fresh water, and successfully deployed in Greenland. This means that the CT system can also be used in fresh water applications.

7.2 Future work

It has been shown that the CT sensor of design 2 has excellent initial accuracy and stability, and was successfully tested in several deployments. The basic functions of the DO sensor have been evaluated and have shown good performance. More experiments need to be carried out to determine the temperature coefficient and stability of this sensor. Several research groups and companies have expressed interest in the CT-DO system, demonstrating potential for commercialisation.

However, there are still some problems that need to be solved before commercialising an ultra miniature, low power, low cost and high accuracy CT-DO system. These problems and recommended solutions are listed as follows:

1. The one month battery life is too short for some autonomous applications, which might require one year battery life. The 200 μA quiescent current

needs to be reduced. Most of the quiescent current is consumed by the FPGA. Therefore this problem can be solved by using a low power microcontroller to power down the FPGA during sleep mode.

2. The electronic circuits for CT and DO sensor are on separated PCBs, and the amplifiers for CT and DO sensor are not shared. A two-electrode DO system requires a trans-impedance amplifier, and another amplifier for the voltage signal. The CT electronics use a trans-impedance amplifier, and a differential amplifier, which can also be used as a voltage amplifier for the DO sensor. The power consumption and cost of the system can be further reduced by sharing these amplifiers using multiplexers.
3. The CT-DO electronics do not support electrochemical bio-fouling mitigation via chlorine generation. This function should be implemented in the next generation of electronics.
4. The Ø10x15 cm package is too large and has a big thermal mass, affecting CT response time and accuracy. More compact package should be made to solve this problem.
5. All the electronics can be integrated into an ASIC (Application Specific Integrated Circuit). This means that the whole system can be packaged into something the size of a pen, enabling further reductions in cost and new applications such as use in a fish tag.
6. Conductivity has a monthly drift of 0.02 mS/cm. This drift is expected to be reduced by coating the SU8 laminate with ECG-2702 to prevent water absorption.
7. The DO sensor needs to be tested to determine the temperature coefficient and long term stability. Calibration in a sealed jar should be able to provide an environment with constant oxygen concentration. This jar can be placed into a water bath with good temperature control. Therefore the temperature coefficient could be measured from the change in the current of the working electrode with temperature. An alternative and high performance strategy is to use the calibration setup described by Sosna et al [83] which would enable precise control of temperature, oxygen concentration and flow (if a magnetic stirrer were included in the sensor cell).

8. A pressure sensor can be added to the system, since many applications also need depth information.

Some of these issues will be explored as part of my post-doctorial work after this PhD study. For example, Figure 7-1 shows the un-finished PCB design for the next generation electronics:

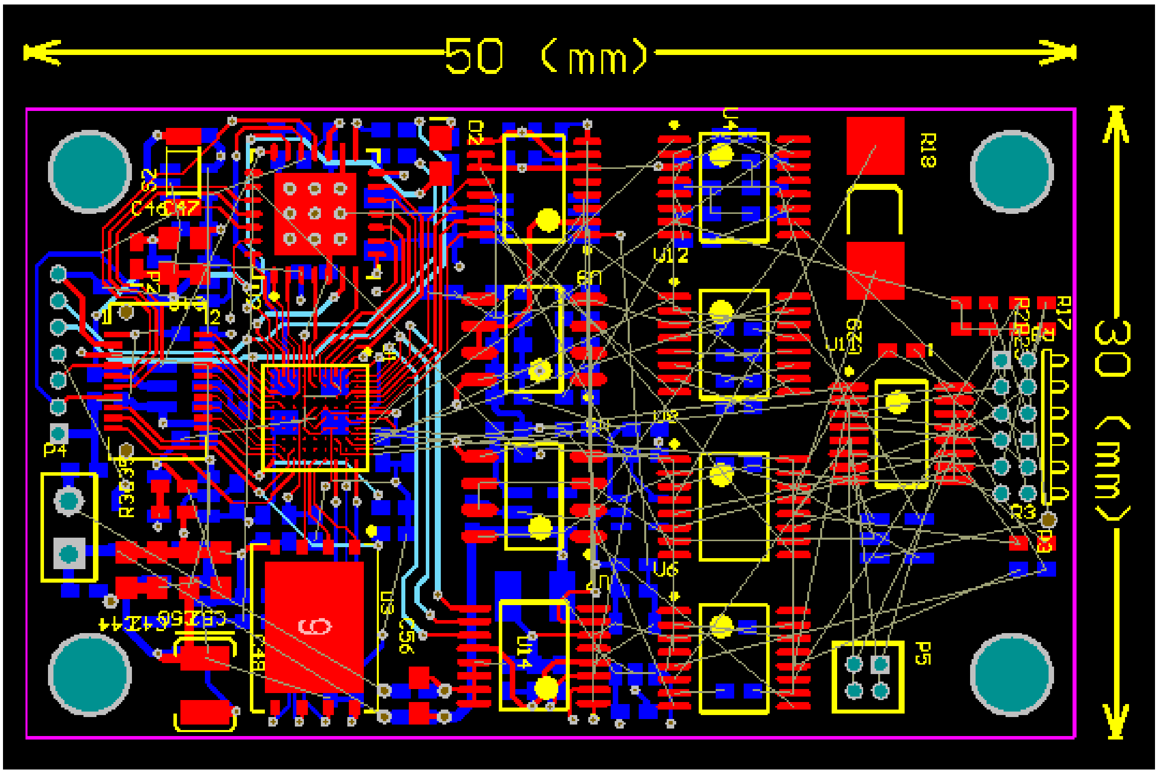

Figure 7-1 Diagram of an unfinished PCB design for CT-DO system with bio-fouling cleaning function.

This electronics is on a 3x5 cm PCB. A microcontroller with 3 µA quiescent current is used for power control. The power switches for all the other components consume 2 µA when switched off; therefore the quiescent current for this system is estimated as 5 µA, which is much smaller than the 200 µA of the current electronics.

These electronics are designed to support the CT-DO sensor of design 3. The CT and DO sensor share the same trans-impedance amplifier and differential amplifiers to reduce power consumption and system cost. All the ring-electrodes on the double-sided chip can be switched to GND using multiplexers, and cleaning wave form is applied using an external Ag/AgCl electrode for bio-fouling removal. Furthermore, an interface (P5 in figure 7-1) is reserved for a third party pressure sensor.

This electronics and sensor chip can be packaged into a Ø5x14 cm stainless steel housing, as shown in figure 7-2. This housing can be deployed to 3000 m depth. The thickness of the housing could be increased to support full ocean depth, at 6000 m.

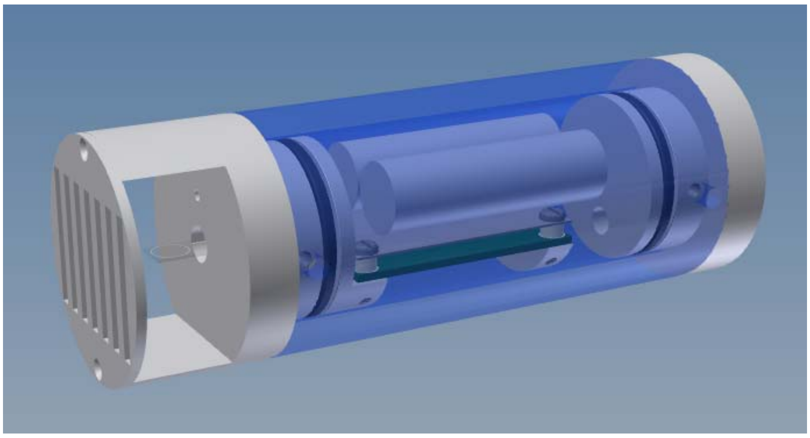

Figure 7-2 3D diagram of the version 3 CT-DO system with a Ø5x14 cm stainless steel packaging and a sensor chip of design 3.

In a collaboration with the University of Bologna, Italy we are developing an ASIC that replaces all the discrete electronics. This ASIC supports 4-channel impedance measurement with sine wave excitation. By replacing the analogue circuit in figure 7-1 with this ASIC, the PCB dimensions are reduced to about Ø1x5 cm. Together with the CT-DO sensor chip of design 3, the whole system can be the size of a pen, which would be similar in size to the commercial fish tags (Star-Oddi DST CTD and Hyldgard's multi-sensor system), but with much superior performance.

References

[1] *Team Indian Ocean 3100.* Available: "http://www.indianocean3100.com/.", 2012.

[2] B. G. Grossman*, et al.*, "In situ device for salinity measurements (chloride detection) of ocean surface," *Optics and Laser Technology,* vol. 37, pp. 217-223, Apr 2005.

[3] D. Malarde*, et al.*, "High-resolution and compact refractometer for salinity measurements," *Measurement Science & Technology,* vol. 20, Jan 2009.

[4] Y. Zhao and Y. Liao, "Novel optical fiber sensor for simultaneous measurement of temperature and salinity," *Sensors and Actuators B: Chemical,* vol. 86, pp. 63-67, 2002.

[5] P. Grosso*, et al.*, "Practical versus absolute salinity measurements: New advances in high performance seawater salinity sensors," *Deep Sea Research Part I: Oceanographic Research Papers,* vol. 57, pp. 151-156, 2010.

[6] J. Cong*, et al.*, "Fiber optic Bragg grating sensor based on hydrogels for measuring salinity," *Sensors and Actuators B: Chemical,* vol. 87, pp. 487-490, 2002.

[7] "Welcome to the World of Salinometry!". Available: "http://www.salinometry.com/salinity-history/?start=5", 2012.

[8] E. L. Lewis, "The Practical Salinity Scale of 1978 and Its Antecedents," *Marine Geodesy,* vol. 5, pp. 351-357, 1982.

[9] UNESCO, "The practical salinity scale 1978 and the international equation of state of seawater 1980. Tenth report of the Joint Panel on Oceanographic Tables and standards,(JPOTS)," *UNESCO Technical Paper in Marine Science,* vol. 36, 1981.

[10] E. L. Lewis, "The Practical Salinity Scale 1978 and Its Antecedents," *Ieee Journal of Oceanic Engineering,* vol. 5, pp. 3-8, 1980.

[11] T. M. Dauphinee, "Special Issue on the Practical Salinity Scale 1978 - Introduction," *Ieee Journal of Oceanic Engineering,* vol. 5, pp. 1-2, 1980.

[12] *MATLAB*. Available: "http://www.mathworks.co.uk/products/matlab/.", 2012.

[13] E. L. Lewis and R. G. Perkin, "The practical salinity scale 1978: conversion of existing data," *Deep Sea Research Part A. Oceanographic Research Papers,* vol. 28, pp. 307-328, 1981.

[14] R. Perkin and E. Lewis, "The Practical Salinity Scale 1978: Fitting the data," *Oceanic Engineering, IEEE Journal of,* vol. 5, pp. 9-16, 1980.

[15] J. Piccard and R. S. Dietz, "Oceanographic observations by the bathyscaph Trieste (1953–1956)," *Deep Sea Research (1953),* vol. 4, pp. 221-229, 1957.

[16] *Star-Oddi.* Available: "http://www.star-oddi.com.", 2012.

[17] *CTD SBE911 plus*. Available: "http://www.seabird.com/products/spec_sheets/911data.htm", 2012.

[18] *Keller-Druck Pressure Sensor*. Available: "http://www.keller-druck.com/english/homee/hmprode.html", 2012.

[19] *Intersima Pressure Sensor.* Available: "http://www.intersema.ch/.", 2012.

[20] *G.E-MEMS Pressure sensor.* Available: "http://www.ge-mcs.com/en/pressure-mems.html", 2012.

[21] Seabird Electronics Inc., "Conductivity Sensors for Moored and Autonomous O peration". Available: "http://www.seabird.com/technical_references/condpaper.htm", 2012.

[22] W. D. Gong*, et al.*, "Oceanographic Sensor for in-situ temperature and conductivity monitoring," *Oceans 2008 - Mts/Ieee Kobe Techno-Ocean, Vols 1-3,* pp. 42-47, 2008.

[23] X. J. Li and G. C. M. Meijer, "A low-cost and accurate interface for four-electrode conductivity sensors," *Ieee Transactions on Instrumentation and Measurement,* vol. 54, pp. 2433-2437, Dec 2005.

[24] P. M. Ramos*, et al.*, "A four-terminal water-quality-monitoring conductivity sensor," *Ieee Transactions on Instrumentation and Measurement,* vol. 57, pp. 577-583, Mar 2008.

[25] T. Horiuchi*, et al.*, "Long-term stability of a new conductivity-temperature sensor tested on the VENUS cabled observatory," in *OCEANS 2010 IEEE - Sydney*, Sydney, NSW, Australia, 2010, pp. 4 pp.-4 pp.

[26] T. Horiuchi*, et al.*, "Long-Term Test of a New Conductivity and Temperature Sensor," *Sea Technology,* vol. 51, pp. 37-40, Feb 2010.

[27] K. Striggow and R. Dankert, "The Exact Theory of Inductive Conductivity Sensors for Oceanographic Application," *Ieee Journal of Oceanic Engineering,* vol. 10, pp. 175-179, 1985.

[28] A. J. Fougere, "New non-external field inductive conductivity sensor (NXIC) for long term deployments in biologically active regions," *Oceans 2000 Mts/Ieee - Where Marine Science and Technology Meet, Vols 1-3, Conference Proceedings,* pp. 623-630, 2000.

[29] S. P. Natarajan*, et al.*, "Contact-less toroidal fluid conductivity sensor based on RF detection," *Proceedings of the IEEE Sensors 2004, Vols 1-3,* pp. 304-307, 2004.

[30] J. E. B. Randles, "Kinetics of rapid electrode reactions," *Discussions Faraday Soc.,* vol. 1, pp. 11-19, 1947.

[31] J. E. B. Randles, "Kinetics of rapid electrode reactions," *Transactions of the Faraday Society,* 1947.

[32] A. J. Bard and L. R. Faulkner, *Electrochemical methods : fundamentals and applications*, 2nd ed. New York: Wiley, 2001.

[33] P. J. Mohr*, et al.*, "CODATA recommended values of the fundamental physical constants: 2006," *Journal of Physical and Chemical Reference Data,* vol. 37, pp. 1187-1284, Sep 2008.

[34] K. F. Han*, et al.*, "High-frequency, complex dielectric permittivity of saline solution at elevated temperatures," *Geoscience and Remote Sensing, IEEE Transactions on,* vol. 29, pp. 48-56, 1991.

[35] *COMSOL*. Available: "http://www.comsol.com/.", 2012.

[36] A. Hyldgard*, et al.*, "Direct media exposure of MEMS multi-sensor systems using a potted-tube packaging concept," *Sensors and Actuators a-Physical,* vol. 142, pp. 398-404, Mar 10 2008.

[37] A. Hyldgard*, et al.*, "Autonomous multi-sensor micro-system for measurement of ocean water salinity," *Sensors and Actuators a-Physical,* vol. 147, pp. 474-484, Oct 3 2008.
[38] H. A. Broadbent*, et al.*, "A miniature, low cost CTD system for coastal salinity measurements," *Measurement Science & Technology,* vol. 18, pp. 3295-3302, Nov 2007.
[39] M. Berger, *et al*., "Measuring Ocean Salinity with ESA's SMOS Mission". Available: "http://esamultimedia.esa.int/docs/Cryosat/ESABulletin111-SMOSOSactivities.pdf", 2012.
[40] "Technical Notes: Thermocouple Accuracy". Available: "http://www.microlink.co.uk/tctable.html", 2012.
[41] "Thermoelectric Materials for Thermocoples". Available: "http://www.msm.cam.ac.uk/utc/thermocouple/pages/ThermocouplesOperatingPrinciples.html", 2012.
[42] *NIST ITS-90 Thermocouple Database*. Available: "http://srdata.nist.gov/its90/main/.", 2012.
[43] *2804A Quartz Thermometer*. Available: "http://www.metrictest.com/catalog/pdfs/product_pdfs/hp_2804a.pdf", 2012.
[44] " The Linear Quartz Thermometer - a New Tool for Measuring Absolute and Difference Temperatures". Available: "http://www.hparchive.com/Journals/HPJ-1965-03.pdf", 2012.
[45] *TS Series Miniature Quartz Temperature Sensor*. Available: "http://www.statek.com/products/pdf/10162.pdf", 2012.
[46] G. C. M. Meijer and A. W. Herwaarden, *Thermal sensors*. Bristol, UK ; Philadelphia: Institute of Physics Pub., 1994.
[47] T. Ricolfi and J. Scholz, *Thermal sensors*. Weinheim, F.R.G. ; New York, N.Y., USA: VCH, 1990.
[48] H. van Haren*, et al.*, "A fast and accurate thermistor string," *Journal of Atmospheric and Oceanic Technology,* vol. 18, pp. 256-265, 2001.
[49] R. A. Petitt*, et al.*, "A new conductivity-temperature-depth device for high resolution oceanographic measurements," in *Oceans 2005, Vols 1-3*, ed New York: Ieee, 2005, pp. 1070-1074.
[50] *SBE 3S*. Available: "http://www.seabird.com/products/spec_sheets/3Sdata.htm", 2012.
[51] "Error Sources That Effect Platinum Resistance Thermometer Accuracy, Part 3 - Stability," 2012.
[52] "Error Sources That Effect Platinum Resistance Thermometer Accuracy Part 4 - Repeatability," 2012.
[53] S. Aravamudhan*, et al.*, "MEMS based Conductivity-Temperature-Depth (CTD) sensor for harsh oceanic environment," in *Oceans 2005, Vols 1-3*, ed New York: Ieee, 2005, pp. 1785-1789.
[54] C. Pedersen*, et al.*, "Highly reliable O-ring packaging concept for MEMS pressure sensors," *Sensors and Actuators a-Physical,* vol. 115, pp. 617-627, Sep 21 2004.
[55] C. Pedersen*, et al.*, "Combined differential and static pressure sensor based on a double-bridged structure," *Ieee Sensors Journal,* vol. 5, pp. 446-454, Jun 2005.
[56] C. W. Waidner*, et al.*, *A Wheatstone bridge for resistance thermometry*. Washington,: Govt; print. off., 1915.
[57] F. Wenner and A. W. Smith, *Measurement of low resistance by means of the Wheatstone bridge*. Washington,: U.S. Govt. Print. Off., 1924.

[58] N. L. Brown, "A High Performance Micro-Power Ctd Sensor," *Ocean 94 - Oceans Engineering for Today's Technology and Tomorrow's Preservation, Proceedings, Vol 1,* pp. A385-A390
905, 1994.
[59] T. Radil*, et al.*, "Impedance measurement with sine-fitting algorithms implemented in a DSP portable device," *Ieee Transactions on Instrumentation and Measurement,* vol. 57, pp. 197-204, Jan 2008.
[60] P. M. Ramos*, et al.*, "Low frequency impedance measurement using sine-fitting," *Measurement,* vol. 35, pp. 89-96, Jan 2004.
[61] *Sea-Bird Electronics, Inc.*. Available: "http://www.seabird.com.", 2012.
[62] *JFE Advantech Co., Ltd.*Available: "http://www.jfe-alec.co.jp/html/english_top.htm", 2012.
[63] *Cefas G5.* Available: "http://www.cefastechnology.co.uk/products_tags_g5.htm", 2012.
[64] W. D. Gong, "Ocean sensors : for marine environmental monitoring," *Thesis (Ph.D.) - University of Southampton, School of Electronics and Computer Science,* 2010.
[65] N. Brown, " 4-electrode Conductivity Sensor with Zero External Field". Available: "http://www.patentgenius.com/patent/6720773.html.", 2012.
[66] R. W. Schmitt and R. A. Petitt, "A fast response, stable CTD for gliders and AUVs," in *Oceans 2006*, Boston, MA,, 2006, pp. 5 pp.-5 pp.
[67] *Argo Float*. Available: "http://www.argo.ucsd.edu/.", 2012.
[68] "the Argo CTD -- SBE 41/41CP CTD Module for Autonomous Profiling Floats". Available: "http://www.seabird.com/alace.htm", 2012.
[69] *Cefas G5.*Available: "http://www.cefastechnology.co.uk/g5/G5tag.pdf.", 2012.
[70] F. J. Millero, *Chemical oceanography*, 3rd ed. Boca Raton: CRC/Taylor and Francis, 2006.
[71] L. C. Clark, Jr., "Continuous recording of blood oxygen content," *Surg Forum,* vol. 11, pp. 143-4, 1960.
[72] L. C. Clark, Jr.*, et al.*, "Continuous recording of blood oxygen tensions by polarography," *Journal of Applied Physiology,* vol. 6, pp. 189-93, Sep 1953.
[73] J. W. Severinghaus and P. B. Astrup, "History of blood gas analysis. IV. Leland Clark's oxygen electrode," *J Clin Monit,* vol. 2, pp. 125-39, Apr 1986.
[74] D. Pletcher and S. Sotiropoulos, "A Study of Cathodic Oxygen Reduction at Platinum Using Microelectrodes," *Journal of Electroanalytical Chemistry,* vol. 356, pp. 109-119, Sep 15 1993.
[75] *YSI 5300A Biological Oxygen Monitor.* Available: "http://www.ysilifesciences.com/index.php?page=ysi-5300a-biological-oxygen-monitor", 2012.
[76] *SBE 43 Dissolved Oxygen (DO) Sensor*. Available: "http://www.seabird.com/products/spec_sheets/43data.htm", 2012.
[77] Available: "http://www.warneronline.com/product_info.cfm?id=375", 2012.
[78] Available: "http://www.rankbrothers.co.uk/prod1.htm", 2012.
[79] N. P. Revsbech, "An Oxygen Microsensor with a Guard Cathode," *Limnology and Oceanography,* vol. 34, pp. 474-478, Mar 1989.
[80] *Oxygen Sensor (Model 1302)*, Available: "http://www.unisense.com/Default.aspx?ID=443", 2012.
[81] R. Prien*, et al.*, "Development and first results of a new fast response microelectrode DO-sensor," *Oceans 2005 - Europe, Vols 1 and 2,* pp. 744-747, 1430, 2005.

[82] R. D. Prien*, et al.*, "Development and first Results of a new mesoporous Microclectrode DO-Sensor," *Oceans 2001 Mts/Ieee: An Ocean Odyssey, Vols 1-4, Conference Proceedings,* pp. 1910-1914, 2714, 2001.

[83] M. Sosna*, et al.*, "Development of a reliable microelectrode dissolved oxygen sensor," *Sensors and Actuators B-Chemical,* vol. 123, pp. 344-351, Apr 10 2007.

[84] M. Sosna*, et al.*, "Field assessment of a new membrane-free microelectrode dissolved oxygen sensor for water column profiling," *Limnology and Oceanography-Methods,* vol. 6, pp. 180-189, Apr 2008.

[85] S. M. Borisov and I. Klimant, "Ultrabright oxygen optodes based on cyclometalated lridium(III) coumarin complexes," *Analytical Chemistry,* vol. 79, pp. 7501-7509, Oct 1 2007.

[86] R. N. Glud*, et al.*, "An in situ instrument for planar O-2 optode measurements at benthic interfaces," *Limnology and Oceanography,* vol. 46, pp. 2073-2080, Dec 2001.

[87] I. Klimant*, et al.*, "Fast response oxygen micro-optodes based on novel soluble ormosil glasses," *Mikrochimica Acta,* vol. 131, pp. 35-46, 1999.

[88] G. Holst*, et al.*, "A novel measuring system for oxygen microoptodes based on a phase modulation technique," *Chemical, Biochemical, and Environmental Fiber Sensors Vii,* vol. 2508, pp. 387-398, 1995.

[89] A. Sharma and O. S. Wolfbeis, "Fiberoptic Oxygen Sensor Based on Fluorescence Quenching and Energy-Transfer," *Applied Spectroscopy,* vol. 42, pp. 1009-1011, Aug 1988.

[90] *AADI.* Available: "http://www.aadi.no/Default.htm", 2012.

[91] *AADI Oxygen Sensors*. Available: "http://www.aadi.no/Aanderaa/Document%20Library/1/Data%20Sheets/Oxygen%20Optode.pdf", 2012.

[92] *AADI Oxygen Sensors*. "http://www.marine.calpoly.edu/PDF/2-oxygen_temperature_sensor_3930.pdf", 2012.

[93] *AADI Oxygen Optode 4330/4330F.* Available: "http://www.rsaqua.co.uk/uploads/pdfs/Products/AADI/Optode/Brochure_4330%28F%29_Oxygen_Sensor.pdf", 2012.

[94] C. Janzen*, et al.*, "Getting more mileage out of dissolved oxygen sensors in long-term moored applications," *2007 Oceans, Vols 1-5,* pp. 1889-1893, 2007.

[95] ACT, "State of Technology in the Development and Application of DO Sensors," ed, 2004.

[96] J. Lyklema*, et al.*, "DLVO-theory, a dynamic re-interpretation," *Advances in Colloid and Interface Science,* vol. 83, pp. 33-69, Dec 1 1999.

[97] H. G. L. Coster*, et al.*, "Impedance spectroscopy of interfaces, membranes and ultrastructures," *Bioelectrochemistry and Bioenergetics,* vol. 40, pp. 79-98, Aug 1996.

[98] B. W. Ninham, "Surface Forces - the Last 30 A," *Pure and Applied Chemistry,* vol. 53, pp. 2135-2147, 1981.

[99] *Molar Gas Constant*. Available: "http://physics.nist.gov/cgi-bin/cuu/Value?r|search_for=gas", 2012.

[100] *Faraday Constant.* Available: "http://physics.nist.gov/cgi-bin/cuu/Value?f|search_for=faradic", 2012.

[101] A. G. Dickson and C. Goyet, "Handbook of methods for the analysis of the various parameters of the carbon dioxide system in sea water.Version 2," *ORNL/CDIAC-74.,* 1994.

[102] N. N. Grenwood, *Chemistry and the elements*. [S.l.]: Butterworth Elsevier, 1997.

[103] R. C. Weast, *CRC handbook of chemistry and physics*, 1st Student ed. Boca Raton, FL: CRC Press, 1988.

[104] P. W. Atkins and J. De Paula, *Physical chemistry*, 9th ed. New York: W.H. Freeman, 2010.
[105] A. J. Bard*, et al.*, *Standard potentials in aqueous solution*. New York: M. Dekker, 1985.
[106] P. W. Atkins, *Physical chemistry*, 6th ed. New York: Freeman, 1998.
[107] J. Zhang, Ed., *PEM Fuel Cell Electrocatalysts and Catalyst Layers: Fundamentals and Applications*. 2008, p.^pp. Pages.
[108] J. Rossmeisl*, et al.*, "Electrolysis of water on (oxidized) metal surfaces," *Chemical Physics,* vol. 319, pp. 178-184, 2005.
[109] T. Morimoto*, et al.*, "Oxygen reduction electrode in brine electrolysis," *Electrochimica Acta,* vol. 45, pp. 4257-4262, 2000.
[110] P. T. Kissinger and W. R. Heineman, *Laboratory techniques in electroanalytical chemistry*. New York; Basel: Dekker, 1996.
[111] L. Delauney*, et al.*, "Biofouling protection for marine environmental sensors," *Ocean Science,* vol. 6, pp. 503-511, 2010.
[112] P. Woerther and A. Grouhel, "MAREL: Automated measurement network for the coastal environment," *Oceans'98 - Conference Proceedings, Vols 1-3,* pp. 1149-1154, 1998.
[113] L. Delauney and C. Compère, "An Example: Biofouling Protection for Marine Environmental Sensors by Local Chlorination
Marine and Industrial Biofouling." vol. 4, H.-C. Flemming*, et al.*, Eds., ed: Springer Berlin Heidelberg, 2009, pp. 119-134.
[114] P. Woerther, "Coastal environment of the Seine Bay area monitored by a new French system of automated measurement stations," *Operational Oceanography,* vol. 66, pp. 255-264, 2002.
[115] R. S. Patil*, et al.*, "Oxidation of Chloride Ion on Platinum Electrode: Dynamics of Electrode Passivation and its Effect on Oxidation Kinetics," *Industrial & Engineering Chemistry Research,* vol. 50, pp. 12946-12959, Dec 7 2011.
[116] *Candence ORACD*. Available: "http://www.cadence.com/", 2012.
[117] D. Halliday*, et al.*, *Fundamentals of physics*, 6th ed. New York: Wiley, 2001.
[118] *Resistance Thermometer*. Available: "http://en.wikipedia.org/wiki/Resistance_ thermometer" , 2012.
[119] R. W. Balluffi*, et al.*, *Kinetics of materials*. Hoboken, NJ: Wiley-Interscience, 2005.
[120] *Electrochemical methods*. New York: J. Wiley, 1986.
[121] R. G. Compton and C. E. Banks, *Understanding voltammetry*. Singapore [u.a.]: World Scientific, 2007.
[122] R. T. Ferrell and D. M. Himmelblau, "Diffusion coefficients of nitrogen and oxygen in water," *Journal of Chemical & Engineering Data,* vol. 12, pp. 111-115, 1967/01/01 1967.
[123] R. M. Wightman, "Microvoltammetric Electrodes," *Analytical Chemistry,* vol. 53, pp. 1125-&, 1981.
[124] K. Aoki and J. Osteryoung, "Formulation of the Diffusion-Controlled Current at Very Small Stationary Disk Electrodes," *Journal of Electroanalytical Chemistry,* vol. 160, pp. 335-339, 1984.
[125] K. Aoki and J. Osteryoung, "Diffusion-Controlled Current at the Stationary Finite Disk Electrode - Theory," *Journal of Electroanalytical Chemistry,* vol. 122, pp. 19-35, 1981.
[126] K. Aoki and J. Osteryoung, "Diffusion Controlled Current at a Stationary Finite Disk Electrode - Experiment," *Journal of Electroanalytical Chemistry,* vol. 125, pp. 315-320, 1981.

[127] U. Kaatze, "Fundamentals of Microwaves," *Radiation Physics and Chemistry,* vol. 45, pp. 539-548, Apr 1995.

[128] J. A. Schetz and A. E. Fuhs, *Handbook of fluid dynamics and fluid machinery*. New York: Wiley, 1996.

[129] V. L. Streeter, *Handbook of fluid dynamics*, 1st ed. New York,: McGraw-Hill, 1961.

[130] M. Sosna, "Oxygen reduction at microelectrodes : application to the dissolved oxygen sensor for in situ oceanographic measurements " *Thesis (Ph.D.) - University of Southampton, School of Chemistry,* 2006.

[131] A. M. Bond*, et al.*, "A comparison of the chronoamperometric response at inlaid and recessed disc microelectrodes," *Journal of Electroanalytical Chemistry and Interfacial Electrochemistry,* vol. 249, pp. 1-14, 1988.

[132] P. N. Bartlett and S. L. Taylor, "An accurate microdisc simulation model for recessed microdisc electrodes," *Journal of Electroanalytical Chemistry,* vol. 453, pp. 49-60, 1998.

[133] R. Ferrigno*, et al.*, "Finite element simulation of the chronoamperometric response of recessed and protruding microdisc electrodes," *Electrochimica Acta,* vol. 42, pp. 1895-1903, 1997.

[134] *Analog devices, AD822*. Available: "www.analog.com/static/imported-files/data_sheets/AD822.pdf", 2012.

[135] *Analog Devices, AD623*. Available: "http://www.analog.com/static/imported-files/data_sheets/AD623.pdf", 2012.

[136] *CQPIC*. Available: "http://www002.upp.so-net.ne.jp/morioka/cqpic.html.", 2012.

[137] *VHDL*. Available: "http://en.wikipedia.org/wiki/VHDL.", 2012.

[138] *Verilog*. Available: "http://en.wikipedia.org/wiki/Verilog.", 2012.

[139] *Microchip PIC16F84*. Available: "http://www.microchip.com/wwwproducts/devices.aspx?ddocname=en010230", 2012.

[140] *CCS Compiler*. Available: "http://www.ccsinfo.com/", 2012.

[141] T. E. Tang*, et al.*, "The operation of platinum oxygen sensing microelectrodes," *J Bioeng,* vol. 2, pp. 381-8, 1978.

[142] D. Pletcher and S. Sotiropoulos, "Towards a microelectrode sensor for the determination of oxygen in waters," *Analytica Chimica Acta,* vol. 322, pp. 83-90, 1996.

[143] R. Lyons and R. Yates, "Reducing ADC quantization noise," *Microwaves & Rf,* vol. 44, pp. 72-+, Jun 2005.

[144] *FLUKE Hart 7012.* Available: "http://www.fluke.co.uk/", 2012.

[145] *SBE 35 Deep Ocean Standards Thermometer*. Available: "http://www.seabird.com/products/spec_sheets/35data.htm", 2012.

[146] *Epcos NTC Thermistors.* Available: "http://docs-europe.electrocomponents.com/webdocs/07eb/0900766b807eb3ba.pdf", 2012.

[147] *Grant GD100 Immersion Thermostat*. Available: "http://www.grantinstruments.com/gd100-immersion-thermostat/ ", 2012.

[148] *Isotechna F250 Thermometer.* Available: "http://www.isotechna.com/", 2012.

[149] *Portasal Salinometer 8410A.* Available: " http://www.osil.co.uk/Products/Marine/tabid/56/agentType/View/PropertyID/68/Default.aspx", 2012.

[150] *Araldite 2020 Epoxy Glue.* Available: "http://www.huntsmanservice.com/Product_Finder/ui/PSDetailProductList.do?pInfoSBUId=9&PCId=3353", 2012.

[151] *YSI Model 30 CTD Probe.* Available: "http://www.ysi.com/productsdetail.php?30-28", 2012.

[152] *Epo-tek 302-3M Epoxy Glue.* Available: "http://www.epotek.com/SSCDocs/datasheets/302-3M.PDF", 2012.

[153] M. K. Harun*, et al.*, "The effect of surface modification on the cathodic disbondment rate of epoxy and alkyd coatings," *Progress in Organic Coatings,* vol. 54, pp. 317-321, 2005.

[154] *Trimethoxysilane*. Available: "http://www.2spi.com/catalog/chem/trimethoxysilane.php", 2012.

[155] *Idronaut Ocean Seven 320 Plus CTD Probe.* Available: "http://www.idronaut.it/products-multiparameter-probes", 2012.

[156] *3M ECG-2702 Coating Material.* Available: "http://solutions.3m.co.uk/wps/portal/3M/en_GB/NovecSurface/Modifers/Performance", 2012.

[157] *NASA Log Skin Fitting*. Available: "http://www.nasamarine.com/proddetail.php?prod=14_Log_skin_fitting", 2012.

[158] *YSI 3100 Laboratory Conductivity Instrument.* Available: "http://www.ysi.com/productsdetail.php?3100-31", 2012.

[159] *National Simeconductor LMP7721.* Available: "www.national.com/pf/LM/LMP7721.html", 2012.

Appendix A – Matlab Script for Salinity Calculation

```
function s=salinity_cal(c,t,p)
% A function for salinity calculation
% Created by Xi Huang in 12/11/2009
% s - salinity between 2 ~ 42, in psu
% c - conductivity in mS/cm
% t - temperature between -2 ~ 35, in ºC
% p - pressure between 0 ~ 10,000, in dbar

k15=42.91416; %conductivity for K15
R=c./k15; %conductivity K15 ratio

%polynomial coefficients for s from K15 ratio R^0.5
a=[0.008, -0.1692, 25.3851, 14.0941, -7.0261, 2.7081];

%polynomial coefficients for modification of s for different
%temperature and pressure from K15
b=[0.0005, -0.0056, -0.0066, -0.0375, 0.0636, -0.0144];

%polynomial coefficients for temperature factor 1
ct=[0.6766097, 2.00564e-2, 1.104259e-4, -6.9698e-7, 1.0031e-9];

%polynomial coefficients for numerator of pressure factor
d=[3.426e-2, 4.464e-4, 4.215e-1, -3.107e-3];

%polynomial coefficients for denominator of pressure factor
e=[2.070e-4, -6.370e-8, 3.989e-12];

%temperature factor 2
k=0.0162;

%temperature factor 1
rrt=ct(1)+ct(2).*t+ct(3).*t.^2+ct(4).*t.^3+ct(5).*t.^4;

%pressure factor
Rp=1+(p.*(e(1)+e(2).*p+e(3).*p.^2))./(1+d(1).*t+d(2).*t.^2+(d(3)+d(4).
*t).*R);

%K15 ratio modified by temperature and pressure factors
Rt=R./rrt./Rp;

%calculate total salinity
s=0;
ds=0;
for m=1:6
    Rtc=Rt.^(0.5*(m-1));
    s=s+a(m).*Rtc;
    ds=ds+b(m).*Rtc;
end
s=s+(t-15)./(1+k.*(t-15)).*ds;
```

Appendix B – Chip Fabrication Flow

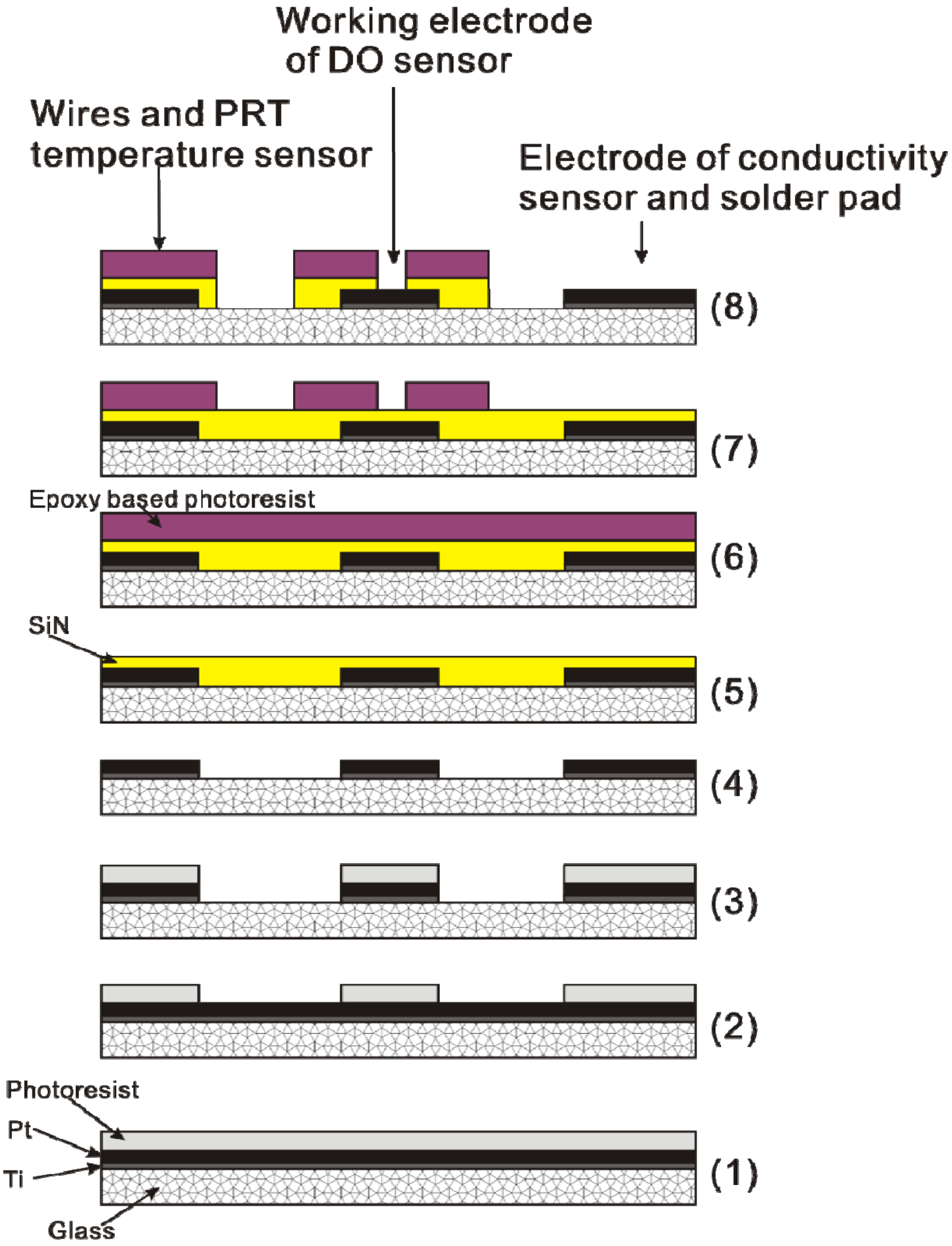

A diagram demonstrating the fabrication flow of the sensor chip.

As shown in the diagram. There are 8 steps in the fabrication:

1. Photoresist is coated to a wafer, which has glass substrate covered with 20 nm Titanium (Ti) and then 100~300 nm Platinum (Pt).
2. Photoresist is exposed and developed to form the pattern where Pt needs to remain after the fabrication.
3. Uncovered Pt and Ti are removed by ion beam milling.
4. Photoresist is removed by acid cleaning.
5. Wafer is coated by silicon nitride (SiN).
6. Wafer is coated by epoxy based photoresist.
7. Epoxy based photoresist is exposed and developed to form the pattern where Pt and glass should not be exposed.
8. Uncovered SiN is etched.

In this process, the epoxy based photoresist is SY320 for design 1 and SU8 for design 2. Step (5) and (8) are not applied to design 1 as there is no SiN in this design.